Electrochemical Oxidation of 5-Hydroxymethylfurfural Using the Supported Ionic Liquid Phase Approach

Elektrochemische Oxidation von 5-Hydroxymethylfurfural durch Nutzung der Supported Ionic Liquid Phase

TECHNISCHE UNIVERSITÄT DARMSTADT

Vom Fachbereich Chemie
der Technischen Universität Darmstadt

zur Erlangung des Grades

Doktor-Ingenieur
(Dr.-Ing.)

Dissertation
von Sebastian Wöllner

Erstgutachter: Prof. Dr.-Ing. Dipl.-Kfm. Bastian J. M. Etzold

Zweitgutachter: Prof. Dr. Marcus Rose

Darmstadt 2023

Tag der Einreichung: 16. Mai 2023

Tag der mündlichen Prüfung: 03. Juli 2023

Erklärungen laut Promotionsordnung

§8 Abs. 1 lit. c PromO

Ich versichere hiermit, dass die elektronische Version meiner Dissertation mit der schriftlichen Version übereinstimmt und für die Durchführung des Promotionsverfahrens vorliegt.

§8 Abs. 1 lit. d PromO

Ich versichere hiermit, dass zu einem vorherigen Zeitpunkt noch keine Promotion versucht wurde und zu keinem früheren Zeitpunkt an einer in- oder ausländischen Hochschule eingereicht wurde.

§9 Abs. 1 PromO

Ich versichere hiermit, dass die vorliegende Dissertation selbständig und nur unter Verwendung der angegebenen Quellen verfasst wurde.

§9 Abs. 2 PromO

Die Arbeit hat bisher noch nicht zu Prüfungszwecken gedient.

Darmstadt, den 16.05.2023

_____
Sebastian Wöllner, M. Sc.

Publikationen

Die vorliegende Arbeit wurde bereits in Teilen veröffentlicht und auf Tagungen vorgestellt.

Publikationen

Wöllner, S., Nowak, T., Zhang, G. R., Rockstroh, N., Ghanem, H., Rosiwal, S., Brückner, A. & Etzold, B. J. M. (2021). Avoiding Pitfalls in Comparison of Activity and Selectivity of Solid Catalysts for Electrochemical HMF Oxidation. *ChemistryOpen*, *10*(5), 600-606.

Poster

Wöllner, S., Zhang, G.-R., Rockstroh, N., Brückner, A. & Etzold, B. J. M. (2018). Electrooxidation of water and 5-Hydroxymethylfurfural (HMF) on non-noble multi metal catalysts. *Electrochemistry 2018, 24.-26.9., Ulm*.

Wöllner, S., Nowak, T., Zhang, G.-R. & Etzold B. J. M. (2019). Full Cell Study of Electrooxidation of 5-Hydroxymethylfurfural (HMF) on Copper Foam. *52. Jahrestreffen Deutscher Katalytiker, 13.-15.3., Weimar*.

Danksagung

Bevor es zu der eigentlichen Arbeit geht, würde ich gerne die Gelegenheit nutzen, um mich bei all denjenigen zu bedanken, die mich auf dem langen Weg durch Studium und Promotion begleitet und auf verschiedenste Weisen unterstützt haben.

Zuallererst muss hier meine Mutter, Sylke, erwähnt werden, ohne die ich in meinem Leben niemals diesen Weg hätte gehen können, da sie mich von Anfang an auf verschiedenste Arten und Weisen gefordert und gefördert hat. Auch wenn es durch die Jahre nicht immer leicht war, hat sie mich auf dem richtigen Weg gehalten und war mir immer ein Anker in jeder Lebenssituation.
Der nächste Dank geht an meine Schwester, Lara, die mir mehr als einmal den Rücken freigehalten und mich in diversen Gesprächen oder Abendstunden so aus dem Alltag holen konnte, dass der Kopf auch mal frei hatte – wie es eben nur Geschwister können.

Des Weiteren würde ich gerne Prof. Dr.-Ing. Bastian Etzold als meinem Doktorvater danken, dass er mich schon für die Masterthesis und anschließend noch für die Promotion in seine Arbeitsgruppe aufgenommen hat. In den Jahren haben mich die vielen konstruktiven Gespräche immer wieder in die Spur zurückgeführt und mein Verständnis für Problemlösung geschärft, was mir schon häufiger außerhalb der Universität geholfen hat. Außerdem sei hier das entgegengebrachte Vertrauen sowie die Zusammenstellung der Arbeitsgruppe erwähnt.

Vielen Dank an die Mitglieder der Forschungsgruppe Etzold, die mir in den verschiedensten wissenschaftlichen Themen mit Rat und Tat zur Seite standen und dank derer ich lernen durfte, wie wichtig es ist, dass man gerne morgens auf die Arbeit geht. Spezieller Dank gilt hierbei Lucas Hüfner, Miriam Geißler, Stephan Schultheis, Andreas Widjaja, Felix Herold, Kai Brunnengräber, Katharina Jeschonek, Jana Schmidpeter und Jan Gläsel. Des Weiteren muss das gesamte V1-Büro und der restliche AK Etzold erwähnt werden.

Weiterer Dank geht auch an Dr. Gui-Rong Zhang, der über lange Jahre mein Gruppenleiter war und mir das Gebiet der Elektrochemie eröffnet und nähergebracht hat. Die Iterationsschleifen und wissenschaftlichen Gespräche waren ausschlaggebend für mein Verständnis wissenschaftlicher Arbeiten.
Auch Prof. Alfons Drochner soll hier nicht unerwähnt bleiben, der als vertrauensvoller Ansprechpartner in jeglicher Hinsicht für Ruhe und Entlastung sorgen konnte, wobei seine Expertise im Bereich der Reaktionstechnik, technischen Chemie und Didaktik gerade aus wissenschaftlicher Sicht noch wichtiger waren.

Auch den Teams aus den Werkstätten des Fachbereichs Chemie sei hier nochmals gedankt. Ohne eure Unterstützung wären manche Ideen nicht umsetzbar gewesen.

Zudem sei meinen Studenten, die in Form von Abschlussarbeiten oder Praktika meine Arbeit vorangebracht haben, gedankt. Ohne euren Einfallsreichtum, euren Fleiß und euren Input wäre diese Arbeit im jetzigen Umfang nicht möglich gewesen. Besonderer Dank gilt hierbei meinen beiden Masteranden Timothy Nowak und Simon Horsinka, aber natürlich auch Ariane Funk, Michael Gölz und Christian Schmitt.

Neben den Leuten aus der Arbeitsgruppe Etzold möchte ich natürlich noch den anderen Wegbegleitern meiner akademischen Laufbahn für viele kurzweilige Lerneinheiten, schweißtreibende Praktika, „unmögliche“ Klausuren sowie auch gesellige Abende, Kumpirbesuche und dem Zusammenhalt, was das viel zitierte Studentenleben ausmacht, danken. Neben den oben erwähnten Personen müssen hier noch Hanna Hübner, Charlotte Fritsch, Jannik Mayer, Florian Knaus, Bastian Brehm, Daniel Huth, Nicolai Schmitt, Julia Kießling, Martina Plank, Sabine Kanbach, Sina Stegmaier und Timo Imhof genannt werden.

Mein weiterer Dank geht an die vielen Menschen außerhalb der Universität, die Darmstadt für 9 Jahre lang zu einem unvergleichlichen Zuhause gemacht haben. Vorneweg führt kein Weg an der WG in der 16a vorbei, die durch David Dähn, Markus Frericks, Martin Büttner, Max Kaltschnee, Lukas Koog, Lucas Hüfner und Nicolas Hohmann eine Wohlfühloase für mich und jedwede Gäste war, welche immer eine offene Tür vorgefunden haben. Des Weiteren sei in dem Zusammenhang Pupistan mit den (weiteren) Personen Alicia Eitenmüller, Joanne Jung, Suse Streng, Katja Weber, Niels Hofacker und Lenard Kritzer erwähnt, welches gerade in Pandemiezeiten dafür gesorgt hat, dass man bei Verstand bleibt und die einen immer wieder daran erinnern, dass man sich Familie eben nicht aussuchen kann – Wo man es am wenigsten vermutet, da sitzt nunmal im Strudel der Fisch. Weiterer Dank geht an An-Phuc Hoang, Andreas Hoff, Benedikt Herbert, Jakob Kaufmann, Philipp Schlögl, Jensi und Timm.

Zu guter Letzt sei noch meiner restlichen Familie inkl. der Paten gedankt, die mich immer wieder auf verschiedenste Art und Weisen unterstützt haben – dieser bedingungslose Rückhalt war mir immer viel Wert. Ebenso sei auch der restliche Freundeskreis mit den Wasenjungs aus der Schule, der KV Krawallbrause, den Selboldern und den Äppler Fanatics genannt, deren Menschen so manche Freizeitgestaltung unvergesslich gemacht haben und mich auch mal aus dem Alltag holen konnten.

German abstract / Deutsche Zusammenfassung

Die Suche nach erneuerbaren Energien, die fossile Energieträger ersetzen, hat in den letzten Jahren an Aufmerksamkeit gewonnen. Für eine nachhaltigere Zukunft sind zwei Möglichkeiten in den Fokus gerückt: Zum einen könnten Abfälle und Energieverluste vorhandener Prozesse durch geschlossene Material- und Energiekreisläufe minimiert werden. Auf der anderen Seite besteht die Möglichkeit, nachhaltiges, umweltfreundliches Rohmaterial zu nutzen, um einen natürlichen Materialkreislauf zu erhalten. Eines dieser Materialien ist 5-Hydroxymethylfurfural (HMF), welches aus C_5- oder C_6-Zuckern hergestellt werden kann, welche wiederum in Biomasse vorkommen. Dessen Oxidationsprodukt 2,5-Furandicarbonsäure (FDCA) wird als möglicher Ersatz für die Terephthalsäure gehandelt, welche heutzutage für die Herstellung des Kunststoffs Polyethylenterephthalat (PET) genutzt wird, und welche aus Rohöl gewonnen wird. PET hat zusätzlich dazu mit über 50 Millionen hergestellten Jahrestonnen einen großen Markt, der der Forschung bezüglich der Reaktion von HMF zu FDCA auch einen wirtschaftlichen Anreiz gibt. Die Kombination aus nachhaltigem Rohstoff und großer wirtschaftlicher Möglichkeit macht aus HMF und FDCA mögliche zukünftige Plattformchemikalien.

Um das Potential von HMF weiter zu unterstreichen, können von diesem Molekül ausgehend weitere Monomere hergestellt werden. Caprolactam und Adipinsäure zählen zum Beispiel dazu, welche die Ausgangsmaterialien für die bekannten Polymere Perlon und Nylon bilden. HMF selbst kann aus Cellulose, Glucose oder auch Fructose gewonnen werden, welche in verschiedenen Pflanzen zu finden sind und somit einen natürlichen Rohstoff darstellen. Das Oxidationsprodukt FDCA hat als Monomer die Möglichkeit in verschiedenen Polymeren eingebunden zu werden: Verpackungen, wie eben erwähntes PET, aber auch erweiterte Technologien wie z.B. Kevlar sind Möglichkeiten.
Die Herstellung von FDCA aus HMF wurde bisher zum größten Teil mit Edelmetallen (Platin, Palladium, Rhodium) oder unedleren Katalysatoren (Eisen, Mangan) thermisch realisiert. Obwohl Ausbeuten an FDCA von bis zu über 99 % erhalten wurden, waren erhöhte Reaktionsbedingungen wie Temperatur und/oder Druck sowie ein Oxidationsmittel notwendig, um dies zu erreichen. Zusätzlich war das Reaktionsmedium stark basisch, was sich auf die Stabilität des Edukts auswirkt, da HMF bei alkalischer Umgebung mit einem pH > 12 zu langkettigen Huminen reagiert.
Ein weiteres Konzept ist die Aufwertung der Wasserelektrolyse, bei der an der Kathode Wasserstoff (H_2) und an der Anode Sauerstoff (O_2) entsteht. Während H_2 vielfältig in der chemischen Industrie aber auch als Energiequelle genutzt werden kann, ist O_2 in dem Falle ein nicht benötigtes Nebenprodukt. Hier setzt die Oxidation von HMF als Konzept an, welches anstelle des O_2 an der Anode zu FDCA oxidiert werden kann. Auch hier wurden erste Katalysatoren getestet, die bei Raumtemperatur und –druck FDCA Ausbeuten von bis zu 98 % erreicht haben, jedoch wiederum in stark basischen (pH = 14) Elektrolyten. Ein Nachteil hierbei ist auch, dass das Potential nicht beliebig erhöht werden kann, da ansonsten die Sauerstoffentwicklung primär gefördert wird. Homogene Katalysatoren oder Mediatoren könnten diese Herausforderung lösen, da sie eine hohe Selektivität besitzen und mildere Bedingungen benötigen.
Die supported ionic liquid phase (SILP) bietet sich dementsprechend als weiterer Ansatz an. Hierbei wird ein homogener Katalysator in einer hydrophoben ionischen Flüssigkeit (IL) gelöst und dieses Gemisch wird wiederum auf einer porösen Oberfläche immobilisiert. Damit wird im besten Fall der homogene Katalysator in der IL gehalten und die Reaktion zwischen Edukt und

Katalysator findet an der Phasengrenze zwischen IL und wässriger Phase statt. Dadurch wird das Abtrennen des homogenen Katalysators nach der Reaktion, welches als großer Nachteil dessen gilt, umgangen. 2,2,6,6-Tetramethylpiperidinyloxyl (TEMPO) käme als solcher Katalysator infrage, da es schon in elektrochemischen Oxidationsreaktionen zum Einsatz kommt und sich darüber hinaus noch selbst regenerieren kann.
In dieser Arbeit wird untersucht, ob TEMPO/IL-Kombinationen SILP-Katalysatoren bilden können, die zum einen katalytische Aktivität bezüglich der Oxidation von HMF, zum anderen aber auch die nötige Stabilität im Elektrolyten aufweisen. Letztgenannter muss zusätzlich so gewählt werden, dass die Reaktion mit genügend Oxidationsmittel versorgt wird, ohne eine Nebenreaktion mit dem Edukt HMF einzugehen.

Um diese Fragestellung bearbeiten zu können, wurden verschiedene Katalysatorsysteme hergestellt. Als heterogener Katalysator wurde Kupferschaum mit Hilfe von Kupfersulfatlösung elektrisch auf Kupfer abgeschieden. TEMPO Derivate mit Hydroxy-TEMPO (HT) oder Amino-TEMPO (AT) als Ausgangsmaterial wurden mit Acylchloriden (C12, C14, C16, C18) zu den entsprechenden Estern und Amiden umgesetzt, ebenso wurde Pyren-TEMPO (PT) synthetisiert. Zusätzlich dazu wurden kovalent an die IL gebundene TEMPO-Derivate (ATMIM und HTMIM BETI) hergestellt. Alle Produkte auf TEMPO Basis wurden mittels ESR und ^{1}H-NMR überprüft. Die erfolgreiche Synthese konnte an der chemischen Verschiebung des Protons an der funktionellen Gruppe überprüft werden, weil dessen chemische Umgebung am stärksten verändert wurde. Für die ILs fand ein Ionenaustausch zwischen einem Imidazoliumhalogenid (CnMIM X) und Li BETI statt, so dass CnMIM BETI mit n = 6, 10, 12, 14 hergestellt werden konnte. Alle ILs wurden mittels ^{1}H- und ^{19}F-NMR überprüft.
Elektrochemische Messungen wurden mit drei oder zwei Elektroden in selbstgebauten Elektrolysezellen durchgeführt, bei denen die anodische und die kathodische Kammer mittels einer Fritte getrennt werden können. Im Dreielektrodenaufbau wurden Cyclovoltammogramme (CVs), Elektrische Impedanzspektroskopie (EIS) und chronoamperometrische Messungen (CA) aufgenommen, während alle Elektrolyseergebnisse im Zweielektrodenaufbau mittels HPLC erhalten wurden. Hierbei wurde die Ausbeute an FDCA, die Faraday'sche Effizienz (*FE*) und der Verlust bestimmt sowie die Produktionsrate als neue Leistungszahl, bei der bestimmt wird, wieviel Produkt pro Zeit und pro benutztem Katalysator hergestellt wird.

Um verschiedene Katalysatorsysteme zu testen, musste zuerst ein einheitliches Messprotokoll entwickelt werden, so dass alle Ergebnisse miteinander vergleichbar sind. Hierfür wurde das Verhalten der involvierten Moleküle HMF, DFF, HMFCA, FFCA und FDCA in verschieden alkalischen Lösungen ohne angelegte Spannung getestet und mittels HPLC überwacht. Während HMFCA und FDCA keinerlei Reaktion aufwiesen, sind HMF, DFF und FFCA Nebenreaktionen eingegangen, deren Produkte nicht mehr detektiert werden konnten, womit auf eine Zerfallsreaktion geschlossen wurde. Hierbei war zu erkennen, dass eine höhere alkalische Konzentration einen schnelleren Abbau der Komponenten begünstigte. Als gut untersuchter Beispielkatalysator wurden die Messungen zur Erstellung des Messprotokolls mit Kupferschaum als Arbeitselektrode (WE) durchgeführt. Zuerst wurde dieser in 0,1 und 1 M KOH Lösung in einer ungeteilten und geteilten Zelle mit Platin (Pt) als Gegenelektrode (CE) genutzt. Hierbei fiel auf, dass die Ausbeute an FDCA in 0,1 und 1 M KOH um 29 bis 37 % anstieg, während der Verlust um 76 bis 84 % abfiel, sobald eine getrennte Zelle genutzt wurde. Dies ließ darauf schließen, dass an der Kathode auch ungewollte Nebenreaktionen stattfinden, weswegen für alle weiteren Messungen nur noch in getrennten Elektrolysezellen gemessen wurde. Für weitere Katalysatormessungen war ein inertes, aber leitfähiges Elektrodenmaterial

nötig, welches mit bordotiertem Diamant (BDD) gefunden wurde, bei dem jegliche Aktivität nur vom aufgetragenen Katalysator stammen kann. In weiteren Messungen erwies sich Pt als bestes Material für die Gegenelektrode, da die Hauptreaktion nicht gehemmt wurde.
Nachdem die Parameter bezüglich der Zelle festgesetzt waren, musste eine Routine zur Bestimmung der katalytischen Aktivität und Selektivität erstellt werden. Dabei wurden im Dreielektrodenaufbau CVs ohne und mit HMF aufgenommen, die anschließend voneinander abgezogen wurden. Somit wird die Hintergrundaktivität abgezogen und übrig bleibt das Potentialfenster, in dem eine Aktivität bezüglich der HMF Oxidation erwartet wird. Bei diesen mit Hilfe von EIS korrigierten Potentialen wurden nun CA durchgeführt, aus denen das Zellpotential zwischen WE und CE hervorging. Dieses Zellpotential wurde anschließend für eine Elektrolyse im Zweielektrodenaufbau genutzt, deren Ergebnisse mittels HPLC ausgewertet wurden. Hierbei wurde so viel Ladung in das System gegeben, wie ein theoretischer Umsatz von 100 % HMF zu FDCA gebraucht hätte.
Die eben genannten Parameter bezüglich der Zelle sowie die Reihenfolge des Messprotokolls wurden für jedes weitere Katalysatorsystem genutzt, welches in dieser Arbeit behandelt wurde.

Vorversuche mit TEMPO als Katalysator für die HMF Oxidation wurden mit homogen gelöstem Mediator durchgeführt. Dafür wurde ein Phosphatbuffer von pH 10 genutzt, um die Stabilität von TEMPO zu gewährleisten. Im Dreielektrodenaufbau zeigten sowohl TEMPO als auch das kommerziell zu erhaltende Derivat Methoxy-TEMPO (MT) eine Aktivität bei Zugabe von HMF, wobei diese bei Letzterem wesentlich deutlicher zu sehen war. MT wurde folglich in Lösung und immobilisiert auf einer MPL untersucht, wobei Ausbeuten von 59 und 39 % FDCA sowie *FEs* von 63 und 40 % erreicht wurden, während der Verlust bei 25 und 54 % lag, respektive. Diese höhere Aktivität für HMF Oxidation von MT in Lösung ergab auch eine fünf Mal höhere Produktionsrate. Da eine grundsätzliche Aktivität und Selektivität für die Oxidation von HMF zu FDCA zu erkennen war, wurden TEMPO, 4-Hydroxy-TEMPO-Benzoat (TB) als weiteres Derivat und MT in verschiedenen ILs gelöst und anschließend auf der MPL immobilisiert. TEMPO und TB zeigten nur in kurzkettigen ILs wie C3MIM NTf_2 Aktivität und erreichten FDCA Ausbeuten von bis zu 21 und 4 %, während der Verlust bei bis zu 33 und 13 % lag, respektive. MT wiederum erreichte auch in langkettigen ILs wie C6 und C10MIM NTf_2 Ausbeuten und *FEs* an FDCA von bis zu 57 %, während der Verlust nie 9 % überschritt. Ein klarer Trend, der sich hier zeigte, war der Anstieg der Reaktionszeit und damit die Verringerung der Produktionsrate je langkettiger die IL wurde, was mit der zunehmenden Viskosität einhergeht.

Bevor auf Basis der vielversprechenden ersten Versuche weitere SILP Kombinationen untersucht wurden, wurde das verwendete Elektrodenmaterial MPL 39 BB, eine kohlenstoffbasierte, mikroporöse Schicht, auf mögliche Aktivität bezüglich der HMF Oxidation getestet, was jedoch negativ ausfiel. Folglich wurden die ILs und die TEMPO Derivate zuerst einzeln auf die MPL aufgetragen. Dabei kamen die HT Derivate auf gerade mal eine FDCA Ausbeute von 8 % und mindestens 29 % Verlust. Die AT Derivate zeigten hingegen Ausbeuten an FDCA von 21 bis 69 % und Verluste von 3 bis 29 %. Die ILs wandelten zwar 29 bis 66 % um, jedoch nicht zu FDCA, da hier 3 % das Maximum waren. Stattdessen wuchs der Verlust parallel zum Umsatz auf 23 bis 55 % an.

Anschließend wurde zuerst das vorher schon vielversprechende MT mit den neuen ILs getestet und dabei waren Ausbeute und *FE* von FDCA nie niedriger als 64 bzw. 60 %, der Verlust nie höher als 5 % und die Produktionsrate lag zwischen 0.57 und 1.75 $mmol_{FDCA}\ s^{-1}\ mmol_{cat}^{-1}$. Besonders in C12MIM BETI konnte MT mit 99 % Ausbeute und *FE* bezüglich FDCA sowie mit

keinem Verlust und einer Produktionsrate von 1.03 $mmol_{FDCA}\ s^{-1}\ mmol_{cat}^{-1}$ ein nahezu ideales Ergebnis erzielen. Nachfolgend wurden die HT Derivate in den ILs gelöst, doch die Aktivität war ähnlich niedrig wie bei der einzelnen Messung: FDCA Ausbeute und dazugehörige *FE* blieben unter 9 %, der Verlust lag zwischen 13 und 40 % und die Produktionsrate überstieg nie 0.13 $mmol_{FDCA}\ s^{-1}\ mmol_{cat}^{-1}$. Die AT Derivate zeigten mit Ausbeuten und *FE*s bezüglich FDCA von bis zu 80 bzw. 78 %, nur einmal detektiertem Verlust von 29 % und Produktionsraten bis zu 1.78 $mmol_{FDCA}\ s^{-1}\ mmol_{cat}^{-1}$ wieder eine deutlich höhere Aktivität.
Das Problem war jedoch, dass keines dieser Systeme die Aktivität bei wiederholtem Benutzen halten konnte. Als bestes Beispiel dient MT in C12MIM BETI, welches nach der hohen Aktivität im ersten Durchgang bei wiederholtem Benutzen der gleichen Elektrode in frischem Elektrolyt keine Aktivität mehr aufweisen konnte. Ein Hinweis war im Elektrolyten nach zwölf Stunden CA zu finden, in dem sowohl IL als auch TEMPO gefunden wurde. Einzig C14-AT in C14MIM BETI konnte die FDCA Ausbeute (von 34 auf 30 %) mit einer ähnlichen Produktionsrate (von 0.21 auf 0.19 $mmol_{FDCA}\ s^{-1}\ mmol_{cat}^{-1}$) bei Wiederbenutzung halten. Im dritten Durchgang war dann allerdings auch keine Aktivität mehr zu sehen, da die Ausbeute von FDCA auf 5 % fiel und folgerichtig auch die Produktionsrate (0.03 $mmol_{FDCA}\ s^{-1}\ mmol_{cat}^{-1}$).

Um diesem Trend entgegenzuwirken wurde PT getestet, in der Hoffnung, dass das konjugierte π-System eine größere Wechselwirkung mit der kohlenstoffbasierten MPL eingeht. Bezüglich der Aktivität konnten 60 bzw. 64 % Ausbeute und *FE* bezüglich FDCA festgestellt werden bei keinem Verlust und 0.26 $mmol_{FDCA}\ s^{-1}\ mmol_{cat}^{-1}$ Produktionsrate. Die Wiederbenutzung dieser Elektrode führte allerdings wieder zu einem Verlust der Aktivität, so dass die Produktionsrate auf 0.07 $mmol_{FDCA}\ s^{-1}\ mmol_{cat}^{-1}$ fiel, was sich auch in der Ausbeute von nur 7 % FDCA widerspiegelte.

Ein weiterer Versuch, das aktive TEMPO auf dem Kohlenstoff zu halten, war die kovalente Verknüpfung von TEMPO und IL, wodurch HTMIM BETI und ATMIM BETI untersucht wurden. HTMIM BETI zeigte wie die restlichen HT Derivate kaum Aktivität bezüglich der HMF Oxidation auf. Folglich wurde hier kein Stabilitätstest durchgeführt. ATMIM BETI konnte in C12MIM BETI eine Ausbeute und eine *FE* von 93 % FDCA erreichen, was sich auch in der Produktionsrate von 1.11 $mmol_{FDCA}\ s^{-1}\ mmol_{cat}^{-1}$ und einem Verlust von 2 % niederschlägt. In diesem Zuge wurde auch ein Unterschied in der Aktivität bezüglich der HMF Oxidation in dem Verhältnis von ATMIM BETI zu C12MIM BETI festgestellt: Je konzentrierter das ATMIM BETI wurde, desto geringer wurden Ausbeute und *FE* von FDCA. Nichtsdestotrotz konnte das pure ATMIM BETI seine Performance bei einmaligem Wiederbenutzen halten, während beim dritten Durchgang wieder keine Aktivität zu sehen war. Alle anderen Verhältnisse konnten bei Wiederbenutzung nicht an ihre Performance anschließen, was sich wieder durch sowohl IL als auch ATMIM BETI im Elektrolyten erklären ließ.

Als letzte Variation wurde nun das Trägermaterial geändert, da anstatt eines direkten Auftragens auf die MPL nun kommerzielles Vulcan oder ein „polymer Derivat Carbon“ (PDC) zur Immobilisierung genutzt wurden. Hierfür wurde MT in einer kurzkettigen IL (C4MIM BETI) untersucht, um so wenig Transportlimitierung wie möglich zu generieren. Bei Vulcan als Trägermaterial war keine Aktivität bezüglich HMF Oxidation zu erkennen, das Elektrolyseergebnis war sehr ähnlich zu dem der blanken MPL, also zu reinem Kohlenstoff. Folglich konnte HMF nie von MT umgesetzt werden, da es den Katalysator nicht erreicht hat. Auf PDC konnte bei einem Umsatz von 38 % zumindest eine Ausbeute von 8 % FDCA erzielt werden. Auch das vorher aktive C14-AT in C6MIM BETI wurde auf PDC immobilisiert, wodurch

bei einem Umsatz von 35 % insgesamt 7 % Ausbeute und *FE* bezüglich FDCA detektiert werden konnten. Die Ausbeute von 26 % an FFCA wies darauf hin, dass dies das Hauptprodukt war und der letzte Schritt zu FDCA nicht bevorzugt wurde. Diese Hypothese bestätigte sich beim Verdreifachen der Ladung, bei der sich der HMF Umsatz und die Ausbeuten von FFCA und FDCA jeweils verdreifachten, das Selektivitätsmuster also im Verhältnis gleichblieb. Durch die geringe Aktivität wurden auch hier keine Stabilitätstests durchgeführt.

Abbreviations

Abbreviation	Meaning
^{1}H-NMR	Nuclear magnetic resonance with hydrogen as studied nucleus
^{19}F-NMR	Nuclear magnetic resonance with fluorine as studied nucleus
AA	Ascorbic acid
AC	Activated carbon
AT	4-Amino-TEMPO
ATMIM/HTMIM	4-Amino- or 4-hydroxy TEMPO coupled with methylimidazolium
BDD	Boron doped diamond
BETI	Bis(pentafluoroethylsulfonyl)imide
BHMF	2,5-Bishydroxymethylfuran
BTX	Mixture of benzene, toluene, xylene
C	Carbon
CA	Chronoamperometry
CE	Counter electrode
CnAT/CnHT	4-Amino- or 4-hydroxy TEMPO coupled with a chain of n carbon atoms
C_x sugar	Sugar molecule made of x carbon atoms
C_xMIM	1-C_x-3-methylimidazolium
CV	Cyclic voltammogram
DCM	Dichloromethane
DFF	2,5-Diformylfuran
DMAP	4-Dimethylaminopyridine
DMF	2,5-Dimethylfuran
DMSO	Dimethyl sulfoxide
DOE	US Department of Energy
e^-	Electron
EDC	N-(3-Dimethylaminopropyl)-N′-ethylcarbodiimide hydrochloride
EDX	Energy-dispersive X-ray spectroscopy
EG/GLY	Ethylene glycol
EIS	Electrochemical impedance spectroscopy

ESR	Electron spin resonance
EtOAc	Ethyl acetate
FAD	Flavin adenine dinucleotide
FDCA	2,5-Furandicarboxylic acid
FTO	Fluorine-doped tin oxide
GDL	Gas diffusion layer
GF	Graphite foil
HAP	Hydroxyapatite
HER	Hydrogen evolution reaction
HMF	5-Hydroxymethylfurfural
HMFCA	5-Hydroxymethylfuroic acid
HT	4-Hydroxy-TEMPO
IL	Ionic liquid
IP	Ionic polymer
LD_x	Lethal dose at which x percent of subjects will die
LDH	Layered double hydroxide
LIKAT	Leibniz-Institut für Katalyse e.V.
MeCN	Acetonitrile
MeOH	Methanole
MPL	Microporous layer
NF	Nickel foam
NTf_2	Bis(trifluoromethylsulfonyl)imide
OER	Oxygen evolution reaction
PBF	Poly(butylene 2,5-furandicarboxylate)
PDC	Polymer derived carbon
PEF	Polyethylene 2,5-furandicarboxylate
PET	Polyethylene terephthalate
POP	Porous organic polymer
PPF	Poly(propylene 2,5-furandicarboxylate)
PT	Pyrene-TEMPO

PTFE	Polytetrafluoroethylene
PVA	Polyvinyl alcohol
RE	Reference electrode
RHE	Reversible hydrogen electrode
SCILL	Solid catalyst with ionic liquid layer
SEM	Scanning electron microscope
SILP	Supported ionic liquid phase
TEMPO	(2,2,6,6-Tetramethylpiperidin-1-yl)oxyl
WE	Working electrode
wt-%	Weight percentage

Symbols

Symbol	Meaning	Unit
E/U	Electric potential versus reference electrode	kg m^2 A^{-1} s^{-3} vs. RE
F	Faraday constant	96485 A s mol^{-1}
FE (x)	Faradaic efficiency to product x	mol A s mol^{-1} A^{-1} s^{-1}
I	Current	A
j	Current density	A m^{-2}
m	Mass	kg
n	Amount of substance	mol
n_0	Amount of substance at $t = 0$	mol
p	Pressure	bar
Q	Amount of passed charge	A s
R	Resistance	kg m^2 A^{-2} s^{-3}
R_u	Uncompensated resistance	kg m^2 A^{-2} s^{-3}
S	Selectivity	mol mol^{-1}
T	Temperature	K
t	Time	s
X	Conversion	mol mol^{-1}
Y (x)	Yield of product x	mol mol^{-1}
z	Number of transferred electrons	-

Content

1 Introduction

The search for renewable instead of fossil resources gained attention in recent years, and sustainability and future-oriented aspects are paramount for chemical processes to replace finite fossil resources.[1],[2] To render chemistry more sustainable, there are two possibilities, which attract attention right now: 1) Waste streams and energy leakages are minimized or even diminished by closing material and energy loops.[3] 2) Sustainable grown biomass as environmentally friendly feedstock, thus utilizing natural materials cycle.[4] Regarding production, use of bio-based feedstock platform chemicals plays a major role, such as *e.g.* 5-Hydroxymethylfurfural (HMF) and its oxidation product 2,5-Furandicarboxylic acid (FDCA).[1] HMF itself can be derived from biomass (*e.g.* C_5/C_6 sugars[5]), which is considered a sustainable feedstock. FDCA on the other hand can substitute terephthalic acid, which is produced from crude oil and is primarily used as a precursor for polyethylene terephthalate (PET) that has an annual production of over 50 million tonnes.[6] So HMF oxidation (Scheme 1) features one of the most interesting synthesis routes involving a biomass based platform chemical and leading to a highly requested substitute for the polymer sector.[6]

Using anodic HMF oxidation in water-based electrolyte to yield FDCA opens the opportunity to generate hydrogen (H_2) as the cathodic product.[7] H_2 itself is suited to overcome issues like sustainability, environmental emissions and energy security in a possible hydrogen economy.[8],[9] Furthermore, it can be integrated in already existing energy and transport systems, while decarbonizing them at the same time as air pollution can be reduced this way.[9],[10] It can be utilized in a broad variety of promising future-oriented applications like power-to-power, power-to-gas, hydrogen refueling and stationary fuel cell.[10] Demand of hydrogen is around 70 million tons per year (2018), while its production is accountable for over 800 million tons of CO_2 per year,[11] which elevates electrolysis into a possible way to create hydrogen more sustainable.

Therefore, researching a suitable electrode and/or catalyst for electrochemical HMF oxidation attracted a lot of attention in recent years as it is the key for high energy and feedstock efficiency.[12],[13]

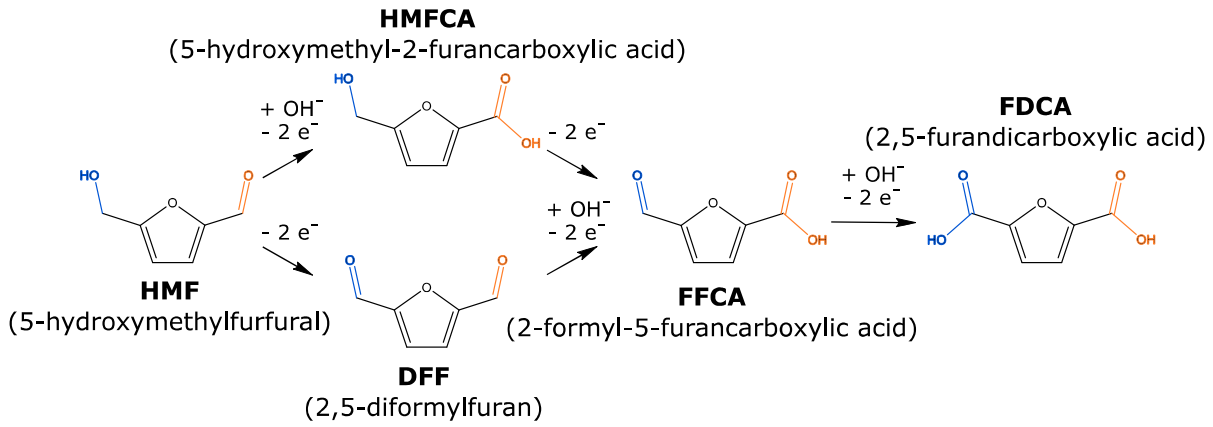

Scheme 1: Pathways of HMF oxidation to FDCA. Upper path: Aldehyde oxidation first to 5-hydroxymethyl-2-furancarboxylic acid (HMFCA) further to 2-formyl-5-furancarboxylic acid (FFCA). Lower path: Alcohol oxidation first to 2,5-diformylfuran (DFF) further to FFCA. Both paths end up with the last oxidation step from FFCA to FDCA.[14] Copyright Royal Society of Chemistry.

2 Research background and state of the art

HMF and FDCA have been considered as bio-based platform chemicals that will sustainably influence the future.[1] HMF stands out especially by its synthesis route starting at biomass and the possibility to be further processed to a broad range of products, as well as an important building block in bio-refinery processes.[15],[6] FDCA on the other side has the potential of a high production volume as it is considered a replacement for terephthalic acid, which has an annual production of over 50 million tons.[16],[17] Therefore, it can be applied in the polymer chemistry in the future.[15],[6]

2.1. HMF as a future platform chemical

In 1991, HMF is firstly described as a potential petro chemical that is easily extracted from renewable resources[18] and as key substance, which can substitute further processed products that are required in a large scale.[19] Almost 20 years later, BOZELL AND PETERSEN elevate HMF into the enlarged circle of future platform chemicals of the *US Department of Energy* (*DOE*),[20] since it meets some essential criteria: On the one hand HMF came to the fore through intensive research, on the other hand leads its broad product range to the classification of an important building block and potential platform chemical.[1]

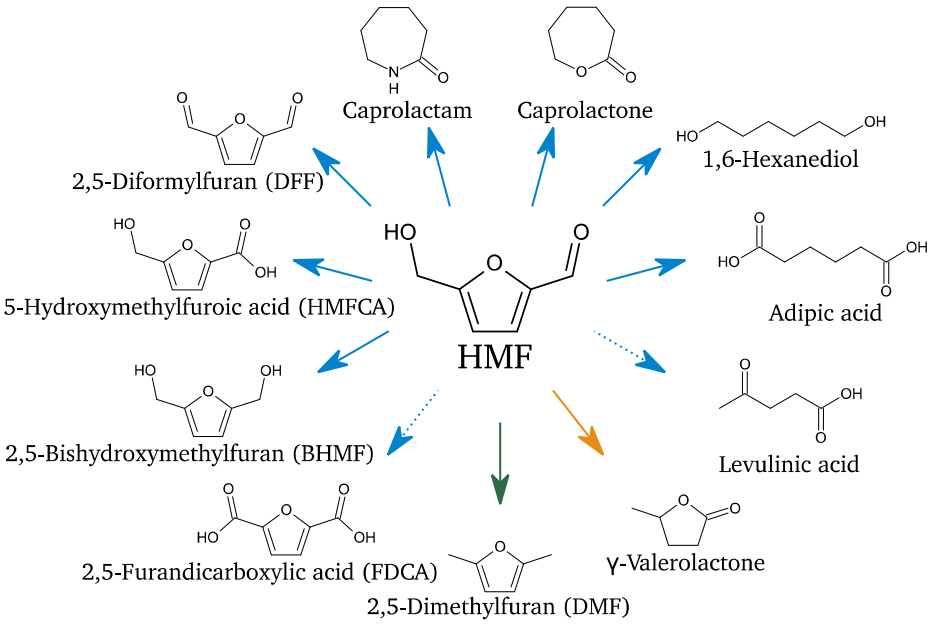

Scheme 2: HMF as a platform chemical.[21] Copyright American Chemical Society.

Some of these products synthesized from HMF can be seen in Scheme 2. They can be divided into different fields by their application as monomer (blue arrow: FDCA, 2,5-Bishydroxymethylfuran (BHMF), 5-Hydroxymethylfuroic acid (HMFCA), 2,5-Diformylfuran (DFF), Caprolactam, Caprolactone, 1,6-Hexanediol, Adipic acid, Levulinic acid), as solvent (orange arrow: γ-valerolactone) and their use in fuels (green arrow: 2,5-Dimethylfuran (DMF)). Some of them also have the potential to stand out as a platform chemical on their own (dashed line: Levulinic acid, FDCA).[21] Starting with the monomers, BHMF can be synthesized via dehydrogenation of HMF by sodium borohydride ($NaBH_4$),[22] different metal-based catalysts like 2 $CuO{\cdot}Cr_2O_3$, Co/SiO_2 or Pt/Al_2O_3[23] as well as even enteric bacteria.[24] The

resulting diol is employed as a standalone product as polyether in polyurethanes[25] or as a building component in polyesters. In the latter, BHMF is used as a monomer (*e.g.*, with FDCA)[26] as well as its completely saturated product (2,5-bis(hydroxymethyl)tetrahydrofuran).[15] HMFCA is an oxidation product of HMF and can be selectively produced by acetic acid bacteria (*Gluconobacteroxydans*)[27] or rod-shaped bacteria (*Serratia liquefaciens*).[28] It is applied in polymer chemistry, due to its alcohol as well as carboxylic acid side group.[29] Furthermore, its antitumor activity has been discovered, which makes HMFCA an interesting compound in the medical sector.[30]

Another oxidation product of HMF is DFF that is oxidized at the hydroxyl group rather than the aldehyde group as HMFCA is. For a selective oxidation, a broad variety of catalysts can be used: MnO_2 in CH_2Cl_2,[31] 4-acetamido-TEMPO (TEMPO: (2,2,6,6-Tetramethylpiperidin-1-yl)oxyl) with HNO_3/O_2 as oxidizing agent,[32] different vanadium salts and complexes in DMSO (dimethyl sulfoxide)[33] as well as vanadium and copper species applied onto polyvinyl pyridine in DMSO and toluene.[34] DFF's scope of application reaches from an intermediate for medication,[35] especially antimycotics,[36] over a precursor for conducting polymers[37] to a preparation compound for macrocycles.[38] In polymer chemistry, it is also utilized as a cross-linking agent for PVA (polyvinyl alcohol)[39] or as a monomer itself.[40],[41] FDCA could also be enqueued in this list of HMF oxidation products but chapter 2.2 will be focusing on synthesis and processing possibilities in detail. Scheme 3 shows reaction pathways to further process the so far introduced BHMF, DFF and FDCA to commonly used monomers like diamines, dichlorides and diisocyanates.[42] These can be utilized in polycondensations and polyadditions to create polyesters, polyamides or polyurethanes.[43]

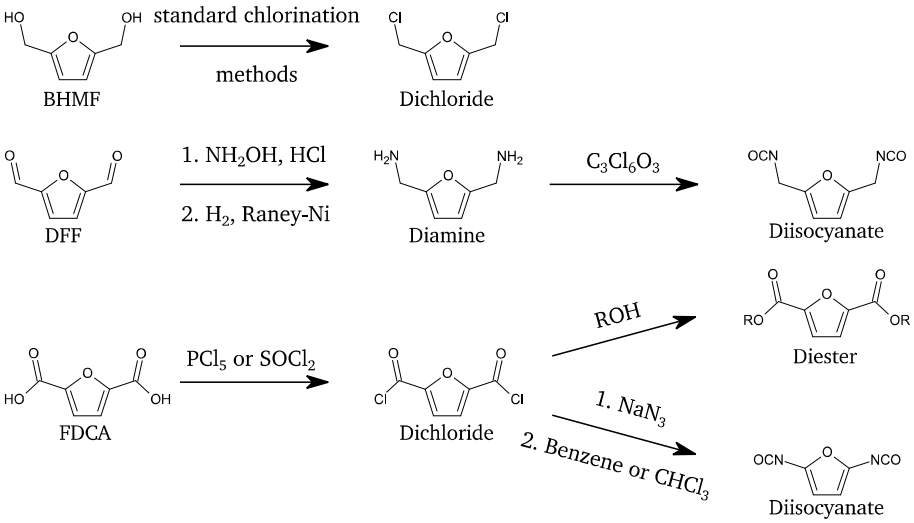

Scheme 3: Processing of BHMF (above), DFF (middle) and FDCA (below) to different monomers.[42] Copyright John Wiley & Sons – Books.

Caprolactam is mainly used as a monomer for resins and especially Nylon-6 fiber (Perlon®), which explains the annual production of 5.5 million tons (2016).[44] Almost every commercially used synthesis route depends on benzene out of the BTX (mixture of benzene, toluene, xylene) aromatics, which is converted to cyclohexane, cyclohexanone and finally cyclohexanone oxime as intermediate that is further processed to caprolactam via Beckmann rearrangement.[44] Thus, this six-stage process is (starting from benzene) completely based on fossil resources.[45] Scheme 4 shows an alternative synthesis route that allows a caprolactam synthesis starting from HMF in a four- to six-stage process.[45] The reduced product 2,5-THF-dimethanol (1) is generated first, before it is further processed to 1,6-hexanediol, whereat the yield was low (a).

A more fruitful approach is the indirect route over 1,2,6-hexanetriol (2) first, which yields in two additional possibilities to synthesize 1,6-hexanediol: the direct conversion (b) or another intermediate step (c) to tetrahydro-2H-pyran-2-ylmethanol (3). 1,6-Hexanediol stands out itself by an annual production of 70.000 tons and is also used in polymer chemistry, where it can enhance the flexibility and adhesion in polyesters and polyurethanes, due to its two terminal alcohol groups.[46] Furthermore, it can be utilized in the production of elastomers, adhesive agents, plasticizers and pharmaceuticals.[47],[48] The conversion from 1,6-hexanediol to caprolactone is well known and also published with a high yield of over 97 %,[49] but the use of hydrogen peroxide might inhibit an upscaling due to financial reasons.[45] A new approach features ruthenium-based catalysts as an alternative synthesis route from 1,6-hexanediol to caprolactone.[45],[50] Polycaprolactone, which results from ring-opening polymerization of caprolactone,[51] is a biodegradable polymer, which is for that reason used in drug delivery[52] and as a building block in scaffolds for tissue engineering.[53] Additional scopes of application reach from microelectronics,[54] over packaging[55] and adhesive agents[56] to casting resins.[57] The conversion of caprolactone to caprolactam is realized with ammonia and already implemented in industry.[57]

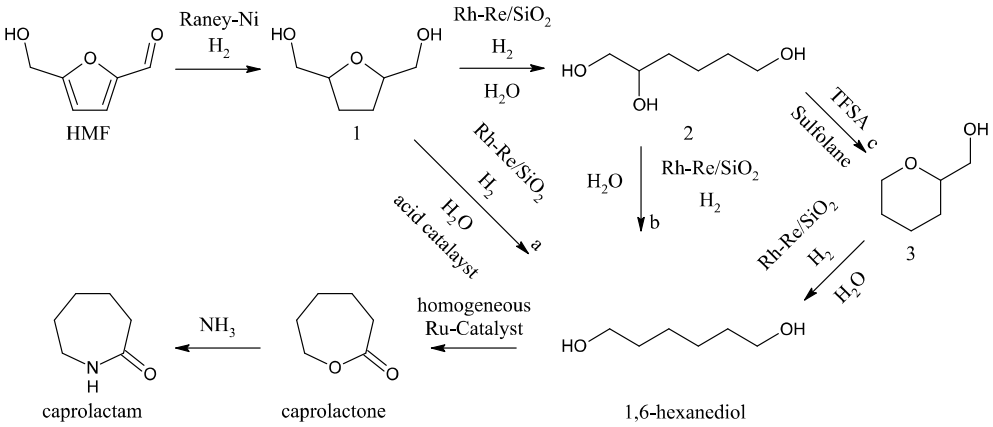

Scheme 4: Possibilities to further process HMF to 1,6-hexanediol, caprolactone and caprolactam.[45] Copyright John Wiley & Sons – Books.

Apart from caprolactam, adipic acid is the second monomer product of HMF that shows its economic importance with an annual production of 2.5 million tons (2014).[58] It is mainly used in polyamide 6,6 that consists of adipic acid and hexamethlyenediamine and is worldwide known as Nylon®.[59] Furthermore, adipic acid is utilized as an acidifying agent in food, as well as a building block in polyesters used as plasticizers, lubricants and polyurethane resins, which are used as foams, coatings or adhesive agents.[60] In industry, it is synthesized by nitric acid oxidation from cyclohexanol, cyclohexanone or a mixture of both,[60] so basically from benzene and phenol[59] that are both extracted from fossil resources.[44] Scheme 5 shows the possibility to synthesize adipic acid via 1,6-hexanediol (a), mentioned earlier in this chapter, or FDCA (b), both products with HMF as possible feedstock.[61] 1,6-hexanediol can be converted to adipic acid using platinum, gold or an alloy consisting of both applied onto zirconia (ZrO_2) as catalyst.[62],[63] FDCA as an oxidation product of HMF can be hydrogenated to tetrahydro-FDCA (4) by palladium applied onto SiO_2. Afterwards, the addition of a halogenic source (HI) leads to a ring-opening resulting in the desired product adipic acid.[64]

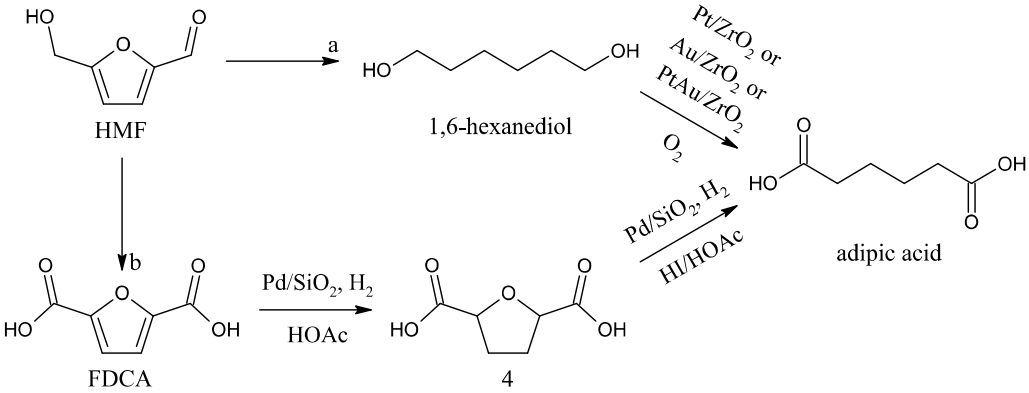

Scheme 5: Reaction pathway from HMF to adipic acid via 1,6-hexanediol (a) or FDCA and tetrahydro-FDCA (4) (b).[61] Copyright Royal Society of Chemistry.

Levulinic acid itself is considered a platform chemical[4] as HMF, due to its broad scope of application: it can be utilized in polymers,[65] lubricants,[66] as adsorbing agent,[67] as a coating material[68] and in electronics.[69] Additionally, the most promising products with levulinic acid as feedstock are methyltetrahydrofuran, a fuel extender[70] and δ-aminolevulinic acid, a broad spectrum herbicide[70]. Furthermore, it can be converted to diphenolic acid, which is a direct replacement for bisphenol A, leading to a sustainable alternative for polycarbonates especially.[70],[71] With the substitution for an industrial chemical, its broad scope of application and the possibility of a scale-up, levulinic acid fulfils important criteria that substantiate its status as future platform chemical.[1] Synthesizing levulinic acid from HMF can be realized by an acid catalyzed (H_2SO_4 or HCl) degradation that also leads to formic acid formation.[72] Formic acid has an industrial market itself with an annual production of 950.000 tons (2014)[73],[74] and is additionally considered an essential part as an H_2-storage in a possible future infrastructure for hydrogen.[75],[76]

Another follow-on product of levulinic acid is γ-valerolactone that can be synthesized via Ru/C catalysts,[77],[78] zeolites[79] or copper alloys.[80] It could be an interesting solvent, due to its low vapor pressure,[81],[82] its comparably high flash point (96 °C) and the easy separation from water since no azeotrope is formed.[82] Additionally, its toxicity is extremely low (LD_{50}: 8.8 g kg^{-1}), its boiling point extremely high (207-208 °C) and its stability is preserved over a long time even in the presence of water, oxygen or air, where no peroxides are formed.[82] It can be possibly applied in synthesis of γ-valerolactone itself starting from fructose, which would have the huge advantage that product and solvent do not have to be separated from one another.[83] GALLO ET AL. additionally demonstrated that HMF synthesis with fructose or glucose as feedstock in γ-valerolactone leads to a higher yield of the desired product.[84] Another application is fuel synthesis as it can be converted to valeric acid by hydrogenation over a bifunctional catalyst with hydrogenation and acidic functions (Pt-loaded SiO_2-bound H-ZSM-5).[85] Subsequently, valeric acid is esterificated to alkyl mono- and divalerate esters that have comparable blending research octane numbers and boiling points to common fuels and more appropriate polarities than alternative candidate biofuels.[85]

Another HMF product that can be used as a fuel or fuel additive is DMF.[86] Its high research and motor octane numbers of 101.3 and 88.1, respectively, (cf. gasoline: 96.8 and 85.7, respectively)[87] make DMF an interesting prospect as future fuel. Additionally, its heat of combustion is with 31.5 MJ L^{-1} similar to that of gasoline (35 MJ L^{-1}) and even 30 % higher than that of ethanol (23 MJ L^{-1}). Other advantages of DMF are a better knock resistance than gasoline[88] and its use as an additive that can lead to a higher auto ignition resistance[89] as well as a lower fuel consumption.[90] The synthesis route from HMF to DMF needs a

dehydrogenation catalyst *e.g.*, Pd/C in a mixture of ionic liquid and acetonitrile[86] or Ruthenium in Ru/Co_3O_4.[91] Another approach features the aforementioned formic acid that supports the reaction steps from fructose to HMF, from HMF to BHMF and ultimately from BHMF to DMF.[92]
Summarizing these HMF products, a broad application range can be observed: monomers, which can be used in *e.g.*, medicine or electronics, own platform chemicals with a high economical ceiling, alternative solvents as well as also fuels and fuel additives. This spectrum confirms the status of HMF as a future platform chemical that was defined by the DOE in 2004[20] and extended by BOZELL AND PETERSEN in 2010.[1]

Biomass as feedstock for HMF synthesis

Apart from the possibilities to further process HMF, its synthesis also received attention. A future platform chemical should be manufactured sustainably and thus, its feedstock should be renewable and abundant, which is why biomass is considered as a suitable source.[1]
HMF can be extracted from C_5 and C_6 sugars (monosaccharides) that themselves stem from cellulose or lignocellulose.[5] Glucose is nature's most abundant monosaccharide,[93] especially as it is produced by photosynthesis from carbon dioxide and water.[94] Due to its stable ring structure, the amount of open glucose in solution is low and thus its enolisation rate.[95] On the contrary, fructose has a high enolisation rate and its open form shares a higher amount in solution.[95] Scheme 6 shows that this enolisation (E) is a crucial step to start acidic dehydration to HMF, regardless of the present structure.[96] The last molecule structure in both ways (5, 6) that consists of a ketone and a double bond could be isolated and determined via ^{1}H-NMR,[97] leading to the perception that the isomerization from glucose to fructose is a key step in HMF synthesis with glucose as feedstock.[95],[96]

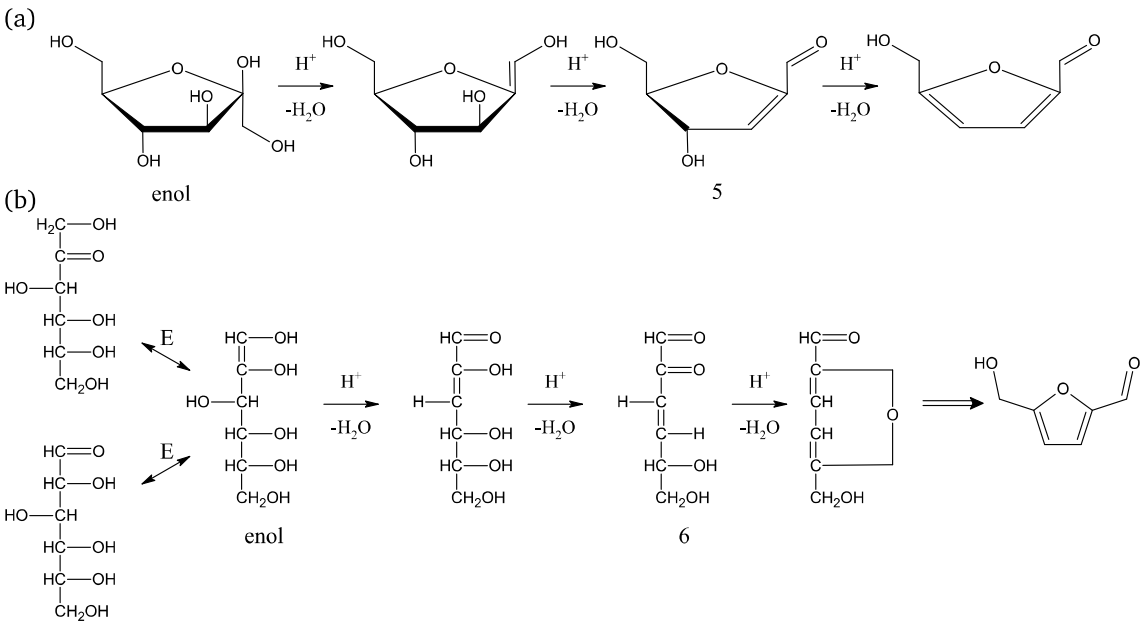

Scheme 6: Dehydration mechanism of fructose to HMF in its ring (a) or open structure (b) in acidic media.[96] Copyright Elsevier Science & Technology.

Cellulose and hemicellulose are in contrast to both aforementioned monosaccharides because up to 60 – 90 wt-% are directly stored in plant-based biomass,[98] whereby especially cellulose that consists of β-1,4-glycosidic connected D-glucose units can be considered an interesting

feedstock for HMF synthesis.[99] Herein, the difficulty consists of breaking up these glycosidic bonds to obtain glucose.[99] Considering these perceptions, catalysts extracting HMF from biomass need to break up the glycosidic bonds, favor the isomerization from glucose to fructose and ultimately convert fructose to HMF, as shown in Scheme 7.[100] Since these requirements are nearly impossible to fulfil by one catalyst itself, coupled catalyst systems seem to be the key for a successful synthesis from cellulose and glucose to HMF.[100]

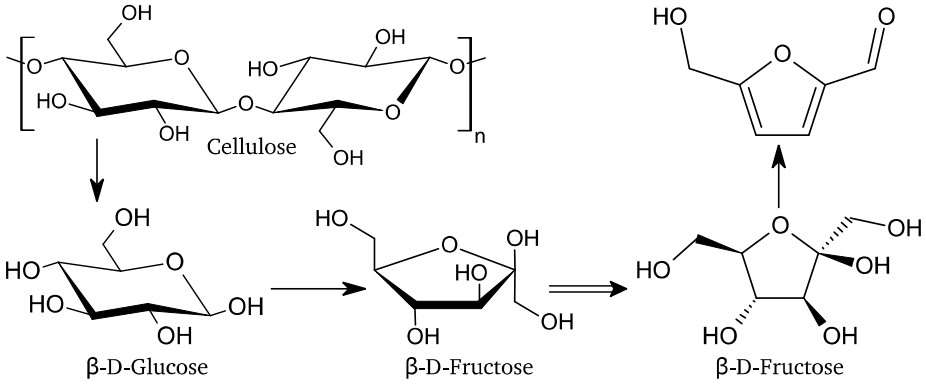

Scheme 7: Reaction pathway starting from cellulose to HMF with glucose and fructose as intermediates.[101] Copyright John Wiley & Sons – Books.

Inorganic catalysts like nitrogen doped carbons on halloysite nanotubes convert fructose, glucose, as well as inulin, an oligosaccharide consisting of fructose that can be found in *e.g.*, chicory,[102] to HMF with yields of 91, 63 and 78 %, respectively.[103] The combination of catalysts that feature Lewis and Brønsted acids is another possibility to approach this challenge. HCl and $AlCl_3$ were used as catalyst system in dioxane/water (4:1) to convert corn stover, switch grass, poplar wood and loblolly pine with HMF yields of 69, 65, 69 and 60 %, respectively.[104] FENG ET AL. tried combining betaine-based Brønsted acids ($(CH_3)_3NCH_2COOH^+$) with chlorine (Cl^-), hydrogen sulfate (HSO_3^-), benzenesulfonate ($(C_6H_5)SO_3^-$) and para-toluenesulfonic acid ($(p\text{-}CH_3(C_6H_5)SO_3^-$) as counterions with $AlCl_3$ as Lewis acid.[101] HMF yields of 88, 66, 37 and 53 % were achieved with fructose, glucose, cellulose and lignocellulose as well as feedstock, respectively.[101] Furthermore, bamboo, corn stover, wheat straw and rice straw used as lignocellulose lead to HMF yields of 41, 53, 43 and 51 %, respectively.[101] Zeolite ZSM-5, which is often utilized in solid state acid catalysis and modified with sulfonic acid groups, features both Lewis and Brønsted acid sites and is therefore able to solely convert glucose hydrolysate, which is derived from rice straw, to HMF with a yield of 54 %.[105]

The synthesis of HMF with the aforementioned poly- and monosaccharides as feedstock can also be realized using ionic liquids (IL) as possible catalysts.[101],[106] The yield could be enhanced by the use of polar solvents, such as DMSO, or elevated temperatures.[107] 1-Butyl-3-methylimidazolium hexafluorophosphate (BMIM PF_6) and 1-butyl-3-methyl-imidazolium tetrafluoroborat (BMIM BF_4) are two examples of ILs and can be combined with DMSO and an acid catalyst (Amberlyst-15) to convert fructose to HMF with a yield of 87 %.[108] Another Amberlyst (Amberlyst-70) yields 72 % HMF starting from fructose after just ten minutes with the aforementioned γ-valerolactone as solvent and 59 % Y_{HMF} after 20 minutes starting from glucose using a tin-zeolite (Sn-β) as catalyst.[84] N-Heterocyclic carbenes can also be utilized as catalysts and convert 96 % and 78 % of fructose and glucose, respectively, to HMF by pairing it with $CrCl_3$ in 1-butyl-3-methylimidazolium chloride (BMIM Cl), so the IL as the

solvent.[109] A catalyst system consisting of BMIM Cl and $CrCl_3$ is also possible, leading to an HMF-yield of 71 %.[110]
A disaccharide like sucrose, which consists of one molecule fructose and one molecule glucose that are connected by a glycosidic bond and which is better known as table sugar,[111] can also be a feedstock for HMF synthesis. Therefore, N-Methyl-2-pyrrolidine hydrogen sulfate (NMP HSO_4) in 1-allyl-3-methylimidazolium chloride (AMIM Cl) converts sucrose to HMF with a yield of 87 %.[112] SHI ET AL. also used maltose (two units of glucose connected by an α-1,4-gylcosidic bond[113]) and lactose (galactose and glucose connected by an α,β-1,4-glycosidic bond[113]) as an additional feedstock for HMF synthesis.[112] 1-(4-Sulfonic acid)-propyl-3-methylimidazolium hydrogen sulfate ($C_3SO_3HMIM\ HSO_4$) in AMIM Cl proved to be the best combination but a yield of only 56 % and 36 %, respectively, could be achieved, while both also needed $CoCl_2$ as co-catalyst.[112] Galactose itself was also used as HMF feedstock under the same conditions but it yielded in just 19 % HMF.[112] Cellulose can be converted to HMF by a combination of $C_3SO_3HMIM\ HSO_4$ with $CrCl_3$ that react to $Cr(C_3SO_3HMIM\ HSO_4)_3$ which leads to a 53 % yield of HMF.[114]
Concluding these results, biomass and its further processed products can all be used as feedstock to synthesize HMF with or without IL in the catalyst system. The achieved yields are dependent on the structure complexity: the monosaccharide fructose chemically resembles HMF the most (see Scheme 7) and is therefore the most suitable starting component, while the polysaccharide cellulose leads to lower yields as all glycosidic bonds have to be broken up in an additional step. Afterwards, biomass-based HMF can be further converted to FDCA that itself is considered a future platform chemical.[1]

2.2. FDCA as future platform chemical

FDCA is strongly considered a direct substitute for terephthalic acid, which has an annual production of over 50 million tons.[16],[17] Furthermore, its use in the monomer chemistry for other polyesters or new nylons addresses another big market.[20] Due to these application possibilities to high volume products and its flexibility as starting compound for further processed products, FDCA is also considered a future platform chemical.[1]

FDCA in polymer chemistry

FDCA, seen in Figure 1, is a symmetrical molecule consisting of a furan ring and two carboxylic acid side groups, which makes it a predestined monomer for polyesters and polyamides, that is crystalline and stable at room temperature with a melting point of more than 300 °C.[42]

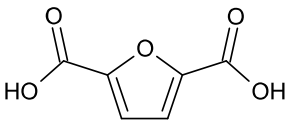

Figure 1: 2,5-Furandicarboxylic acid (FDCA).[42]

The first detailed study of a polyester synthesis containing FDCA was published in 1978 and describes a *trans*-esterification technique, in which the methyl ester of FDCA (dimethyl-2,5-furan dicarboxylate) reacts with 1,6-hexanediol.[115] Afterwards in 2009, 40 years after the last publication, a group of polyesters and polyamides with different chain lengths of the diol and diamine were synthesized using the same technique to compare their properties, as seen in Scheme 8.[116] Higher chain lengths of the comonomer led to lower melting points

for both polymer species, lower glass transition temperatures for the polyamides and a higher viscosity for the polyamides, while the viscosity for all polyesters was extremely low.[116]

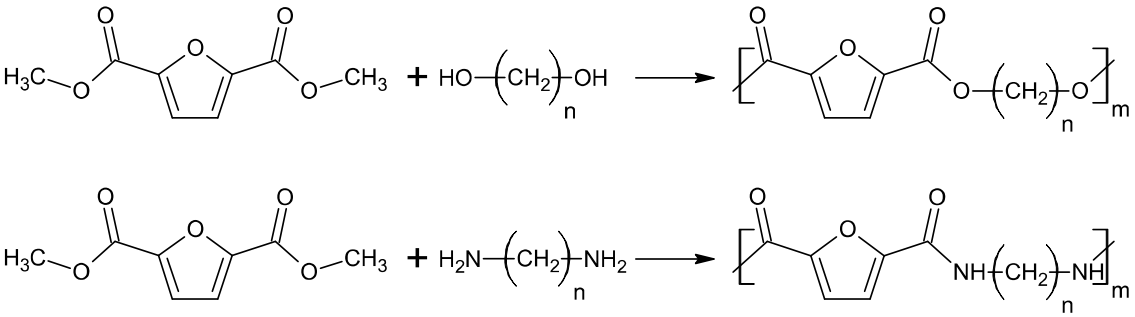

Scheme 8: Synthesis of FDCA-based polyesters starting from n-methylene diol and dimethyl-2,5-furan dicarboxylate (above)[115],[116] and FDCA-based polyamides starting from n-methylene diamine and dimethyl-2,5-furan dicarboxylate (below)[116] using trans-esterification technique. Copyright American Chemical Society and John Wiley & Sons – Books.

Also in 2009, GANDINI ET AL. revived the interest in the most obvious polyester starting from FDCA by reacting with ethylene glycol (EG), namely polyethylene 2,5-furandicarboxylate (PEF).[117],[118] PEF is the furan homologue to the most important commercial polyester polyethylene terephthalate (PET) that has an annual production of over 50 million tons.[117],[118],[119] At first, FDCA reacted with the hundredfold excess of EG to the diester diol at 75 °C under vacuum with small amounts of aqueous HCl.[117] Afterwards, the aforementioned *trans*-esterification started the polymerization with Sb_2O_3 as catalyst under high vacuum by raising the temperature progressively from 70 to 220 °C, while released EG was trapped at -196 °C (liquid nitrogen).[117] This synthesis results in PEF as a white solid that is only soluble in trifluoroacetic acid and hot tetrachloroethane.[117] Following this revival of PEF, BURGESS ET AL. researched its barrier properties in comparison to PET and found out that PEF has a ~ 11 x lower oxygen permeability, although the oxygen solubility is comparable.[120] Furthermore, it demonstrates a ~ 19 x lower CO_2 permeability,[121] a ~ 5 x lower water diffusion coefficient[122] and a ~ 1.8 x higher water sorption capacity.[123] They traced these better barrier properties back to the ring structures: the furan ring-flipping in PEF is suppressed due to its nonlinear rotation axis coupled with the ring polarity in contrast to the active phenyl ring-flipping in PET.[124] These observations are complemented by its crystallization behavior: an amorphous phase occurs in semi-crystalline PEF, which impacts barrier[125] and mechanical[126] properties, that grows with an increase in crystallinity.[127] Furthermore, PEF exhibits a slower crystallization rate than PET,[128],[129] which is a disadvantage since high crystallinity enhances the barrier properties.[125],[130] Concluding its properties, PEF is considered to be suitable for applications in packaging and as a direct substitute for PET and seems to be commercialized in 2023[131] while reaching a market value of $129.3 million in 2025,[132] emphasizing its economical ceiling. Additionally to its better barrier properties, PEF can be produced using 100 % abundant and renewable materials using bio-based EG that can be synthesized from bioethanol,[133] which can be derived from various biomass sources like corn stover, wheat straw or switch grass.[133],[134] The industrial approach to synthesize EG is the hydration of ethylene oxide[135] that is derived from ethylene,[136] which is historically extracted from naphtha, thus from crude oil.[137] 42 million tons of EG have been produced in 2019 and its production is expected to reach 65 million tons in 2024.[138] In 2016, just 1 % of EG was produced from bio-based feedstock,[139] but the demand of bio-based EG rises, which will propel the growth of the global market in the years to follow.[140] Nevertheless, PET relies on crude oil as the source for terephthalic acid, which is synthesized with p-xylene as starting

material[141] that itself is derived from crude oil.[142] Summarizing these results, Figure 2 shows three possible routes to produce PET. The black arrows on the left show a pathway of fossil-based PET, which is state of the art right now. Using bio-based EG and fossil-based terephthalic acid leads to partially bio-based PET (~ 30 wt-%, center pathway), which might be a solution for near future applications, since a high-volume production infrastructure for PET already exists.[119] At last, the green arrows on the right side show a route to produce completely bio-based PEF that consists of bio-based EG and terephthalic acid, which could be the future of former PET-based plastics. Economic projections estimate that PEF will only substitute PET and also bio-based PET by its lower manufacturing costs, if emission certificate prices of greenhouse gases will rise as politics decide to focus on sustainability management regarding their economy.[143] Every other scenario ends in PET and/or bio-based PET being economically more feasible than PEF until at least 2040.[143]

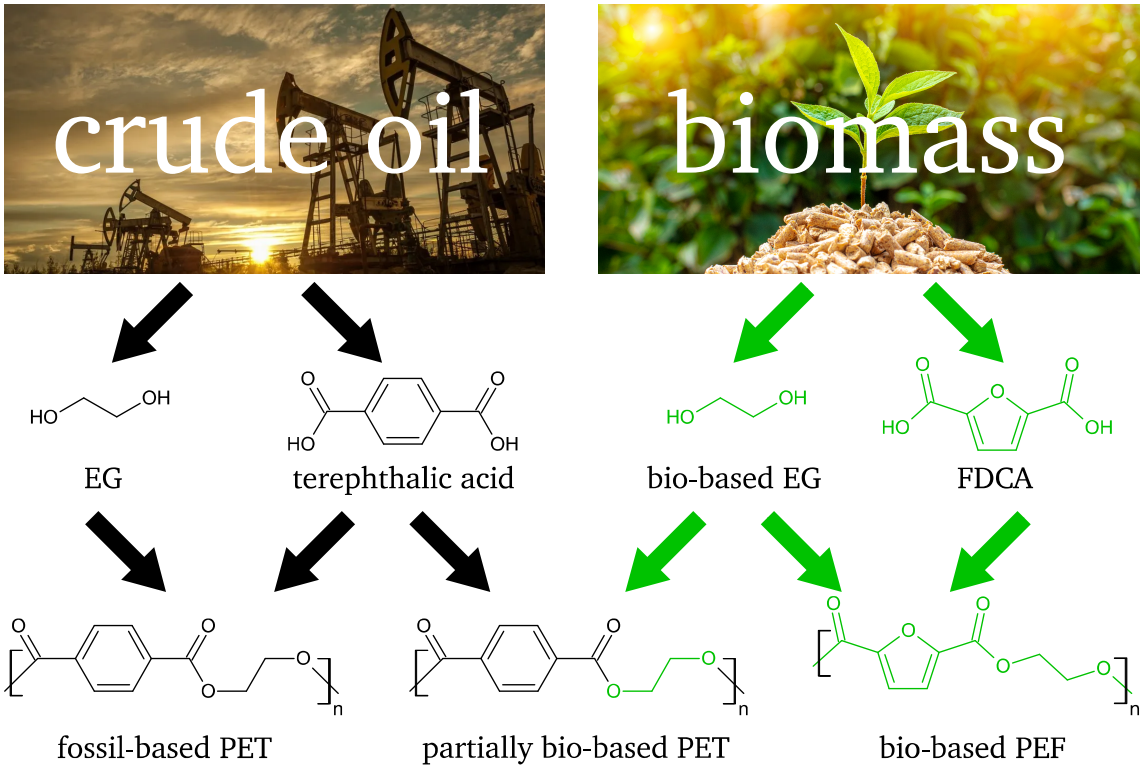

Figure 2: Different pathways from crude oil[144] or biomass[145] to fossil-based PET (lower left), partially bio-based PET (lower middle) and bio-based PEF (lower right) through EG, terephthalic acid, bio-based EG and FDCA (middle row, left to right).

Additionally to PEF, the polyesters poly(propylene 2,5-furandicarboxylate) (PPF) and poly(butylene 2,5-furandicarboxylate) (PBF) with 1,3-propanediol and 1,4-butanediol as monomers, respectively, have been investigated for their application in polymer chemistry. They were also synthesized by *trans*-esterification as shown in Scheme 8 and examined for their thermal stability: the longer the carbon chain of the diol, the lower the decomposition temperature.[146] Furthermore, the crystallization rates of PPF and PBF were compared to their terephthalic counterparts and it was slower, the same as PEF, so it seems that the crystallization ability of FDCA-based polyesters is lower than that of the corresponding terephthalic acid ones.[147] Nevertheless, 30 % crystalline PPF shows outstanding oxygen and water barrier performances that can be led back to its chemical structure with a dense, packed crystal phase as well as two rigid and also asymmetrical monomers in contrary to PEF.[147] Table 1 summarizes the barrier properties of PEF and PET, PPF and PPT as well as PBF and PBT against

oxygen (O_2) carbon dioxide (CO_2) and water vapor. FDCA-based polyesters exhibit better barrier properties than their terephthalic-based homologue for every inspected substance. As the difference in oxygen transmission of PPF depending on its crystallinity (0 %: 0.04; 30 %: < 0.005 cm^3 cm m^{-2} d^{-1} atm^{-1}) shows, accelerating the crystallization time of FDCA-based polyesters is crucible for its application as packaging material with outstanding barrier properties.

Table 1: O_2 transmission rate, CO_2 transmission rate and H_2O vapor transmission rate for FDCA-based and terephthalic-based polyesters with different length of the carbon chain of the diol (C_2 – C_4). [a] 23 °C, 50 % relative humidity (RH); [b] 38 °C, 100 % RH; [c] 35 °C, 50 % RH; [d] estimated from BURGESS ET AL.[122]; [e] 30 % crystallinity; [f] 30 °C, 0 % crystallinity; [g] 23 °C, 0 % RH; [h] no comment on reaction conditions; [i] 90 % RH; [j] 23 °C, 85 % RH.

	O_2 transmission rate[a] / cm^3 cm m^{-2} d^{-1} atm^{-1}	**CO_2 transmission rate[a] / cm^3 cm m^{-2} d^{-1} atm^{-1}**	**H_2O vapor transmission rate[b] / g mm m^{-2} d^{-1} atm^{-1}**
PEF	0.07[120]c	0.17[121]c	~ 0.32[122]d
PET	0.75[120]c	3.22[121]c	1.60[148]
PPF	< 0.01[147]e – 0.04[149]f	0.07[149]f	0.24[147]
PPT	0.50[150]g	12.80[151]h	-
PBF[152]	0.11	0.27	2.01[i]
PBT[148]	1.52	13.90	2.50[j]

Other comonomers for FDCA-based polymers can provide improved or new properties opening new possibilities for special application fields as comonomers of terephthalate-based polymers in specialty packaging, agriculture, medicine, biodegradability.[153] TERZOPOULOU ET AL. summarized all reported polyesters derived from FDCA mainly focusing on their sustainability and biodegradability.[153] They also investigated their thermal, mechanical and gas barrier properties, which can be comparable or even better than that of commercial, fossil-based ones.[153]

As shown before, not only FDCA-based polyesters can be synthesized, but also FDCA-based polyamides with linear[116] (Scheme 8) or aromatic diamines (Scheme 9, aramid) as comonomers.[154] Latter ones were thoroughly investigated in 1991 displaying good thermal stability, high molecular weight and a regular structure.[155] Kevlar® consists of terephthalic acid and 1,4-phenylenediamine (poly(p-phenylene terephthalamide)) is the most popular of these aramid fibers.[156] It is used in industrial and advanced technologies *e.g.*, ballistic armor, helicopter blades and pneumatic reinforcement.[157] Kevlar® shows extraordinary thermal stability (up to 600 °C)[154] as well as a high glass transition temperature of ~ 350 °C.[157],[154] Its bio-based homologue derived from FDCA seen in Scheme 9 (poly(p-phenylene furanoate); PPF) also shows high resistance to organic solvents and a fully amorphous structure leading to a glass transition temperature of ~ 300 °C and a thermal stability up to ~ 420 °C.[154] These properties can be explained by the rigid backbone stemming one more time from the furan ring.[124],[154] The before-mentioned characteristics as well as the mechanical properties like Young's modulus (E) and tensile strength (σ) are inferior to its petroleum-based counterpart.[154] Nevertheless, PPF's advantage is the higher solubility in common solvents like DMSO or DMF, which makes it easier to process.[154]

As mentioned in chapter 2.1, FDCA can be further processed to a diisocyanate. Unfortunately, its activity towards alcohol groups was extremely high leading to an excessive sensitivity to resinification and furthermore to unstable urethane polymers.[42],[118] The dienic character of the furan ring promotes an electronic conjugated effect that seems to be the origin of this extremely enhanced reactivity.[118]

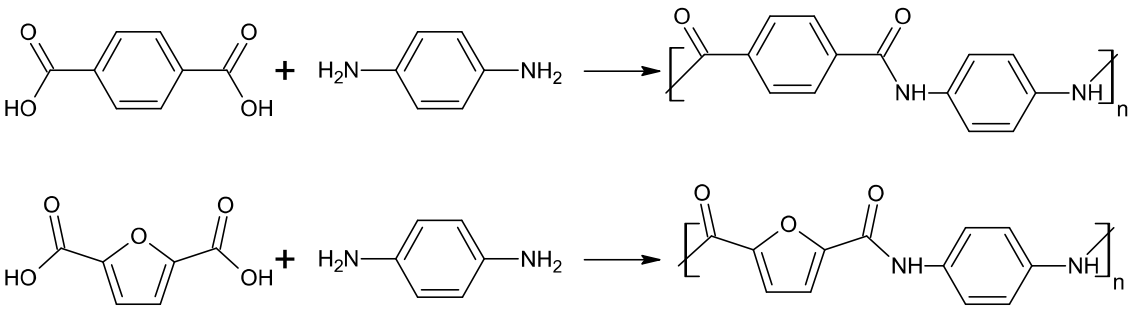

Scheme 9: Reaction pathway to Kevlar® aramid polymers derived from terephthalic acid (above)[156] and FDCA (below).[154] Copyright Taylor & Francis and Royal Society of Chemistry.

Concluding this chapter, FDCA has a broad range of application in polymer chemistry with its highest ceiling substituting terephthalic acid as a renewable and abundant monomer source for high throughput products like PET. While the furan-based polyesters showed enhanced properties compared to their fossil-based counterparts, the polyamides still need improvement to reach the high standards of *e.g.*, Kevlar®. Additionally to a diverse application field, a future platform chemical should have an abundant feedstock.[1] Fortunately, FDCA can be synthesized from HMF, which itself stems from a renewable source as seen in chapter 2.1.

2.3. Oxidation of HMF to yield FDCA

FDCA was first reported in 1876 as FITTIG AND HEINZELMANN synthesized it by accident trying to reduce mucic acid to a bromide derivative of adipic acid by treating it with hydrogen bromide.[158] Afterwards, also glucaric acid, an isomer of mucic acid (7; 1888),[159] furfural (8) or rather its further processed diester (9; 1962)[160] and the potassium salt of furoic acid (10; 1963)[161] were used as starting material for FDCA, as summarized in Scheme 10. Since the synthesis of FDCA starting from mucic acid required long reaction times over several days[158] and the synthesis way from furfural is complex with many intermediates[160],[161] HMF gathered the attention as feedstock for FDCA production.[162]

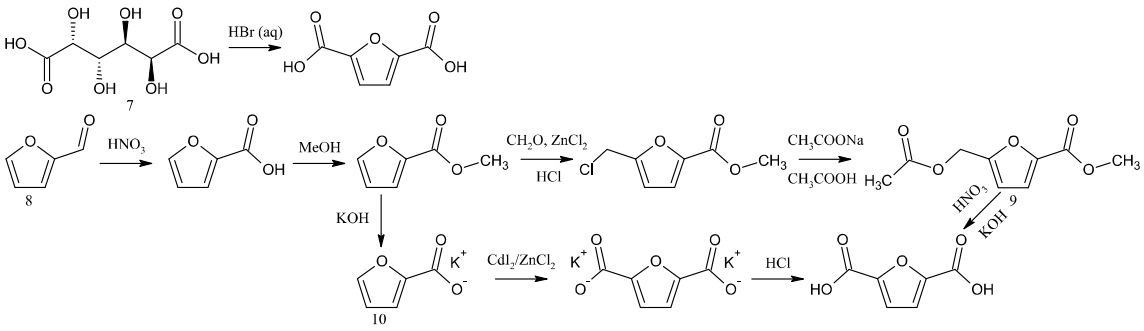

Scheme 10: Historic ways of synthesizing FDCA from mucic acid (7; above)[158] and differently processed furfural (8, 9, 10; middle and below).[160],[161] Copyright American Chemical Society.

Scheme 1[6] shows the HMF oxidation reaction pathway that could be selectively followed by many different catalyst types, such as homogeneous and heterogeneous catalysts.[162] Homogeneous catalysts such as $Co(OAc)_2$, $Mn(OAc)_2$ paired with HBr, known as the so called *Amoco Mid-Century system*, were able to convert 61 % of HMF to FDCA at 125 °C and 70 bar air pressure.[163] Additionally, a similar catalyst system based on metal salts consisting of $Co(OAc)_2$, $Zn(OAc)_2$ and NaBr mainly produced DFF until trifluoroacetic acid promoted the yield to FDCA to 60 % at 90 °C and atmospheric O_2-pressure.[164] Besides pure oxygen as oxidizing agent, also

tert-butylhydroperoxide was investigated combined with CuCl but the yield to FDCA never exceeded 45 % at room temperature, although the conversion was 100 %.[165] These examples summarize the problem of homogeneous catalysts for HMF oxidation: The yield of FDCA is rather low and byproducts form additionally in the reaction solution.
Due to the disadvantages provided by homogeneous catalysts, heterogeneous catalysis might be an attractive alternative for HMF oxidation to FDCA. Therefore, especially noble metals like Au, Pt or Pd are utilized as heterogeneous catalysts for HMF oxidation to FDCA and some showed promising results in aerobic oxidation, as summarized in Table 2.[162],[166],[167] As most of these catalysts worked in a basic environment, a conversion at lower pH is advantageous since HMF decomposes in alkaline media to insoluble humins via ring-opening polymerization leading to smaller FDCA yields and problems closing the mass balance.[168],[169]

Table 2: Reported works on the aerobic oxidation of HMF to FDCA over different noble metal catalysts, presenting the solvent, temperature (*T*) and oxidant (incl. pressure *p*) as reaction conditions, as well as conversion of HMF (*X*) and yield of FDCA (*Y*).

Catalyst	Solvent	*T* / °C	Oxidant, *p* / bar	*X* (HMF) / %	*Y* (FDCA) / %	Ref.
Au/CeO_2	NaOH	130	Air, 10	100	> 99	[170]
Au/TiO_2	NaOH	130	Air, 10	100	> 99	[170]
Au/HY	NaOH	60	O_2, 0.3	> 99	> 99	[171]
Au/HT	H_2O	95	O_2, 1	> 99	> 99	[172]
Au/HT-AC	H_2O	100	O_2, 5	100	> 99	[173]
Pt/Al_2O_3	KOH	60	O_2, 0.2	100	> 99	[174]
Pt/C	NaOH	25	O_2, 1	100	81	[175]
Pt-Pb/C	NaOH	25	O_2, 1	100	99	[175]
Pt/C	Na_2CO_3	100	Air, 40	99	69	[176]
Pt-Bi/C	Na_2CO_3	120	Air, 40	100	> 99	[176]
Pt-IP-GLY	H_2O	80	O_2, 1	100	99	[177]
Pd/C	NaOH	23	O_2, 6.9	100	71	[178]
Pd-PVP	NaOH	90	O_2, 1	> 99	90	[179]
$Pd/ZrO_2/La_2O_3$	NaOH	90	O_2, 1	> 99	90	[180]
Pd/HT	H_2O	100	O_2, 1	> 99	> 99	[181]
Ru/C	$CaCO_3$	120	O_2, 2	100	95	[182]
$Ru/MnCo_2O_4$	H_2O	120	Air, 24	100	99.1	[183]
Ru/HAP	H_2O	120	O_2, 10	100	99.6	[184]
Ru/HAP	H_2O	140	O_2, 10	100	99.9	[184]
Rh/C	NaOH	50	O_2, 10	81.2	12.6	[168]

In 1990, VINKE ET AL. reported one of the first active heterogeneous catalysts towards oxidation of HMF to FDCA at pH 9, which was a Pt catalyst supported on alumina (Al_2O_3) that was found accidentally as FFCA was the main targeted product.[174] Nevertheless, it was able to convert HMF in KOH at 0.2 bar of O_2 and 60 °C to FDCA in quantitative yields.[174] Using air instead of pure oxygen as oxidant only worked with switching the electrolyte to Na_2CO_3 and increasing the pressure (40 bar) and temperature (100 °C).[176] It led to an FDCA yield of 69 % for pure Pt/C and 98 % for adding Bi to it, while increasing the temperature to 120 °C even lead to a > 99 % yield.[176] Furthermore, Pt nanoparticles were synthesized using ethylene glycol (GLY) and stabilized with an ionic polymer (IP; poly-1,3-bis(4-vinylbenzyl)imidazolium chloride) that is hydrophobic.[177] In a base-free approach it was able to yield 99 % of FDCA at 80 °C and 1 bar O_2 in water, which represents the most ambient reaction conditions for the aerobic oxidation from HMF to FDCA.[177]

A similar performance with slightly higher temperature was achieved by immobilizing Pd on HT (hydrotalcite), which led also to a 99.9 % yield of FDCA at base free conditions and an air pressure of 1 bar at 100 °C.[181] Even if noble metal catalysts show some very promising performances and are additionally considered stable in the field of heterogeneous catalysis, its large-scale application is limited due to their high cost and poor availability.[162],[166] Therefore, research focused on non-noble, mainly transition-metal catalysts that can selectively convert HMF to FDCA, as summarized in Table 3.

One of the first reported non-precious metal catalysts was a porous organic polymer (POP) consisting of basic porphyrin subunits with Fe^{III} as its metal center that was published in 2013.[185] It converted 100 % HMF with a yield of 85 % FDCA in H_2O at 100 °C and 10 bar.[185] HAYASHI ET AL. investigated the crystal structure of MnO_2 in $NaHCO_3$ as catalyst for HMF oxidation, which led to β-MnO_2 outperforming its polymorphic forms λ- > α- ≈ γ- > δ- > ε-MnO_2, respectively, due to its planar and bent oxygen sites with lower vacancy formation energies.[186] A successful synthesis of high-surface-area β-MnO_2 (82 $m^2\ g^{-1}$) led to a ~ 3 times higher reaction rate per area than that of activated MnO_2, while they also registered that a high surface area enhances the catalytic activity.[186] Unfortunately, a pressure of 10 bar oxygen is needed to synthesize FDCA with a 91 % yield.[186] A base free approach also led to a high performance catalyst using Co_3O_4 nanoparticles well dispersed on amorphous Mn-Co-O solid solution.[187] It formed Co_3O_4/Mn_xCo, which exhibited > 99 % yield of FDCA in H_2O at 140 °C and 1 bar O_2 with x = 0.2, while it was also possible to entirely regenerate the catalyst by calcination in air.[187]

Table 3: Reported works on the aerobic oxidation of HMF to FDCA over different non-noble metal catalysts, presenting the solvent, temperature (*T*) and oxidant (incl. pressure *p*) as reaction conditions, as well as conversion of HMF (*X*) and yield of FDCA (*Y*).

Catalyst	Solvent	*T* / °C	Oxidant, *p* / bar	*X* (HMF) / %	*Y* (FDCA) / %	Ref.
Fe-POP	H_2O	100	O_2, 10	100	85	[185]
$Li_2CoMn_3O_8$ / NaBr	CH_3COOH	150	O_2, 55	100	80	[188]
MnO_2	$NaHCO_3$	100	O_2, 10	≥ 99	91	[189]
2D Mn_2O_3	$NaHCO_3$	100	O_2, 14	100	99.5	[190]
$Co_3O_4/Mn_{0.2}Co$	H_2O	140	O_2, 1	100	> 99	[187]

Apart from aerobic conversion, biochemical HMF conversion also offers a possibility for FDCA production under more ambient conditions as these catalysts work at mild temperature, pressures and are usually biodegradable.[191] Enzymes are often restricted to oxidize either alcohol or aldehyde side groups, which makes HMF oxidation to FDCA challenging since both features are needed.[166] Nevertheless, DIJKMAN ET AL. discovered a flavin adenine dinucleotide (FAD) dependent enzyme that was able to oxidize HMF to FDCA with a 95 % yield.[192],[193] It achieved full conversion at room temperature and in potassium phosphate buffer with its only disadvantage in the long reaction time (24 h).[192],[193] Recent progress in this field of catalysis has been summarized by TROIANO ET AL. regarding the production of FDCA including HMF oxidation.[191]

Concluding this chapter, higher temperature (> 50 °C) or pressure (> 1 bar of oxygen) is necessary to convert HMF to FDCA or alkaline media, in which HMF degrades into insoluble humins.[168],[169] Therefore, an alternative route could solve this challenge.

2.4. Anodic HMF oxidation

Another approach of converting HMF to FDCA is anodic oxidation. Contrary to the aforementioned aerobic oxidation, an electrochemical approach for oxidation of HMF to FDCA can be solely driven by potential at ambient conditions.[194] Therefore, no oxidant like air or oxygen at high pressures is necessary, which could elevate electrocatalysis into a serious alternative.[194] An aqueous reaction medium seems to be the most straightforward option as it delivers hydroxide ions at the anode that convert HMF to FDCA (Scheme 1[6]). Unfortunately, a competing reaction occurs in aqueous media because classic water splitting electrolysis produces oxygen (oxygen evolution reaction, OER) on the anodic side at theoretically 1.23 V vs. RHE[195] (reversible hydrogen electrode) according to the Nernst equation.[168],[195] Furthermore, OER faces sluggish reaction kinetics because its four electron process is more complex as it involves several surface adsorbed intermediates.[7],[196] On top of that, oxygen also has a low economic value, reaching just 150 € per ton in 2018.[197] Thus, an upgrade to FDCA as anodic product, whose possible economical value has been described in chapter 2.2, seems to be an upgrade, if HMF oxidation occurs at lower potentials than OER. In contrast to oxygen, hydrogen, which is the cathodic product in classic water splitting electrolysis (HER: hydrogen evolution reaction),[7] is considered a promising energy source and storage.[8],[9] Keeping these advantages on the cathodic site and upgrading the anodic product to FDCA with a high economic capability would be an overall upgrade of the classic electrochemical water splitting.[7],[198] Figure 3 summarizes the differences between alkaline water electrolysis with H_2 and O_2 as products as well as the upgraded solution with H_2 and FDCA that should also operate at lower potentials.

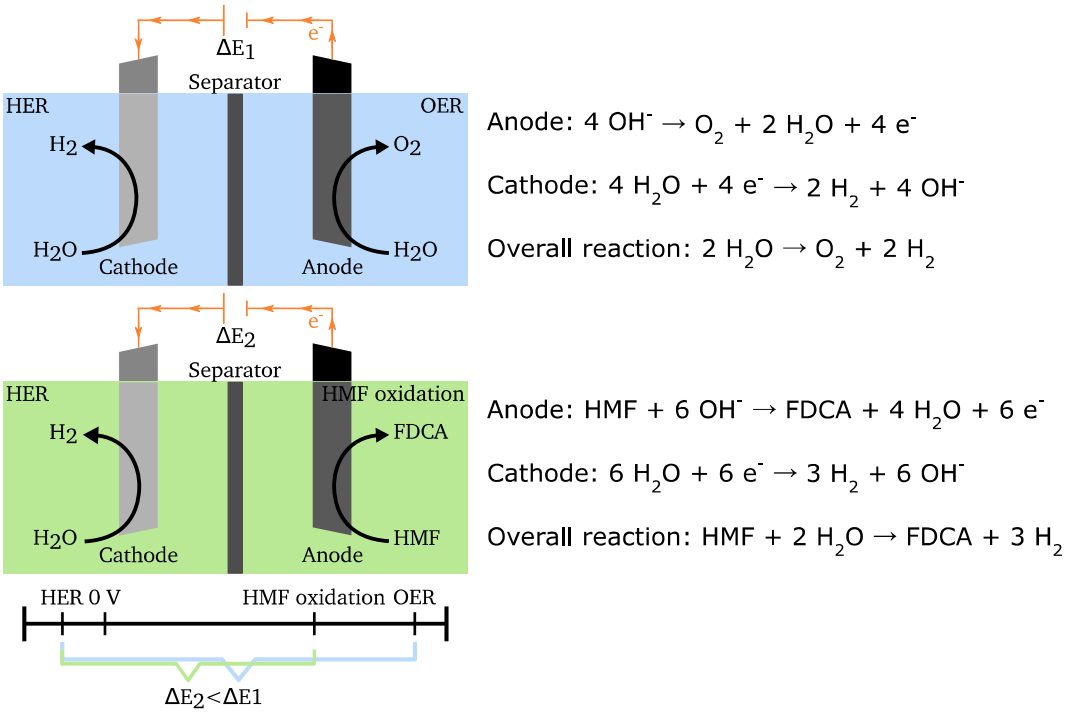

Figure 3: Upgrading alkaline water electrolysis by replacing OER (upper scheme)[199] with HMF oxidation (lower scheme)[14] at the anode that should operate at lower potentials (line graph at the bottom) and HER at the cathode.[200] Copyright American Chemical Society and Springer Nature.

The first reported electrolysis regarding FDCA synthesis starting from HMF has been published in 1991.[201] Nickel oxide/hydroxide was used as anode material in 1 M NaOH at a constant

current density of 16 mA cm^{-2} leading to 57 and 71 % yield of FDCA in an undivided and divided cell, respectively.[201] In a divided cell, the anodic and cathodic compartment are separated by a semi permeable material.[202] After a Pt electrode at a constant current density of 0.44 mA cm^{-2} only led to small traces of FDCA (yield < 1 %),[168] CHADDERDON ET AL. found that besides the electrocatalyst also the potential influences and affects the reaction rather than the current density.[203] For this purpose, they investigated different combinations of Pd and Au alloys supported on carbon at different potentials that revealed the strong dependence of conversion and selectivity on the applied potential: 25, 83 and 36 % yield of FDCA at full conversion while applying 0.6, 0.9 and 1.2 V vs. RHE, respectively.[203] Similar to the aerobic oxidation processes, electrocatalysis also focused on non-noble metal catalysts often supported on porous, high surface electrodes like Cu-foam (CF), Ni-foam (NF) or carbon substrates, sometimes even used as cathode material as well. These results are summarized in Table 4.

Table 4: Reported works on the oxidation of HMF to FDCA via electrolysis over different electrocatalysts, presenting the solvent and potential as reaction conditions, as well as conversion of HMF (*X*), yield of FDCA (*Y*) and faradaic efficiency (*FE*) of H_2 production. [a)] Cell potential in two electrode setup.

Catalyst	Solvent	Potential *E* / V vs. RHE	*X* (HMF) / %	*Y* (FDCA) / %	*FE* (H_2) / %	Ref.
Pd_1Au_2/C	0.1 M KOH	0.9	100	83	-	[203]
NiOOH/FTO	0.1 M KOH	1.47	99.8	96	-	[204]
Ni_2P/NF	1 M KOH	1.423	100	98	100	[7]
Ni_2S_3/NF	1 M KOH	1.423	100	98	100	[205]
Ni*FE* LDH/C	1 M KOH	1.33	98	98	-	[206]
Ni_xB/NF	1 M KOH	1.45	100	98.5	-	[207]
Ni_3N/C	1 M KOH	1.45	100	98	-	[208]
Co-P/CF	1 M KOH	1.423	~ 100	~ 90	100	[209]
CoB/NF	1 M KOH	1.45	100	94	-	[202]
CoNW/NF	1 M KOH	1.504[a)]	100	96.8	100	[210]
Cu-foam	0.1 M KOH	1.62	100	~ 96	-	[211]
TiO_x/MnO_x	0.1 M $HClO_4$	1.69	100	~ 24	-	[212]
MnO_x	H_2SO_4	2.0	> 99.9	53.8	0	[213]

TAITT ET AL. studied for Ni, Co and *FE* layers on fluorine-doped tin oxide (FTO) HMF oxidation catalysts, if the oxyhydroxides of these metals are the catalytically active sites. This is true for NiOOH, where 98 % FDCA were yielded in 0.1 M KOH at 1.47 V vs RHE.[204] CoOOH was able to yield 35.5 % FDCA with a conversion of 95.5 % at 1.56 V vs RHE, while FeOOH only managed to convert 16 % HMF at 1.71 V vs RHE with a FDCA yield of 1.59 %.[204] Keeping the activity of NiOOH in mind, other Ni-based catalysts also showed outstanding HMF oxidation ability.[205],[206],[208] For example, Ni_2P on Ni-foam works as a bifunctional catalyst as it was able to convert 98 % HMF to FDCA in 1 M KOH at 1.423 V vs. RHE, while also reaching a 100 % faradaic efficiency (FE) for H_2 production on the cathodic side.[7] Apart from the batch approach, also a continuous flow reactor was able to produce FDCA using Ni_xB on NF as catalyst system.[207] It required a slightly higher potential (1.45 V vs RHE) to convert 98.5 % of HMF to FDCA in 1 M KOH at full conversion at a flow rate of 18 mL min^{-1}.[207] Not only Ni is active towards HMF oxidation, also cobalt is, even if CoOOH has not been that active towards HMF oxidation.[204] Co-P deposited on copper-foam was able to yield 90 % of FDCA at nearly full conversion at 1.423 V vs. RHE in 1 M KOH, while also producing hydrogen at the cathode with a *FE* of 100 %.[209] Furthermore, Cu-foam is not only used as porous substrate but can also be a

HMF oxidation catalyst itself as it produces ~ 96 % of FDCA at full conversion at 1.62 V vs RHE in 0.1 M KOH for several cycles.[211]
All these catalysts convert HMF to FDCA with high yields at high conversions, but their disadvantage is the alkaline media in which it takes place. As mentioned in chapter 2.3, HMF degrades at pH values over 12 and therefore, 0.1 M KOH supports this unwanted reaction and other aqueous media have to be investigated.[168],[169]
Therefore, HMF oxidation in acidic media poses a challenge as less hydroxide ions, which are needed for FDCA production from HMF (Scheme 1), are available than in alkaline media but which also possesses a significant advantage. Apart from HMF not degrading, FDCA is not soluble at low pH values and precipitates but HMF is, so direct separation of the product is possible.[212],[213] Mn-based catalysts seem to be capable of meeting this challenge, even if elevated temperatures are necessary, at which FDCA is soluble again.[212],[213] TiO_x supported on MnO_x is able to yield 24 % of FDCA with FFCA as the other main product in 0.1 M $HClO_4$ at 1.69 V vs RHE and 60 °C.[212] They were able to increase the catalyst performance by raising the temperature up to 80 °C, but the electrolyte started vaporizing.[212] KUBOTA ET AL. were able to even reach 53.8 % yield of FDCA at full conversion at 2.0 V vs RHE in H_2SO_4 (pH = 1) and 60 °C with maleic acid being the most present side product (21.9 % yield), which is also a valuable building-block with economical value.[213]
Anodic oxidation of HMF to FDCA via heterogeneous catalysts is able to solve the problems occurring with aerobic oxidation but does not achieve the desired performance. However, homogeneous electrocatalysts could solve this issue, even if it failed in aerobic oxidation of HMF to FDCA.[163],[164],[165] Firstly, chemical reactions can take place under mild conditions[214], which is necessary for HMF oxidation.[168],[169] In addition, the electron transfer between electrode and substrate, often associated with undesired kinetic inhibition, can be removed by using a mediator[214], *e.g.*, TEMPO.[215]

2.5. TEMPO as mediator in homogeneous catalysis

2,2,6,6-tetramethylpiperidine N-oxyl, better known as TEMPO, represents an organic radical that is stable under ambient conditions.[216] Since both sites adjacent to the aminoxyl radical are fully substituted, disproportionation to the corresponding nitrone and hydroxylamine with α-protons can be prevented.[215] It can be used in a broad variety of applications as a spin label in electron spin resonance (ESR) studies,[217] antioxidant in biological processes,[218],[219] *e.g.*, in the human body to prevent possible brain damage,[220] charge carrier for energy storage in batteries[221] or solar-to-electric devices[222] and electrode material in batteries.[223],[224] Above all, TEMPO is mainly utilized as catalyst and electrocatalyst in oxidation reactions[225] as it is able to recover itself via electron transfer, as seen in Scheme 11.[215],[225] Due to the electrochemical approach in this work, TEMPO as electrocatalyst will be highlighted in this chapter.
In 1973, TEMPO has been electrochemically investigated for the first time as cyclic voltammetric (CV) studies proved that the reaction from the aminoxyl radical to the oxoammonium cation (**2** and **-2**) is a reversible one electron process, which was furthermore confirmed by ESR studies.[226] 15 years later, the electron transfer process from the aminoxyl radical to the hydroxylamine (**-1**) could be confirmed via CV as well.[227] Though, the reverse reaction (**1**) could not be confirmed as its signal appears close to the one of **2** leading back to a sluggish electron transfer between this redox couple.[228] Additionally, the very large peak separation between these two reactions (**1** and **-1**) assign to a quasi-reversible behavior.[215]

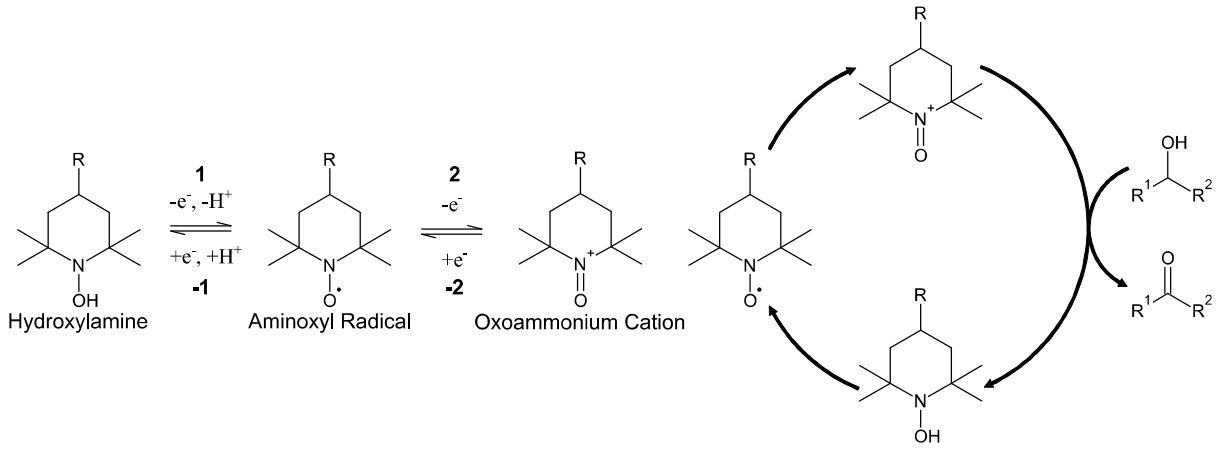

Scheme 11: Left: the three oxidation states of TEMPO species and the transition between them. Right: the oxidation of an alcohol group to a carbonyl group via TEMPO as mediator that is able to regenerate itself.[215],[225] Copyright American Chemical Society and John Wiley & Sons – Books.

At a low pH, the signal for **1** even showed up at more positive potentials than that of **2**, shifting to more negative potentials with rising pH, diminishing the large gap of peak separation.[229] Furthermore, TEMPO and its derivatives can undergo deactivation reactions in acidic and alkaline media leading to an occupancy of the nitroxyl group, as seen in Scheme 12.[215],[230]

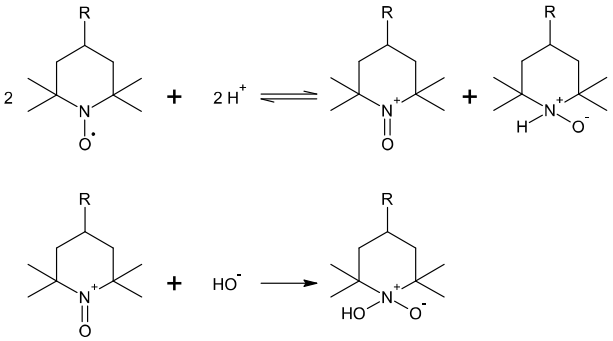

Scheme 12: Equilibrium of TEMPO dis- and comproportionation in acidic media (above) and adduct formation of TEMPO in alkaline media (below).[215],[230] Copyright American Chemical Society.

The before mentioned nitroxyl group or rather the oxoammonium cation is considered the active center of TEMPO in oxidation reactions, which GOLUBEV ET AL. reported as early as 1965.[231] The alcohol group is deprotonated, so the negatively charged oxygen can attack the positively charged nitrogen as a nucleophile (11), as depicted in Scheme 13, upper path.[232] Afterwards, an intramolecular ring forms with a connecting hydrogen bond that can transfer a hydride to result in the hydroxylamine and the aldehyde group (12).[232] Another possibility is the nucleophilic attack on the positively charged oxygen to form a peroxide (13), before another intramolecular ring evolves (14).[232] In this case, the nitrogen grabs a hydrogen of the attacking alcohol group, which results in the aldehyde side group and a TEMPO dipolar ion that transforms intramolecular to the hydroxylamine.[232] Nevertheless, the attack on the electrophilic nitrogen position is the preferred route for the oxidation of alcohol to aldehydes.[232],[233] Since also steric effects influence the nucleophilic attack, primary alcohols can be faster converted than secondary ones, which happens at best in buffered solutions with a pH of around 10 to accelerate the deprotonation of the alcohol group, while guaranteeing the stability of TEMPO itself,[234] as mentioned before and in Scheme 12.[215],[230] The oxidation of the aldehyde group runs similarly to the alcohol oxidation. At first, a hydroxide ion attacks the

carbonyl to create a negatively charged oxygen, which subsequently attacks the positively charged nitrogen of the oxoammonium cation, before the same intramolecular ring as before forms to finally yield in the hydroxylamine and the carboxylic acid.[235],[236] Both reaction mechanisms are depicted in Scheme 13.

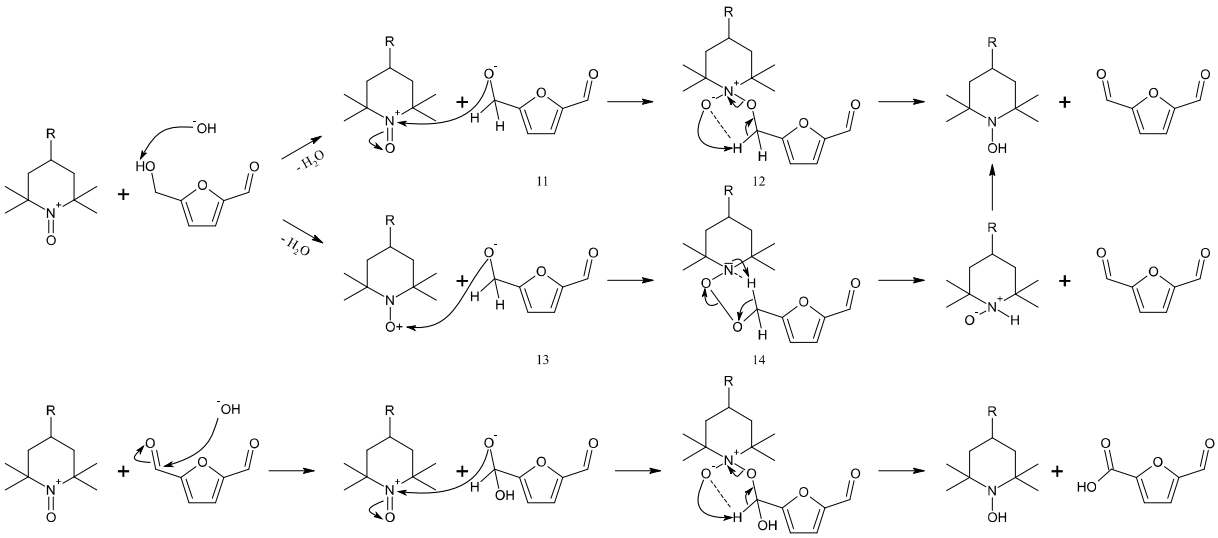

Scheme 13: Reaction mechanisms of TEMPO mediated alcohol side group (above)[231],[232] and aldehyde side group oxidation (below)[235],[236] in alkaline media with HMF and DFF as example substrates, respectively. Copyright Springer Nature, American Chemical Society, John Wiley & Sons – Books and Elsevier.

RAFIEE ET AL. investigated the electrochemical oxidation of different alcohols with TEMPO and other aminoxyl radicals and proved the conversion to their corresponding carbonyl product independent from their steric hindrance.[234] It was possible with primary, secondary, sterically hindered primary, secondary aliphatic alcohols as well as primary and secondary benzylic alcohols.[234] Furthermore, the primary aliphatic alcohols like 1-butanol and neopentyl alcohol yielded in their corresponding carboxylic acid.[237] Additionally, 4-acetamido-TEMPO, a TEMPO derivative with an acetamido side group, not only exhibited faster conversions than TEMPO itself due to a higher turnover frequency but also a better stability in alkaline media up to pH 13.[237] Concurrently, they could prove that electrochemical regeneration of TEMPO and therefore the reaction rate enhances with higher potential applied even if steric effects should hinder a faster conversion.[237] Nevertheless, co-catalysts/co-mediators were often used to regenerate TEMPO or its derivatives chemically, so stoichiometric amounts of oxidants like bleach (NaOCl),[237] iodide,[238] bromite[239] and mainly bromide[240],[241],[242] were used to oxidize different alcohols. Among them, a broad range of alcohols like before mentioned aliphatic and benzylic alcohols,[237],[240] HMF,[238] dihydroxyalkanoates,[239] cyclopropyl-carbinols[241] or menthol[242] were converted. Furthermore, TEMPO mediated oxidation of different carbohydrates derived from biomass have been extensively studied as no co-catalyst was necessary to oxidize primary alcohol groups of mono-, di-, oligo- and also polysaccharides to their corresponding carboxylic acids.[243] Additionally, even the primary alcohols and the anomeric position of maltose and cellobiose were converted to their corresponding carboxylic acids.[244] Furthermore, cellulose was oxidized to polyglucuronic acid[245] that might be utilized as solvent, stabilizer, binder, swelling agent and carrier for active substances.[246]

Also even HMF was successfully converted to DFF via TEMPO mediated oxidation with iodide or bromide as co-mediator and 4-acetamido-TEMPO as catalyst.[238] Furthermore, HMF to FDCA oxidation with TEMPO or its derivatives as mediator was also investigated. An electrochemical approach with a TEMPO derivative as mediator can also lead to FDCA starting from HMF:

4-acetamido-TEMPO and a carbon felt electrode in the anode compartment yielded in 96 % FDCA (same FE) at full conversion in a borate buffer solution with pH 10 at 40 °C.[247] A combination of HMF oxidation and a cathodic reaction similar to the approach mentioned in chapter 2.4 is also possible with TEMPO as mediator as CHADDERDON ET AL. were able to use HMF as substrate for both reactions.[248] Again, a carbon felt electrode with 4-acetamido-TEMPO as mediator was used as anode with Ag nanoparticles supported on carbon as cathode to yield in 98 % of FDCA and 85 % of BHMF.[248] The overall *FE* corresponded to 187 % at -1.3 V at the cathode and an uncontrolled potential at the anode in borate buffer solution with pH 9.2.[248]
In 2020, LI ET AL. used an innovative approach for TEMPO mediated alcohol oxidation by using an ionic liquid phase to immobilize TEMPO on the electrode, so it does not have to be separated from the electrolyte after reaction.[249] It is better known as supported ionic liquid phase (SILP)[249] and might be an interesting alternative for future electrochemical applications.

2.6. Supported Ionic Liquid Phase

The supported ionic liquid phase (SILP) concept describes the heterogenization of a homogeneous catalyst by dissolving it in ionic liquid that itself is immobilized on a porous support material.[250] It was first reported in 2002 by MEHNERT ET AL. who used it as catalyst system for the hydroformylation of 1-Hexene in a fixed-bed reactor.[251]

2.6.1. Characteristics of Ionic Liquids

Ionic liquids (ILs) consist of a cation that is mostly obtained by the quaternization of an amine or a phosphane *e.g.*, by reaction with an alkyl halide, and a conjugate Brønsted base as an anion that was generated during an ionic exchange with the halide *e.g.*,. as it can be a metal salt or a Brønsted acid.[252] The most common cations and anions processed in ILs are shown in Figure 4, while halides as chloride, bromide or iodide are not depicted, even if they are common anions.

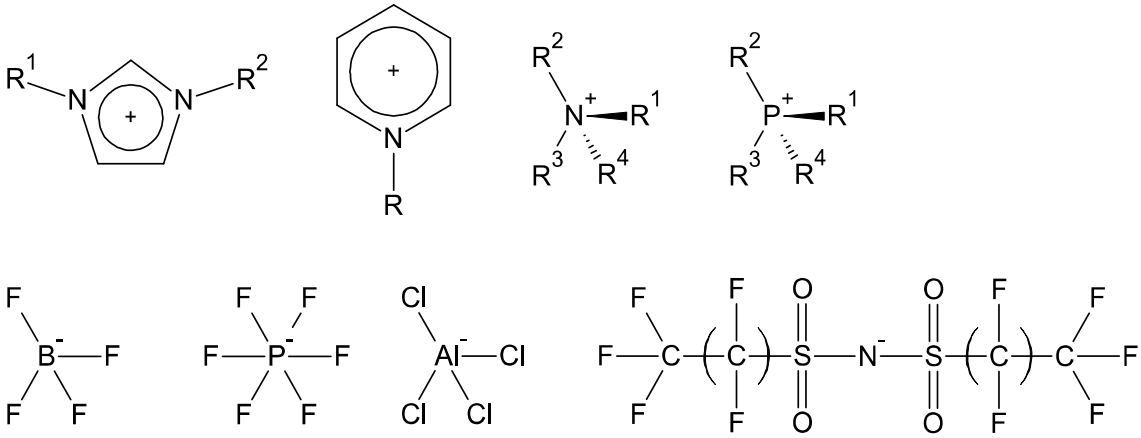

Figure 4: Common cations (above) and anions (below) that ILs are consisting of. Left to right: imidazolium ion, pyridinium ion, ammonium ion, phosphonium ion, tetrafluoroborate, hexafluorophosphate, tetrachloroaluminate, bis(trifluoromethylsulfonyl)imide (NTf_2; without CF_2-group in bracket), bis(pentafluoroethylsulfonyl)imide (BETI; with CF_2-group in bracket).[252],[253] Copyright John Wiley & Sons – Books.

Due to the almost infinite combinations of different anions or cations, it is possible to tailor the properties of the desired IL by choosing anions for a specific cation or vice versa leading to a broad variety of application possibilities for ILs.[254] By definition, an IL should have a melting

point below 100 °C, which emphasizes the relationship between the structure and the chemical composition[252]: low symmetry[255] and a good distribution of charge[256],[257] are favorable in a cation for a low melting point, whereas a big anion leads to a further decrease.[252] Interestingly, molecular interactions like H-bonding and van der Waals forces seem to have just a minor influence on the melting point.[257]

One of the most advantageous properties of ILs is their not measurable vapor pressure,[255] which makes them superior to organic solvents that emit vapors and therefore contribute to air pollution.[254] Furthermore, separation problems like azeotrope formation can be excluded, which simplifies purification steps *e.g.*, product isolation.[252] Most ILs are also stable until temperatures of up to 150 to 200 °C,[258],[259] while some can operate at temperatures as high as 400 °C,[257],[259] which underlines their thermal stability and liquid range that consequently is advantageous over water and other organic solvents.
The density of ionic liquids is also tunable by choosing different anions and cations as it increases with a decreasing alkyl chain of the cation[260] and an increasing size of the anion.[261],[262] In contrary to the melting point, molecular interactions like van der Waals forces or H-Bonding do affect the viscosity of ionic liquids as anions with both of these interactions enhance viscosity as well as cations with a high molecular weight and low side chain mobility.[257] Viscosity can be lowered by adding a small amount of organic cosolvents[263] or higher temperatures.[264] Besides these properties that can be tailored to their application, most ILs also show a broad electrochemical window, in which they are inert, that makes them also interesting for electrochemical applications.[257],[265]
The stability of ILs depends on the anion and its stability against water and oxygen, as especially chloroaluminate anions are extremely hygroscopic and can release superacid protons in reactions with water.[252] In alkaline media, imidazolium-based cations tend to a ring opening reaction at the C2 position, which results in a degradation of the ionic liquid itself that also happens under elevated temperature of 80 °C.[266],[267] A disadvantage of ILs is their (eco)toxicity and non-biodegradability that stems from long branched alkyl chains as well as N-substituted cations and fluoroorganic or cyano anions.[268] Even biodegradable ILs can still be toxic to biological systems, which is dependent on its chemical structure, the length of the cation side chain as well as its core and the nature of the anion that has to be kept in mind while choosing an IL for a specific application.[268] Nevertheless, hydrolyzable groups in side chains (*e.g.*, esters) can help to overcome this issue on an intramolecular level or the degradation via photo-, electro- and biochemical processes to remove poorly biodegradable ILs from water.[268]

2.6.2. Applications of Ionic Liquids

Due to the before mentioned broad range of several physical and chemical properties, the range of possible applications for ILs is similarly versatile. From an engineering point of view, ILs can be utilized as lubricant since they are non-flammable, have no vapor pressure and a good thermal stability as they also can have superior tribological properties that lead to reduction of friction and wear as well as non-corrosive behavior.[269],[270],[271] Another engineering application is as plasticizer, because ILs are able to break up hydrogen bonds of starch or cellulose to realize their plasticization.[272] They can furthermore enhance the liquid uptake capability, porosity and ionic conductivity of a gel electrolyzer.[273] Magnetic ILs show promising performance of heat, mass transfer and good conductivity,[272] as it is possible to implement

magnetic active metals (*e.g.*, Dysprosium) as complex ions into ILs ("magnetic ILs"), which in case of Dy resulted in not only magnetic but also luminescent properties.[274]
Besides these mechanical features, ILs with an olefinic side chain at the imdazolium cation can be tailored that have a similar density to water, which decreases rapidly with increasing temperature that leads to a reversible phase reversion in a two-phase system with water.[275] A possible application could be the following: At first, water is in the upper phase, where reactions can take place and with rising temperature the density of the IL would decrease, which would lead to a phase reversion and a possible protection of the reaction mixture.[272]
Furthermore, ILs can be used in a variety of chemical applications as they have a high gas capacity and are therefore able to absorb gases like NO_x,[276] H_2S[277] or SO_2[278] and most importantly keep them due to their low vapor pressure and thus nearly nonexistent volatility.[277] As mentioned in chapter 2.1 for HMF oxidation from biomass as feedstock, ILs are on one hand also able to dissolve natural biomaterials like cellulose, glucose or fructose and can on the other hand be used as catalysts. Other IL-catalyzed reactions are the nitration or halogenation of toluene,[279] the synthesis of 1,4-dibromonaphthalene starting from naphthalene and molecular bromine[280] or the synthesis of cyclic carbonates by chemical fixation of CO_2, in which the before mentioned gas capacity plays an important role.[281]
The application of ILs in another field, the electrochemistry, started in 1951 when they were used as bath solutions to electroplate platinum.[282] Their investigation went on in the 1970s[283] and early 1980s with the first publications about their broad electrochemical window,[265] which still makes them attractive for electrochemical applications until now.[284] They became highly interesting for research in the early 1990s[285] as it was discovered that ILs can be stable against water and oxygen which is also used until now to protect catalysts like Platinum.[286] Moreover, ILs show a broad variety of application possibilities in electrochemistry. Water-sensitive metals like aluminum or magnesium are impossible to electrodeposit in water-based electrolytes.[287] However, IL-based ones allow the electrodeposition of Al[288],[289] and Mg[290] onto an electrode, while also affecting and tuning film properties like grain size.[289] ILs can also be used to electrodeposit ultrapure materials *e.g.*, photoluminescent Si_xGe_{1-x} used in semiconductors, whereby photoluminescence effects could be observed during deposition, which underlines the ultra-high purity of the used IL and the Si_xGe_{1-x}.[291] ILs are also considered as electrolyte in batteries due to their non-flammability, which prevents the thermal runaway and therefore erases a significant safety issue.[287] Mostly, they are utilized as metal- and IL-containing electrolyte in different setups like Lithium ion batteries,[292] in which the IL can also be grafted onto a polymeric backbone,[293] Li-S batteries[294] or even sodium metal batteries.[295]

2.6.3. Applications of Supported Ionic Liquid Phase

Another step for utilizing ILs was made in the early 2000s with the invention of the supported ionic liquid phase (SILP) concept by RIISAGER, FEHRMANN, HAUMANN AND WASSERSCHEID: a homogeneous catalyst is mixed with a small amount of IL, which is then immobilized on a high surface area support material.[296] Since ILs have practically no vapour pressure,[252] the catalyst keeps being dissolved in the IL phase which is also promoted by the high solvent polarity.[296] Another significant advantage is good catalyst immobilization in ILs by use of charged ligands[250] as well as an efficient use of a small amount of expensive IL that is needed because IL distributes evenly onto the surface of the porous support.[296] All of these points lead to a "heterogenization" of the homogeneous catalyst since it does not need to be removed from the reaction mixture, invalidating its most limiting weakness.[296] A remarkable disadvantage is the possible leaching of IL into the aqueous phase that can also lead to leaching of the homogeneous

catalyst, which demonstrates the opposite of the desired SILP effect.[297] Figure 5 illustrates this approach schematically while also depicting the heterogeneous catalyst approach (solid catalyst with ionic liquid layer; SCILL)[298] for comparison. In electrocatalysis, the heterogeneous SCILL system has drawn attention for a long period *e.g.*, for oxygen reduction reaction.[286],[299],[300] The IL can suppress the metal catalysts dissolution, while the activity can also be enhanced by *e.g.*, the good dissolving capacity of O_2 into the IL.[299],[300]

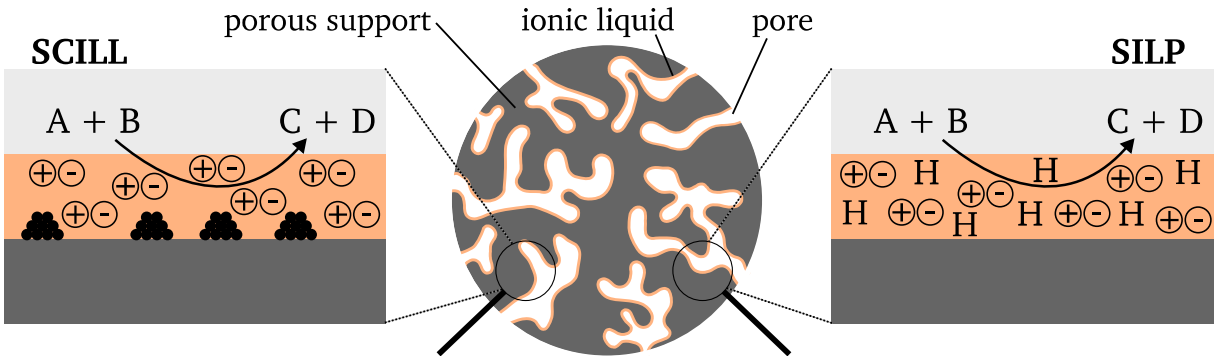

Figure 5: Schematic illustration of an ionic liquid (orange) coated porous support (grey) with a heterogeneous catalyst (black pile, SCILL, left) or a dissolved homogeneous catalyst ("H", SILP, right) in contact with an electrolyte (blue).[301] Copyright John Wiley & Sons – Books.

The before mentioned SILP concept was proven by Rh catalyzed hydroformylation reactions with 1-hexene[251] and propene[250] as feedstock and since, other chemical conversions have been successful using SILP catalysts. The hydrogenation of different aromatic and aliphatic aldehydes with yields over 98 % was possible at 25 °C and 50 bar hydrogen with an Fe(II) PNP (2,6-bis-(di-tert-butylphosphinomethyl)pyridine) homogeneous catalyst in C_4C_1MIM (1-butyl-2,3-dimethylimidazolium) NTf_2 onto powdered silica.[302] The surface of the silica support was also functionalized with an IL to enhance the interaction of the used IL with the surface and prevent leaching.[302] Another iron catalyst paired with Ru immobilized in an imidazolium-based IL (1-butyl-3-(triethoxysilylpropyl)imidazolium NTf_2) grafted onto SiO_2 was able to convert hydroxyacteophenones to their corresponding ethyl-substituted phenol in a hydrodeoxgenation reaction at 175 °C and 50 bar hydrogen with yields over 90 % for different derivatives.[303] IL was not able to leach as it is covalently connected to the support material, but SEM-EDX was used to investigate leaching of the homogeneous catalyst, which could not be confirmed.[303] Another investigated reaction is the water-gas-shift reaction (WGSR), in which CO and H_2O are converted to CO_2 and H_2 that is shifted to the desired hydrogen at lower temperatures due to the exothermic and reversible nature of the WGSR.[304] Therefore, a catalyst system that converts CO and H_2O at lower temperatures as usual in industry (at 350 °C as high-temperature shift and around 200 °C as low-temperature shift) is desired and could be found in Ru-based complexes employed as anion with imidazolium-based cation on SiO_2.[305] Even if it was able to produce CO_2 and H_2 at temperatures as low as 120 °C and was stable over 24 h, it is not suitable for industrial applications since the turnover frequency of around 2 $mol_{CO2}\ mol_{Ru}\ h^{-1}$ is too low, but the SILP approach was ideal for catalyst screening.[305]
As mentioned before, ILs are able to trap metal ions *e.g.*, to purify water.[306],[307],[308],[309] This characteristic can also be used in SILP approaches to recover minor elements like Germanium (Ge) and Indium (In) from waste streams that can rarely be found in natural ores.[310],[311] Aliquat 336, a mixture of quaternary ammonium cations with chloride as anion, immobilized on Amberlite XAD-16N has been used as extractant, while citrate for Ge and chloride or iodide for In was added as complexing agent, which led to the extraction of both into the IL with both

systems showing no indications of leaching.[310],[311] As the scarce Ge is used in fiber optic systems and electronics[312] and the rare In in liquid crystal displays, better known as LCDs, semiconductors and solar cells[313] the extracting approach might be future-oriented. Additionally, also scandium (Sc), which belongs to the rare earth metals[314] and cannot be found as easily in nature as there are just a few minerals or ores containing it and which is used in halide lamps and fuel cells,[315] has been successfully extracted by a SILP approach. Therefore, a betaine-based cation with an NTf_2-based anion covalently connected to a polystyrene backbone extracted Sc(III) from acidic media with nitrate or chloride as complexing agent, which is furthermore reusable and shows no signs of leaching.[315] Besides liquid purification, also gas purification is possible with a SILP system as mostly imidazolium-based ILs immobilized on metal organic frameworks, silica or polymeric materials were able to remove CO_2, CH_4 and SO_2 as air pollutants as well as H_2S, NH_3 and volatile organic compounds as malodors from air.[316],[317]

SILP offers another "purification" application as a sulfated imidazolium-based cation paired with heteropolyacids ($PMo_{12}O_{40}^{3-}$ or $PW_{12}O_{40}^{3-}$) as anions on γ-Al_2O_3 or silica had the ability to oxidize sulfur-containing substrates like thiophene, thioanisole and dibenzothiophene.[318] Due to these catalytic activities, an important application is the possible desulfurization of diesel fuel to an amount of < 100 ppm under mild conditions at 60 °C.[318] Furthermore, pharmaceutically active compounds in their ionic form can be integrated into ILs *e.g.*, ibuprofen as negatively charged ibuprofenate with tetrabutylphosphonium or lidocainium as cations.[319] They were immobilized onto non-toxic silica and released the drugs under aqueous conditions with no leaching at all.[319]

However, an electrocatalysis application using SILP has not been published until 2020 when LI ET AL. investigated the first SILP approach, which consisted of a TEMPO derivative in IL immobilized onto graphite to oxidize three different alcohols.[249] The scheme of this approach is depicted in Figure 6.

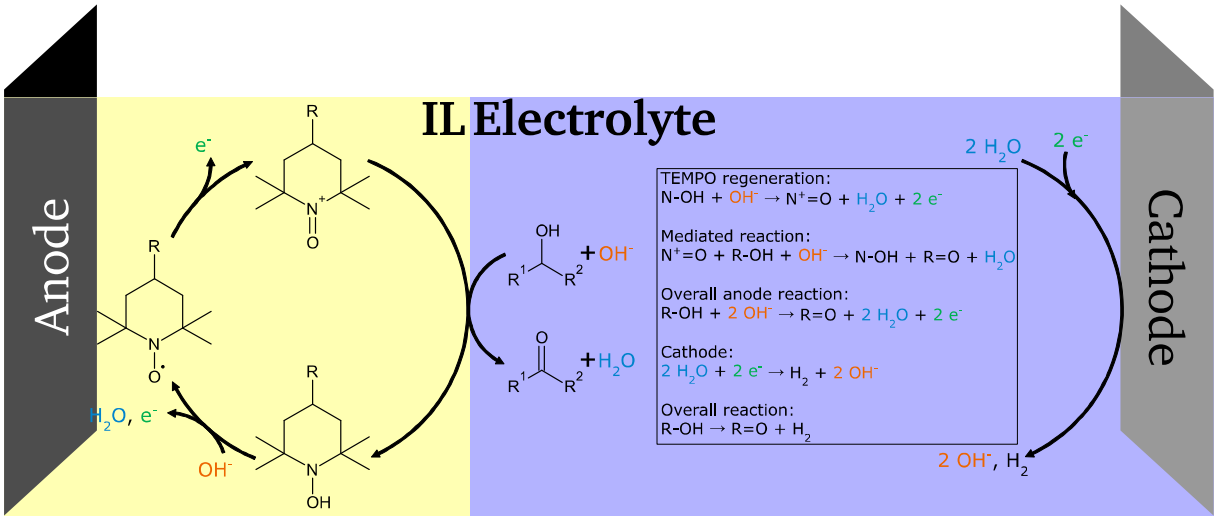

Figure 6: Schematic illustration of the SILP system used in electrocatalysis with TEMPO mediated alcohol oxidation and regeneration[225] in IL at the anode and HER in alkaline electrolyte at the cathode.[200] Copyright John Wiley & Sons – Books and Springer Nature.

4-acetamido-TEMPO and pyrene-TEMPO could be immobilized in several ILs like C4MIM and C10MIM NTf_2 by mixing them with graphite powder and a polymer as binding material. Afterwards, benzyl alcohol, 1-butanol and glycerol have been oxidized at pH 10 in carbonate buffer solution, which led to promising results. Especially pyrene-TEMPO in C_{10}MIM NTf_2

exhibited an active and stable alcohol oxidation performance, which is a perfect example of SILP used in electrocatalysis.[249] Since this approach led to a promising result, SILP systems could be useful in other electrocatalytic systems as well.

3 Objectives and Experimental Approach

As seen in chapter 2, HMF oxidation to FDCA is a promising reaction, but even if electrocatalysts can offset the disadvantages of aerobic ones due to ambient reaction conditions, they do not reach the catalytic performance needed. However, anodic HMF oxidation is the key for high energy and feedstock efficiency and homogeneous mediators could be a platform, which allows an optimization of catalysts. Thus, SILP immobilization is an attractive concept and therefore scope of this work, which can be broken down into three aspects.

At first, there is no protocol for comparison of different catalytic systems regarding HMF oxidation. Thus, a measurement protocol has to be developed at first, which allows aforementioned comparison independently of the used catalytic material. Therefore, the influence of used electrolyte and its interaction with every reactant from Scheme 1 has to be investigated using HPLC to check for possible degradation reactions and progress of HMF oxidation to FDCA. Next, the used cell design is modified to minimize the influence of possible occurring side reactions by separation of anodic and cathodic chamber, checking the stirring rate, as well as by variation of different counter electrode materials and their area. After these fundamental aspects have been investigated and set, different electrode materials are tested to find an inert but conducting one. Then, a three electrode setup is used to determine the potential window with the highest activity for HMF oxidation using cyclic voltammetry, electrochemical impedance spectroscopy and chronoamperometry. Catalytic activity can be determined by electrolysis using a two electrode setup and once again HPLC to check for reaction progress: Yield, faradaic efficiency and tracking of side products are used to identify the selectivity of the examined catalyst, while a new figure of merit, production rate, allows to further compare different catalytic systems.

Another challenge that arose from catalytic systems so far investigated (chapters 2.3 and 2.4) is the use of either high temperature, pressure or noble metals for aerobic oxidation or highly alkaline electrolytes for electrochemical oxidation. Therefore, TEMPO is investigated as an easy to modify homogeneous catalyst to circumvent these disadvantages. At first, its catalytic activity towards HMF oxidation is proven using the aforementioned measurement protocol, in which TEMPO is dissolved in the reaction solution. As a next step, other TEMPO derivatives are also investigated in solution, in which a clear HMF oxidation activity can be observed. As explained in chapter 2.6.3, the disadvantage of homogeneous catalysts is their presence in reaction solution, which can be overcome by using the SILP method. Using this approach, TEMPO is dissolved in IL and immobilized onto a microporous support before HMF oxidation activity is examined using the aforementioned protocol. As different TEMPO derivatives immobilized by long chain ILs demonstrate the most promising catalytic behavior, hydrophobic long chain ILs are synthesized as well as a variety of also long chain TEMPO derivatives. Every newly synthesized molecule is analyzed via ^{1}H- and/or ^{19}F-NMR for the right structure and via electron spin resonance to check for the activity of the TEMPO derivatives' free radical. In another approach, also TEMPO covalently connected to an IL as well as an aromatic TEMPO derivative are prepared and investigated. Last, different porous carbons are used as support for the SILP systems.

However, not only activity towards HMF oxidation is examined for all different SILP combinations but also stability. Therefore, chronoamperometry is used to observe activity over 12 and 24 h as well as ^{1}H- and ^{19}F-NMR to control TEMPO and/or IL concentration in used electrolyte.

4 Experimental Section

4.1. Chemicals

Table 5: Used chemicals, their supplier and their purity.

Chemicals	Supplier	Purity / %
HMF	*Südzucker*	99
DFF	*Sigma Aldrich*	97
HMFCA	*ABCR*	98
FFCA	*ABCR*	95
FDCA	*Alfa Aesar*	98
$CuSO_4 \cdot 5\ H_2O$	*Fisher Scientific*	98
H_2SO_4	*Acros Organics*	96
$NiSO_4 \cdot 6\ H_2O$	*Acros Organics*	> 98
CuCoO	*LIKAT, Rostock*	99
$NaH_2PO_2 \cdot H_2O$	*Acros Organics*	99
TEMPO	*Alfa Aesar*	98
4-Hydroxy-TEMPO-benzoate	*Sigma Aldrich*	97
4-Methoxy-TEMPO	*Sigma Aldrich*	97
4-Hydroxy-TEMPO	*Sigma Aldrich*	97
4-Amino-TEMPO	*Sigma Aldrich*	97
4-Dimethylaminopyridine (DMAP)	*Sigma Aldrich*	99
N-(3-Dimethylaminopropyl)-N -ethylcarbodiimide hydrochloride (EDC)	*Sigma Aldrich*	98
Dichloromethane (DCM)	*Fisher Scientific*	99
$MgSO_4$	*Fisher Scientific*	99.9
NaCl	*VWR-Chemicals*	99.9
$NaHCO_3$	*Alfa Aesar*	99
Lauroyl chloride ($C_{12}H_{23}ClO$)	*Sigma Aldrich*	97
Myristoyl chloride ($C_{14}H_{27}ClO$)	*Sigma Aldrich*	97
Palmitoyl chloride ($C_{16}H_{31}ClO$)	*Sigma Aldrich*	98
Stearoyl chloride ($C_{18}H_{31}ClO$)	*Sigma Aldrich*	97
1-Pyrenebutyric acid	*Sigma Aldrich*	97
Chloroacetic acid	*TU Darmstadt*	99
Ethyl acetate (EtOAc)	*Fisher Scientific*	99
n-Hexane	*Fisher Scientific*	95
1-Methylimidazole	*Sigma Aldrich*	99
Acetonitrile (MeCN)	*Carl Roth*	99.9
Diethyl ether	*Sigma Aldrich*	99.5
Acetone	*TU Darmstadt*	99
1-Propyl-3-methylimidazolium bis(trifluoromethylsulfonyl)imide (C3MIM NTf_2)	Self-made	-
C4MIM NTf_2	*Sigma Aldrich*	98
C5MIM NTf_2	Self-made	-
C6MIM NTf_2	*Merck KGaA*	98
C4MIM bis(pentafluoroethylsulfonyl)imide (C4MIM BETI)	*Merck KGaA*	98

1-Hexyl-3-Methylimidazolium chloride (C6MIM Cl)	*Merck KGaA*	97
C10MIM Cl	*Sigma Aldrich*	95.5
C12MIM iodide (C12MIM I)	*Sigma Aldrich*	95.5
C14MIM Cl	*Merck KGaA*	96
1-Hexylpyridinium NTf_2 (HPy NTf_2)	Self-made	-
Lithium BETI (Li BETI)	*Io-li-tec*	99
$AgNO_3$	*Sigma Aldrich*	99
HCl (36 wt-% aqueous solution)	*Alfa Aesar*	-
Vulcan	*Cabot*	-
Polymer derived carbon (PDC)	Self-made[320]	-
Isopropyl alcohol (ultrapure)	*Carl Roth*	99.9
Polytetrafluoroethylene (60 wt-% dispersion in H_2O) (PTFE)	*Sigma Aldrich*	-
KOH	*Acros Organics*	85
Ammonium formate	*Acros Organics*	97
Methanol (MeOH)	*Carl Roth*	99.9
Ascorbic acid	*Sigma Aldrich*	99.9
D_2O	*Sigma Aldrich*	99.9
DMSO-d_6	*Sigma Aldrich*	99.8
Methanol-d_4 (MeOH-d_4)	*Sigma Aldrich*	99.8

4.2. Materials

Table 6: Used materials and their supplier.

Materials	**Supplier**
Copper sheet (Cu-sheet)	*Mechanical Workshop TU Darmstadt*
Stainless steel mesh	*Beisser Metall*
Graphite foil (GF)	*Sigraflex*
Boron doped diamond (BDD) on titanium	*WTM Nürnberg-Erlangen*
Microporous layer (MPL) with gas diffusion layer (GDL) 39 BB	*Sigracet*
Hg/HgO electrode (RE-61AP)	*ALS Japan*
Plated platinum	*IKA*
Glass frit	*Lenz Laborglass*

4.3. Syntheses

4.3.1. Electrodeposition of copper and nickel

Copper foam electrodes were prepared in a two electrode setup using an HMP 4040 power supply from *Rhode & Schwarz*, which was controlled by a *LabVIEW* software that was provided by the research group of Prof. Waldvogel from the Johannes Gutenberg University in Mainz (Waldvogel Lab) allowing constant current or constant potential control with a built-in coulomb counter. A stainless steel mesh was used as anode and a copper sheet (thickness: 0.5 mm; width: 7 mm; depth: 7 mm) as cathode, which was dipped into the deposition solution that contained 0.2 M $CuSO_4 \cdot 5\ H_2O$ and 1.5 M H_2SO_4. The whole exposed area ($\sim 0.5\ cm^2$ ($0.49\ cm^2$)) is afterwards covered with foam, so no sheet is visible anymore that could be in contact with any

electrolyte. The deposition solution was stirred during each deposition and replaced after every electrode preparation to maintain replicable starting conditions for each electrode. Standard parameters for copper foam electrode preparation were 3 A cm^{-1} and 10 C, which results in a thickness of 20 - 30 μm.[321] Due to the high potentials occurring at the high current density, the copper sheet produces hydrogen simultaneously, which results in a foam-like structure that is depicted in Figure 7 (a). Figure 7 (b) shows SEM (high-resolution SEM XL-30 FEG from *Philips*; acceleration voltage: 20 kV; spot size: 4; working distance: 7.8, 6.9, 6.8 mm (from left to right); magnification: 100, 1000, 3500 (from left to right)) images of an as prepared copper foam, approving the honeycomb pore structure and dendritic like microstructure that is indicated by literature.[322],[323]

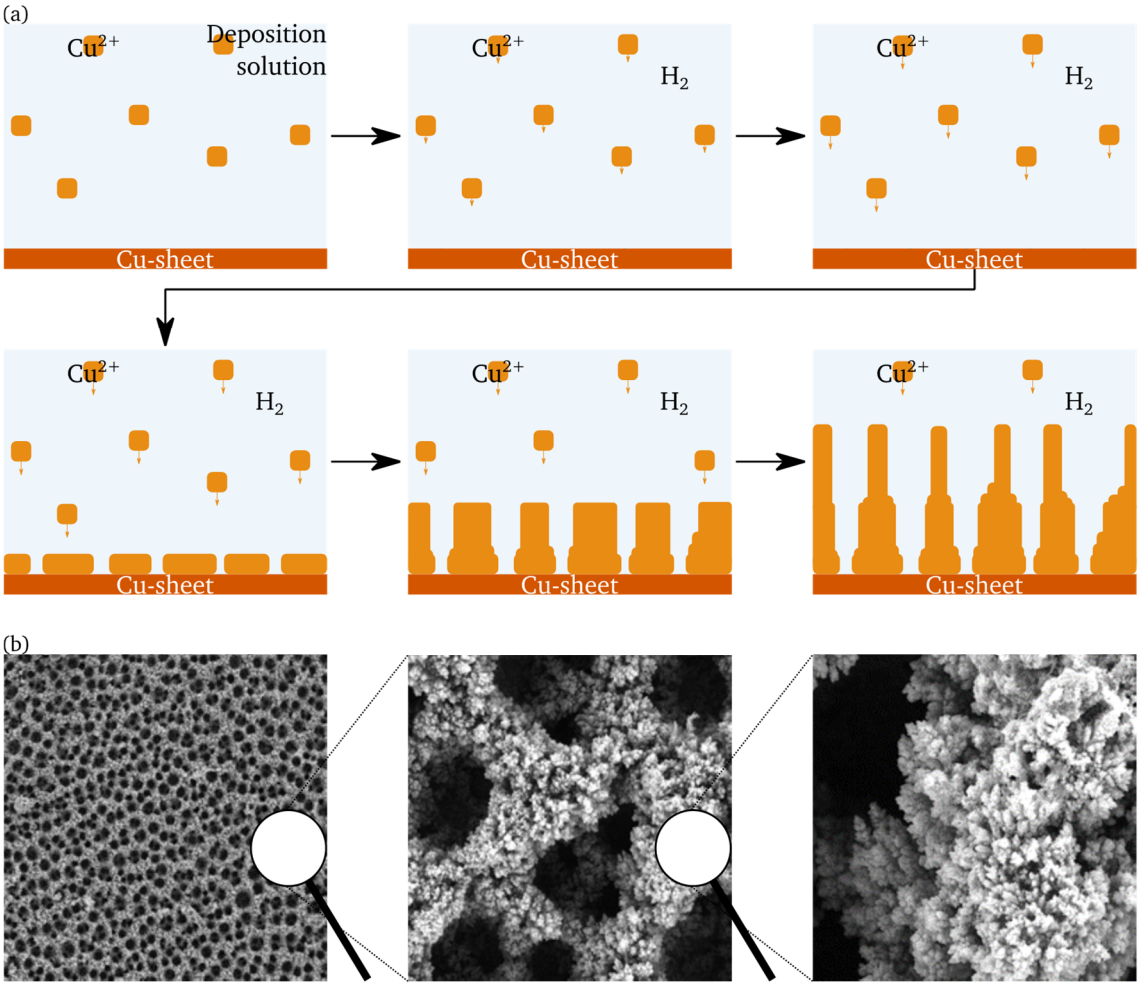

Figure 7: (a) Schematic pathway of copper deposition on a copper sheet to create a copper foam.[322] (b) SEM pictures of a synthesized copper foam with honeycomb pore structure and dendritic microstructure in 100, 1000 and 3500 fold magnification (left to right).

The deposition of nickel proceeded similarly to the one of copper foam with stainless steel mesh as anode and a current density of 3 A cm^{-1}. The differences were the deposition solution, which contained 75 mM $NiSO_4 \cdot 6\,H_2O$, the amount of charge with 5 C and the deposition onto BDD, which itself was coated on titanium with a thickness of 8 - 12 μm.[324] Since BDD is not active for hydrogen evolution, nickel is deposited as a plain layer without any porous structure.

4.3.2. Post treatment of bimetallic oxide catalyst

The bimetallic oxide catalyst CuCoO was synthesized by the LIKAT in Rostock, which followed a literature protocol: The nitrates of Cu and Co were dissolved in a mixture of water and citric acid that are stirred at room temperature, before a gelation at 90 °C, drying at 120 °C and calcination at 300 °C took place to get CuCoO (atomic ratio of Cu:Co = 6:1).[325] Afterwards, the from LIKAT prepared and provided sample was further processed following another literature protocol: After thoroughly grounding it with $NaH_2PO_2 \cdot H_2O$, it was placed in a tubular furnace (SR 70-200/12 *Carbolite Gero* 30 - 3000 °C with an X0004516/-V2 quartz glass tube (length: 900 mm; diameter: 46 mm)) at 300 °C for two hours under nitrogen atmosphere.[326] Subsequently, the powder was washed with water, centrifuged and dried at 80 °C under vacuum to get CuCoO_P.[326],[169] 1 g of catalyst powder is dispersed in 1 mL of isopropyl alcohol by a vial tweeter and afterwards, 50 μL of the ink are drop-coated onto a conductive substrate, so 50 μg of catalyst is immobilized on the electrode.

4.3.3. Synthesis of long chain TEMPO derivatives

4-Amino- (AT)[327] and 4-hydroxy-TEMPO (HT)[328] derivatives were synthesized using a literature protocol: AT or HT were dissolved in DCM, before the acyl chloride (C12, C14, C16, C18) and EDC as cross-linking agent (see chapter 9.1) were added[327]; for the HT derivatives, DMAP as catalyst was also added[328] (see chapter 9.2). The solution was stirred for 24 hours at room temperature, in which the solution turned from a murky red to a clear dark orange, which was reprocessed by saturated $NaHCO_3$ solution as well as saturated NaCl solution, before water was trapped with $MgSO_4$. Solid residues were removed by filtering, before the solution was dried under vacuum to obtain a dry TEMPO derivative Cn-AT or Cn-HT (n = 12, 14, 16, 18), as seen in Scheme 14.[327]

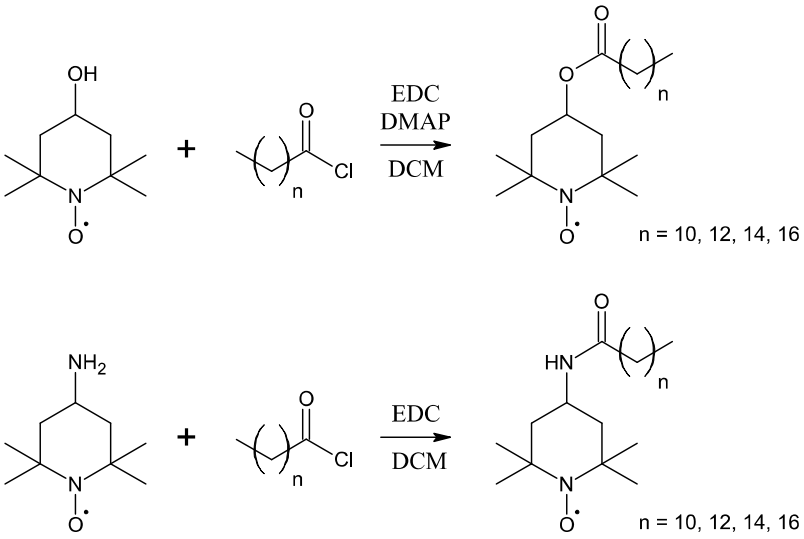

Scheme 14: Synthesis route of 4-hydroxy- and 4-amino-TEMPO derivatives with long chain aliphatic acid chlorides to their corresponding ester (above) and amide (below).[327],[328]

All educts and products were evaluated by proton nuclear magnetic resonance spectroscopy (^{1}H-NMR; 300 MHz Avance II NMR spectrometer from *Bruker BioSpin GmbH* at 300 K and 300 MHz) and electron spin resonance (ESR; ESR-Miniskop MS-400 from *Magnettech* with an A TC H03 temperature controller and a TE102-resonator that works at 9.43 GHz). ESR spectra

were recorded in a 15 mM solution in acetonitrile with a modulation amplitude of 0.1 mT, a modulation frequency of 100 kHz, a microwave damping of 24 dB, a Mantisse- and exponential amplification of 1, at room temperature, in a magnetic field range of 25 mT with a central B_0-field of 337 mT for 60 seconds.
Since every TEMPO derivative possesses a radical, they have a strong hyperfine interaction with other chemical cores, which influences the chemical shift, broadens the signals and shortens the relaxation time that leads to inconclusive NMR spectra.[329] Therefore, ascorbic acid as radical scavenger had to be added to NMR spectra of TEMPO derivatives, which leads to the hydroxylamine as shown in Scheme 15 and thus, conclusive results.

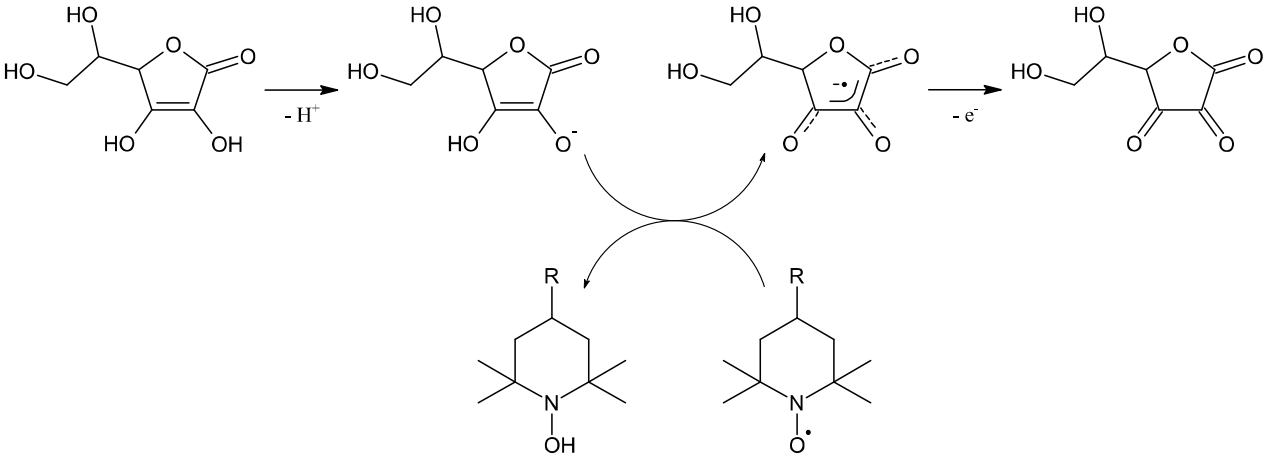

Scheme 15: Reaction of ascorbic acid with TEMPO to scavenge its radical.[330]

4.3.4. Synthesis of long chain ionic liquids

The synthesis of long chain ILs included an ionic exchange of the long chain imidazolium cation halide with Li BETI to obtain CnMIM BETI (with n = 6, 10, 12, 14) that is based on a literature protocol, as seen in Scheme 16.[331] Therefore, the halide salt was dissolved in water, which turned milky when Li BETI was added, and the solution was stirred for 24 hours at room temperature. Afterwards, saturated NaCl solution as well as DCM were added to cause a phase separation, in which the organic one was washed with water until the chloride test with $AgNO_3$ is negative. The solid residue was filtered and the remaining solution dried under vacuum to get CnMIM BETI as a viscous liquid and C14MIM BETI as a solid. All synthesized ILs were evaluated by ^{1}H- and ^{19}F-NMR (same instrument as for ^{1}H-NMR).

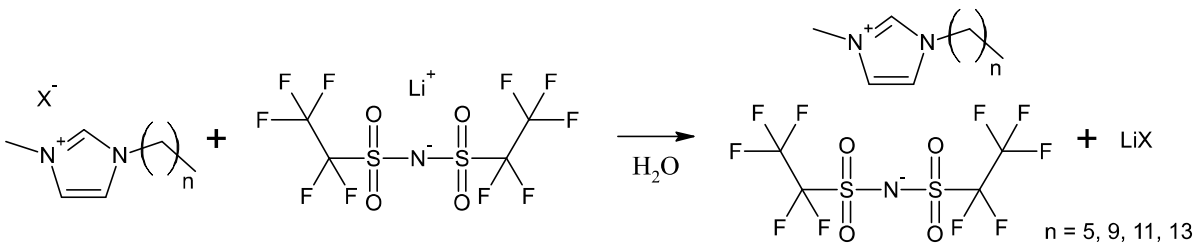

Scheme 16: Synthesis route of CnMIM BETI via ion exchange of the CnMIM halide with Li BETI.[331]

4.3.5. Synthesis of Pyrene-TEMPO

The synthesis of pyrene-TEMPO (PT) is a similar route as the TEMPO syntheses before as seen in Scheme 17, still following a literature protocol[332]: 1-Pyrenebutyric acid was dissolved in DCM under nitrogen atmosphere, before 4-amino-TEMPO was added and the solution was stirred for 30 minutes at room temperature. After EDC and DMAP were added as well, the reaction solution was stirred for 20 hours at room temperature and subsequently filtered and evaporated to obtain an oily product. The purification was performed via flash chromatography (EtOAc:n-Hexane = 1:1) and subsequently, solvent evaporation until the light orange solid could be obtained.

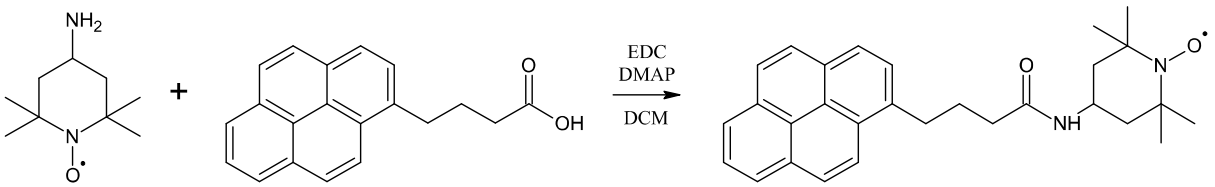

Scheme 17: Synthesis of pyrene-TEMPO.[332]

4.3.6. Synthesis of TEMPO covalently connected to imidazolium based ionic liquid

The synthesis of covalently connected TEMPO to an imidazolium based ionic liquid cation follows a literature protocol[333]: HT or AT was stirred in DCM with chloroacetic acid at 0 °C under nitrogen atmosphere, before EDC (AT) or EDC and DMAP (HT) was added dropwise to the solution. After 12 hours stirring at room temperature, the precipitate was filtered and the liquid phase was washed with 1 M HCl, saturated $NaHCO_3$ solution and saturated NaCl solution. Before $MgSO_4$ was added again to trap remaining water, solid precipitates were filtered and the organic solvent was evaporated under vacuum. The oily residue was purified via flash chromatography (EtOAc:n-Hexane = 1:2) to obtain the first reaction product of Scheme 18 as red crystals. Afterwards, these crystals were dissolved in MeCN, before 1-methylimidazole was added and the solution was stirred for 48 hours at 80 °C. The reaction solution was evaporated to half the volume as the addition of diethyl ether led to a precipitate, which was filtered and washed with acetone and diethyl ether, before it was dried under vacuum to gain the second product of Scheme 18 (HTMIM Cl or ATMIM Cl) as a light red powder. The last step included an ionic exchange of HTMIM Cl or ATMIM Cl with Li BETI to obtain HTMIM BETI or ATMIM BETI, respectively, that is based on the before mentioned literature protocol again.[331] ATMIM BETI has been further processed by dissolving it in isopropyl alcohol, DCM as well as acetone, separating the solid residue each time and evaporating the solvent afterwards. HTMIM BETI and ATMIM BETI were obtained as a light red gel, which were evaluated by ^{1}H-NMR, ^{19}F-NMR and ESR.

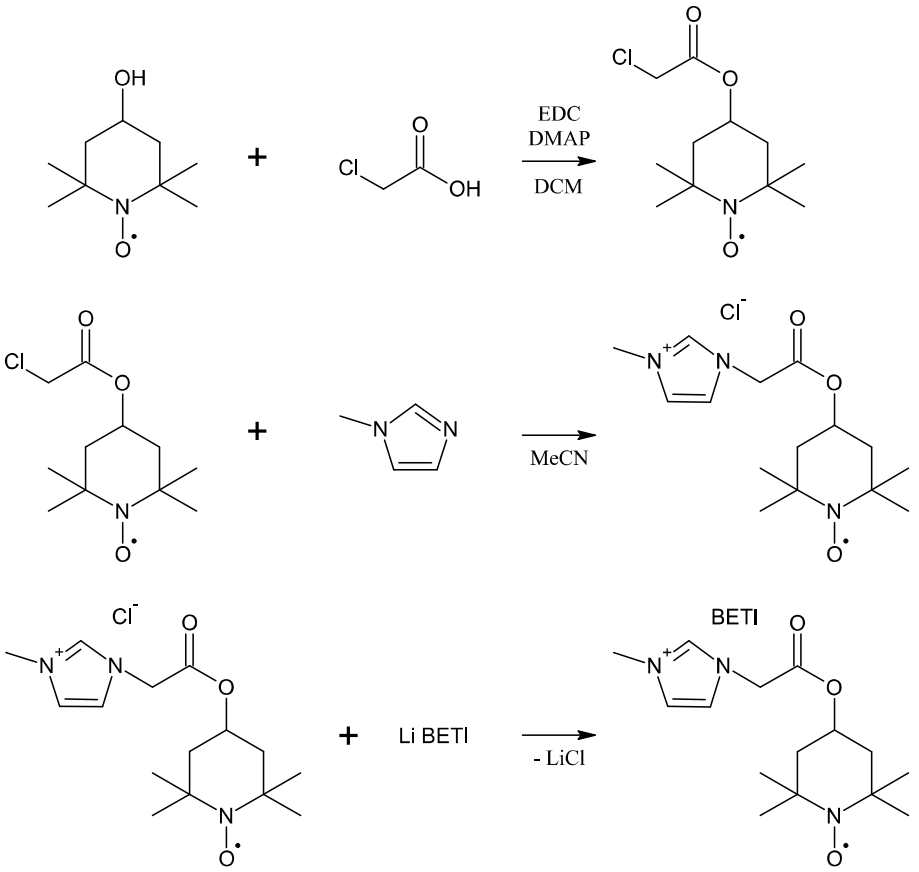

Scheme 18: Synthesis route of HTMIM BETI. The first step of ATMIM BETI synthesis follows the same route as in Scheme 14, step two and three stay the same as for ATMIM BETI.[331],[333]

4.3.7. Preparation of ink suspension

An ink of the active substance was prepared to apply it onto an electrode. A TEMPO derivative was dissolved in IL, so the concentration was as high as 1 μmol TEMPO per mg IL. The solution was diluted with isopropyl alcohol and the density of the IL in mind, which led to a concentration of 0.2 μmol TEMPO per μL ink solution. Afterwards, 50 μL of the ink were applied onto 0.5 cm^2 of the electrode material as schematically shown in Figure 8. It was then dried under inert gas to get 10 μmol of immobilized active material that covers the whole MPL area to avoid contact between electrolyte and support.

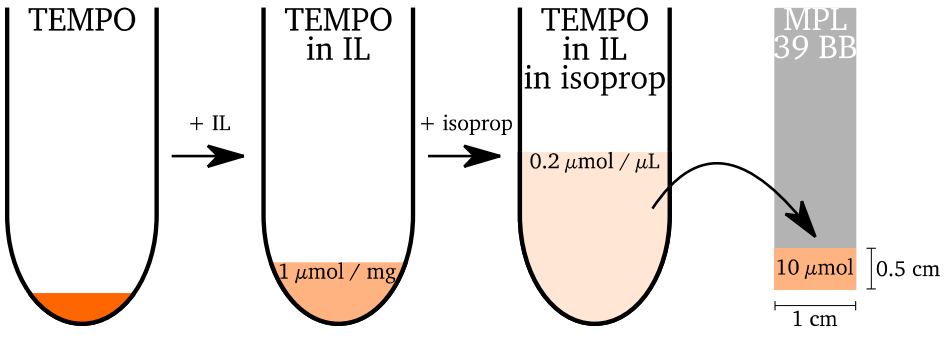

Figure 8: Schematic illustration of the ink and electrode preparation.

Another approach was the immobilization of TEMPO in IL onto a porous carbon source (Vulcan or PDC). Therefore, a literature protocol was applied[253] and is shown in Figure 9: TEMPO in IL, isopropyl alcohol and the carbon source were stirred for an hour and afterwards ultrasonicated for another hour to guarantee a homogeneous mixture, before the solvent was removed by rotary evaporation, so the pores of the carbon are impregnated with IL[286] (~ 20 wt-%) and consequently TEMPO. The ink was similarly prepared as before, only PTFE was added to the ink as a binding agent, the ink was ultrasonicated and the amount of TEMPO on the electrode (1 cm^2) is half as high as before (5 μmol) as the electrode was completely covered with carbon.

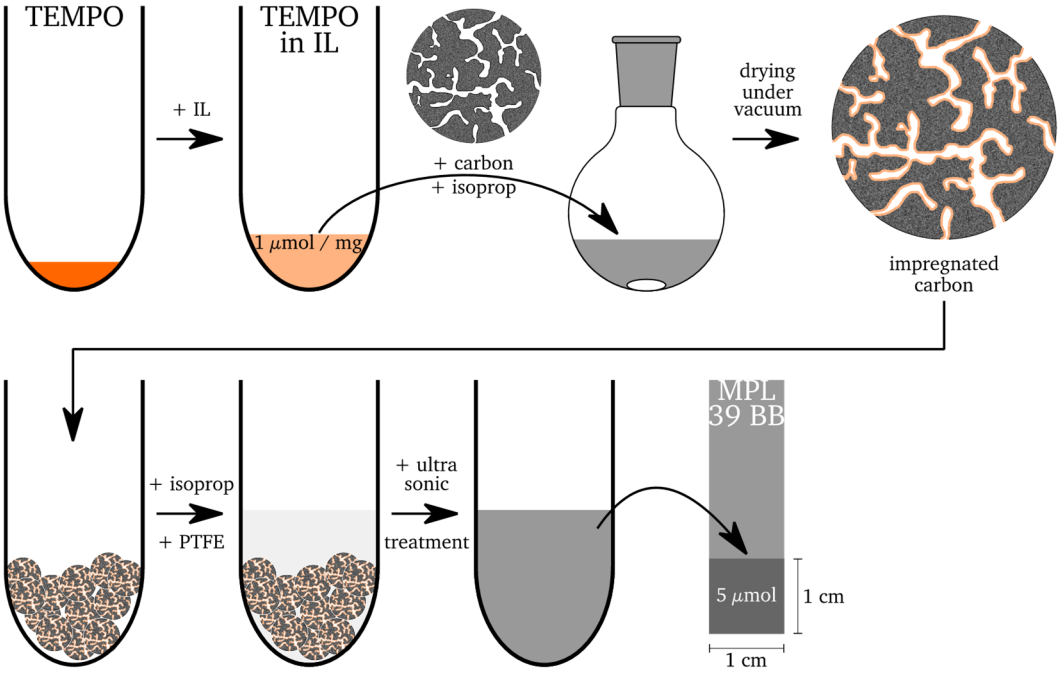

Figure 9: Schematic illustration of SILP synthesis[253] and its corresponding ink and electrode preparation.

4.4. Electrochemical measurements

4.4.1. Two and three electrode setup

The cell setup with two and three electrodes was constructed by the mechanical workshop of the TU Darmstadt based on the publication of GÜTZ ET AL and both are depicted in Figure 10.[334] The three electrode setup was used for the half-cell experiments like cyclic voltammetry (CV), electrochemical impedance spectroscopy (EIS) and chronoamperometry (CA), while the two electrode setup was used for electrolysis. The counter electrode (CE) was plated platinum, the reference electrode Hg/HgO (~ + 0.95 V vs. RHE), while the working electrode differed. The electrode area was kept constant at 0.5 cm^2 (1 cm^2 Vulcan and PDC) for the , while the two chambers were separated by a glass frit with 10 mm diameter, 2.5 mm thickness and 4 μm pore size.

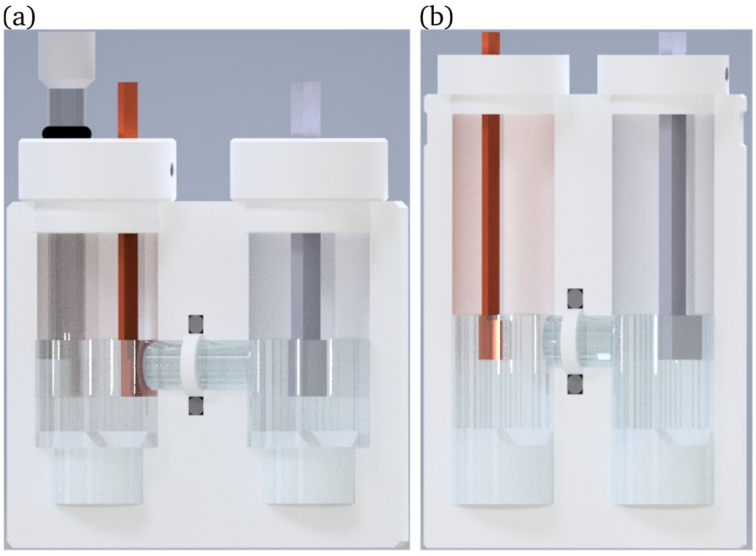

Figure 10: 3 (a) and 2 (b) electrode setup used in half cell experiments and electrolysis, respectively. WE: brown, RE: glass, CE: grey, glass frit: white.

4.4.2. Cyclic voltammetry

Cyclic voltammetry measurements (CVs) were conducted by a *Parstat multichannel* with PMC-1000 channels from *Ametek* for the protocol measurements as well as a *Parstat 4000* from *Ametek* for the TEMPO measurements, while all data were processed by *VersaStudio*. 5 mL per chamber of 0.1 and 1 M KOH were used as electrolyte to measure CVs in the absence or presence of HMF (5 mM). The CVs were conducted with a scan rate of 20 mV s^{-1} in a potential range of 0 - 0.8 V vs. Hg/HgO for the protocol measurements and -1.3 - 0.8 V vs. Hg/HgO for the TEMPO measurements. All measured potentials were converted from vs. Hg/HgO to vs. RHE.

4.4.3. Electrochemical impedance spectroscopy

EIS was performed after every CV with a frequency rate of 10 kHz to 1 Hz at 0.6 V vs. Hg/HgO for the protocol measurements and 0.55 V vs. Hg/HgO for the TEMPO measurements. Since the current flow between WE and RE through the electrolyte results in a potential drop, all CVs were corrected by equation (1)[335]:

$$U_{corr.} = U_{measured} - I \cdot R_u \quad (1)$$

$U_{corr.}$ is the by equation (1) corrected potential, $U_{measured}$ the potential of the conducted CVs, at which the measurement is recorded, I the complementary recorded current and R_u the uncompensated resistance, which is assessed by EIS, while $I \cdot R_u$ is summarized as uncompensated potential.

4.4.4. Chronoamperometry

The chronoamperometry measurements were conducted at the potential vs. RHE, at which the current density (j) difference between the CV with and without HMF was the biggest, described as $j_{Delta.}$ in equation (2). The potential between the WE and CE has also been determined over

the measurement time and was consequently used as potential in electrolysis conducted in the two electrode setup.

$$j_{Delta} = j_{with\ HMF} - j_{without\ HMF} \tag{2}$$

4.4.5. Electrolysis and evaluation via high performance liquid chromatography

Electrolysis was conducted in the two electrode setup with 4.5 mL of electrolyte in each chamber and a starting concentration of 5 mM of HMF ($n_0(HMF)$) at the before-mentioned potential that was obtained by chronoamperometry. The amount of charge Q needed for a theoretical conversion of 100 % HMF to FDCA has been calculated by equation (3), in which z describes the number of transferred electrons to oxidize one molecule HMF to FDCA (z = 6, see Figure 1) and F the Faraday constant (F = 96485 C mol^{-1}). It is also possible to calculate the charge Q using the current I and the passed time t.

$$Q = n_0(HMF) \cdot z \cdot F = I \cdot t \tag{3}$$

Samples of the reaction mixture before and after electrolysis were examined by HPLC (*Shimadzu* LC-20 AD) with a *Waters* Symmetry C18 column with 5 μm particle size, 100 Å pore size, 4.6 mm internal diameter and 250 mm length and a UV-Vis detector (D_2 lamp). A mixture of methanol and an aqueous solution of 5 mM ammonium formate with a volume ratio of 20:80 for the protocol measurements and 10:90 for the TEMPO measurements. Standard evaluation methods yield and faradaic efficiency towards FDCA ($Y\ (FDCA)$ and $FE\ (FDCA)$) were calculated by equation (4) and (5) with the conversion of HMF as $X(HMF)$, the selectivity to FDCA as $S(FDCA)$ and the amount of FDCA after electrolysis as $n\ (FDCA)$. F, z and Q are the same physical quantities as mentioned in equation (3). "Overall loss" of equation (6) refers to all compounds that do not belong to the reaction network (Figure 1) and cannot be detected by the UV detector of the HPLC. Thus, the sum of all reactants ($\sum n\ (reactants)$) comprises HMF, DFF, HMFCA, FFCA and FDCA and is subtracted of the initial amount of HMF, which closes the mass balance. Equation (7) describes the production rate, which allows comparison of catalysts between differently sized setups,[169] and that includes the amount of FDCA after reaction, the reaction time ($t_{reaction}$) and the mass of catalyst (m_{cat}) for the protocol measurements and the amount of catalyst (n_{cat}) for the TEMPO measurements.

$$Y\ (FDCA) = X(HMF) \cdot S(FDCA) \cdot 100 \tag{4}$$

$$FE\ (FDCA) = \frac{n\ (FDCA) \cdot z \cdot F}{Q} \cdot 100 \tag{5}$$

$$overall\ loss = \frac{n_0\ (HMF) - \sum n\ (reactants)}{n_0\ (HMF)} \cdot 100 \tag{6}$$

$$production\ rate = \frac{n\ (FDCA)}{t_{reaction} \cdot m_{cat}}\ \ or\ \ \frac{n\ (FDCA)}{t_{reaction} \cdot n_{cat}} \tag{7}$$

4.4.6. Stability test of HMF and its oxidation products

HMF, DFF, HMFCA, FFCA and FDCA were separately placed into a 5 mL cell filled with 0.1 or 1 M KOH and samples of the mixture were taken after different times up to 120 minutes. HMF stability was additionally investigated in 0.01 and 3 M KOH as well. All samples were afterwards evaluated by HPLC, so degradation and amount of substances were calculated by equations (8) and (9). The amount of different products after a specific time t is included as $n_t(product)$, the initial amount of them as $n_0(product)$, while the same procedure was applied to the investigated molecule as $n_t(educt)$ and $n_0(educt)$, respectively. Furthermore, equation (10) closes the mass balance by implementing the sum of all possible products ($\sum n_t(product)$) similar to equation (6), referred to as "thermal loss" as no potential was applied.

$$amount\ of\ substance = \frac{n_t(product) - n_0(product)}{n_0(educt)} \cdot 100 \tag{8}$$

$$degradation = 100 - \frac{n_t(educt)}{n_0(educt)} \cdot 100 \tag{9}$$

$$thermal\ loss = 100 - \frac{n_t(educt) + \sum n_t(product)}{n_0(educt)} \cdot 100 \tag{10}$$

4.4.7. Leaching test of the used SILP systems and electrodes

SILP electrodes were investigated for leaching using ^{1}H- and ^{19}F-NMR. Firstly, the inks were layered by electrolyte, at which two different phases (IL and electrolyte) occurred immediately. After 24 hours of stirring without any applied potential, part of the electrolyte was dried under vacuum, the organic residue diluted with deuterated methanol (MeOH-d_4) and measured by ^{1}H-NMR. Another approach included an electrochemical applied voltage. Therefore, after one CV, one EIS measurement, 12 h of chronoamperometric measurement and again one CV and EIS measurement, the electrolyte was neutralized using HCl and afterwards dried under vacuum. The organic residue was diluted with MeOH-d_4 and measured by ^{1}H- and ^{19}F-NMR. This procedure was repeated once again.

5 Developing a measurement protocol for accurate kinetic studies of electrochemical HMF oxidation

5.1. Suppression of side reactions not induced by the catalyst

5.1.1. Non-electrochemical degradation of HMF and its oxidation products

Due to the instability of HMF in alkaline media,[168] HMF and its oxidation products have been investigated regarding their degradation in different concentrated KOH solutions by stirring them at room temperature and collecting samples after specific amount of times.
Figure 11 shows the degradation behavior of HMF in 0.01 (blue squares), 0.1 (orange squares), 1 (green squares) and 3 M KOH (dark red squares) over 120 minutes without any applied potential. After 120 minutes, no thermal loss is detectable in 0.01 M KOH, while 4, 29 and 56 % of initial HMF degrades in 0.1, 1 and 3 M KOH, respectively. Furthermore, this study shows that after one hour already 35 and 12 % of the reactant degrades in 3 and 1 M KOH, respectively. Besides the behavior in 3 M KOH, in which 5 % HMFCA forms after 120 minutes, degradation is equivalent to the thermal loss mentioned in equation (10) as no via HPLC detectable product is formed, resulting in humin formation.

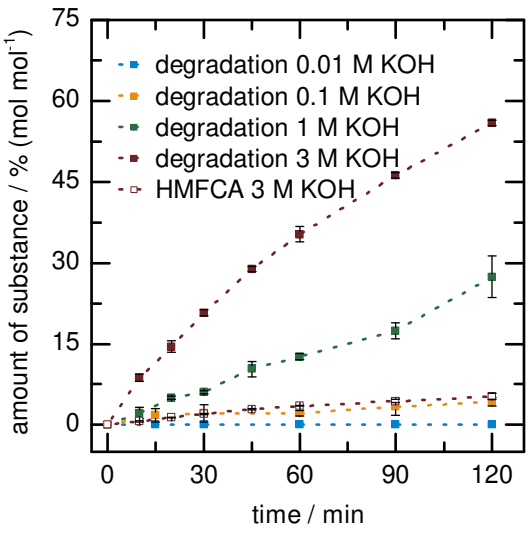

Figure 11: Degradation of HMF in 0.01 (blue squares), 0.1 (orange squares), 1 (green squares) and 3 M KOH (dark red squares) over time. HMFCA production in 3 M KOH is also shown in blank squares.

Degradation behavior of DFF (blue squares) in 0.1 and 1 M KOH has been investigated as shown in Figure 12 (a) and (b), respectively, over 120 minutes. In 0.1 M KOH 32 and 53 % of initial DFF degrades after 60 and 120 minutes, respectively, which is 13 times higher as HMF degradation in the same electrolyte, while also 7 and 14 % thermal loss (black diamonds) is detected, respectively. The rest DFF converts to HMF (orange circles) and FFCA (green triangles) in a similar amount of 14 % after 60 as well as 19 and 20 % after 120 minutes, respectively, which leads to the assumption of a parallel hydroxide ion catalyzed oxidation and reduction of two DFF molecules that lead to one HMF and one FFCA molecule. A similar behavior can be detected in 1 M KOH as 56 and 73 % of DFF degrades after one and two hours with a thermal loss of 37 and 44 %, respectively. The amount of HMF and FFCA are similar to each other again, even if their total is lower than before with 9 and 12 % after 120 minutes, respectively.

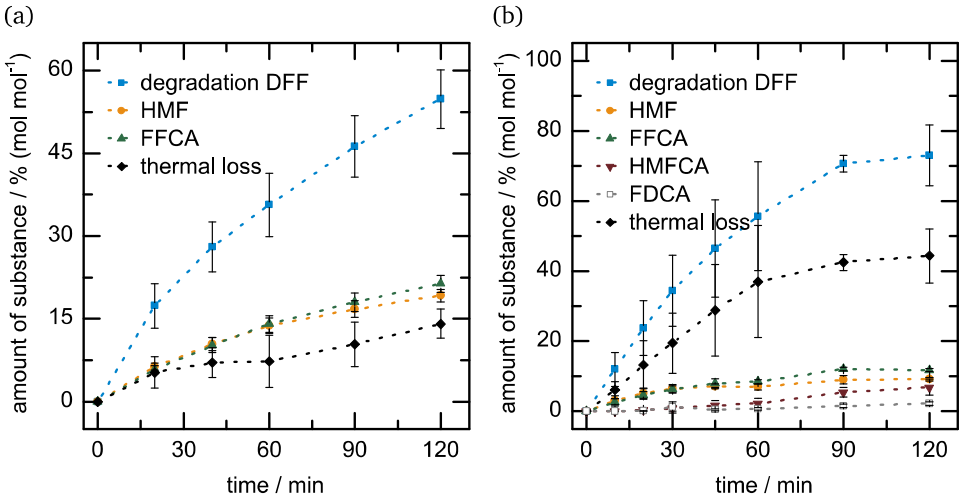

Figure 12: Degradation of DFF (blue squares) in 0.1 (a) and 1 M KOH (b) with HMF (orange circles), FFCA (green triangles), HMFCA (dark red upside down triangles), FDCA (grey blank squares) and thermal loss (black diamonds).

Additionally, 7 % HMFCA and 2 % FDCA formation can be observed in 1 M KOH, which can be explained by the FFCA degradation that is shown in Figure 13 (a) and (b). Accordingly, 62 % FFCA degradation in 1 M KOH leads to HMFCA and FDCA formation of similar amount with 27 and 29 % after 120 minutes, respectively, which can be explained by a similar parallel reaction as before in DFF degradation. The remaining FFCA degradation leads to a 6 % thermal loss. In 0.1 M KOH, FFCA degradation and thermal loss are similar to each other with 2.65 and 2.50 % after 120 minutes, respectively, as well as traces of FDCA (0.15 %). Since HMFCA and FDCA show no reaction in alkaline media at all, an aldehyde group seems responsible for degradation reaction that accelerates with higher electrolyte concentration.

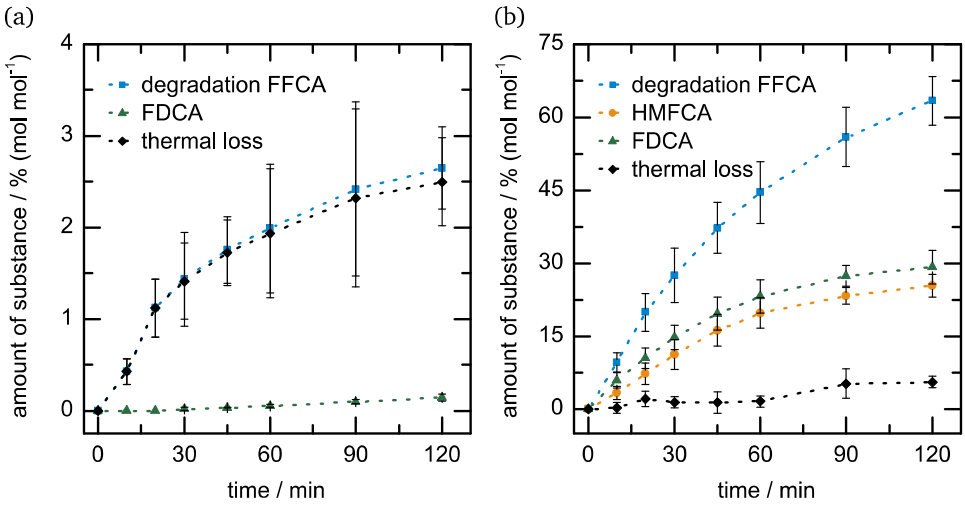

Figure 13: Degradation of FFCA (blue squares) on 0.1 (a) and 1 M KOH (b) with HMFCA (orange circles), FDCA (green triangles) and thermal loss (black diamonds).

5.1.2. Influence of electrolyte concentration on anodic oxidation

The influence of electrolyte concentration on electrolysis itself is shown in Figure 14, as yield and *FE* towards FDCA are depicted in blue and orange, while overall loss (green), which combines thermal loss and possible additional loss, and production rate (grey) are evaluated as well. Therefore, a divided two electrode setup is used with Cu-foam on a pure copper plate as anode and plated Pt as cathode. The reactions take place at 30 °C with a stirring rate of 600 rpm,

while the potential was varied to 3, 2.4, 1.8 and 1.6 V in 0.01, 0.1, 1 and 3 M KOH, respectively, according to the result of the three electrode measurements.

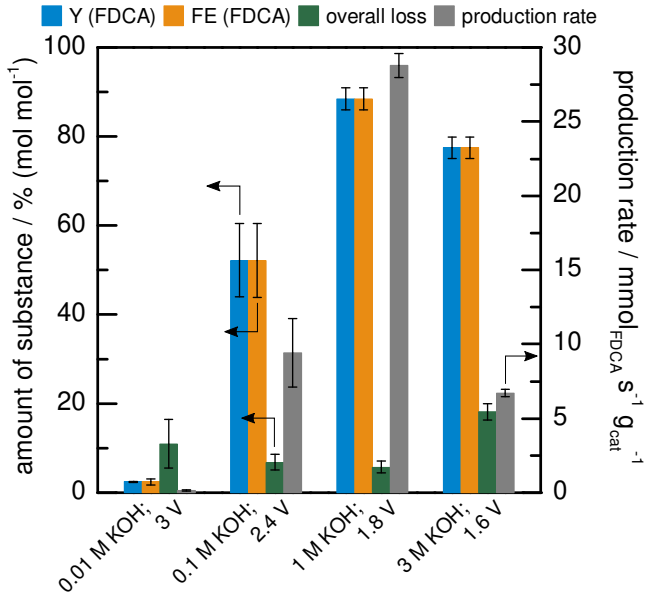

Figure 14: Yield and faradaic efficiency towards FDCA (*Y* (FDCA) (blue) and *FE* (FDCA) (orange), respectively), as well as overall loss (green) and production rate (grey) for complete HMF electrolysis (5 mM) in 0.01, 0.1, 1 and 3 M KOH of Cu-foam vs. Pt at 3, 2.4, 1.8 and 1.6 V, respectively, 30 °C and 600 rpm in a divided cell.

After 250 minutes, a yield of 2 % and a *FE* towards FDCA of 3 % with a production rate of 0.15 $mmol_{FDCA}\ s^{-1}\ g_{cat}^{-1}$ is achieved in 0.01 M KOH, only, while an overall loss of 11 % was measured. This loss needs to stem from unselective catalytic side reactions since no degradation and thermal loss was measured at this electrolyte concentration (cf. Figure 11). Increasing the electrolyte concentration to 0.1 M leads to an enhanced electrolysis performance with a 52 % FDCA yield and a 53 % *FE* towards FDCA as well as a production rate of 9.6 $mmol_{FDCA}\ s^{-1}\ g_{cat}^{-1}$. The overall loss of 7 % after 90 minutes reaction time is twice the amount of 3.5 % degradation/thermal loss measured after the same time (cf. Figure 11). Electrolysis in 1 M KOH accelerated the reaction to 45 minutes and increased the yield and *FE* towards FDCA to 88 % each, as well as the production rate to 29 $mmol_{FDCA}\ s^{-1}\ g_{cat}^{-1}$. Overall loss even dropped to 6 %, which is 4 % less than thermal loss of HMF implies (cf. Figure 11), leading to the assumption that a higher rate of the main reaction counterbalances the thermal losses induced by degradation. Against the trend, the reaction time in 3 M KOH rises to 150 minutes and consequently, the overall loss does as well to 18 % that is still roughly four times less than thermal loss of 69 % (cf. Figure 11), which underlines the assumption made for 1 M KOH that the main reaction rate counterbalances the degradation and thermal loss rate. Yield and *FE* towards FDCA drops to 77.5 % each, while production rate also declines to 8 $mmol_{FDCA}\ s^{-1}\ g_{cat}^{-1}$. Concluding these results, yield and *FE* towards FDCA increase with higher KOH concentration, as well as production rate, while overall loss drops until 1 M KOH is reached and afterwards, the higher overall loss in 3 M KOH explains the decrease in yield and *FE* towards FDCA as well as production rate. Additionally, a higher electrolyte concentration leads to faster reaction times, which counterbalance the formation of side products referred to as thermal losses.

5.1.3. Separation of anodic and cathodic chamber

The influence of the separator that divides the anodic and cathodic chamber is investigated as well and all results are shown in Figure 15. The used setup was the same as before with Cu-foam as anode, Pt as cathode, a stirring rate of 600 rpm and potentials of 2.4 and 1.8 V (divided) and 2.3 and 1.85 V (undivided) in 0.1 and 1 M KOH at 30 °C, respectively. For undivided electrolysis, the separator shown in Figure 10 (white) is removed, while the results with separator are the same as shown in Figure 14 and explained in chapter 5.1.2.

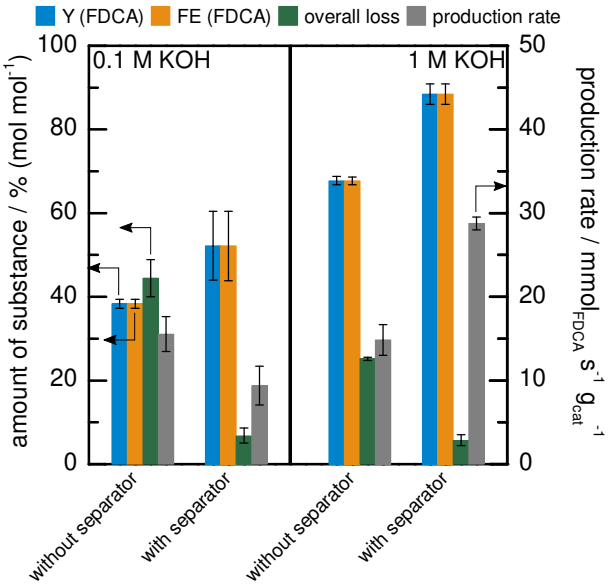

Figure 15: Yield and faradaic efficiency towards FDCA (*Y* (FDCA) (blue) and *FE* (FDCA) (orange), respectively), as well as overall loss (green) and production rate (grey) for complete HMF electrolysis (5 mM) in 0.1 (left) and 1 M KOH (right) of Cu-foam vs. Pt at 30 °C and 600 rpm in a setup without and with a separator.

Electrolysis in 0.1 M KOH without a separator leads to a yield and *FE* towards FDCA of 38 % with a production rate of 18 $mmol_{FDCA}\ s^{-1}\ g_{cat}^{-1}$ and an overall loss of 44 %. This corresponds to a 21 times higher amount than thermal loss regarding degradation would imply for a reaction time of 35 minutes (2.1 %, cf. Figure 11). A similar behavior can be observed in 1 M KOH without a separator as the overall loss is as high as 25 %, which is twice as high as the degradation for a reaction time of 70 minutes (13 %, cf. Figure 11). Nevertheless, a 68 % yield and *FE* towards FDCA is achieved as well as a production rate of 15 $mmol_{FDCA}\ s^{-1}\ g_{cat}^{-1}$.
Thus, yield and *FE* are 37 and 29 % higher as the overall loss is 84 and 76 % lower in 0.1 and 1 M KOH, respectively, if electrolysis chambers are separated, implying an influence of the cathode on HMF side reactions. In conclusion, divided setups have to be used to suppress unwanted side reactions mainly promoted by the cathode, wherefore only divided setups have been used in subsequent measurements.

5.1.4. Reactivity of different electrode substrates

Powder catalysts for electrocatalysis are mostly immobilized onto a substrate with a high electrical conductivity, which should be chemically inert and therefore inactive towards any reaction that could occur to avoid interferences while investigating catalyst activity. Therefore, the reactivity of different substrates (BDD, graphite foil, Cu-sheet) towards HMF oxidation is

assessed in 1 M KOH in a divided cell vs. Pt at 600 rpm and 30 °C in a three electrode setup, see Figure 16 (a), as well as in a two electrode setup at 1.8 V shown in Figure 16 (b)-(d).

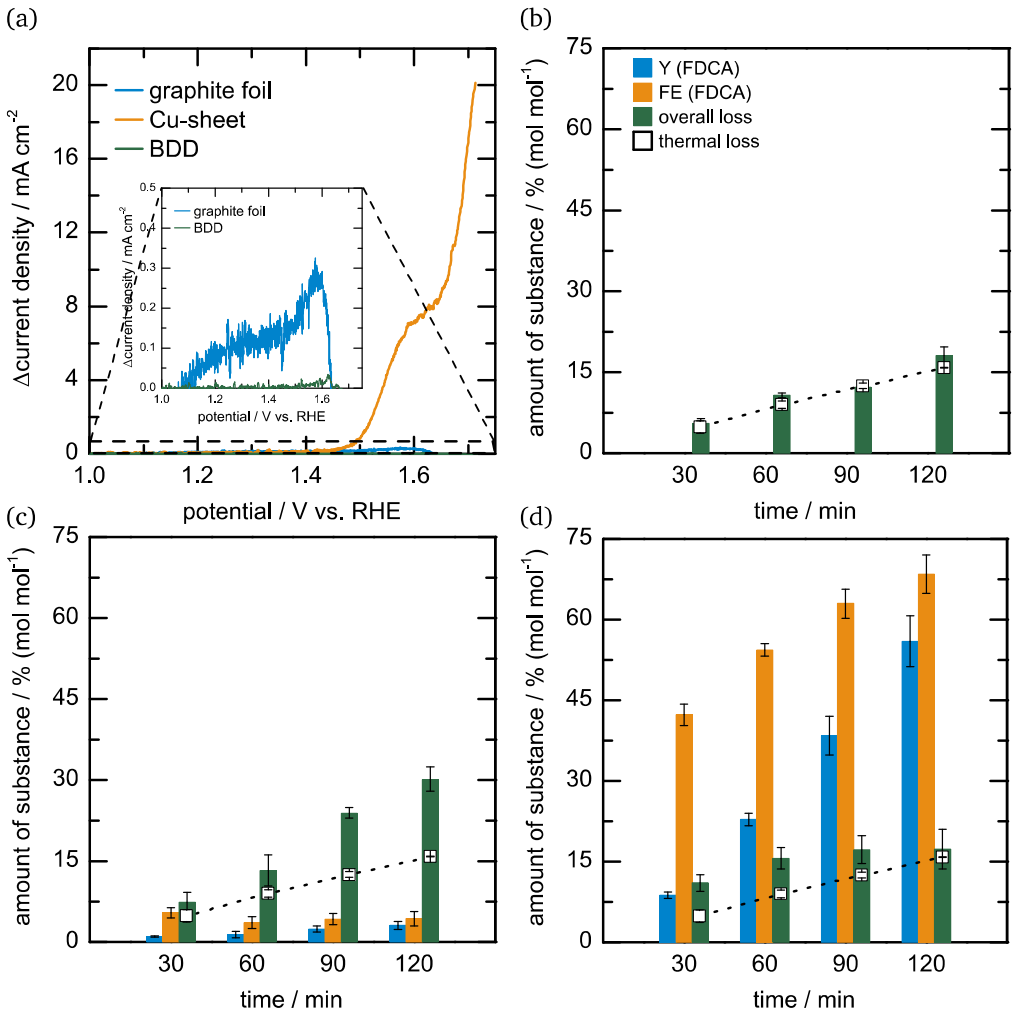

Figure 16: (a) ΔCVs of graphite foil, Cu-sheet and BDD as anode materials, in which the CV with HMF (5 mM) is subtracted from the CV without HMF present. (b) – (d) Yield and faradaic efficiency towards FDCA (*Y* (FDCA) (blue) and *FE* (FDCA) (orange), respectively), as well as overall loss (green) for HMF electrolysis (5 mM) over 30, 60, 90 and 120 minutes using BDD (b), graphite foil (c) and Cu-sheet (d) as anode material with no additional catalyst immobilized on them vs. Pt at 1.8 V, 30 °C and 600 rpm in 1 M KOH in a divided cell.

At first, the bare substrates without any catalyst are studied in half-cell experiments as the delta CVs (CVs with HMF (5 mM) subtracted from CVs without HMF) are depicted in Figure 16 (a) including a magnification shown in the inlet. Cu-sheet shows a high current density as well as a signal at 1.6 V vs. RHE that stems from HMF oxidation, while graphite foil and BDD show very small current densities, even if a small HMF oxidation can be observed for graphite foil. Thus, Cu-sheet is clearly no inert support material, while graphite foil and BDD seem to be more suitable, although graphite foil shows the HMF oxidation at a very low current density. These results are verified by the electrolysis results after 30, 60, 90, and 120 minutes, in which BDD shows no activity at all in Figure 16 (b) and additionally, overall loss equates to thermal loss after every reaction time. Graphite foil on the other hand shows a small activity with a yield and *FE* towards FDCA of 3 and 4 % after 120 minutes, respectively, as well as an overall loss of 30 %, which is two times the amount of thermal loss after the same time. Consequently, the activity seen in in Figure 16 (a) results in HMF side reaction rather than HMF oxidation. Figure 16 (d) confirms the CV results of Cu-sheet as the electrolysis results in a yield and a *FE*

towards FDCA of 56 and 68 %, respectively, as well as an overall loss of 15 %, which is roughly the same as thermal loss after 120 minutes.
Thus, Cu-sheet is no suitable support material as it contributes to HMF oxidation, while graphite foils HMF oxidation activity could be neglected if the high side reaction activity was not present, which result in an overall loss twice as much as the thermal loss. BDD does not contribute to HMF oxidation or side reaction at all, so it is utilized as substrate for immobilizing electrocatalysts.

5.2. Influence of further parameters

5.2.1. Dimension and type of counter electrode

A limitation of the whole reaction system can occur at the counter electrode if the electron cycle is hindered by *e.g.*, sluggish electron transfer, wherefore the influence of the counter electrode material on the performance of the investigated catalyst has to be nullified. For HMF oxidation, the reaction at the counter electrode is hydrogen evolution reaction (HER). Therefore, graphite foil, Cu-sheet and Cu-foam are investigated as different cathode materials in Figure 17 (a) with Cu-foam as anode and compared to Pt, which is the best HER catalyst in alkaline media according to literature.[200]
Using graphite foil and Cu-foam as CE leads to a similar yield to FDCA of 80 % and *FE* towards FDCA of 80 and 81 %, respectively, while production rate differs from 21 to 25 $mmol_{FDCA}\ s^{-1}\ g_{cat}^{-1}$, respectively. The overall loss is also different with 6 and 9 % for graphite foil and Cu-foam, respectively, which is both lower than the overall loss of Cu-sheet as CE that is 13 %. That can be explained by the highest reaction time of 200 minutes, which also indicates the lowest production rate of 10 $mmol_{FDCA}\ s^{-1}\ g_{cat}^{-1}$ as well as the lowest yield and *FE* towards FDCA of 76 % each. The electrolysis results with Pt as CE outperform the ones of every other cathode material with 88 % yield and *FE* towards FDCA, a production rate of 29 $mmol_{FDCA}\ s^{-1}\ g_{cat}^{-1}$ as well as an overall loss of 6 %. Therefore, Pt is used as cathode material in all upcoming measurements.

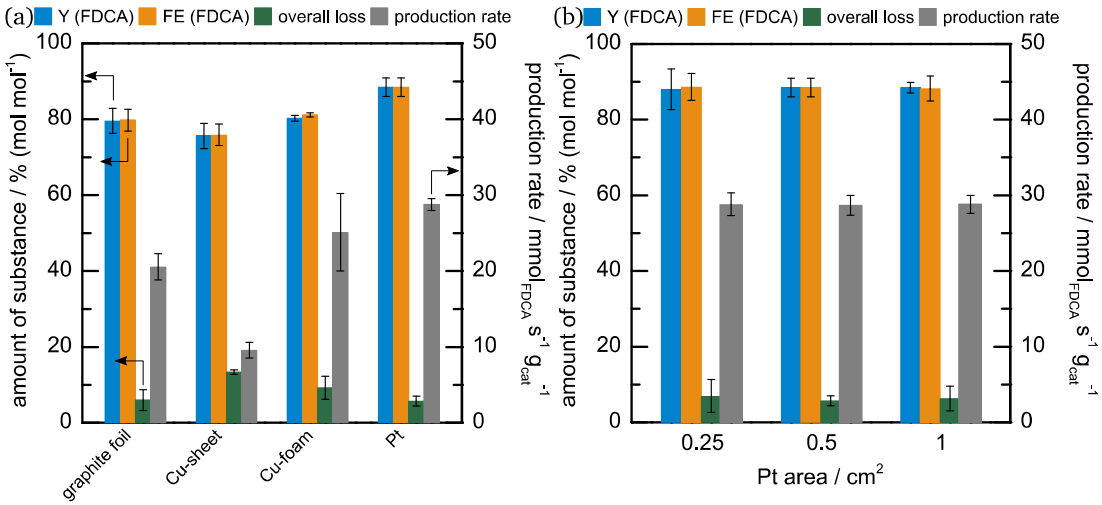

Figure 17: Yield and faradaic efficiency towards FDCA (*Y* (FDCA) (blue) and *FE* (FDCA) (orange), respectively), as well as overall loss (green) and production rate (grey) for complete HMF electrolysis (5 mM) in 1 M KOH of Cu-foam vs. different cathodic electrode materials (a) and different areas of Pt as cathode electrode (b) at 30 °C and 600 rpm in a divided setup.

Furthermore, the area of Pt into the electrolyte is investigated in Figure 17 (b) by varying it from 0.25 to 1 cm^2 to exclude any before-mentioned limitations stemming from a too small CE area. As can be seen, the differences are minor in every figure of merit with yields to FDCA of 88 for 0.25 and 88.5 % for 0.5 and 1 cm^2, FEs towards FDCA of 88.5 for 0.25 and 0.5 and 88 % for 1 cm^2 as well as a production rate of 29 $mmol_{FDCA}\ s^{-1}\ g_{cat}^{-1}$ for every Pt area. The differences in the overall loss are within the margin of error with 7, 6 and 6.5 % for 0.25, 0.5 and 1 cm^2, respectively. Thus, the CE area of Pt is kept constant at 0.5 cm^2 for all upcoming measurements.

5.2.2. Stirring rate

Mass transfer limitation can also hinder the performance of an investigated catalyst system. Therefore, stirring rate variation from 100 to 800 rpm during electrolysis is examined with Cu-foam as anode and Pt as cathode at 30 °C in a divided setup with all results shown in Figure 18. In this case, conversion of HMF is shown in light grey instead of production rate.
At 100 rpm, an HMF conversion of 86 % was reached with a yield and *FE* towards FDCA of 73 and 74 %, respectively, as well as an overall loss of 7.5 %. These results improve at 200 rpm with a conversion of 91 %, a yield and *FE* towards FDCA of 78 % and an unexpected higher overall loss of 8.5 %, which is still in the margin of error in comparison to the result of 100 rpm. Doubling the stirring rate again to 400 rpm leads to another improvement with a conversion of 95 %, a yield and *FE* towards FDCA of 83 % and a now expected lower overall loss of 7 %. This trend continues while stirring at a rate of 600 rpm with improved conversion, yield and *FE* towards FDCA with 97, 88 and 88 %, respectively, while overall loss decreases again to 6 %. Unexpectedly, all figure of merits get worse while increasing the stirring rate to 800 rpm with similar results as at smaller stirring rates: conversion drops to 95 % as do yield and *FE* towards FDCA to 77 and 83 % respectively when overall loss hits 8 %.
In conclusion, a clear trend can be seen for the whole variation as conversion, yield and *FE* towards FDCA rise while overall loss drops with higher stirring rate until 600 rpm. Further enhancement of the stirring rate to 800 rpm leads to a worse catalytic activity, which might stem from a bigger vortex inside the cell, whereby the electrode is not evenly in contact with the electrolyte anymore. Thus, all upcoming measurements are conducted at 600 rpm.

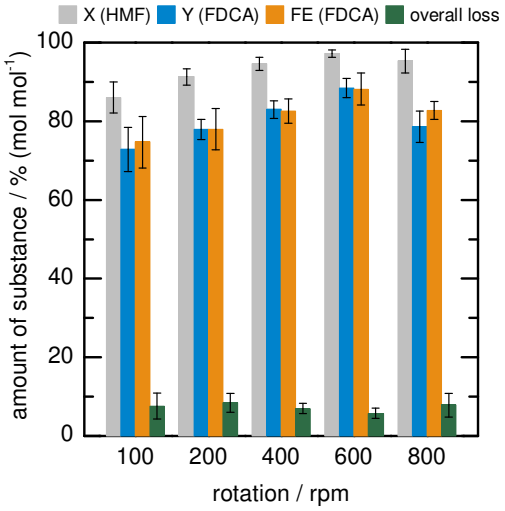

Figure 18: Conversion of HMF (*X* (HMF), light grey), yield and faradaic efficiency towards FDCA (*Y* (FDCA) (blue) and *FE* (FDCA) (orange), respectively), as well as overall loss (green) for complete HMF electrolysis (5 mM) in 1 M KOH of Cu-foam vs. Pt at 30 °C and different stirring rates in a divided setup.

5.3. Determination of catalytic activity and selectivity

Keeping all previous results in mind, two catalysts CuCoO_P and Ni are immobilized on BDD as inert substrate as mentioned in chapter 5.1.4, and compared to Cu-foam vs. Pt in divided cells at 600 rpm and 30 °C to suppress side reactions not induced by the catalyst and assess true catalyst performance.

5.3.1. Half-cell experiments to identify potential of HMF oxidation

At first, half-cell experiments in the three electrode setup are carried out in 1 M KOH vs. Pt in a divided setup to deduce the optimal potential, at which electrolysis is performed afterwards. Therefore, CVs with 5mM HMF are subtracted from CVs without HMF, which are utilized as a "background", to identify the potential regime, at which HMF oxidation takes place as seen in the inlets of Figure 19 (a) – (c) for CuCoO_P, Ni and Cu-foam, respectively. As mentioned in chapter 2.4, OER is the competing reaction at high potentials in alkaline media ($\Delta E_0 = 1.23$ V[195]), so the "background" subtraction offsets OER activity to assess HMF oxidation activity. Although both reactions might be dependent from each other, which can generate a source of error here, this methodology serves as a catalyst screening to quickly determine a suitable electrolysis potential that is otherwise achieved by several constant potential electrolysis runs including quantitative evaluation, which would slow down the catalyst screening process.[169]

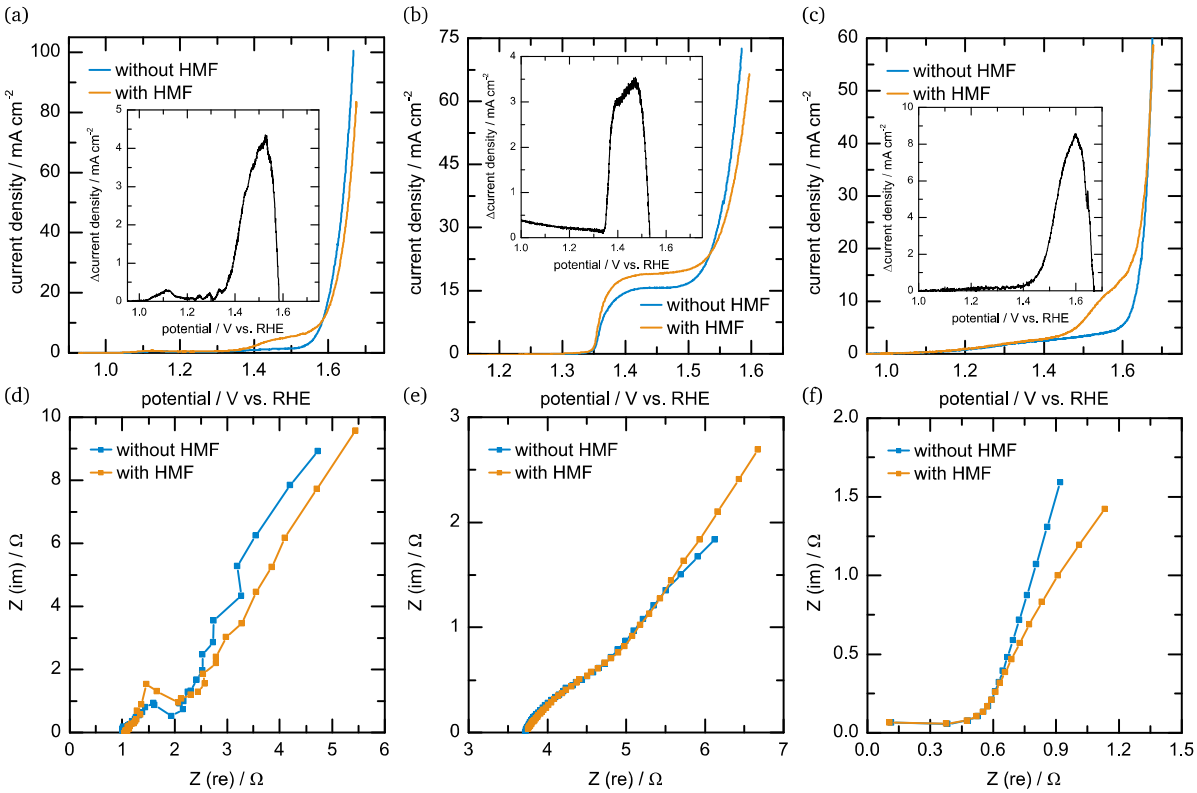

Figure 19: (a) – (c) CVs from 0 – 0.8 V vs. Hg/HgO at a scanning rate of 20 mV s^{-1} in 1 M KOH vs. Pt without (blue) and with HMF (5 mM, orange) as well as their difference (inlet) for CuCoO_P (a), Ni (b) and Cu-foam (c). (d) – (f) EIS measurements at 0.55 V vs. Hg/HgO without (blue) and with HMF (5 mM, orange) for CuCoO_P (d), Ni (e) and Cu-foam (f).

Nevertheless, CuCoO_P shows a clear HMF oxidation signal with its peak at around 1.52 V vs. RHE, at which chronoamperometry is performed afterwards and consequently electrolysis potential is determined. The difference in current density at this potential is as high as 4.5 mA cm^{-2}, which can be calculated using equation (2). Cu-foam performs with the highest difference in current density of 9 mA cm^{-2} at a peak potential of 1.6 V vs. RHE. On the contrary, Ni shows a plateau with its highest point at 1.46 V vs. RHE at a difference in current density of 3.5 mA cm^{-2}. All CVs are potential corrected as mentioned in equation (1) with their corresponding EIS spectra depicted in Figure 19 (d) – (f), in which a difference between without and with HMF can be identified. The presence of HMF seems to slightly affect CuCoO_P, as the curve shape is similar to the one without HMF, unlike Ni, which shows a higher mass transport limitation at lower frequencies, which might suggest a worse activity towards HMF oxidation. In contrast to both immobilized catalysts, Cu-foam shows another EIS behavior with HMF as the beginning of a semi-circle can be detected, which emphasizes a charge transfer resistance and consequently an ongoing reaction.

5.3.2. HMF electrolysis with quantitative evaluation

After deducing the HMF oxidation potential via chronoamperometry, CuCoO_P, Ni and Cu-foam have been used as anode in the two electrode setup vs. Pt at 1.55, 1.6 and 1.8 V, respectively, 600 rpm and 30 °C in 1 M KOH in a divided setup. Figure 20 (a) shows a typical current density progression (blue) as well as accumulated charges (orange) over time in a conducted electrolysis of CuCoO_P vs. Pt at 1.55 V. Current density stays stable over the whole reaction time after the double layer has formed[336],[337] and current density dropped from over 6 to over 3 mA cm^{-2}. Consequently, the passed charge, which is calculated by equation (3), rises proportionally to the current density and therefore linearly until 100 % is reached after 135 minutes.

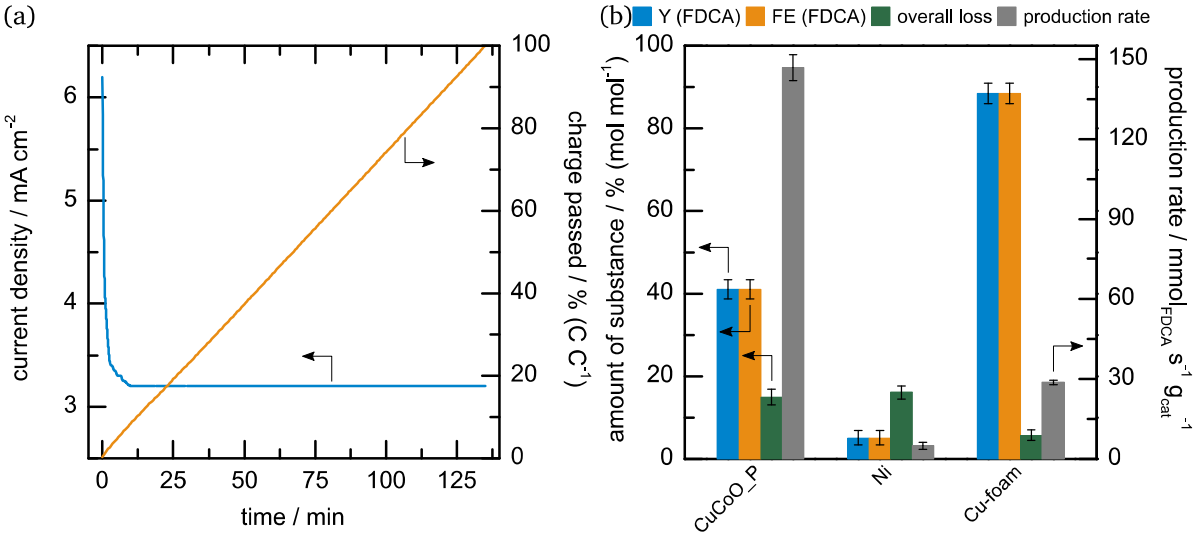

Figure 20: (a) current density (blue) and passed charge (orange) over time for an electrolysis with CuCoO_P as anodic material for the same parameters as follows in (b). (b) Yield and faradaic efficiency towards FDCA (*Y* (FDCA) (blue) and *FE* (FDCA) (orange), respectively), as well as overall loss (green) and production rate (grey) for complete HMF electrolysis (5 mM) of CuCoO_P and Ni on BDD and Cu-foam at 1.55, 1.6 and 1.8 V, respectively, in 1 M KOH vs. Pt at 30 °C and 600 rpm in a divided setup.

CuCoO_P achieved an HMF conversion of 75 % that leads to a yield and *FE* towards FDCA of 41 % as well as a production rate of 147 $mmol_{FDCA}\ s^{-1}\ g_{cat}^{-1}$, which is the highest measured yet

as can be seen in Figure 20 (b). An overall loss of 15 % is half as much as the thermal loss of 30 % after 135 minutes implies, which is the same trend as Cu-foam shows with 6 % overall loss and 10 % thermal loss after 42 minutes. Cu-foam still shows the best performance with a conversion of 97 %, a yield and *FE* towards FDCA of 88 % as well as a production rate of 29 $mmol_{FDCA}\ s^{-1}\ g_{cat}^{-1}$. Ni shows the worst performance, as it is able to convert only 26 % of HMF that results in a yield and *FE* towards FDCA of 5 % and therefore, a lower production rate of 5 $mmol_{FDCA}\ s^{-1}\ g_{cat}^{-1}$. Additionally, an overall loss of 16 % is detected, which is still less than the thermal loss of 28 % after 128 minutes.

Concluding these results, the measurement protocol to assess the performance of heterogeneous catalysts regarding HMF oxidation can be applied successfully. At first, undesired side reactions are suppressed by separating the anodic and cathodic chamber, accelerating the reaction using higher electrolyte concentration as well as using BDD as inert electrode material. After immobilizing heterogeneous catalysts onto inert BDD electrodes, it is possible to deduce the optimal HMF oxidation potential by half-cell experiments evaluating CV and EIS measurements. An electrolysis is performed at this deduced HMF oxidation potential, which is afterwards quantitatively evaluated for yield and *FE* towards FDCA, overall loss and production rate.

6 Electrochemical HMF oxidation via Supported Ionic Liquid Phase

6.1. Orienting electrochemical studies of TEMPO in ionic liquids

6.1.1. Homogeneous phase

First measurements regarding HMF oxidation via TEMPO as homogeneous catalyst have been carried out in IL or buffer solution as electrolyte with a silver wire as quasi-RE (q-RE). Figure 21 (a) shows the CV of TEMPO in C4MIM NTf_2 with BDD as WE, silver wire as q-RE and plated Pt as CE, in which typical TEMPO oxidation and reduction signals as mentioned in Scheme 11 appear. In a pursuing experiment, the same setup is used besides a pH 10 phosphate buffer solution as electrolyte. The blank CV measurement without any TEMPO or HMF is depicted in black in Figure 21 (b), while the CV with TEMPO is blue and the one with TEMPO and HMF is orange. For TEMPO, a clear signal at around 0.5 V vs. q-RE can be observed as well as a TEMPO oxidation signal at around 1.2 V vs. q-RE. The difference of both curves ("Delta", green) underlines this result with the HMF oxidation signal clearly visible, which points to a successful TEMPO-mediated oxidation of HMF in alkaline media.

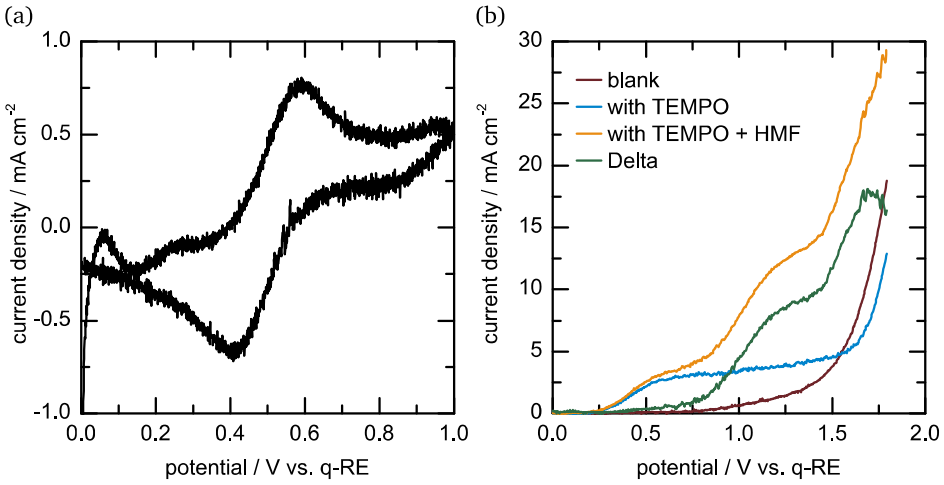

Figure 21: (a) CV of TEMPO in C4MIM NTf_2 with BDD as WE, Pt as CE and a silver wire as quasi-RE ("q-RE"). (b) CVs of the blank electrode (black; BDD as WE, Pt as CE, silver wire as q-RE) in phosphate buffer (pH 10), with TEMPO (24 µmol) in solution (blue), with TEMPO and HMF (5 mM) in solution (orange) as well as their difference ("Delta", green).

Subsequently, first experiments comparing the TEMPO derivative 4-methoxy-TEMPO (MT) in solution as well as on a porous carbon were carried out. The support used in this work is MPL 39 BB (MPL) from *Sigracet*, or more precisely the microporous layer, which consists of Vulcan as conductive carbon black and PTFE as binder material on top of a gas diffusion layer. To study the resulting selectivity pattern, the MPL is used as WE in the following experiments and the same amount of MT is inserted into the electrolyte or immobilized (without any IL) on the electrode, while Hg/HgO functions as RE and Pt as CE. Figure 22 (a) shows the behavior of MT in solution over a broad range of applied potential in 0.1 M KOH without (blue) and with 5 mM HMF in solution. A clear HMF oxidation signal can be observed starting at around 1.3 V vs. RHE with another big rise in current density at lower potentials around 0.5 V vs. RHE that leads back to the MPL itself (cf. Figure 33). Immobilizing MT on the MPL itself leads to a different curve progression seen in Figure 22 (b) as HMF oxidation starts at 100 mV lower potentials, the activity at smaller potentials is half as strong and the oxidative and reductive

branches show more space between them, indicating a higher capacitive current,[338] than before. Using the before-mentioned protocol, the applied potentials for electrolysis of both approaches have been determined at 1.6 V and their results are shown in Figure 22 (c). The yield towards FDCA of 59 % at a conversion of 72 % and the production rate of 0.22 $mmol_{FDCA}$ s^{-1} $mmol_{cat}^{-1}$ are higher and the overall loss of 25 % is lower when MT is used in solution than used on MPL with 39 % at 99 %, 0.04 $mmol_{FDCA}$ s^{-1} $mmol_{cat}^{-1}$ and 54 %, respectively. *FE* of MT on MPL is with 40 % lower than the one in solution with 63 %, as well. The higher production rate can be explained by MT being in solution together with HMF and therefore these two can easier react with each other. Since HMF is converted to the desired product FDCA by a TEMPO derivative, the next approach includes the use of TEMPO in IL immobilized on MPL, which describes the SILP approach as the homogeneous catalyst is "heterogenized" at the MPL electrode.

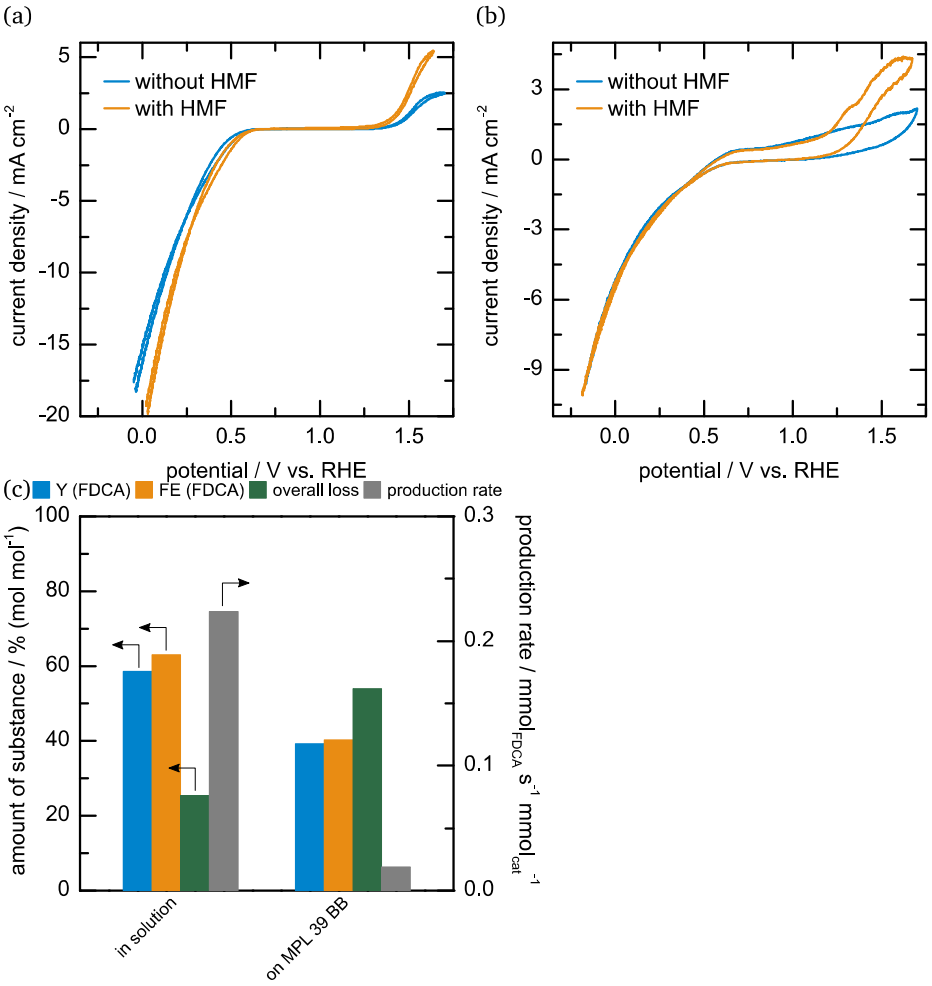

Figure 22: CVs of pure MT in solution (a) and immobilized (without IL) on MPL 39 BB (b) in 0.1 M KOH vs. Hg/HgO without (blue) and with 5 mM HMF (orange) with MPL 39 BB as WE and Pt as CE. (c) Yield and faradaic efficiency towards FDCA (*Y*(FDCA) (blue) and *FE*(FDCA) (orange), respectively) as well as overall loss (green) and production rate (grey) for complete HMF electrolysis (5 mM) in 0.1 M KOH of pure MT in solution or immobilized (without IL) on MPL 39 BB vs. Pt at 1.6 V each, 30 °C and 600 rpm in a divided cell. Note: The electrolysis with MT immobilized on MPL 39 BB had to be terminated after 22 hours and 6.19 C as no current flow could be detected anymore.

6.1.2. Immobilized TEMPO employing the SILP approach

At first, TEMPO or its derivatives are dissolved in IL, diluted with isopropyl alcohol and afterwards drop-coated onto the MPL so the amount of active TEMPO species (10 μmol) stays the same for every measurement independent from the IL and TEMPO derivative.
Figure 23 (a) and (b) show the CVs of TEMPO in C4MIM NTf_2 immobilized as described before on the MPL with 0.1 and 1 M KOH as electrolyte, respectively. In 0.1 M KOH, a TEMPO signal at 1.5 V vs RHE can be observed (blue) as well as an increase in activity after adding HMF (orange) starting at around 1.2 V vs RHE that results in a maximum of their difference ("Delta", green) at around 1.6 V vs RHE and 12 mA cm^{-2}. On the contrary, TEMPO does not show any electron transfer in 1 M KOH as no signal can be seen (blue) until adding HMF (orange), which shows its activity at around 1.5 V vs RHE. Thus, their difference in curve progression (green) has its point of highest activity at the same potential and 4 mA cm^{-2}. Due to the lack of TEMPO signal and the higher current density of the Delta curve, 0.1 M KOH is utilized as electrolyte in all following experiments. The corresponding electrolysis results in 0.1 M KOH of TEMPO in C3MIM and C4MIM NTf_2 as well as in 1-hexylpyridinium NTf_2 as a non imidazolium-based IL at 1.4, 2.7 and 1.9 V, respectively, are shown in Figure 23 (c).

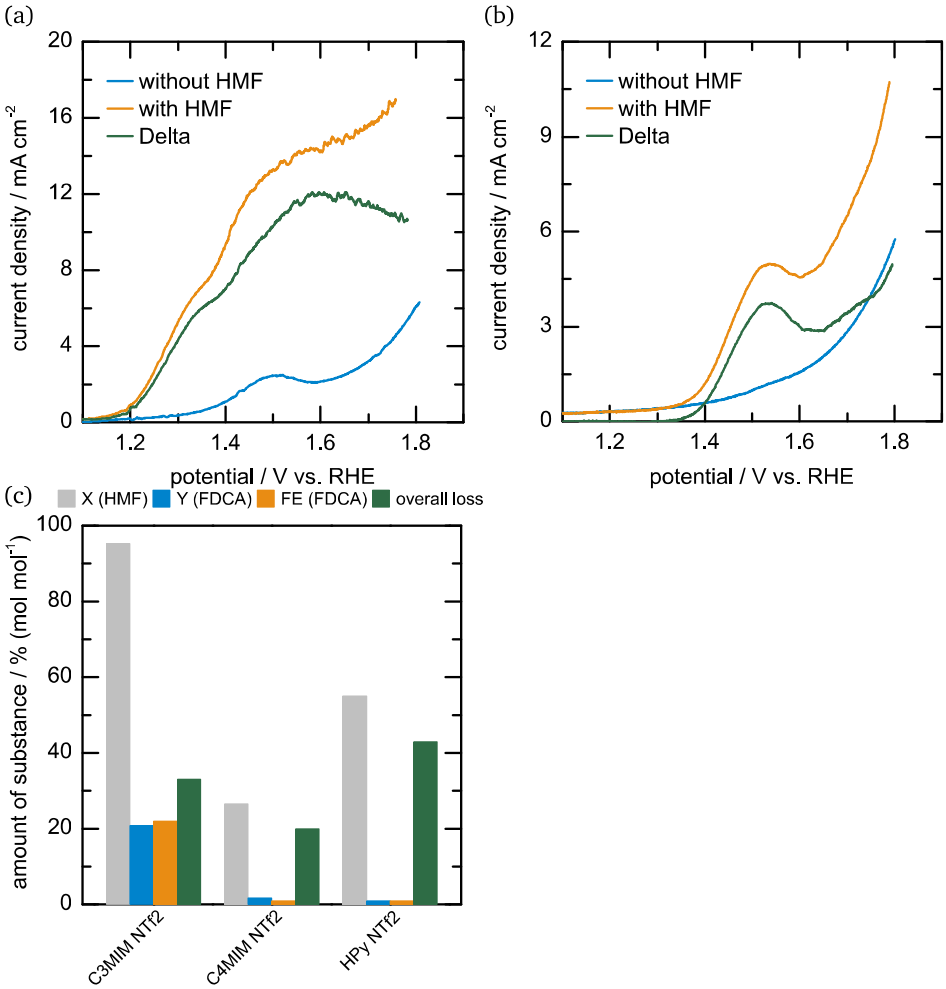

Figure 23: CVs of TEMPO in C4MIM NTf_2 on MPL 39 BB in 0.1 (a) and 1 M KOH (b) vs. Hg/HgO without (blue), with 5 mM HMF (orange) and their difference ("Delta", green) with Pt as CE. (c) Conversion (*X* HMF, light grey), yield and faradaic efficiency towards FDCA (*Y* (FDCA) (blue) and *FE* (FDCA) (orange), respectively) as well as overall loss (green) for complete HMF electrolysis (5 mM) in 0.1 M KOH of TEMPO in different ILs on MPL 39 BB vs. Pt at 1.4, 2.7 and 1.9 V, respectively, 30 °C and 600 rpm in a divided cell.

Conversion, yield and *FE* towards FDCA are highest for TEMPO in C3MIM NTf_2 with 95, 21 and 22 %, respectively. Neither TEMPO in C4MIM NTf_2 nor in HPy NTf_2 shows any selective activity with yields towards FDCA of 2 and 1 %, respectively, and FEs regarding FDCA of 1 % each. The conversion in HPy NTf_2 is higher (55 %) as in C4MIM NTf_2 (27 %), even if the overall loss behaves the other way round with 43 and 20 %, respectively. Overall loss in the most active C3MIM NTf_2 is as high as 33 %, which leads in conclusion to an unselective TEMPO derivative or unsuitable ILs for HMF oxidation to FDCA using TEMPO as homogeneous catalyst.
Thus, two TEMPO derivatives, 4-hydroxy-TEMPO-benzoate (TB) and MT, are investigated in imidazolium-based ILs with different chain lengths and NTf_2 as anion. Figure 24 (a) and (c) show CVs of TB and MT, respectively, in C4MIM NTf_2 with 0.1 M KOH as electrolyte, Pt as CE and Hg/HgO as RE. TB shows a higher activity towards OER reaching over 15 mA cm^{-2} without HMF added to the electrolyte (blue), while MT reaches up to 7 mA cm^{-2}. Adding HMF to the electrolyte (orange) leads to an earlier onset of current density at around 1.3 V vs RHE for TB with no clear signal for HMF oxidation, even if the Delta curve progression (green) shows one at 1.5 V vs RHE. MT behaves similarly regarding the earlier current density onset at 1.4 V vs RHE and contrary regarding HMF oxidation signal, which is clearly visible at around 1.55 V vs RHE, which is conclusively the same for the Delta function.

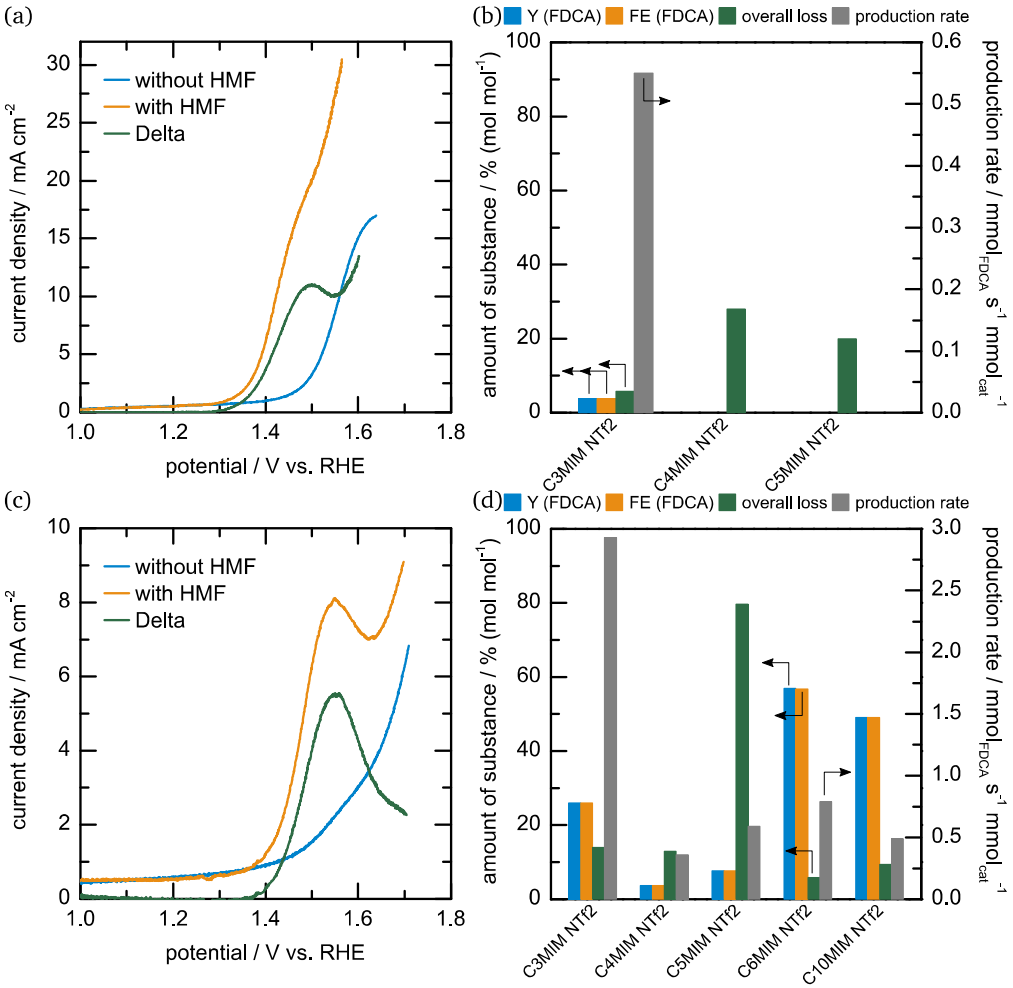

Figure 24: CVs of TB (a) and MT (c) in C4MIM NTf_2 on MPL 39 BB in 0.1 M KOH without (blue), with 5 mM HMF (orange) and their difference ("Delta", green) vs. Hg/HgO with Pt as CE. Yield and faradaic efficiency towards FDCA (*Y* (FDCA) (blue) and *FE* (FDCA) (orange), respectively) as well as overall loss (green) and production rate (grey) for complete HMF electrolysis (5 mM) in 0.1 M KOH of 4-hydroxy-TEMPO-benzoate (b) and MT (d) in different ILs on MPL 39 BB vs. Pt at 30 °C and 600 rpm in a divided cell. Applied electrolysis potentials from left to right: (b) 1, 2.57 and 1.21 V, respectively; (d) 1.86, 1.83, 1.72, 0.91 and 1.5 V, respectively.

These results can be confirmed in the electrolysis results as TB seems to be no suitable TEMPO derivative for HMF oxidation with 0 % yield and *FE* towards FDCA in C4MIM and C5MIM NTf_2 showing just an overall loss of 28 and 20 %, respectively, as seen in Figure 24 (b). HMF oxidation performance is more promising in C3MIM NTf_2 with a yield and *FE* towards FDCA of 4 % each, an overall loss of 6 % and a production rate of 0.55 $mmol_{FDCA}\ s^{-1}\ mmol_{cat}^{-1}$. In comparison, MT in C3MIM NTf_2 converts HMF with a yield and *FE* towards FDCA of 26 %, an overall loss of 14 % and a production rate of 2.93 $mmol_{FDCA}\ s^{-1}\ mmol_{cat}^{-1}$. C4MIM and C5MIM NTf_2 seem to be unsuitable ILs for TEMPO-mediated HMF oxidation as both underperform again with a yield and *FE* towards FDCA of 4 % each and 8 % each with according production rates of 0.36 and 0.59 $mmol_{FDCA}\ s^{-1}\ mmol_{cat}^{-1}$, respectively. Even if MT exhibits a higher HMF oxidation capability in C5MIM NTf_2 the overall loss of 80 % is six times as high as in C4MIM NTf_2 (13 %). The most promising HMF oxidation performance delivers MT in C6MIM NTf_2 with a yield and *FE* towards FDCA of 57 % each, an overall loss of 6 % and a production rate of 0.79 $mmol_{FDCA}\ s^{-1}\ mmol_{cat}^{-1}$. The lower production rate compared to C3MIM NTf_2 stems from the longer reaction time (737 and 55 minutes, respectively), which might originate in the higher viscosity of the IL with growing chain length.[339] This trend is continued for MT in C10MIM NTf_2 with an even lower production rate of 0.49 $mmol_{FDCA}\ s^{-1}\ mmol_{cat}^{-1}$, even if yield an *FE* towards FDCA are as high as 49 % at an overall loss of 9 %.
These results underline the previous perceptions that HMF oxidation using a SILP system consisting of TEMPO in IL is possible. Furthermore, the combination of used IL and TEMPO derivative seems to play a major role in activity and selectivity pattern regarding the desired HMF oxidation product FDCA, which opens up numerous combination possibilities.

6.2. Synthesis of TEMPO derivatives and hydrophobic long chain ionic liquids

As described in chapter 4.3.3 and 4.3.4, Cn-HT and Cn-AT derivatives with n = 12, 14, 16, 18 have been synthesized by esterification and amidification of HT and AT, respectively, as well as long chain imidazolium-based ILs CnMIM BETI with n = 6, 10, 12, 14 using ionic exchange.

6.2.1. Structure analysis of TEMPO derivatives

Cn-HT and Cn-AT have been synthesized using HT or AT and the corresponding acyl chloride (C12, C14, C16, C18) as well as EDC and DMAP as cross linking and esterification agents. The purity of all used chemicals and synthesized TEMPO derivatives has been examined using ^{1}H-NMR. Every ^{1}H-NMR spectrum is shown in the appendix, cf. chapters 9.3 and 9.4. Investigating TEMPO and its derivatives in ^{1}H-NMR leads to a problem illustrated in Figure 25: Each TEMPO derivative possesses a radical, which interacts with other chemical cores leading to an inconclusive and non-evaluable NMR spectra. Reasons are an influence of the chemical shift, a broadening of signals and a relaxation time shortening.[329]
Therefore, ascorbic acid as radical scavenger[330], which converts TEMPO to its hydroxylamine form, has to be added to the NMR solution. Figure 26 illustrates the NMR spectrum of AT with ascorbic acid (AA) seen in the spectrum as well as H_2O from the deuterated solvent D_2O.

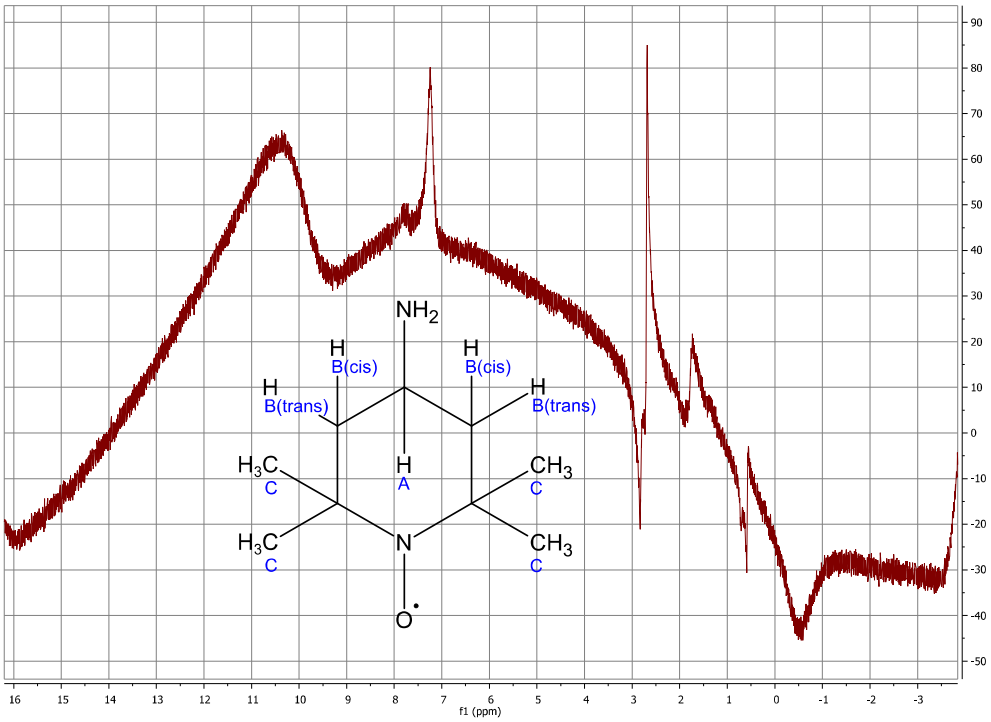

Figure 25: ^{1}H-NMR of AT in $CDCl_3$ without ascorbic acid.

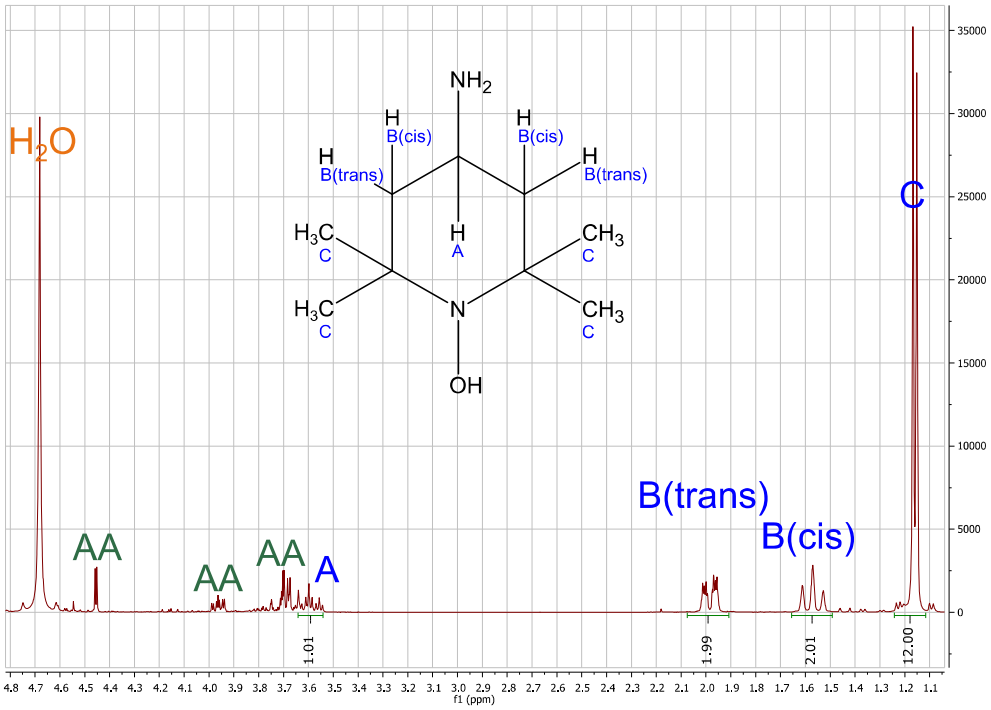

Figure 26: ^{1}H-NMR of AT with ascorbic acid (AA) in D_2O.

H_A, which bonds to the carbon next to the heteroatom, generates special interest as its chemical surroundings are influenced the most by the reaction with the acyl chloride. As the chemical shift of H_A is 3.59 in the spectrum of AT, it is 3.93 for C14-AT as seen in Figure 27, which can be explained by the amide group, which pulls electrons to it and therefore deshields this proton resulting in a downfield shift.[340]

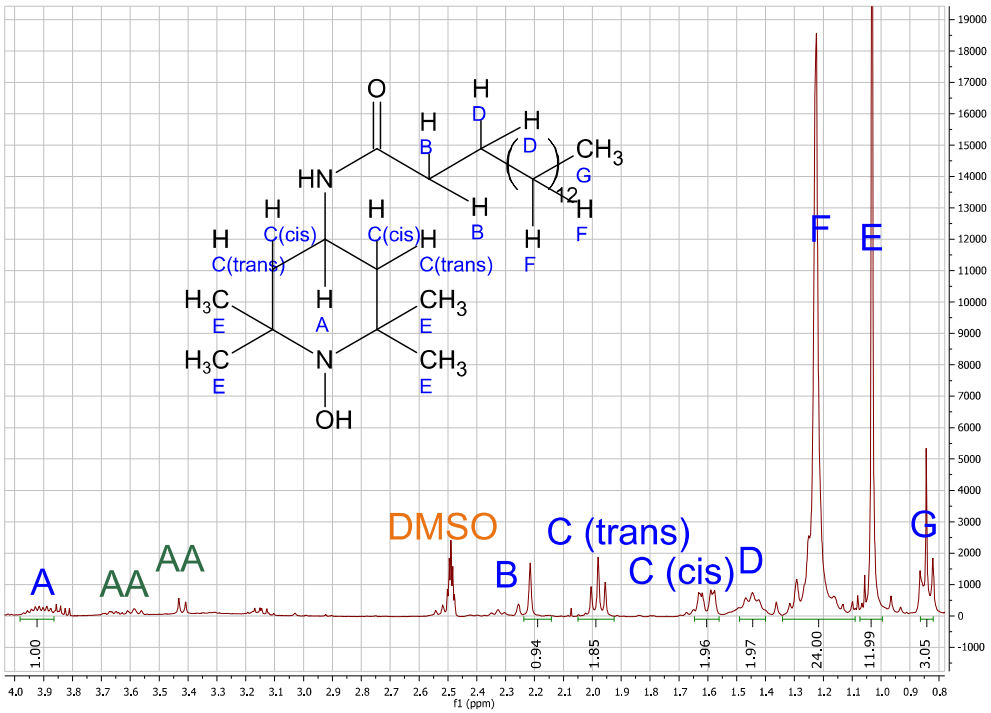

Figure 27: ^{1}H-NMR of C14-AT in DMSO.

This influence is also observable for HT and its long chain derivatives, which Figure 28 (a) illustrates as every chemical shift (δ) of the proton H_A is plotted for HT (orange, 4.12 ppm) and its derivatives (4.19 – 4.21 ppm) as well as for AT (blue) and its derivatives (3.91 – 3.96 ppm). Furthermore, no or just minor signals of EDC, DMAP or the educts can be detected in either NMR spectrum of the long chain products that hints at a successful synthesis and pure products, cf. appendix chapters 9.4 and 9.5.
Besides NMR, every TEMPO derivative has been investigated regarding its radical activity via ESR in a 15 mM solution in acetonitrile and afterwards compared to the radical activity of its corresponding educt. Figure 28 (b) shows the results of this comparison for the products of HT (orange) and AT (blue), whereas the products of HT show less radical activity with 45 – 77 % than their corresponding AT derivatives with 84 – 94 %. This might be explained by an easier electron and proton acceptance at the radical, which results in the hydroxylamine form of the TEMPO derivative similar to the process with ascorbic acid. The electrochemical activity provides insight into this theory and is investigated via CV measurements to validate the use of these derivatives in HMF oxidation experiments.

6.2.2. Electrochemical characterization of TEMPO derivatives

As mentioned before, the electrochemical operational capability of all TEMPO derivatives is investigated via CV over a broad potential window. Figure 29 (a) shows the CV of TEMPO in C4MIM BETI on MPL and in it every electron transfer possible for TEMPO species as shown before in Scheme 11. Signal 1 at around 1.2 V vs RHE describes the transition from hydroxylamine to the aminoxyl radical and therefore -1 at 0 V vs RHE is the other way round, while 2 at around 1.65 V vs RHE and -2 at 1.5 V vs RHE represent the electron transfer from the aminoxyl radical to the oxoammonium cation and vice versa.

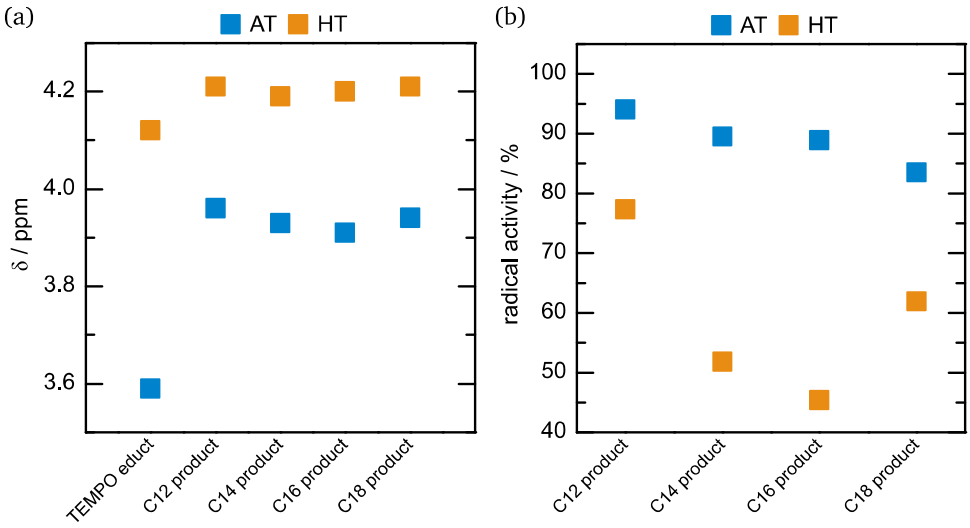

Figure 28: (a) Chemical shift of the C_4-proton (H_A) of AT (blue), HT (orange) and their corresponding long chain products, cf. chapter 9.4. (b) Radical activity of the long chain products of AT (blue) and HT (orange) compared to the TEMPO educts determined by ESR, cf. chapter 9.6.

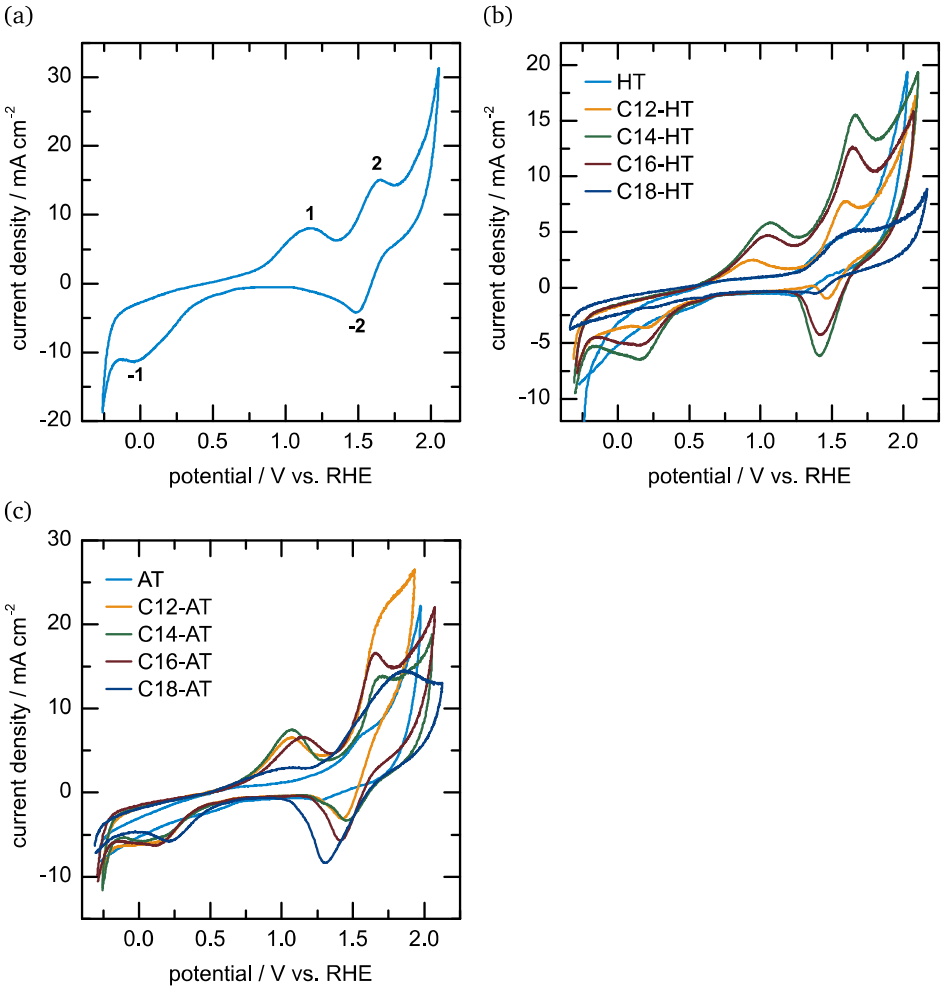

Figure 29: (a) CV of TEMPO in C4MIM BETI on MPL 39 BB in 0.1 M KOH vs. Hg/HgO with Pt as CE that shows all possible electron transfers for TEMPO (c.f. Scheme 11). CVs of HT (b) and AT (c) and their corresponding long chain derivatives in C4MIM BETI on MPL 39 BB in 0.1 M KOH vs. Hg/HgO with Pt as CE.

Thus, every TEMPO derivative synthesized should exhibit a similar behavior in C4MIM BETI. HT itself (blue) displays only small 2/-2 signals at 1.5 and 1.25 V vs RHE, respectively, while the ones for 1 and -1 are missing, which is the same case for the C18-HT (dark blue) as seen in Figure 29 (b). On the contrary, C12- (orange), C14- (green) and C16-HT (dark red) present all four signals, even if C12-HT not as pronounced and at slightly lower potentials for the oxidative processes (0.9 to 1.1 V vs RHE for signal 1 and 1.6 to 1.7 V vs RHE for signal 2, respectively) and slightly higher potentials for the reductive ones (0.25 to 0.2 V vs RHE for signal -1 and 1.5 to 1.45 V vs RHE for signal -2, respectively) in comparison to C14- and C16-HT. In Figure 29 (c), the results of AT and its derivatives are illustrated and highlight that AT (blue) behaves similarly to HT with minor signals for 2 and -2 at 1.5 and 1.25 V vs RHE, respectively, only. The C18 derivative (dark blue) shows clearly observable signals for 2 and -2 at 1.8 and 1.3 V vs RHE, respectively, but only minor ones for 1 and -1 at 1 and 0.25 V vs RHE, respectively, distinguishing it in that point from C18-HT. C12-AT (orange) presents a unique curve progression, as the signal for electron transfer 2 at 1.7 to 1.8 V vs RHE does not stand out from the curve as seen in the remaining CVs. The signals for 1, -1 and -2 at 1, 0.2 and 1.5 V vs RHE, respectively, look similar to the ones of C14- (green) and C16-AT (dark red). C14-AT displays its signals for oxidation at 1 and 1.7 V vs RHE and for reduction at 0 and 1.5 V vs RHE, while C16-AT exhibits them at 1.15 and 1.65 V vs RHE for signals 1 and 2, respectively, as well as at 0.15 and 1.45 V vs RHE for the signals -1 and -2, respectively.
The CVs show an intact electrochemical behavior of all synthesized TEMPO derivatives besides the ones with a C18 chain, which seems to stay at the hydroxylamine state or on the other hand cannot transfer electrons to create it, similar to both reactants HT and AT. Every other derivative presents clear signals for the electron transfers and should therefore be suitable systems for a SILP application regarding the activity.

6.2.3. Structure analysis of ionic liquids via ^{1}H- and ^{19}F-NMR

All ILs have been synthesized by an ionic exchange using the imidazolium-based halides and Li BETI in water, which is why a pure and in particular dry product is desired. ^{1}H-NMR is the easiest and most efficient way to examine these products. Figure 30 illustrates the NMR spectrum of C6MIM BETI in MeOH-d_4 and all proton signals can be seen besides the one for proton A at the C_2-position. It is known that this particular proton is very acidic and easy to subtract from the imidazolium ring,[341] which is why the used solvent methanol that builds a hydrogen bond with the C_2-proton[342] could make it invisible for ^{1}H-NMR due to this interaction. Nevertheless, changing the deuterated solvent to $CDCl_3$ leads to the proton A to appear in NMR spectra, as seen in appendix chapter 9.7 of the other synthesized long chain ILs. No spectrum shows any signs of impurities or excess water that stems from the IL itself as the used methanol already showed signs of water in previous NMR spectra like the one of ascorbic acid, Figure 65. Additionally, Figure 31 depicts the ^{19}F-NMR of the corresponding BETI anion and no impurities can be discovered in it as well.
Thus, the ionic exchange and vacuum drying led to pure and more importantly water free ILs of CnMIM BETI (n = 6, 10, 12, 14) that can be used in SILP approaches to immobilize TEMPO derivatives in them.

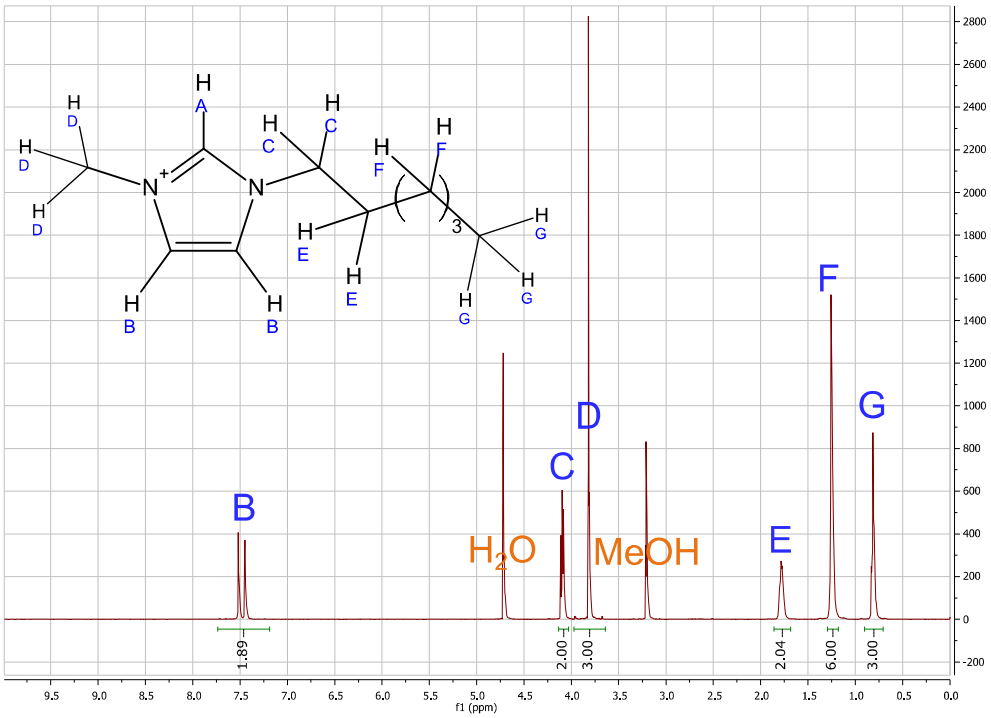

Figure 30: ^{1}H-NMR of the cation C6MIM in MeOH-d$_4$.

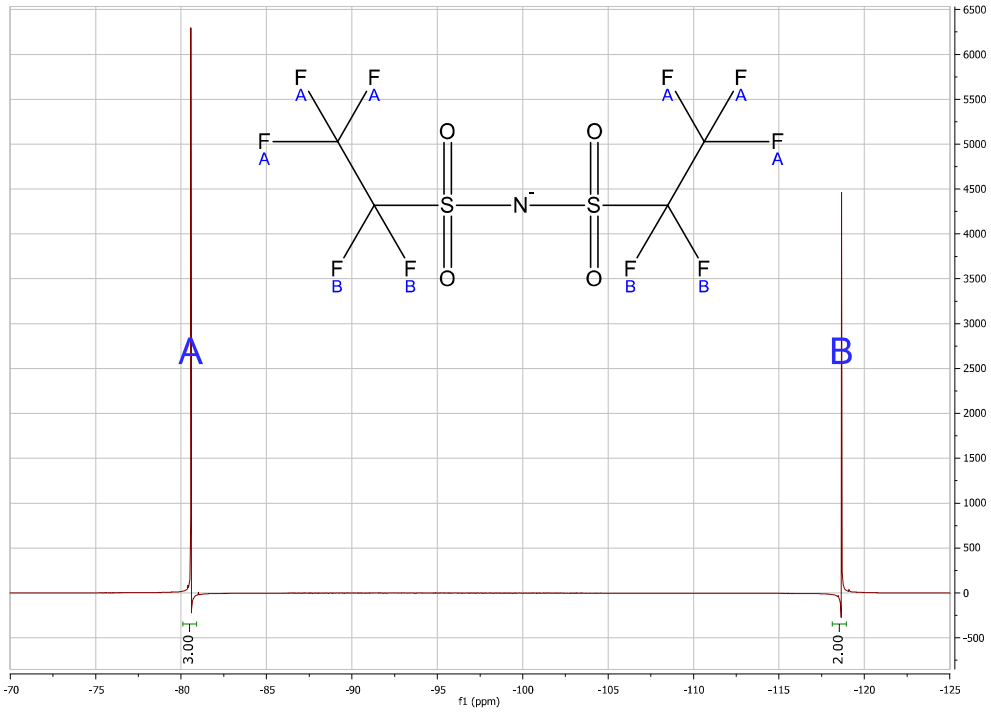

Figure 31: ^{19}F-NMR of the anion BETI in MeOH-d$_4$.

6.3. Solubility of TEMPO derivatives in employed ionic liquids

Different inks of all synthesized TEMPO derivatives in four different ILs have been investigated regarding their solubility in the later used electrolyte 0.1 M KOH. Therefore, 50 μL of ink, which is equivalent to the amount of ink that is applied onto the electrode, is layered by 1 mL of 0.1 M KOH and two phases (IL and electrolyte) occur immediately. After 24 h of stirring without any applied potential and 20 min of phase separation, the electrolyte phase is investigated via

^{1}H-NMR and all results can be seen in Figure 32 (a), (b), (c) and (d) for C6MIM NTf_2, C4MIM BETI, C10MIM BETI and C12MIM BETI, respectively. The amount of TEMPO derivative (blue) and IL (orange) is referred to the amount of substance used, which would be 100 %. As Figure 32 demonstrates, no long chain TEMPO derivative can be detected in the electrolyte besides of C14-AT, which shows negligible concentrations of 0.26 and 0.05 % in C4MIM and C12MIM BETI. All concentrations as small are negligible since they are hard to detect as they lie within the error margin of the used instrument. HT and AT are detected in every used IL in concentration between 0.08 and 0.47 % and between 0.07 and 0.19 %, respectively, which is both negligible due to the before-mentioned reasons. The amount of C6MIM NTf_2 and C4MIM BETI leached into the electrolyte is below 0.37 % and therefore negligible. Only C10MIM and C12MIM BETI display higher leaching of up to 2.44 %, even if their long chain should make them more hydrophobic than the short chained ones. A possible reason for the higher concentration might be a too short separation time of 20 min, in which not every IL droplet sets down and is still emulsified in the electrolyte leading to an uptake of it into the investigated amount of electrolyte.

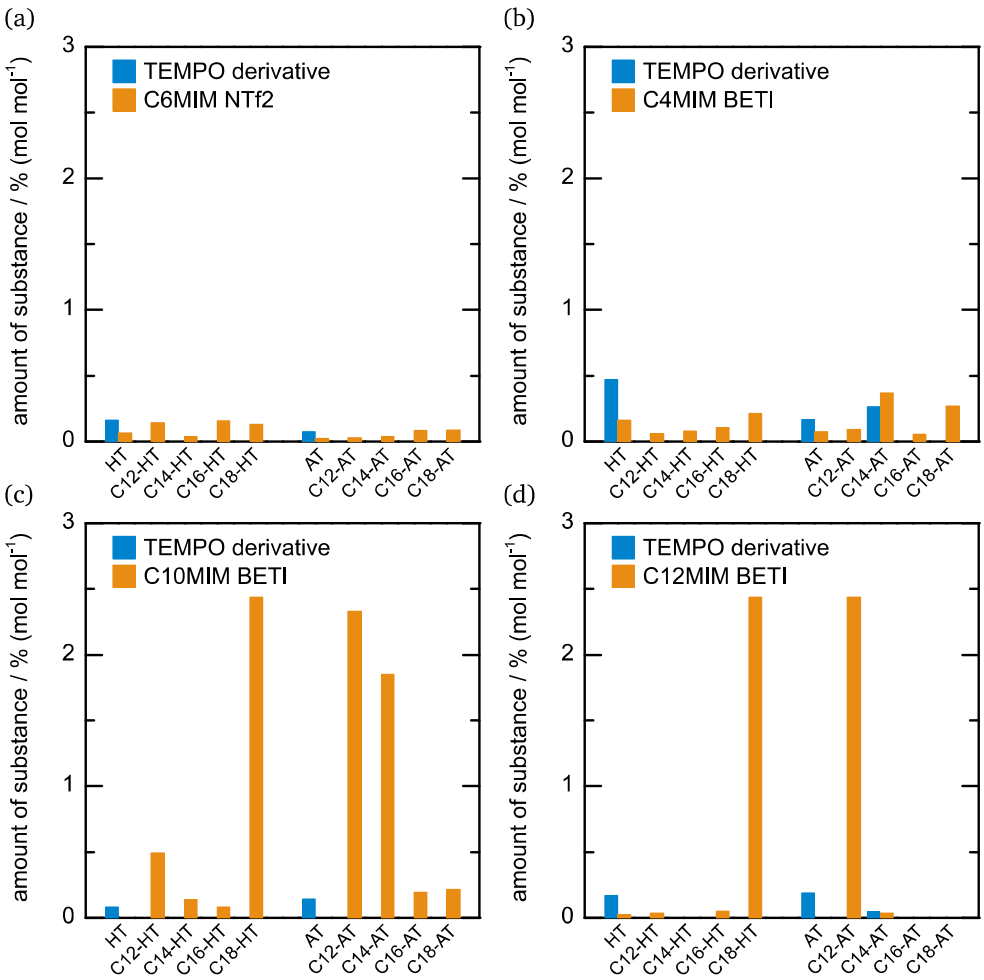

Figure 32: Leaching results into 0.1 M KOH of HT, AT and their corresponding long chain derivatives (blue) in C6MIM NTf_2 (a), C4MIM BETI (b), C10MIM BETI (c) and C12MIM BETI (d, orange in each case).

Nevertheless, all inks show a negligible hydrophobicity without any applied potential in the utilized electrolyte and therefore can be used as SILP inks for electrochemical HMF oxidation applied onto a porous support.

6.4. Microporous carbon as support material

The before-mentioned MPL 39 BB is used as microporous carbon support in the SILP system to apply the inks onto. SEM images of it can be found in Figure 85. 0.5 cm^2 of MPL are completely covered with 50 μL of ink so no carbon material contacts the electrolyte and an amount of 10 μmol active species is immobilized in IL onto it.

6.4.1. Reactivity of support material

As mentioned in chapter 5.1.4, the reactivity of the support material has to be tested first to exclude any later measured activity stemming from the MPL. Therefore, CVs of pure MPL in 0.1 M KOH over a broad potential range and at the HMF oxidation potential range are illustrated in Figure 33 (a) and (b), respectively. At high potentials there seems to be some potential HMF oxidation as the current density doubles to around 0.8 mA cm^{-2} with the adding of HMF, even if no HMF oxidation signal can be detected. The current density at lower potentials increases drastically starting at 0.6 V vs. RHE to around -40 mA cm^{-2} without HMF present and to around -45 mA cm^{-2} with HMF. As this activity is in the potential range of TEMPO electron transfer -1 (cf. Figure 29), it is a good indicator if all of the MPL is covered with ink so no drastic rise in activity should be seen anymore. The EIS measurements in Figure 33 (c) indicate the same trend as before in Figure 33 (b) that the adding of HMF leads to an increase in current density and therefore to a decrease in impedance, even if no semicircle can be seen. These results might originate in the wetting behavior of the MPL, which is usually low due to the PTFE in the substrate that is enhanced with HMF. Therefore, the electrochemical double layer is influenced and differences in CVs and EIS measurements appear. Since no HMF oxidation is presented in the CVs, electrolysis has been carried out at different potentials that cover the usual HMF oxidation potential range. As seen in Figure 33 (d), MPL shows no activity towards HMF oxidation as just yields and FEs towards FDCA of 1.1, 0.6 and 0.2 % could be reached at 1.6, 2 and 2.45 V, respectively. The overall loss detected is 30, 26 and 24 %, respectively, which is around 5 times the amount of thermal loss, underlining the CV results, in which no HMF oxidation signal could be detected. It has to be noted that the electrolysis reactions were terminated after 180, 120 and 120 minutes, respectively, which is roughly the time that SILP systems needed to finish an complete HMF oxidation electrolysis at these potentials. The reached amount of charge was 7.57, 5.14 and 5.87 C, which is around half the amount of charge needed for complete conversion of HMF to FDCA (13.03 C).
In another experiment, the long time behavior of MPL has been investigated as 220 CV cycles have been carried out with MPL as electrode. As Figure 34 (a) illustrates, the current density at higher potentials increases with every cycle, which might be due to carbon oxidation that occurs at high positive potentials.[343] The activity at lower potentials does not seem to be affected as much due to small changes in current density. Figure 34 (b) additionally shows the EIS measurements after 1, 20 and 220 cycles, in which a clear decrease in mass transfer can be observed as well as a semicircle that might hint to reactions on the surface of MPL as mentioned before or OER.

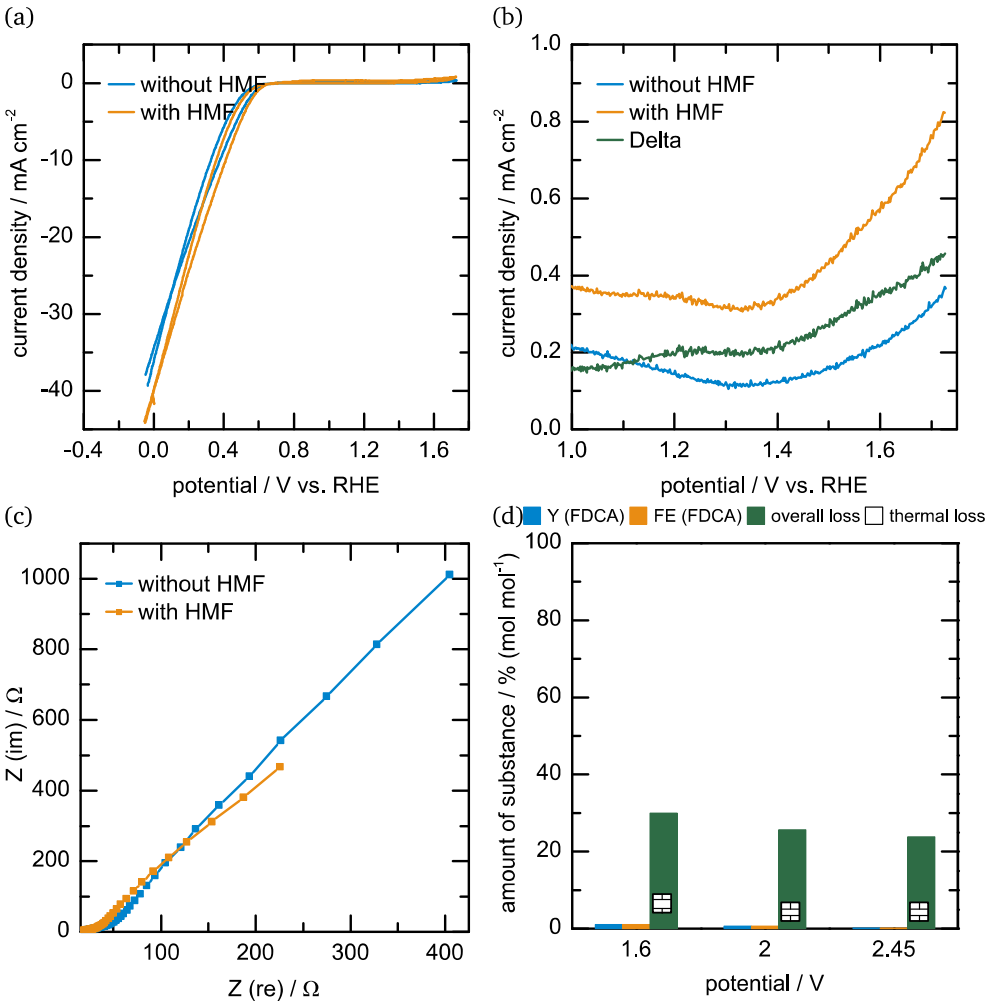

Figure 33: CVs of pure MPL 39 BB over the whole potential window (a) and a close-up of the HMF oxidation potential range (1.0 – 1.75 V vs. RHE) (b) without (blue), with 5 mM HMF (orange) and their difference (green) in 0.1 M KOH vs. Hg/HgO with Pt as CE. (c) EIS without (blue) and with 5 mM HMF (orange). (d) Yield and faradaic efficiency towards FDCA (*Y* (FDCA) (blue) and *FE* (FDCA) (orange), respectively) as well as overall loss (green) and thermal loss (blank squares) for complete HMF electrolysis (5 mM) in 0.1 M KOH of MPL 39 BB vs. Pt at different applied potentials, 30 °C and 600 rpm in a divided cell. Note: the reactions were terminated after 180, 120 and 120 minutes, which equaled 7.57, 5.14 and 5.87 C, respectively.

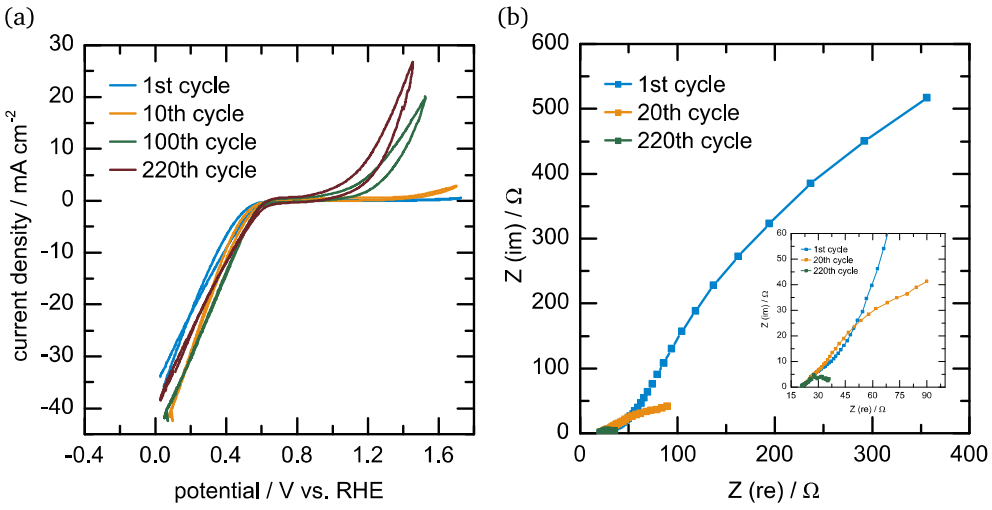

Figure 34: (a) CVs of MPL 39 BB after different numbers of CVs vs. Hg/HgO with Pt as CE in 0.1 M KOH. (b) Corresponding EIS measurements after different numbers of CVs.

Concluding these results, MPL seems to be a suitable support material for HMF oxidation as it does not contribute to any HMF oxidation reactions but does to the unwanted side reactions. Therefore, the CVs over a broad potential range are a good indicator if the MPL is completely covered with ink and does not contact the electrolyte due to the huge activity at lower potentials below 0.5 V vs. RHE that stays in competition with the electron transfer -1 of TEMPO and its derivatives. If no activity at the before-mentioned low potentials can be seen, the MPL should not contribute to any HMF oxidation reactions and true catalytic activity can be assessed. Another advantage is the long time behavior of MPL, which might emphasize a possible leaching of the ink that could be detected by a rising activity in this potential region. If the MPL is completely covered with ink, carbon oxidation should also be suppressed and is therefore negligible.

6.4.2. Pure TEMPO and pure ionic liquid immobilized on microporous carbon

After the innocence of the anode material is proved, all synthesized TEMPO derivatives and ILs as well as the commercially purchased ones are solely investigated regarding their activity towards HMF oxidation to FDCA. Therefore, the usual amount of TEMPO is immobilized directly onto the MPL without any IL and the usual amount of IL is immobilized directly onto the MPL without any TEMPO. Figure 35 illustrates the electrolysis results of HT and its derivatives (a), AT and its derivatives (b) and six different ILs (c).
In Figure 35 (a), HT is the most active derivative with a conversion of 70 %, a yield and *FE* towards FDCA of 8 % each as well as an overall loss of 29 %, which is the least for HT-based TEMPO derivatives. C12-HT is the only other derivative that shows any sign of activity as all other electrolysis runs had to be terminated due to no current flowing anymore with 45 % overall loss, a 58 % conversion as well as a yield and *FE* towards FDCA of 2 % each. AT and its derivatives show a different behavior as just C18-AT had to be terminated due to the before-mentioned reasons and all other electrolysis runs demonstrate more promising results. With a conversion of 82 % and a yield and *FE* towards FDCA of 30 % each, AT itself is more active than any HT-based derivative, while the overall loss of 29 % is comparable to HT. C12- and C14-AT both reach a conversion of 100 % but the selectivity patterns differ from one another. While C12-AT displays the lowest overall loss of just 3 % paired with the highest yield and *FE* towards FDCA of 69 and 63 %, respectively, C14-AT reverses these results with the lowest yield and *FE* towards FDCA with 21 and 20 %, respectively, and one the second highest overall loss of 27 %. C16-AT reaches a 93 % conversion of HMF, a 31 % yield to FDCA and a 29 % *FE* and an overall loss of 4 %, the second lowest of all AT-based derivatives. A clear trend is observable as the HT-based derivatives only reach 8 % as their highest yield towards FDCA at a conversion of 70 % and 29 % as the lowest overall loss, which is the highest recorded for the AT-based ones that achieve 69 % of yield towards FDCA at full conversion. Thus, AT-based derivatives seem to be more active towards HMF oxidation and furthermore seem to produce FDCA selectively. Figure 35 (c) illustrates the electrolysis results of all used ILs, which are all similar as they only show a negligible activity towards FDCA production, besides C10MIM BETI that had to be terminated due to the before-mentioned reasons. The conversion is as high as 29, 51, 66, 38 and 47 % from left to right, respectively and the overall loss rises parallel to the conversion to 23, 37, 55, 31 and 42 %, respectively, as FDCA can hardly be detected in the reaction solution. Some FFCA is produced during electrolysis, which explains the difference between conversion and overall loss. The yield and *FE* towards FDCA is as low as 1, 2, 3, 1 and 0 %, respectively. In conclusion, no IL contributes to FDCA production and can therefore be

used as organic phase, in which TEMPO is immobilized. Thus, all detected activity of the SILP systems can be traced back to the TEMPO derivatives rather than the used IL.

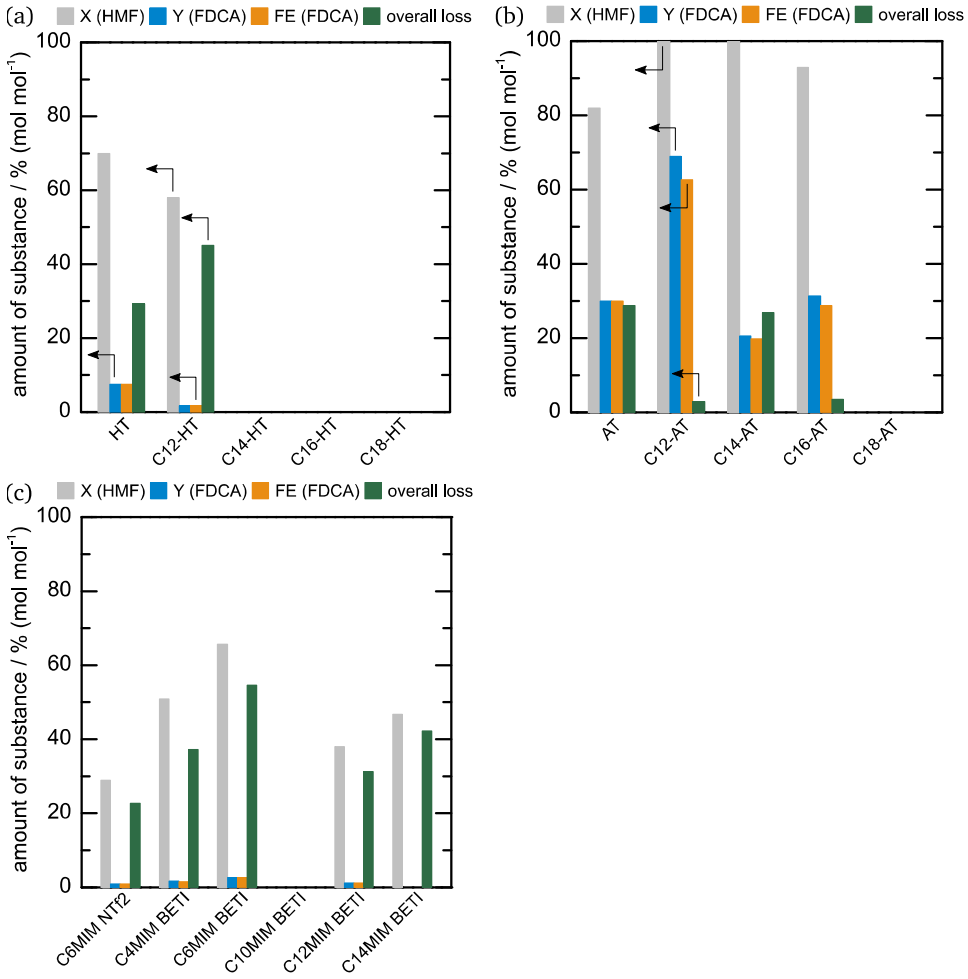

Figure 35: Conversion (*X* HMF, light grey), yield and faradaic efficiency towards FDCA (*Y* (FDCA) (blue) and *FE* (FDCA) (orange), respectively) as well as overall loss (green) for complete HMF electrolysis (5 mM) in 0.1 M KOH of pure HT (a), AT (b) and their long chain derivatives on MPL 39 BB vs. Pt at 30 °C and 600 rpm in a divided cell. (c) Conversion (*X* HMF, light grey), yield and faradaic efficiency towards FDCA (*Y* (FDCA) (blue) and *FE* (FDCA) (orange), respectively) as well as overall loss (green) for complete HMF electrolysis (5 mM) in 0.1 M KOH of pure ILs on MPL 39 BB vs. Pt at 30 °C and 600 rpm in a divided cell. Applied electrolysis potentials from left to right: (a) 1.94, 1.11, 0.76, 0.89 and 0.76 V, respectively; (b) 1.96, 1.94, 2.05, 1.58 and 0.7 V, respectively; (c) 0.87, 0.7, 2.2, 0.65, 0.61 and 2.2 V, respectively.

6.4.3. Methoxy TEMPO immobilized in ionic liquids

Due to the study of the MPL, several TEMPO-derivatives and ILs each on their own, SILP measurements combining all three before-mentioned pieces will be informative regarding the selective HMF oxidation potential of the homogeneous catalysts. At first, commercially purchased MT is tested as HMF oxidation catalyst in different ILs, before the self-synthesized TEMPO derivatives can be compared to it.

Figure 36 (a) – (c) shows the HMF oxidation potential range of the oxidative branch depicted over a bigger potential range in Figure 36 (d) – (f) of MT in C6MIM NTf_2, C6MIM BETI and C12MIM BETI, respectively, as example for different ILs. All three SILP compositions show a strong rise in current density when 5 mM HMF is added to the electrolyte (orange), which is also observable in the Delta branch (green), even if the onset differs between 1.2 V vs. RHE for

C6MIM NTf_2 and C6MIM BETI and 1.4 V vs. RHE for C12MIM BETI. The behavior at smaller potentials draws the conclusion that the whole MPL is covered with IL, as the current density does not grow as high as with pure MPL, cf. Figure 33 (a). Additionally to the CV measurements, all EIS spectra in Figure 36 (g) – (i) with HMF present show a decrease of the impedance in the low frequency range, indicating a lowering of the charge transfer resistance and thus an increase in reaction rate. Nevertheless, only the EIS spectrum of C12MIM BETI fully resolves a semicircle, which typifies an ongoing reaction by charge transfer.

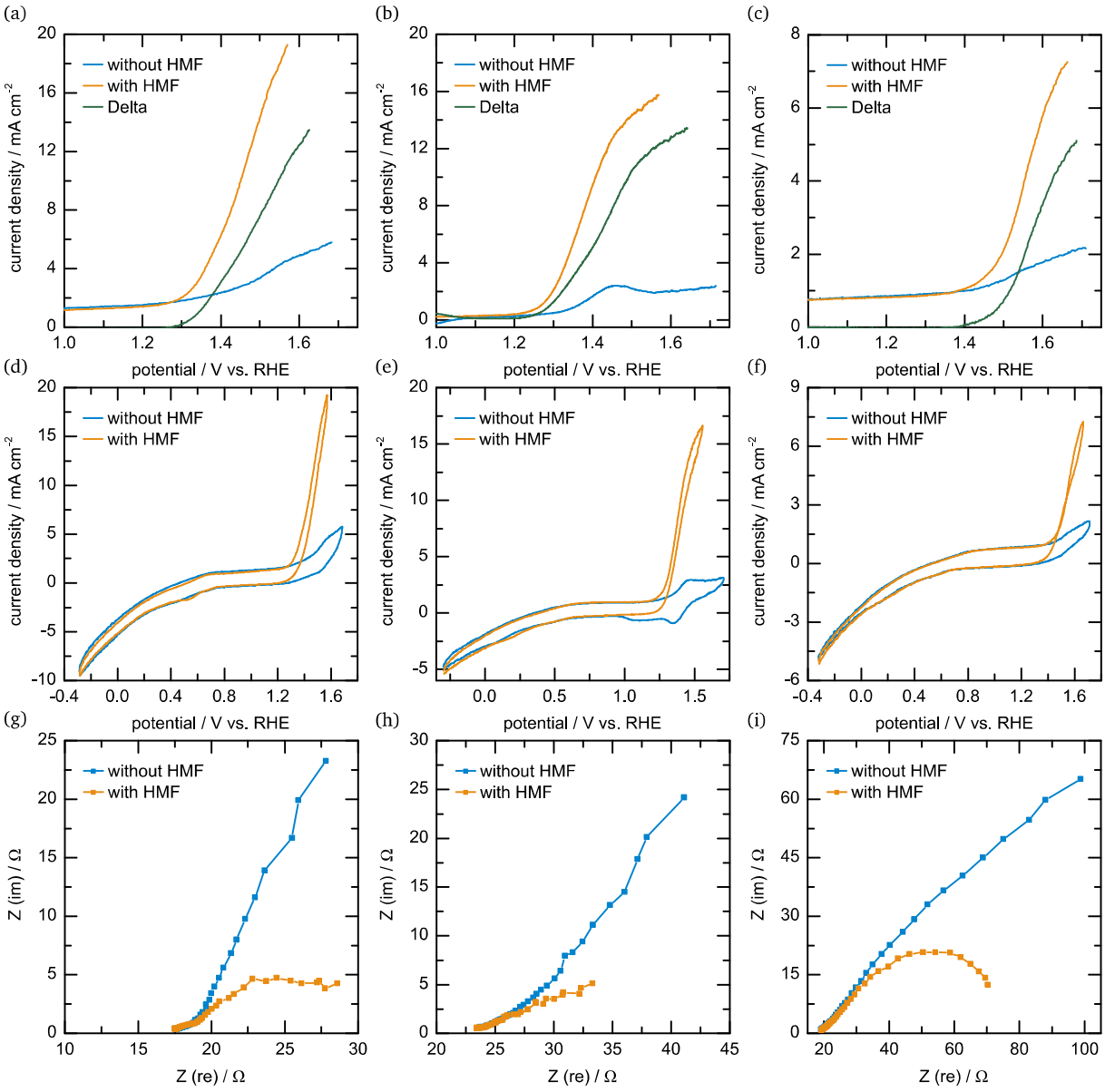

Figure 36: CVs at the HMF oxidation potential range (1.0 – 1.75 V vs. RHE) (a) – (c) and at a broad potential range (-0.3 – 1.75 V vs. RHE) (d) – (f) of MT in C6MIM NTf_2 (a, d), C6MIM BETI (b, e) and C12MIM BETI (c, f) without (blue), with 5 mM HMF (orange) and their difference (green) in 0.1 M KOH vs. Hg/HgO with Pt as CE. EIS measurements of MT in C6MIM NTf_2 (g), C6MIM BETI (h) and C12MIM BETI (i) without (blue) and with 5 mM HMF (orange) in 0.1 M KOH vs. Hg/HgO with Pt as CE.

Suitable to the before-investigated measurements, Figure 37 illustrates the electrolysis results of MT in imidazolium-based ILs with different anions (C6MIM NTf_2, C6MIM BETI, C10MIM NTf_2, C10MIM BETI; (a)) and different cations (C4MIM, C6MIM, C10MIM, C12MIM and C14MIM with BETI as anion; (b)). All SILP compositions containing MT confirm the trend seen

in Figure 36 as they show a high activity towards HMF oxidation with FDCA as main product. Comparing C6MIM NTf_2 to C6MIM BETI leads to a slightly higher activity of the BETI-based IL with 78 and 79 % yield and *FE* towards FDCA, respectively, to 73 % each. Even if the overall loss is similar with 5 and 4 % for C6MIM NTf_2 and C6MIM BETI, respectively, the production rate differs more with 1.13 to 1.75 $mmol_{FDCA}\ s^{-1}\ mmol_{cat}^{-1}$. This trend is reversed for the C10MIM-based ILs as C10MIM NTf_2 exhibits a higher activity with 85 % yield and *FE* towards FDCA compared to the 68 and 67 %, respectively, of C10MIM BETI. Overall loss is at its lowest point with 0 and 1 %, while the production rate differs again between both ILs with different anions at 1.2 and 0.99 $mmol_{FDCA}\ s^{-1}\ mmol_{cat}^{-1}$. Both anion variations lead to different results, which does not allow any conclusions. Thus, the cations of BETI-based ILs have been used in following measurements and have additionally been varied in Figure 37 (b) as it has one additional CF_2-group and should therefore be more hydrophobic as the NTf_2,[344] which is important regarding the possible leaching of IL into the electrolyte.[297]
Besides C6MIM and C10MIM BETI that have been exhibited in Figure 37 (a), C4MIM, C12MIM and C14MIM BETI have been investigated with MT as homogeneous catalyst immobilized in them. Compared to C6MIM BETI, C4MIM BETI shows less activity towards HMF oxidation with a yield and *FE* towards FDCA of 73 % each, a better overall loss performance of 2 % and in the end a lower production rate of 1.14 $mmol_{FDCA}\ s^{-1}\ mmol_{cat}^{-1}$. MT in C12MIM BETI presents the best overall performance with a lower production rate of 1.03 $mmol_{FDCA}\ s^{-1}\ mmol_{cat}^{-1}$ but no overall loss and a yield and *FE* towards FDCA of 99 % each. Further enhancement of the chain at the imidazolium cation to C14MIM BETI leads to a drop of activity to 64 and 60 % yield and *FE* towards FDCA, respectively, an overall loss of 2 % and a production rate of 0.57 $mmol_{FDCA}\ s^{-1}\ mmol_{cat}^{-1}$. The drop in activity might be explained by the character of C14MIM BETI, as it is solid at room temperature and therefore might immobilize MT worse than the other imidazolium-based ILs, which are liquid at room temperature, even if they get highly viscous with longer chains.

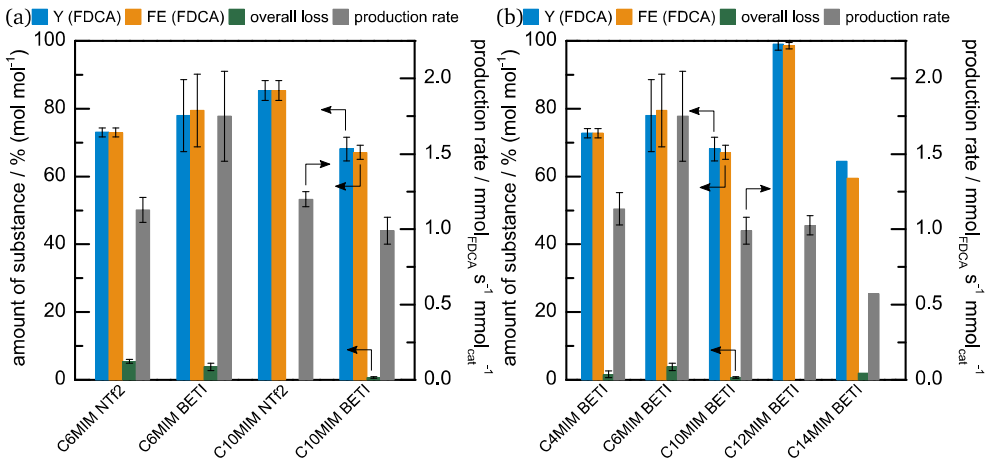

Figure 37: Yield and faradaic efficiency towards FDCA (*Y* (FDCA) (blue) and *FE* (FDCA) (orange), respectively) as well as overall loss (green) and production rate (grey) for complete HMF electrolysis (5 mM) in 0.1 M KOH of MT in different ILs on MPL 39 BB vs. Pt , respectively, 30 °C and 600 rpm in a divided cell. (a) Comparison of different anions at from left to right 1.85, 2.4, 2 and 1.9 V, respectively; (b) Comparison of different cations at from left to right: 1.9, 2.4, 1.9, 1.8 and 1.6 V, respectively.

Nevertheless, all BETI-based ILs with MT immobilized in them have been investigated regarding their stability. Figure 38 (a) describes the amount of IL and TEMPO in the electrolyte after 12 hours of chronoamperometric measurement without any HMF present at the usual HMF oxidation potential, which is repeated one more time with the same electrode but a fresh

electrolyte. On the contrary, Figure 38 (b) illustrates the electrolysis results of the electrodes with long chained ILs C10MIM, C12MIM and C14MIM BETI and MT applied onto them compared to their second use in fresh electrolyte with a fresh amount of HMF (5 mM) as well. As can be seen, C4MIM BETI seems to be completely washed from the electrode surface as around 100 % of the cation (blue), anion (orange) and MT (green) is detected in the electrolyte after the first 12 hours (filled bars). Thus, nearly nothing of the IL and MT can be detected in the second electrolyte (striped bars), which has been freshly added. With longer chains, the amount of cation and anion in the first electrolyte decreases consequently from 24 over 15 and 3 to 1 % for C6MIM, C10MIM, C12MIM and C14MIM BETI, respectively. The amount of MT follows this trend as well with 47, 32 and 17 % for C6MIM, C12MIM and C14MIM BETI, respectively, while C10MIM BETI falls out of this trend with 85 % MT in the first electrolyte. This might explain the lower HMF oxidation performance seen in Figure 37 as C10MIM BETI seems to cannot hold MT as good in the organic phase as the other imidazolium-based ILs. Since C10MIM, C12MIM and C14MIM BETI are the most hydrophobic ILs, only 2, 2 and 1 % of cation and anion can be detected in the second electrolyte, respectively, while C6MIM BETI loses 17 %. The amount of MT in the second electrolyte drops down to 4, 8, 6 and 1 %, respectively. Therefore, the electrolysis results of the reused electrodes with long chain ILs (C12MIM and C14MIM BETI) should provide similar activity and selectivity patterns if they can maintain this stability in the presence of HMF, which is reviewed in Figure 38 (b). All reused electrodes exhibit no activity for selective HMF oxidation at all only reaching 1 % of yield and *FE* towards FDCA and therefore extremely small production rates of 0.01 $mmol_{FDCA}\ s^{-1}\ mmol_{cat}^{-1}$. The overall loss varies between 35, 29 and 21 % for C10MIM, C12MIM and C14MIM BETI, respectively.
Concluding these results leads to a high activity regarding electrochemical HMF oxidation of MT in different ILs with high selectivity to the desired product FDCA. On the other hand, these SILP systems are active for only one electrolysis and exhibit an activity drop to nearly 0 % when reusing the same electrode independently of the utilized IL. Since MT is not as hydrophobic as the ILs, it dissolves easier in the electrolyte as shown in Figure 38 (a), which opens the possibility for more hydrophobic TEMPO derivatives to increase the stability of the SILP system.

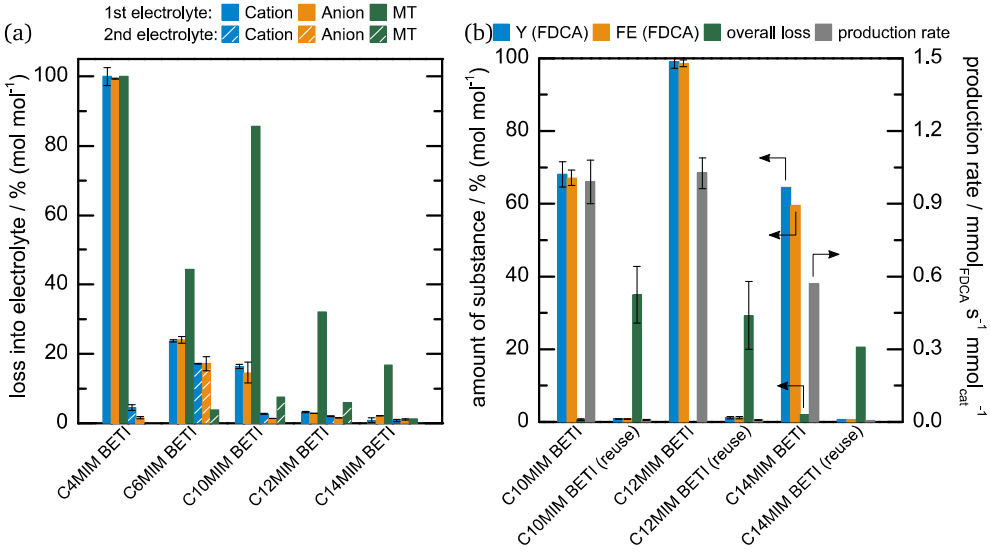

Figure 38: (a) Loss into electrolyte of different cations (blue), BETI (orange) and MT (green) after the leaching test in the first (filled bars) and the second electrolyte (striped bars). (b) Yield and faradaic efficiency towards FDCA (*Y* (FDCA) (blue) and *FE* (FDCA), respectively) as well as overall loss (green) and production rate (grey) for complete HMF electrolysis (5 mM) in 0.1 M KOH of MT in different long chained ILs on MPL 39 BB vs. Pt at from left to right 1.9, 1.8 and 1.6 V, respectively, 30 °C and 600 rpm in a divided cell. Results of a reuse of the same electrodes at the same potentials as before are depicted as well.

6.4.4. Hydroxy TEMPO and its derivatives immobilized in ionic liquids

The synthesized long chain HT and AT derivatives should fulfill the property of more hydrophobicity and therefore more stability of the whole SILP system. At first, HT and its long chain derivatives are investigated regarding their HMF oxidation ability, which is presented in Figure 39: The HMF oxidation potential range in (a) – (c), in which only the delta current density in different ILs is illustrated, the broad potential range in (d) – (f), in which the TEMPO/IL combinations with the highest activity in (a) – (c) are picked, and the EIS measurements in (g) – (i) complementary to the broad potential range CVs.

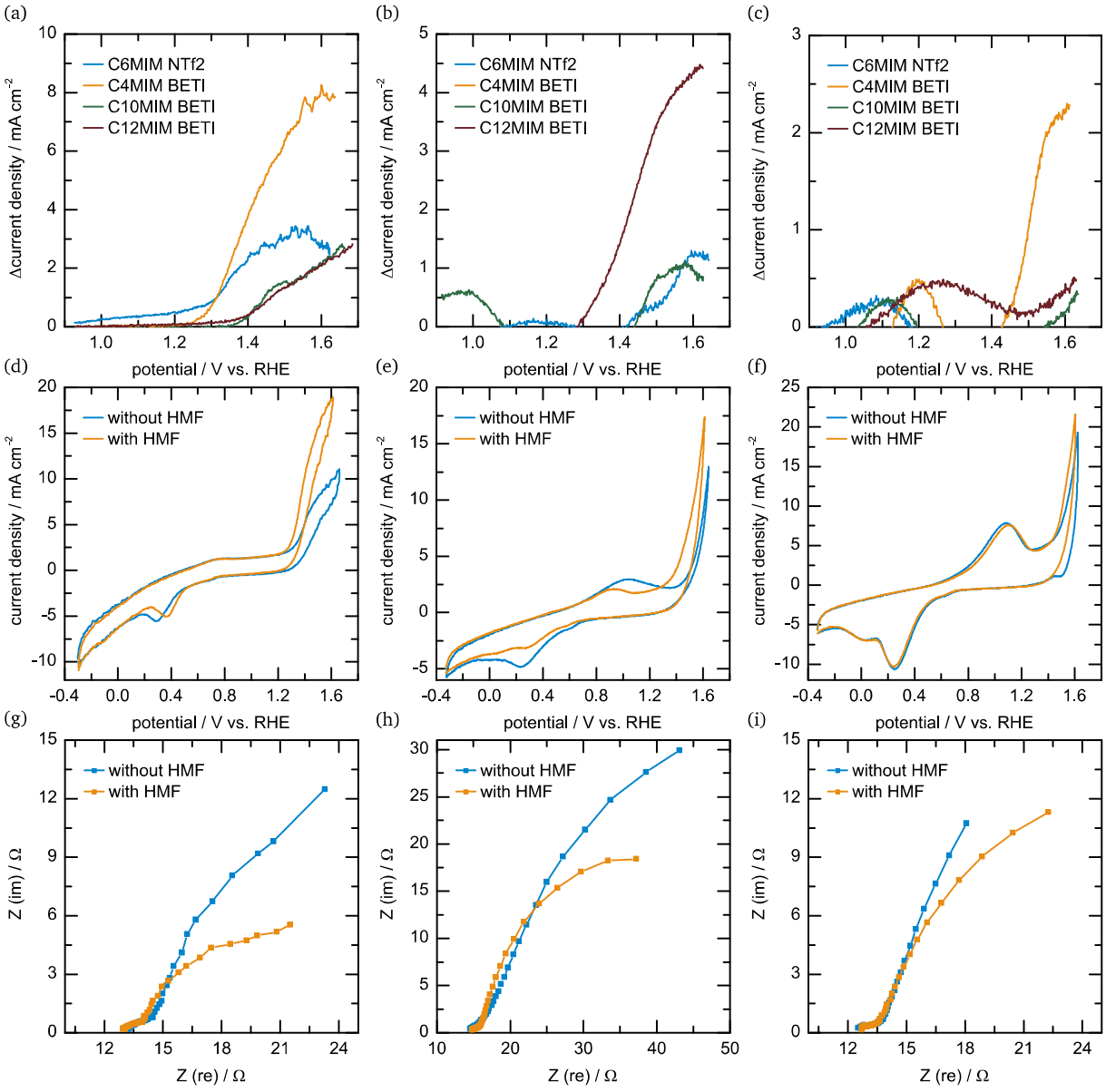

Figure 39: (a) – (c) Delta CVs at the HMF oxidation potential range (1.0 – 1.75 V vs. RHE) of HT (a), C12-HT (b) and C14-HT (c) in C6MIM NTf_2 (blue), C4MIM BETI (orange), C10MIM BETI (green) and C12MIM BETI (dark red). (d) – (f) CVs at a broad potential range (-0.3 – 1.75 V vs. RHE) of HT in C4MIM BETI (d), C12-HT in C12MIM BETI (e) and C14-HT in C4MIM BETI (f) on MPL 39 BB without (blue) and with 5 mM HMF (orange) in 0.1 M KOH vs. Hg/HgO with Pt as CE. EIS measurements of HT in C4MIM BETI (g), C12-HT in C12MIM BETI (h) and C14-HT in C4MIM BETI (i) on MPL 39 BB without (blue) and with 5 mM HMF (orange) in 0.1 M KOH vs. Hg/HgO with Pt as CE.

Here, HT (a) in C4MIM BETI ((d), (g)), C12-HT (b) in C12MIM BETI ((e), (h)) and C14-HT (c) in C4MIM BETI ((f), (i)) are compared to each other as examples due to their different behavior in the CVs and EIS measurements regarding HMF oxidation. The delta current densities exhibit the highest activity for each TEMPO derivative/IL combination, which is 8 mA cm^{-2} in C4MIM BETI (a), 4 mA cm^{-2} in C12MIM BETI (b) and 2 mA cm^{-2} in C4MIM BETI (c) for HT, C12-HT and C14-HT, respectively. Other combinations do not even show any positive delta current density or smaller than 1 mA cm^{-2}. As the differently high delta current densities indicated, the difference between the CVs without (blue) and with 5 mM HMF present (orange) is different for HT in C4MIM BETI (d), C12-HT in C12MIM BETI (e) and C14-HT in C4MIM BETI (f). HT seems to have the highest activity with the biggest difference between both CVs and C14-HT consequently the lowest activity. These results are supported by the EIS measurements, in which the impedance of C14-HT in C4MIM BETI (i) with 5 mM HMF present (orange) is nearly the same as without HMF (blue) as they only differ from another at small frequencies, even if a semicircle could be developing. A bigger difference can be seen for HT in C4MIM BETI (g) and C12-HT in C12MIM BETI (h), in which both the semicircle could set in.
Keeping these results in mind, the electrolysis results of HT in all before-used ILs is presented in Figure 40 (a) and the ones of C12-HT in C12MIM BETI and C14-HT in C4MIM BETI in Figure 40 (b). As can be seen, HT in any IL never exceeds yields or *FE* of 7 and 6 %, respectively, which can only be reached in C4MIM and C10MIM BETI, respectively. HT in C6MIM NTf_2 only reaches a 4 % yield and *FE* towards FDCA, while both are 6 % in C12MIM BETI. Furthermore, the production rate adjusts to the low yields and FEs with 0.09, 0.13, 0.03 and 0.03 $mmol_{FDCA}\ s^{-1}\ mmol_{cat}^{-1}$ for HT in C6MIM NTf_2, C4MIM, C10MIM and C12MIM BETI, respectively. The overall loss also adapts to the unwanted selectivity pattern with 40, 28, 21 and 28 %, respectively. Both investigated long chain derivatives exhibit a similar ability to oxidize HMF to FDCA as C12-HT in C12MIM BETI reaches a yield and *FE* towards FDCA of 5 % and C14-HT in C4MIM BETI of 8.5 %. Their production rates are therefore as low as the ones of HT in different ILs with 0.03 and 0.05 $mmol_{FDCA}\ s^{-1}\ mmol_{cat}^{-1}$, respectively, with as high overall losses of 38 and 13 %, respectively.

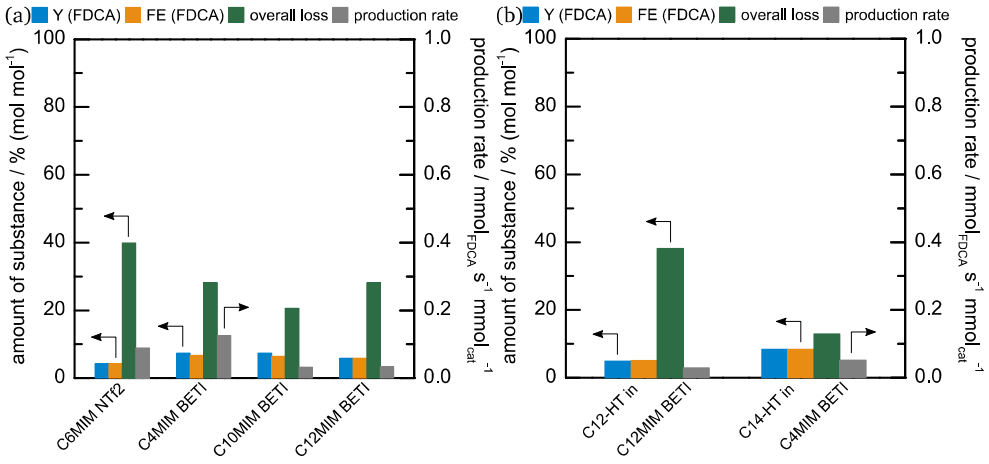

Figure 40: Yield and faradaic efficiency towards FDCA (*Y* (FDCA) (blue) and *FE* (FDCA) (orange), respectively) as well as overall loss (green) and production rate (grey) for complete HMF electrolysis (5 mM) in 0.1 M KOH of HT in different ILs (a) on MPL 39 BB vs. Pt at from left to right 2.3, 2.31, 1.48 and 1.52 V, respectively, 30 °C and 600 rpm in a divided cell and HT derivatives in different ILs (b) at from left to right 1.67 and 1.79 V, respectively.

HT and its derivatives exhibit unintentional results regarding HMF oxidation, as they are not able to produce FDCA in an appropriate amount reaching not even 10 % in yield, although the CVs looked like some SILP combinations might be active. Thus, an activity in the CVs does not

have to conclude that the catalyst selectively converts the reactant to the desired product. Due to the inactivity of all SILP combinations, no stability measurements have been carried out.

6.4.5. Amino TEMPO and its derivatives immobilized in ionic liquids

AT and its derivatives have been investigated equally to HT and its derivatives with delta CVs at the HMF oxidation potential range of AT, C12-AT and C14-AT in the prior employed ILs (Figure 41 (a) – (c)), CVs over the broad potential range in the IL they best performed in (Figure 41 (d) – (f)) and their corresponding EIS spectra (Figure 41 (g) – (i)). The before-mentioned AT derivatives have been chosen as example due to their different behavior in CV and EIS measurements.
In Figure 41 (a), AT presents a similar behavior for all used ILs with the only difference in the onset of the delta current density rise, which is at higher potentials (1.4 V vs. RHE) for long chain ILs than for short chain ones (1.2 V vs. RHE). Nevertheless, in C4MIM BETI the highest current density of 15 mA cm^{-2} is reached. C12-AT exhibits defined signals for every IL in Figure 41 (b) even if the highest delta current density is reached in C6MIM NTf_2 with 9 mA cm^{-2}. On the other hand, C14-AT exhibits no defined signal and reaches delta current densities of 3 mA cm^{-2} only, which is why it is further investigated in C12MIM BETI, due its more promising results regarding its hydrophobicity, cf. Figure 38. As with HT and its derivatives, the differences in the delta current densities are retrieved in the CVs over a broad potential window In Figure 41 (d) – (f), especially for C12-AT, at which the defined signal can be observed at 1.25 V vs. RHE. Interestingly, the corresponding EIS spectrum in Figure 41 (h) indicates a smaller solution resistance and a simultaneously higher mass transfer resistance with 5 mM HMF present (orange) than without (blue). These observations might also relate to a slightly different arrangement in the setup. In contrast to these observations, AT and C14-AT present presumable semicircles that once again indicate a charge transfer and therefore an ongoing reaction. In comparison to HT and its derivatives, the electrolysis results will provide further information of the HMF oxidation and FDCA production ability of these SILP combinations.
Figure 42 (a) illustrates the electrolysis results of AT in C6MIM NTf_2, C4MIM BETI and C10MIM BETI, while the one in C12MIM BETI had to be terminated, because current dropped down to a minimum. The activity is similar with yields of 78, 71 and 80 %, respectively, and FEs towards FDCA of 72, 68 and 78 %, respectively, while no overall loss is detected for any SILP combination. A difference can be observed regarding the production rate, as it is 0.42 $mmol_{FDCA}$ s^{-1} $mmol_{cat}^{-1}$ for C10MIM BETI and therefore more than three times lower than for C6MIM NTf_2 and C4MIM BETI with 1.44 and 1.78 $mmol_{FDCA}$ s^{-1} $mmol_{cat}^{-1}$, respectively, which can be explained by the longer reaction time due to the higher viscosity of C10MIM BETI. A similar trend is observable in Figure 42 (b), in which the electrolysis results of C14-AT in C6MIM NTf_2, C4MIM BETI, C10MIM BETI and C12MIM BETI are presented. Due to the more hydrophobic TEMPO derivative, the production rate drops to around half of the one of AT in every IL with 0.78, 0.72, 0.27 and 0.29 $mmol_{FDCA}$ s^{-1} $mmol_{cat}^{-1}$, respectively. Additionally, the yield of FDCA also decreases to 60, 63, 41 and 45 %, respectively, as does the *FE* towards FDCA to 57, 61, 38 and 46 %, respectively. The overall loss is once again not observable for any SILP combination besides the one of C14-AT in C10MIM BETI, in which 29 % are detected. Furthermore, the electrolysis results of C12- and C16-AT in ILs, in which they exhibited the potential of HMF oxidation, are presented in Figure 42 (b). At first, no overall loss is detected again in either SILP combination, while C16-AT in C4MIM BETI exhibits the most promising results with a yield and *FE* towards FDCA of 50 and 49 %, respectively, which results in a production rate of 0.45 $mmol_{FDCA}$ s^{-1} $mmol_{cat}^{-1}$. If C16-AT in C6MIM NTf_2 is used as SILP system,

the production rate is four times lower with 0.12 $mmol_{FDCA}\ s^{-1}\ mmol_{cat}^{-1}$, which mirrors in the yield and *FE* towards FDCA of only 14 % each. C12-AT has been investigated regarding electrochemical HMF oxidation in C6MIM NTf_2, C4MIM BETI and C10MIM BETI. The yield and *FE* towards FDCA have been highest in C4MIM BETI with 38 and 37 %, respectively, and a production rate of 0.77 $mmol_{FDCA}\ s^{-1}\ mmol_{cat}^{-1}$. With 0.65 $mmol_{FDCA}\ s^{-1}\ mmol_{cat}^{-1}$, the electrolysis in C6MIM NTf_2 exhibited a similar production rate, which resulted in a yield and *FE* towards FDCA of 30 and 32 %, respectively. The lowest HMF activity of C12-AT is observed in C10MIM BETI with a yield and *FE* towards FDCA of 25 and 24 %, respectively, which also results in the lowest production rate of 0.24 $mmol_{FDCA}\ s^{-1}\ mmol_{cat}^{-1}$.

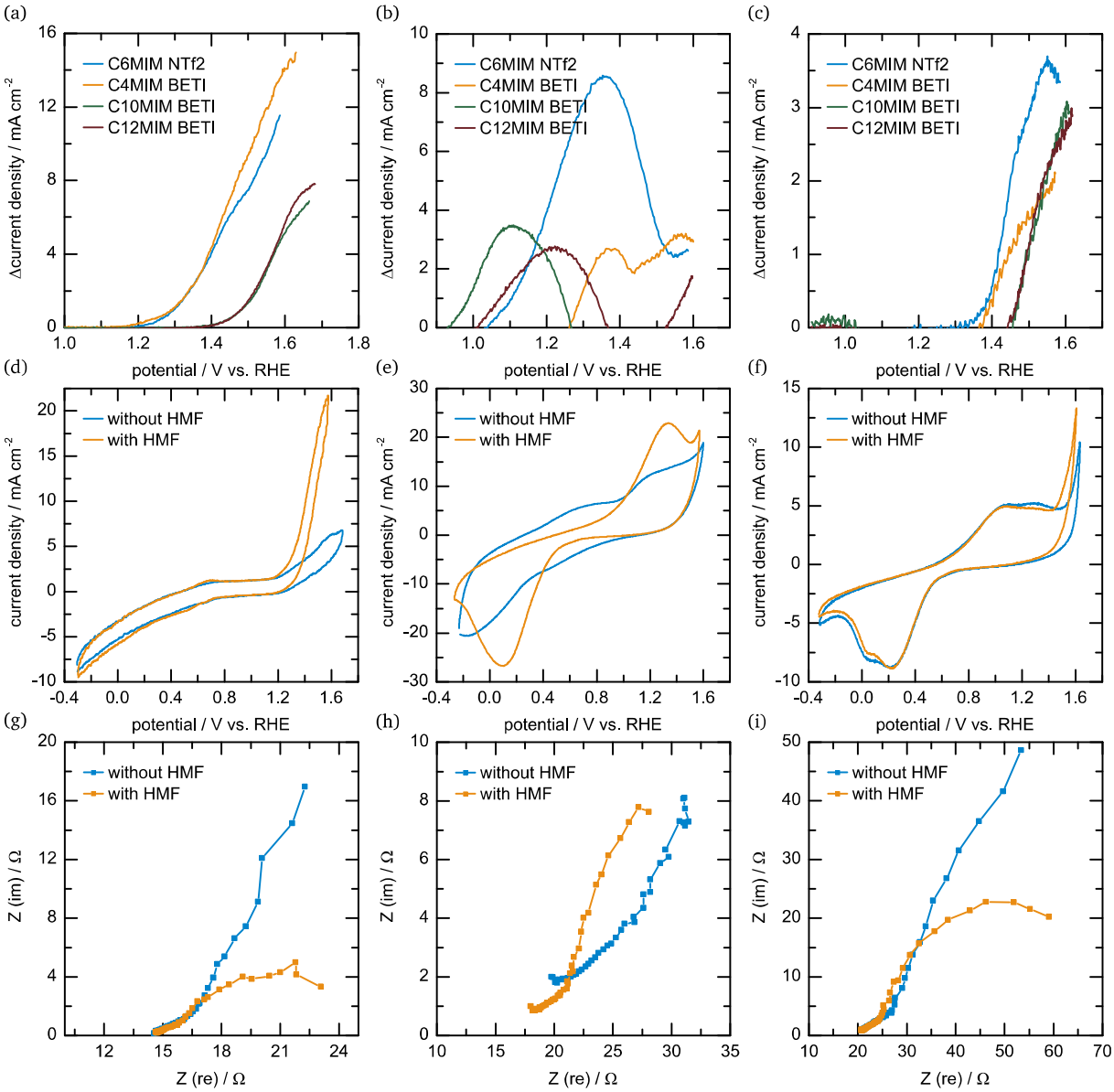

Figure 41: (a) – (c) Delta CVs at the HMF oxidation potential range (1.0 – 1.75 V vs. RHE) of AT (a), C12-AT (b) and C14-AT (c) in C6MIM NTf_2 (blue), C4MIM BETI (orange), C10MIM BETI (green) and C12MIM BETI (dark red). (d) – (f) CVs at a broad potential range (-0.3 – 1.75 V vs. RHE) of AT in C4MIM BETI (d), C12-AT in C6MIM NTf_2 (e) and C14-AT in C12MIM BETI (f) on MPL 39 BB without (blue) and with 5 mM HMF (orange) in 0.1 M KOH vs. Hg/HgO with Pt as CE. EIS measurements of AT in C4MIM BETI (g), C12-AT in C6MIM NTf_2 (h) and C14-AT in C12MIM BETI (i) on MPL 39 BB without (blue) and with 5 mM HMF (orange) in 0.1 M KOH vs. Hg/HgO with Pt as CE.

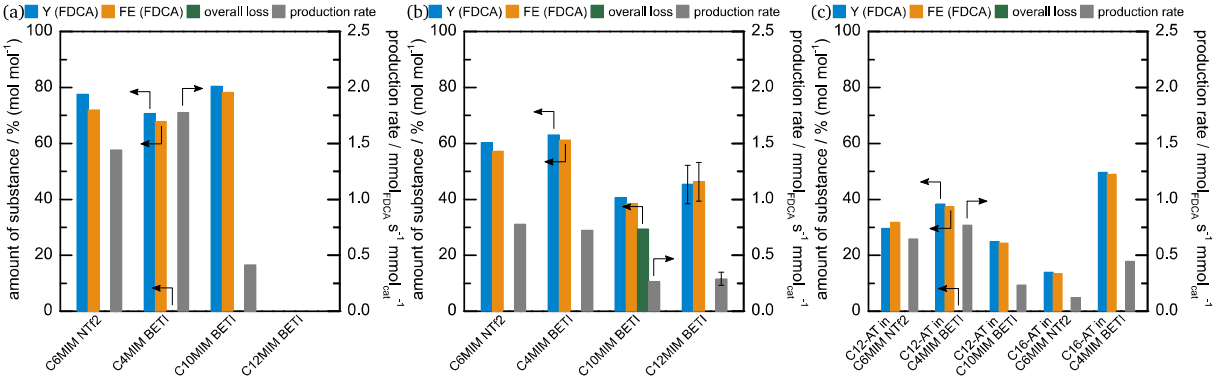

Figure 42: Yield and faradaic efficiency towards FDCA (*Y* (FDCA) (blue) and *FE* (FDCA) (orange), respectively) as well as overall loss (green) and production rate (grey) for complete HMF electrolysis (5 mM) in 0.1 M KOH of AT (a), C14-AT (b) and C12- as well as C16-AT (c) in different ILs on MPL 39 BB vs. Pt at 30 °C and 600 rpm in a divided cell. Applied electrolysis potentials from left to right: (a) 2.2, 2.44, 1.58 and 0.64 V, respectively; (b) 2.0, 1.86, 1.75 and 1.77 V, respectively; (c) 2.21, 2.08, 1.79, 1.75 and 1.95 V, respectively.

Since the stability tests without HMF cannot be used as assessment regarding stability of the SILP system, only reuses of electrodes in electrolysis runs are evaluated. Due to the promising results of C14-AT, which should be more hydrophobic than AT, its stability is investigated in the also hydrophobic C12MIM BETI in Figure 43 (a). As the reuse shows, its yield and *FE* towards FDCA drop to 14 and 13.5 %, respectively, as does its production rate to 0.12 $mmol_{FDCA}$ s^{-1} $mmol_{cat}^{-1}$, while an overall loss of 10 % occurs. Another approach is applying twice the amount of charge (26.06 C) that is needed for a theoretical full conversion of 5 mM HMF to FDCA in on electrolysis run to examine if the SILP combination is washed from the electrode during electrolysis. As Figure 43 (a) illustrates, the *FE* towards FDCA and the production rate stay constant with 47 % and 0.29 $mmol_{FDCA}$ s^{-1} $mmol_{cat}^{-1}$, respectively, while the yield of FDCA rises to 84 %, which is nearly double the amount as before. Thus, leaching into the electrolyte or deactivation of the active material happens with switching off the applied potential, an interaction with air or the transfer into a fresh electrolyte. Further investigation of this challenge led to the use and twice reuse of C12- and C14-AT in C14MIM BETI presented in Figure 43 (b). The yield and *FE* towards FDCA have dropped from 53 and 52 %, respectively, to 28 % each in the first reuse and 6 % each in the second reuse for C12-AT.

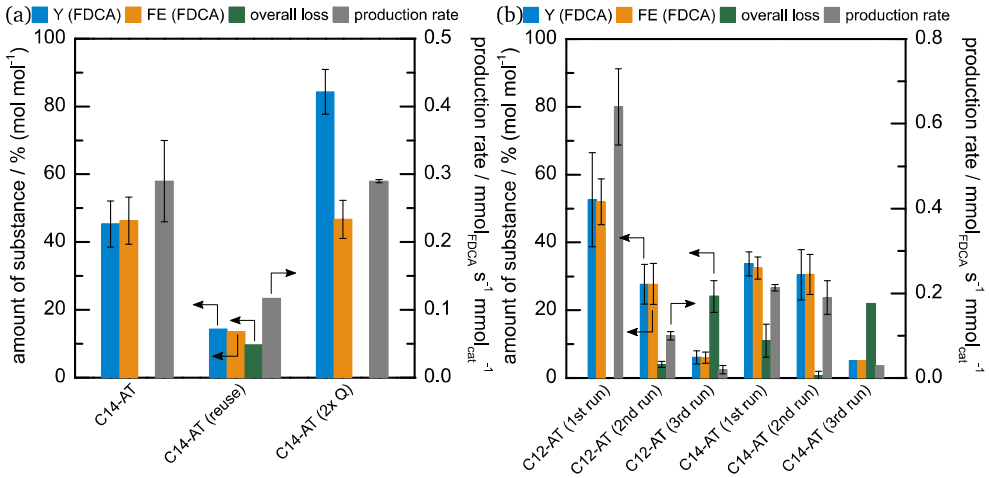

Figure 43: Yield and faradaic efficiency towards FDCA (*Y* (FDCA) (blue) and *FE* (FDCA) (orange), respectively) as well as overall loss (green) and production rate (grey) for complete HMF electrolysis (5 mM) in 0.1 M KOH of C14-AT in C12MIM BETI including one reuse and double the amount of charge (26.06 C) at 1.65 V (a) and C12- at 1.65 V as well as C14-AT in C14MIM BETI at 1.75 V including reuses (b) on MPL 39 BB vs. Pt at 30 °C and 600 rpm in a divided cell.

Furthermore, production rate decreases as well from 0.64 to 0.10 to 0.02 $mmol_{FDCA}\ s^{-1}\ mmol_{cat}^{-1}$, while the overall loss increases from 0 to 4 to 24 %, respectively. On the other hand, C14-AT in C14MIM BETI reaches similar results after one reuse with a change of yield of FDCA from 34 to 30 %, a change of *FE* towards FDCA from 32 to 31 %, which is also verified by the production rate that decreases slightly from 0.21 to 0.19 $mmol_{FDCA}\ s^{-1}\ mmol_{cat}^{-1}$. Interestingly, the overall loss drops from 11 to 1 %, which might be explained by the conversion, which is 94 % in the first run and just 80 % in the second one leading to more overall loss if the same amount of FDCA is produced. Using this electrode a third time, leads to a strong decrease in activity as yield and *FE* towards FDCA drop to 5 % each, as does the production rate to 0.03 $mmol_{FDCA}\ s^{-1}\ mmol_{cat}^{-1}$, while the overall loss rises to 22 %.
Concluding these results, most of the AT derivatives are active towards HMF oxidation, which can be observed in Figure 42, especially comparing them to HT and its derivatives in Figure 40. Nevertheless, not even the most active and long chained C14-AT in the most hydrophobic synthesized IL C14MIM BETI could maintain its activity over two reuses, but over one. Furthermore, it was able to produce twice as much FDCA in C12MIM BETI, while applying twice as much charge and keeping the amount of 5 mM TEMPO constant. Since the SILP system is not deactivated over time in electrolysis, there is the possibility of TEMPO derivatives staying catalytically active in the electrolyte after they have been transferred into the aqueous phase, even if they should not at these pH and potentials,[230] cf. Scheme 12. If TEMPO is extracted from the organic IL phase into the electrolyte during HMF oxidation, the SILP concept is invalidate regarding these TEMPO/IL combinations. Therefore, TEMPO species would need a higher interaction with the electrode material to prevent it from leaching into the electrolyte together. A possibility to circumvent this challenge is a higher interaction of TEMPO to the electrode material.

6.5. Pyrene TEMPO

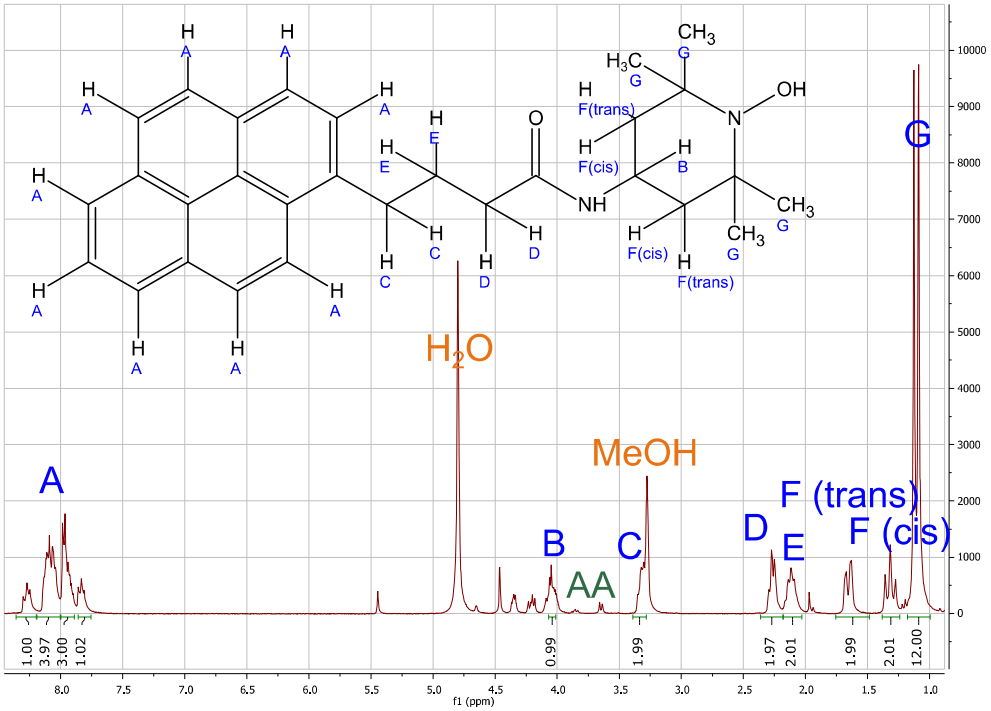

Figure 44: ^{1}H-NMR of PT in MeOH-d_4.

Due to the carbon-based composition of the MPL, a TEMPO species with a conjugated π-system as a side group might enhance the interaction between both and could hinder leaching into the electrolyte. Therefore, 1-pyrenebutyric acid reacted with AT under similar circumstances as the AT derivatives in chapter 6.2 followed by a purification step via flash chromatography to synthesize pyrene-TEMPO (PT). Figure 44 presents its ^{1}H-NMR spectrum in MeOH-d_4 with all expected protons assigned to their signals. The signals at 2.0, 4.0 – 4.5, and 5.4 ppm could not be led back to any of the used reactants as none of them exhibits signals at these chemical shifts, cf. Figure 26, Figure 63 and Figure 71. Therefore, impurities of the used deuterated solvent MeOH-d_4 might be the reason behind these unknown signals.
Nevertheless, PT has been immobilized in C12MIM BETI as it proved to be the most promising IL regarding HMF oxidation activity. Figure 45 (a) and (b) show the CVs of PT in C12MIM BETI at the HMF oxidation potential range and over a broad potential range, respectively. A slight increase in current density can be observed after adding HMF (orange) compared to no HMF present (blue), which is also retrieved in the delta current density (green) as it exhibits a small potential region at 1.4 – 1.6 V vs. RHE, in which it is positive. The EIS spectrum in Figure 45 (c) illustrates a similar result as the addition of HMF (orange) leads to an increasing overall impedance in comparison to the spectrum without any HMF present (blue).

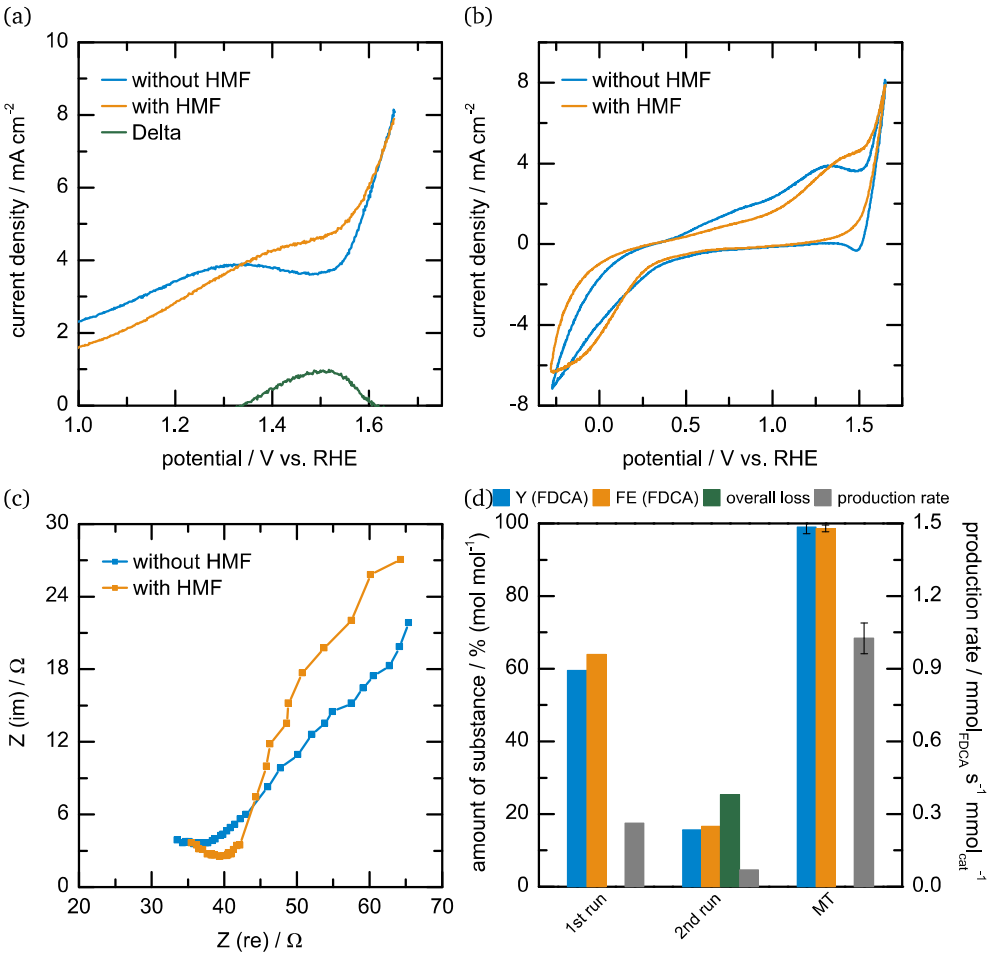

Figure 45: CVs at the HMF oxidation potential range (1.0 – 1.75 V vs. RHE) (a) and at a broad potential range (-0.3 – 1.75 V vs. RHE) (b) of PT in C12MIM BETI on MPL 39 BB without (blue), with 5 mM HMF (orange) and their difference (green) in 0.1 M KOH vs. Hg/HgO with Pt as CE. (c) EIS measurements of PT BETI in C12MIM BETI on MPL 39 BB without (blue) and with 5 mM HMF (orange) in 0.1 M KOH vs. Hg/HgO with Pt as CE. (d) Yield and faradaic efficiency towards FDCA (*Y* (FDCA) (blue) and *FE* (FDCA) (orange), respectively) as well as overall loss (green) and production rate (grey) for complete HMF electrolysis (5 mM) of PT in C12MIM BETI on MPL 39 BB in 0.1 M KOH at 1.6 V vs. Pt at 30 °C and 600 rpm in a divided cell as well as MT in C12MIM BETI on MPL 39 BB as comparison.

Nevertheless, PT is able to convert HMF to the desired product FDCA as Figure 45 (d) demonstrates, in which the electrolysis results of PT in C12MIM BETI on MPL are presented, with a yield and *FE* towards FDCA of 60 and 64 %, respectively, and no overall loss, which results in a production rate of 0.26 $mmol_{FDCA}\ s^{-1}\ mmol_{cat}^{-1}$. Unfortunately, reusing the same electrode leads to an activity drop to 0.07 $mmol_{FDCA}\ s^{-1}\ mmol_{cat}^{-1}$ with a yield and *FE* towards FDCA of 16 and 17 %, respectively, as well as an overall loss of 25 %.
Thus, enhancing the interaction between TEMPO species and electrode surface does not perform as desired, so another possibility might be to enhance the interaction between TEMPO and IL even further, or another electrode material that interacts stronger with the ink and protects it better from extraction.

6.6. TEMPO covalently connected to ionic liquid

Due to the missing stability of the before-investigated SILP systems, TEMPO covalently connected to the IL itself might solve this challenge. Therefore, HT and AT have been linked with an imidazolium ring as cation and BETI as anion, which resulted in HTMIM and ATMIM BETI.

6.6.1. HTMIM BETI

At first, the successful synthesis of HTMIM BETI has been verified via ^{1}H-NMR. In the first synthesis step, HT reacted with chloroacetic acid using EDC as cross-linking agent and DMAP as catalyst for esterification in dichloromethane, resulting in HT-chloroacetate. After flash chromatography, all proton signals can be detected in ^{1}H-NMR in MeOH-d_4 without any of the other reactants present as illustrated in Figure 46.

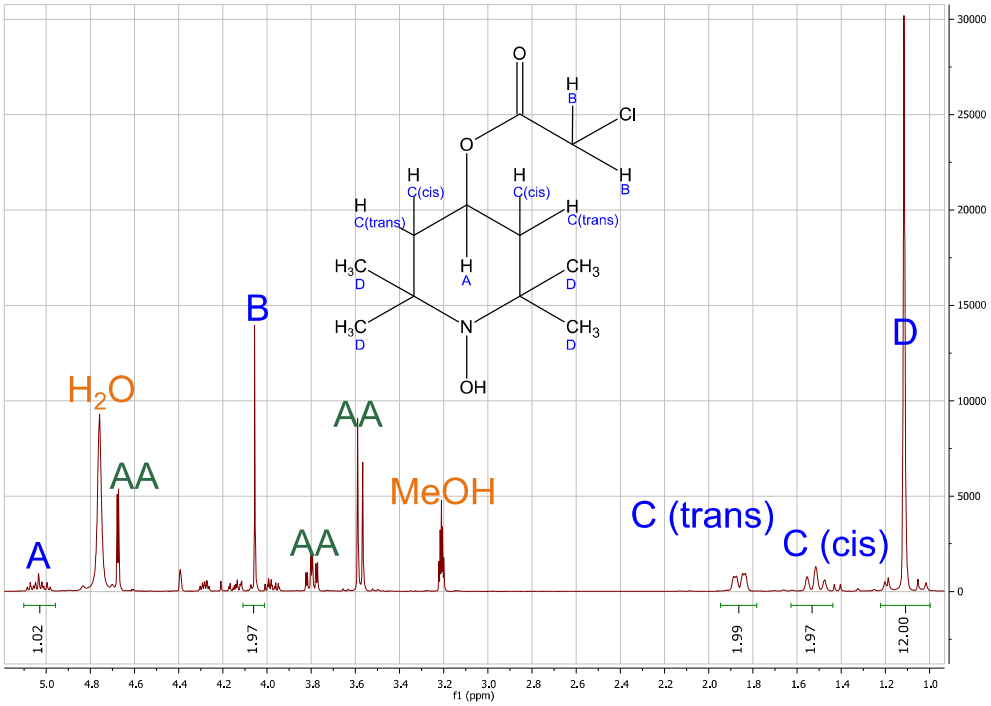

Figure 46: ^{1}H-NMR of the first step product of HTMIM BETI synthesis in MeOH-d_4.

The next synthesis step consisted of the addition of 1-methylimidazole in acetonitrile, which resulted in a positively charged imidazolium ring and chloride as the corresponding anion. As

last step, an ionic exchange has been carried out in water with Li BETI to precipitate LiCl and create HTMIM BETI. Figure 47 shows its ^{1}H-NMR in DMSO-d_6 with every proton detected, just H_D lies under a broad signal, which might be assigned to some residue water, and therefore has a too high integral.
Nevertheless, its chemical shift and its multiplet is the same as in HT-chloroacetate (cf. Figure 46) leading to a clear assignment of the signal to proton H_D. The corresponding ^{19}F-NMR spectrum can be found in the appendix, Figure 79.

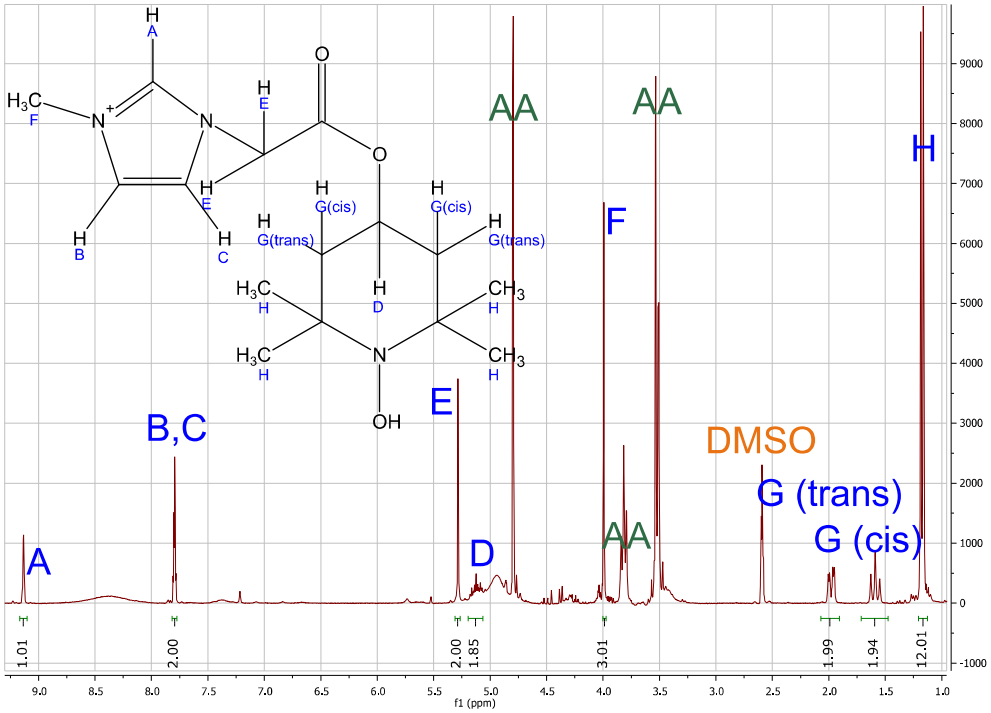

Figure 47: ^{1}H-NMR of the second step product of HTMIM BETI synthesis in DMSO-d_6.

HTMIM BETI has been immobilized in C6MIM and C12MIM BETI afterwards, due to their strong performance with MT, with the same amount of active species (10 μmol per electrode) and investigated according to the protocol introduced in chapter 5. Figure 48 presents the CVs in the HMF oxidation potential range ((a), (d)), over a broad potential range ((b), (e)) as well as the corresponding EIS spectra ((c), (f)). There seems to be the potential of HMF oxidation in C6MIM BETI as the current density rises at 1.25 V vs. RHE with the addition of HMF (orange) in comparison to the CV without HMF present (blue), which is also observable in the Delta branch (green) in Figure 48 (a). The opposite is presented by HTMIM BETI in C12MIM BETI as the addition of HMF leads to a decrease in current density and a disappearance of the TEMPO signals over the broad potential range in Figure 48 (e). Both EIS measurements do not present any hint towards a possible HMF oxidation, as they are both similar independently of HMF being present (orange) or not (blue). Due to the fact that HTMIM BETI in C12MIM BETI performed worse in the CVs with HMF present, only HTMIM BETI in C6MIM BETI is further investigated in electrolysis.
Figure 49 illustrates the electrolysis results of before-mentioned SILP combination at 1.8 and 2 V as well as the one of MT in C6MIM BETI for comparison reasons. Similar to HT and its derivatives HTMIM BETI does show minor activity towards HMF oxidation with a yield and *FE* towards FDCA of 8 and 10 % at the different potentials, respectively. Conclusively, the production rate is low with only 0.05 and 0.06 $mmol_{FDCA}\ s^{-1}\ mmol_{cat}^{-1}$, respectively, and the overall loss is higher with rising potential at 29 and 43 %, respectively.

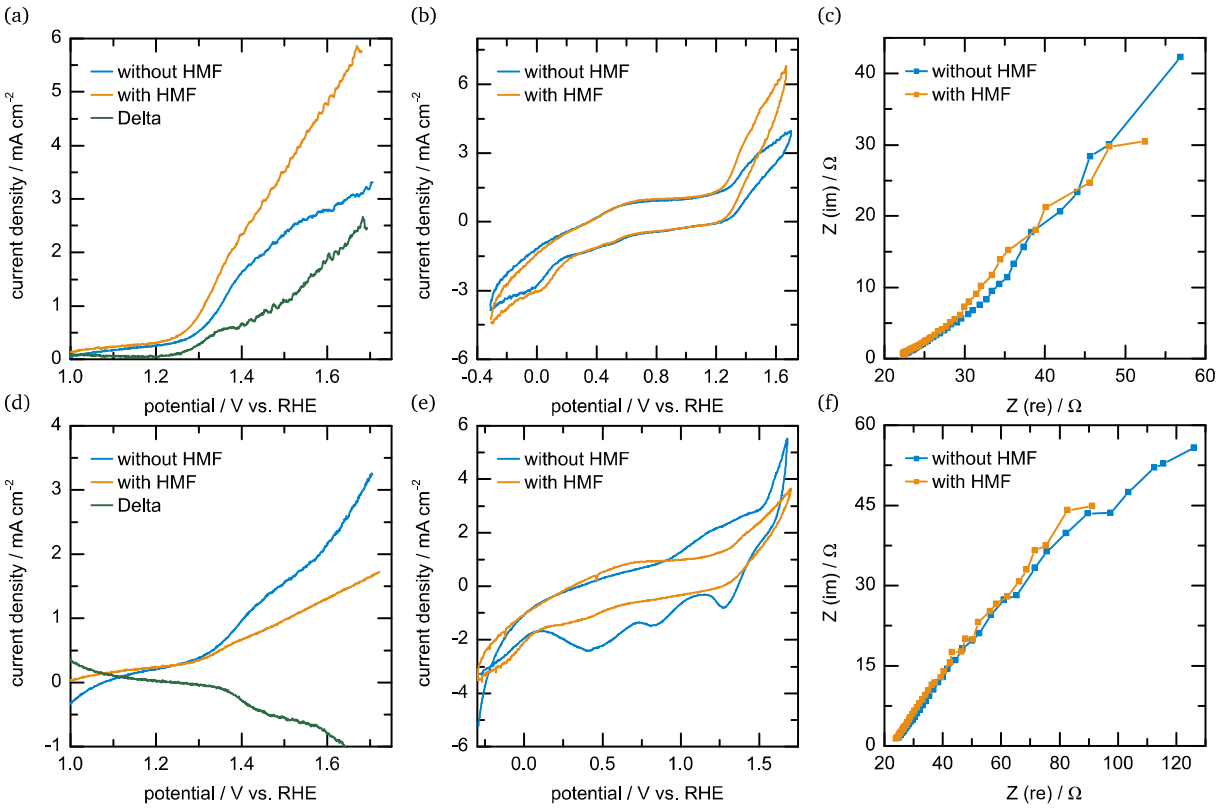

Figure 48: CVs at the HMF oxidation potential range (1.0 – 1.75 V vs. RHE) (a, d) and at a broad potential range (-0.3 – 1.75 V vs. RHE) (b, e) of HTMIM BETI in C6MIM BETI (a, b) and in C12MIM BETI (d, e) on MPL 39 BB without (blue), with 5 mM HMF (orange) and their difference (green) in 0.1 M KOH vs. Hg/HgO with Pt as CE. EIS measurements of HTMIM BETI in C6MIM BETI (c) and in C12MIM BETI (f) on MPL 39 BB without (blue) and with 5 mM HMF (orange) in 0.1 M KOH vs. Hg/HgO with Pt as CE.

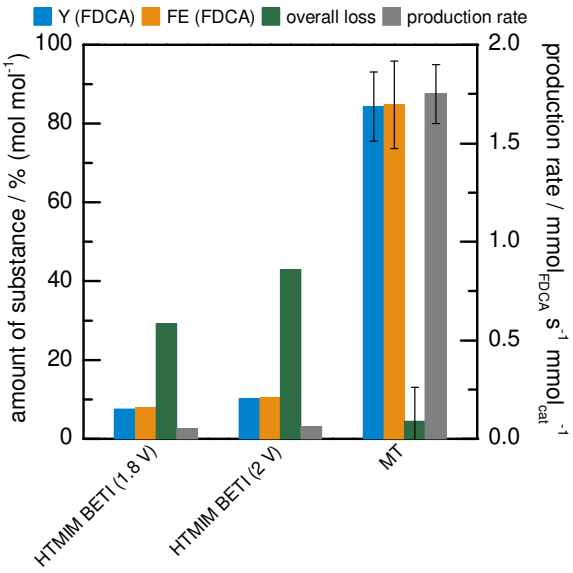

Figure 49: Yield and faradaic efficiency towards FDCA (*Y*(FDCA) (blue) and *FE*(FDCA) (orange), respectively) as well as overall loss (green) and production rate (grey) for complete HMF electrolysis (5 mM) of HTMIM BETI in C6MIM BETI on MPL 39 BB at 1.8 and 2 V as well as MT in C6MIM BETI as comparison on MPL 39 BB in 0.1 M KOH vs. Pt at 30 °C and 600 rpm in a divided cell.

Comparing these results with the ones of HT and its derivatives in chapter 6.4.4, leads to the conclusion that HT as origin just shows minor activity towards HMF oxidation independently of using itself or its derivatives. Thus, ATMIM BETI is also synthesized and investigated regarding HMF oxidation as AT and its derivatives showed more promising results in chapter 6.4.5.

6.6.2. ATMIM BETI

AT-chloroacetate has been synthesized in the same way as HT-chloroacetate besides not using DMAP as esterification catalyst. The ^{1}H-NMR of the first step product, AT-chloroacetate, in DMSO-d_6 is presented in Figure 50, in which all expected signals can be detected, just the one of H_A has a too low integral of 0.87. ATMIM BETI has been further processed by dissolving it in isopropyl alcohol, dichloromethane as well as acetone and separating the solid residue each time, before evaporating the excess solvent, due to impurities in its ^{1}H-NMR spectra. The spectrum of the final product ATMIM BETI is presented in Figure 51 also with every expected signal detected. Similar to HTMIM BETI in Figure 47, H_D lies under a broader signal, but chemical shift and its multiplet in comparison to the one of AT-chloroacetate assign the signal to this specific proton. The corresponding ^{19}F-NMR spectrum can be found in the appendix, Figure 80.

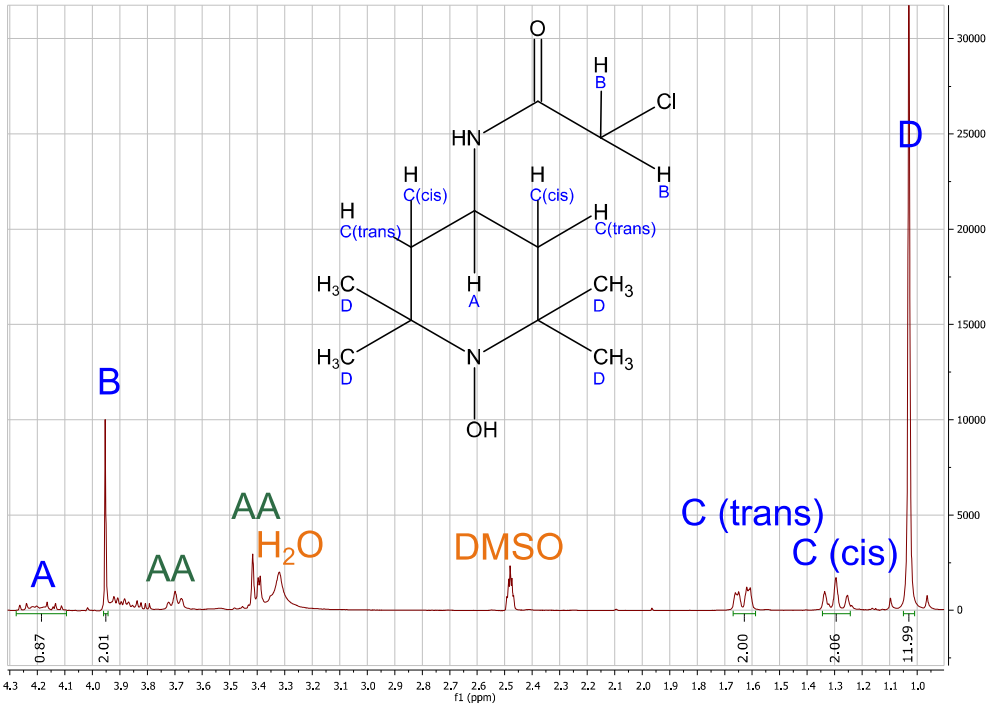

Figure 50: ^{1}H-NMR of the first step product of ATMIM BETI synthesis in DMSO-d_6.

Afterwards, ATMIM BETI has also been immobilized in C6MIM and C12MIM BETI, in the latter one before and after the further purification process for comparison. Furthermore, a variation of the ratio between ATMIM BETI and C12MIM BETI should provide insight if TEMPO covalently connected to IL could be used solely as SILP phase without any additional IL.

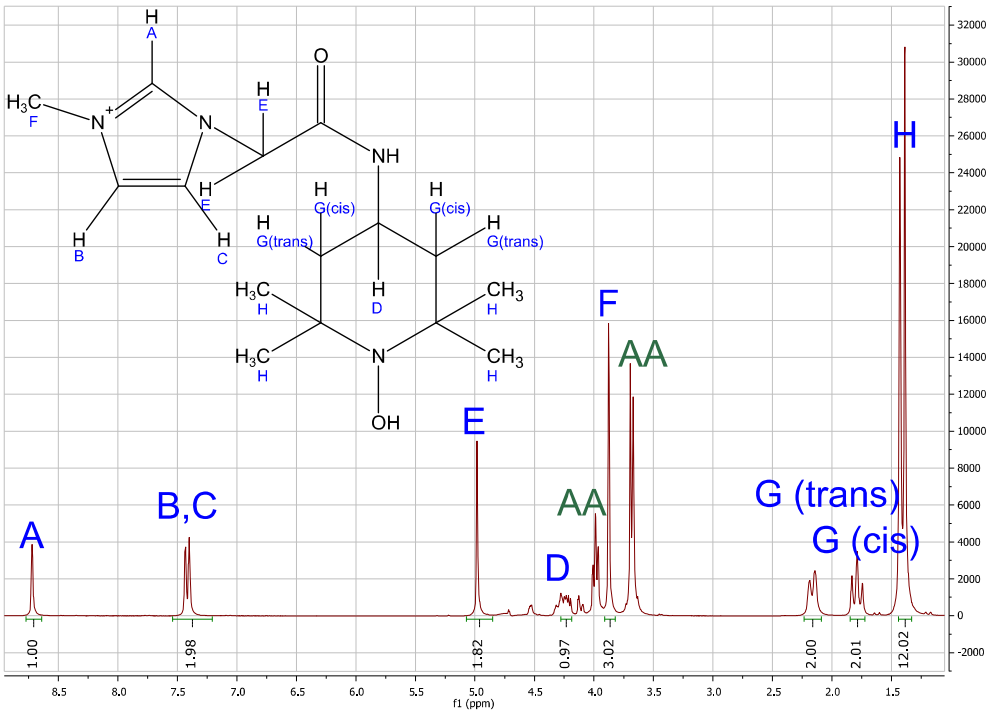

Figure 51: ^{1}H-NMR of the second step product of ATMIM BETI synthesis in DMSO-d$_6$.

Figure 52 (a), (d) and (g) exhibit the CV and EIS results of ATMIM BETI in C6MIM BETI, in which a definite increase in current density can be observed at 1.3 V vs. RHE after adding 5 mM HMF (orange) that also leads to a rise in the delta current density branch (green). Additionally, the behavior of this SILP combination at lower potentials results in the whole MPL being covered with IL again as no activity is observable, cf. Figure 33. The EIS spectrum surmises a semicircle emerging if HMF is added to the electrolyte (orange) in comparison to the one without (blue). In comparison, the behavior of ATMIM BETI before further purification in C12MIM BETI is similar to the one in C6MIM BETI without reaching as high current densities and exhibiting a higher impedance, as seen in Figure 52 (b), (e) and (h). The molar ratio of ATMIM BETI after further purification and C12MIM BETI has been varied: 1:2 is the ratio usually used in ink preparations in this work, so the molar amount of the IL is decreased to create ratios of 1:1, 2:1 and 3:0, which is just ATMIM BETI without any IL. Furthermore, the molar amount of TEMPO species investigated in measurements is kept constant at 10 μmol per electrode for better comparison. Figure 52 (c) presents the delta current densities of the before-mentioned ratios and the pure ATMIM BETI (3:0) exhibits the lowest onset at 1.2 V vs. RHE, while 2:1 and 1:1 onset at 1.3 V vs. RHE, as 1:1 reaches the highest current densities, and 1:2 at 1.4 V vs. RHE with the latter one reaching the lowest current densities. In the broad potential range illustrated in Figure 52 (f), in which the CVs with HMF are depicted, it is observable that the 3:0 ratio is not able to cover the whole MPL as the rising current density at low potentials indicate, cf. Figure 33. Every other ratio combination cover the whole MPL area and suppress this activity. Additionally, the 1:1 ratio reaches the highest current densities, while 1:2 reaches the lowest, which is coherent with the delta current densities in Figure 52 (c). The EIS spectra with HMF in Figure 52 (i) exhibit a developing semicircle for 1:1 and 2:1, which hints to the HMF oxidation, while the overall impedance is lowest for 3:0 and highest with the biggest solution resistance for 1:2. Concluding these results, every ATMIM BETI/IL combination seems to be active towards HMF oxidation and is therefore investigated, additionally regarding their reusability. Furthermore, the purification steps lead to a different behavior in CVs and EIS,

while the ratio of ATMIM BETI to C12MIM BETI influences the performance as well, wherefore only the purified one is used in further electrolysis runs.
Figure 53 (a) presents the electrolysis results of ATMIM BETI in C6MIM and C12MIM BETI (molar ratio of 1:2) as well as the ones of MT in the same ILs for comparison. In C6MIM BETI, the HMF oxidation performance of ATMIM is better than that of MT with a yield and *FE* towards FDCA of 93 % each in comparison to 80 and 81 %, respectively, while overall loss is as low as 2 and 4 %, respectively. Since ATMIM BETI is an IL additionally to being a TEMPO derivative, it exhibits a higher viscosity as MT, which is reflected in the production rate that is lower for ATMIM BETI with 1.11 $mmol_{FDCA}\ s^{-1}\ mmol_{cat}^{-1}$ than for MT with 1.65 $mmol_{FDCA}\ s^{-1}\ mmol_{cat}^{-1}$.

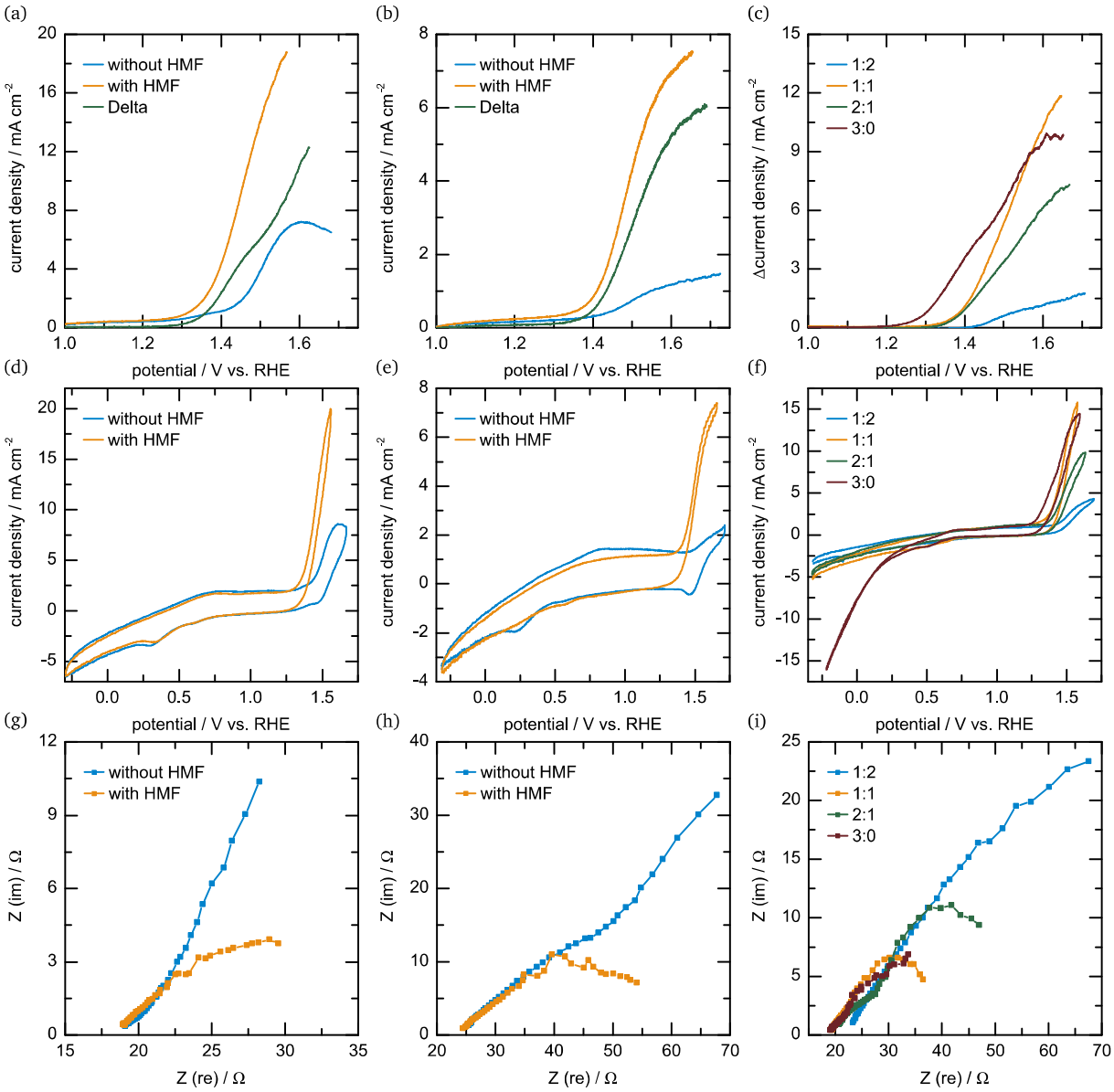

Figure 52: CVs at the HMF oxidation potential range (1.0 – 1.75 V vs. RHE) (a, b) and at a broad potential range (-0.3 – 1.75 V vs. RHE) (d, e) of ATMIM BETI in C6MIM BETI (a, d) and in C12MIM BETI before further purification (b, e) on MPL 39 BB without (blue), with 5 mM HMF (orange) and their difference (green) in 0.1 M KOH vs. Hg/HgO with Pt as CE. (c) Delta CVs of ATMIM BETI after further purification in C12MIM BETI on MPL 39 BB at different molar ratios of ATMIM BETI to IL as well as their CVs at a broad potential range (-0.3 – 1.75 V vs. RHE) with 5 mM HMF (f). EIS measurements of ATMIM BETI in C6MIM BETI (g) and in C12MIM BETI before further purification (h) on MPL 39 BB without (blue) and with 5 mM HMF (orange) in 0.1 M KOH vs. Hg/HgO with Pt as CE. (i) EIS measurements of ATMIM BETI after further purification in C12MIM BETI on MPL 39 BB with 5 mM HMF in 0.1 M KOH vs. Hg/HgO with Pt as CE at different molar ATMIM BETI to C12MIM BETI ratios.

The same phenomenon is recognized in C12MIM BETI with 0.67 and 1.03 $mmol_{FDCA}\ s^{-1}\ mmol_{cat}^{-1}$, respectively, while no overall loss occurred with both SILP combinations. Yield and *FE* towards FDCA of 99 % each for MT is not reached by ATMIM BETI, even if the 93 and 94 %, respectively, are comparable to the one in C6MIM BETI. Since both combinations exhibit high HMF oxidation abilities, they are investigated regarding their stability, while in C12MIM BETI all molar ratio combinations are examined as well.
The electrolysis results of ATMIM BETI in C6MIM BETI including its reuses is presented in Figure 53 (b), which exhibits a drop of activity in the second run to 67 % yield and *FE* towards FDCA and 0.76 $mmol_{FDCA}\ s^{-1}\ mmol_{cat}^{-1}$ production rate. Interestingly, overall loss drops from 2 to 0 %, which rises again to 42 % in the third run though, in which no activity at all is left. The same phenomenon can be observed at every ATMIM BETI/IL ratio combination in Figure 53 (c) – (f), even if a lower amount of IL leads to a smaller drop in activity after the first run. Yield and *FE* towards FDCA drop to 6 % each as does the production rate to 0.04 $mmol_{FDCA}\ s^{-1}\ mmol_{cat}^{-1}$, while overall loss rises to 23 % for the 1:2 ratio in the second run, presented in Figure 53 (c). After another run, overall loss increases again to 35 %, yield and *FE* towards FDCA decrease to 3 % left and production rate does as well to 0.02 $mmol_{FDCA}\ s^{-1}\ mmol_{cat}^{-1}$.

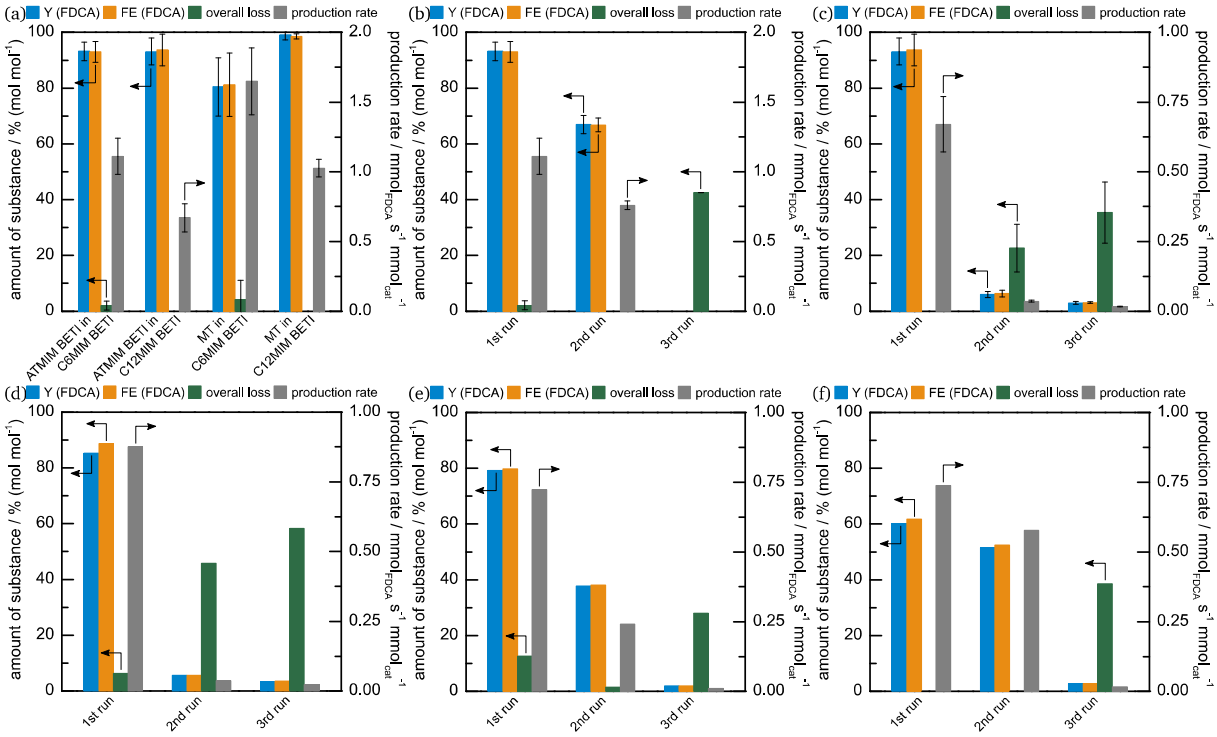

Figure 53: Yield and faradaic efficiency towards FDCA (*Y*(FDCA) (blue) and *FE*(FDCA) (orange), respectively) as well as overall loss (green) and production rate (grey) for complete HMF electrolysis (5 mM) in 0.1 M KOH vs. Pt at 30 °C and 600 rpm in a divided cell. (a) ATMIM BETI in C6MIM and C12MIM BETI (1:2) on MPL 39 BB at 2.2 and 2.0 V, respectively, as well as MT in the same ILs on MPL 39 BB as comparison. (b – f) ATMIM BETI in C6MIM BETI on MPL 39 BB at 2.2 V (b) including two reuses of the same electrode as well as a molar ratio of 1:2 (c), 1:1 (d), 2:1 (e) and 3:0 (f) of ATMIM BETI to C12MIM BETI on MPL 39 BB including two reuses at 2.0 V each.

The first run of the 1:1 ratio exhibits lower activity compared to the 1:2 ratio with a yield and *FE* towards FDCA of 85 and 89 %, respectively, a production rate of 0.88 $mmol_{FDCA}\ s^{-1}\ mmol_{cat}^{-1}$ and an overall loss of 6 %, as seen in Figure 53 (d). Further decreasing the amount of C12MIM BETI leads to even lower activities towards HMF oxidation with yields and FEs towards FDCA of 79 and 80 %, respectively, for 2:1 as well as 60 and 62 %, respectively, for 3:0. The second

run of the 1:1 ratio results in nearly no activity left with yield and *FE* towards FDCA of 6 % each, an as low production rate of 0.04 $mmol_{FDCA}\ s^{-1}\ mmol_{cat}^{-1}$ and an overall loss of 46 %. Similar to the 1:2 ratio, the third run leads to an even lower activity with an overall loss of 58 %, a production rate of 0.02 $mmol_{FDCA}\ s^{-1}\ mmol_{cat}^{-1}$ as well as only 3 % yield and *FE* towards FDCA. In comparison to 1:2 and 1:1, the ratios of 2:1 and 3:0 exhibit a higher activity left in the second run, as seen in Figure 53 (e) and (f), respectively. 2:1 exhibits a production rate of 0.72 $mmol_{FDCA}\ s^{-1}\ mmol_{cat}^{-1}$ and an overall loss of 12 % in the first run, while the latter drops to 2 % in the second run. As does the production rate with only 0.24 $mmol_{FDCA}\ s^{-1}\ mmol_{cat}^{-1}$ as well as the yield and *FE* towards FDCA with 38 % each, which is still around half the amount than in the first run. In the next electrolysis, activity is ultimately lost with only 2 % of yield and *FE* towards FDCA left, a production rate of 0.01 $mmol_{FDCA}\ s^{-1}\ mmol_{cat}^{-1}$ and an overall loss of 28 %. Pure ATMIM BETI presents a production rate of 0.74 $mmol_{FDCA}\ s^{-1}\ mmol_{cat}^{-1}$ and no overall loss at all in its first use. After another electrolysis, 80 % of the activity still exists with still no overall loss, a production rate of 0.58 $mmol_{FDCA}\ s^{-1}\ mmol_{cat}^{-1}$ and a yield and *FE* towards FDCA of 52 % each. As before with the 2:1 ratio, pure ATMIM BETI ultimately loses all activity in the third electrolysis with just 3 % yield and *FE* towards FDCA, a production rate of 0.02 $mmol_{FDCA}\ s^{-1}\ mmol_{cat}^{-1}$ left and an overall loss of 39 %.
As a perception of these results, the presence of ILs seems to have an influence in the activity and selectivity pattern of the used TEMPO species as the different molar ratios exposed as well as an influence on the suppression of MPL activity. Their ability to immobilize TEMPO as homogeneous catalyst leads to higher yields and FEs as observed before, cf. Figure 22 (c) compared to Figure 37. On the other hand, the used ILs seem to get extracted into the electrolyte over multiple usage and therefore seem to extract TEMPO species with them as can be seen in Figure 53, while the activity of pure ATMIM BETI stayed 80 % intact after the first electrolysis. It can also be observed independently of the used IL as Figure 87 shows the loss of IL and ATMIM BETI into the electrolyte after 12 hours of CA and after another 12 hours with the same electrode but a fresh electrolyte (cf. Figure 38).
Therefore, other carbon materials, which might enhance the interaction between IL, TEMPO and the support and furthermore might increase stability of these systems, are investigated as porous support for the inks

6.7. Commercial carbon black as support material

Vulcan as a commercial carbon black is used as porous support material and impregnated with ink by solvent evaporation, which leads to a complete intrusion of IL into the pores.[286] Afterwards, the impregnated carbon is applied onto the MPL as electrode using PTFE as binding agent. Due to the impregnation of around 20 wt-% IL of the carbon, the usually used 10 μmol of TEMPO species are immobilized in around 20 mg of carbon. Consequently, the electrode pictured in Figure 54 is completely covered after just 10 mg of carbon and therefore only half the amount of the usually used amount of TEMPO species (5 μmol) is immobilized on the electrode.

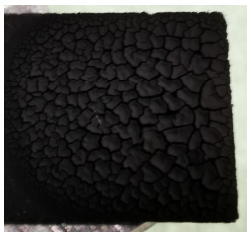

Figure 54: MT in C4MIM BETI on Vulcan on MPL 39 BB.

At first, pure Vulcan applied on the MPL is investigated via CV and EIS in Figure 55. Inspecting the CV over the broad potential range, it shows the same activity as MPL at small potentials below 0.6 V vs. RHE, which was expectable as MPL consists of Vulcan. The behavior at HMF oxidation potential range is different from that of MPL in Figure 33, as it exhibits a broad signal at 0.8 to 1.6 V vs. RHE (blue) independently of HMF being present (orange). Long time CVs of MPL demonstrated an increase in current density with the amount of CVs measured, cf. Figure 34, which is why the difference between the addition of HMF and before (green) might not hint at a potential HMF oxidation rather than an oxidation of Vulcan itself. The EIS spectra strengthen the second perception as the curve progression is similar with (orange) and without HMF.

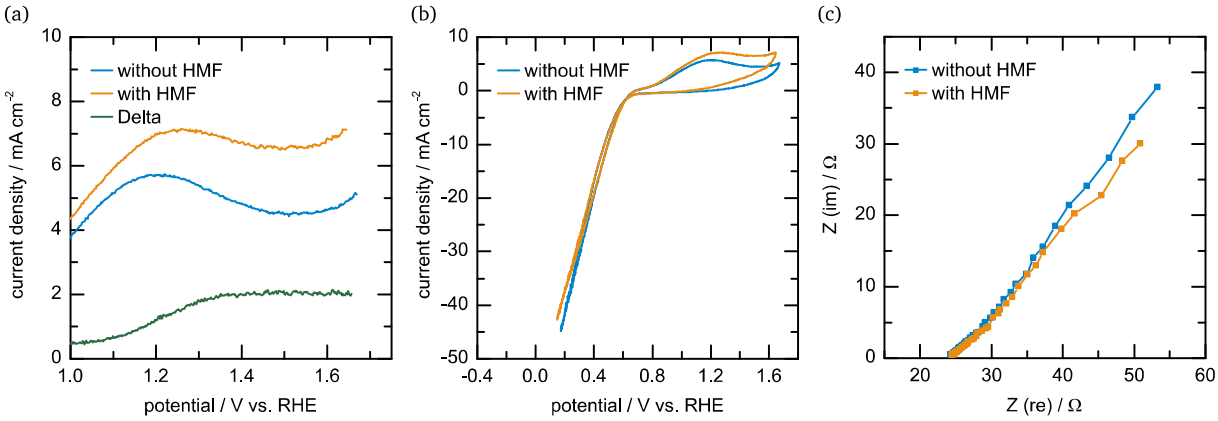

Figure 55: CVs at the HMF oxidation potential range (1.0 – 1.75 V vs. RHE) (a) and at a broad potential range (-0.3 – 1.75 V vs. RHE) (b) of pure Vulcan on MPL 39 BB without (blue), with 5 mM HMF (orange) and their difference (green) in 0.1 M KOH vs. Hg/HgO with Pt as CE. (c) EIS measurements of pure Vulcan on MPL 39 BB without (blue) and with 5 mM HMF (orange) in 0.1 M KOH vs. Hg/HgO with Pt as CE.

MT as the smallest TEMPO derivative with a high activity towards HMF oxidation has been immobilized in C4MIM BETI as the imidazolium-based IL with the shortest chain, in which MT has exhibited a good HMF oxidation performance, cf. Figure 37 (b). The CVs present a different behavior at HMF oxidation potential range after HMF is added (orange) in Figure 56 (a) and (b) as the ones of pure Vulcan, because the shape of the curve differs from the one without HMF present (blue). This results in a Delta curve (green) that is positive from 1.0 to 1.5 V vs. RHE. The behavior at lower potentials does not change as the IL is supposed to be inside the pores and does not cover the surface of the Vulcan as it did on the MPL. In Figure 56 (c), the EIS measurement with (orange) and without HMF (blue) are congruent, which might hint that no HMF oxidation will be observable in electrolysis. Figure 56 (d) underlines this hypothesis as MT in C4MIM BETI on Vulcan is compared to the same ink on MPL and pure MPL and shows similar results than the latter one. A conversion of 32 % with a yield and *FE* towards FDCA of 2 % each and an overall loss of 19 % is slightly better than pure MPL performed with 28, 1, 2 and 26 %, respectively. Therefore, the selectivity pattern is

comparable to that of pure MPL, which concludes that all reaction takes place at Vulcan probably on the surface and not in the pores, in which MT and C4MIM BETI would have produced FDCA.
Thus, Vulcan as porous carbon support is not suited as it exhibits an own activity towards HMF oxidation, which does not result in the desired product FDCA. Therefore, another carbon is investigated as porous support for SILP inks.

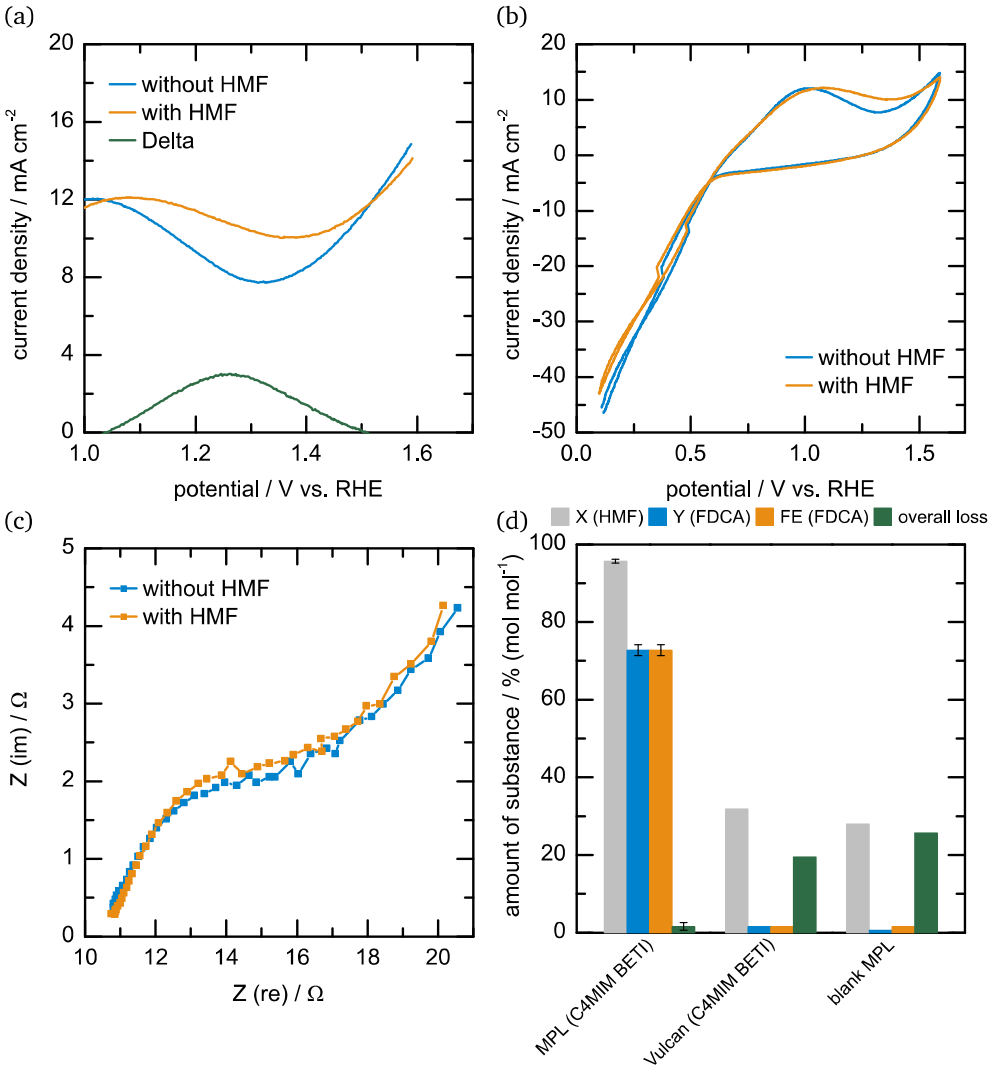

Figure 56: CVs at the HMF oxidation potential range (1.0 – 1.75 V vs. RHE) (a) and at a broad potential range (-0.3 – 1.75 V vs. RHE) (b) of MT in C4MIM BETI on Vulcan on MPL 39 BB without (blue), with 5 mM HMF (orange) and their difference (green) in 0.1 M KOH vs. Hg/HgO with Pt as CE. (c) EIS measurements of MT in C4MIM BETI on Vulcan on MPL 39 BB without (blue) and with 5 mM HMF (orange) in 0.1 M KOH vs. Hg/HgO with Pt as CE. (d) Conversion (*X* HMF, light grey), yield and faradaic efficiency towards FDCA (*Y* (FDCA) (blue) and *FE* (FDCA) (orange), respectively) as well as overall loss (green) for complete HMF electrolysis (5 mM) of MT in C4MIM BETI on Vulcan on MPL 39 BB in 0.1 M KOH at 1.8 V vs. Pt at 30 °C and 600 rpm in a divided cell with the same ink without Vulcan and blank MPL as comparison.

6.8. Polymer derived carbon as porous carbon support

As another carbon support a polymer derived carbon (PDC) has been synthesized by HEROLD ET AL.: 1,3,5-trihidroxy benzene and formaldehyde have been polymerized, before the product is pyrolyzed at 850 °C in presence of the triblock copolymer soft template Pluronic F127, which results in a micro/mesoporous carbon material.[320] All SILP systems on PDC have been prepared

as the ones using Vulcan as porous support material before. Since the loading of IL (~ 20 wt-%) and therefore TEMPO is the same as before on Vulcan, only 10 mg of PDC can be applied onto the MPL until it is fully covered as seen in Figure 57, even if only 5 μmol of TEMPO species is immobilized in total.

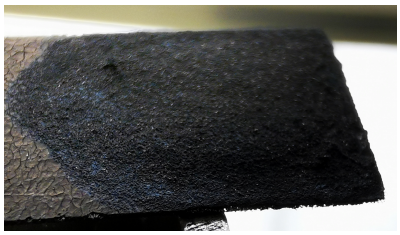

Figure 57: MT in C4MIM BETI on PDC on MPL 39 BB.

At first, pure PDC has been electrochemically examined using CV and EIS as seen in Figure 58. At potentials below 0.5 V vs. RHE, it behaves similar to Vulcan as the current density rises, while it reveals just a slight increase in current density at higher potentials when HMF is added (orange) in comparison to the CV without HMF (blue). This results in a Delta curve (green) that is slightly above zero, which fits to the EIS results, in which the curve progressions without (blue) and with HMF (orange) are congruent, although higher impedances are reached without HMF.

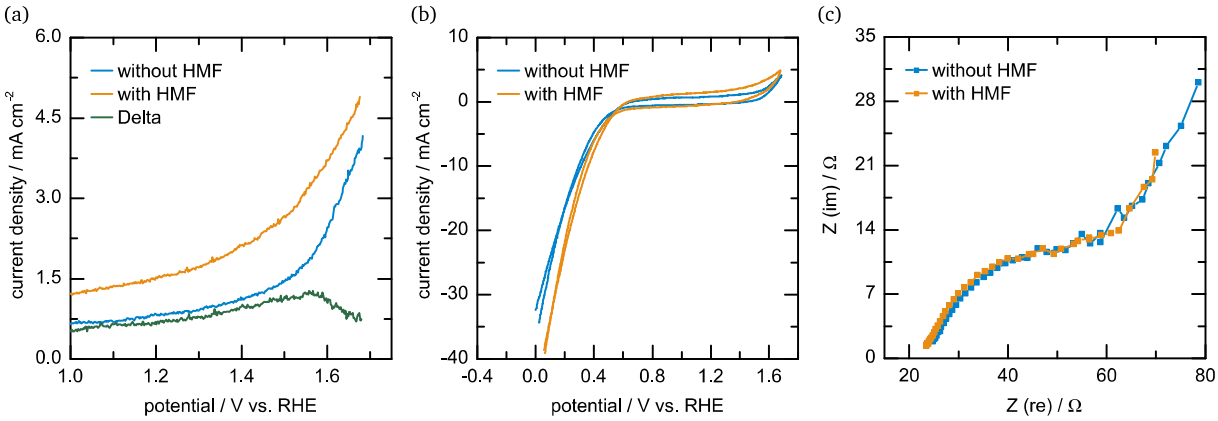

Figure 58: CVs at the HMF oxidation potential range (1.0 – 1.75 V vs. RHE) (a) and at a broad potential range (-0.3 – 1.75 V vs. RHE) (b) of pure PDC on MPL 39 BB without (blue), with 5 mM HMF (orange) and their difference (green) in 0.1 M KOH vs. Hg/HgO with Pt as CE. (c) EIS measurements of pure Vulcan on MPL 39 BB without (blue) and with 5 mM HMF (orange) in 0.1 M KOH vs. Hg/HgO with Pt as CE.

6.8.1. Methoxy TEMPO immobilized onto polymer derived carbon

Inks including MT in C4MIM BETI again as well as in C6MIM NTf_2 have been prepared and immobilized onto PDC. The CVs and EIS measurements of MT in C4MIM BETI are presented in Figure 59 (a) – (c), in which a similar behavior is observable as pure PDC exhibited in Figure 58, even if higher current densities are reached. The addition of HMF (orange) leads to a different curve progression than without (blue) at slightly higher current densities, which is also exhibited by the Delta curve (green) that has a positive value over the whole HMF oxidation potential range without a clear signal. Additionally, the EIS spectra without (blue) and with HMF (orange) indicate no clear HMF oxidation activity as both curves seem to be congruent. The CVs and EIS measurements of MT in C6MIM NTf_2 look similar to the ones in C4MIM BETI, cf. Figure 86. In Figure 59 (d), the electrolysis results of MT in C6MIM NTf_2 and in C4MIM BETI

on MPL and on PDC are presented as well as the one of pure MPL. The conversion of 52 and 38 % of MT in C6MIM NTf_2 and C4MIM BETI on PDC, respectively, is higher than the one of MT in C4MIM BETI on Vulcan. Both SILP combinations exhibit a yield and *FE* towards FDCA of 5 % each and 8 and 9 %, respectively, which is both more than pure MPL produces (1 and 2 %, respectively). Additionally, the overall loss of 15 and 14 %, respectively, is lower than the one of pure MPL with 26 %, which again differentiates the SILP combinations on PDC from the pure MPL/Vulcan. In comparison to the electrolysis results on MPL, both IL/TEMPO combinations on PDC underperform. Therefore, an AT derivative immobilized in IL and on PDC is also investigated to examine if the TEMPO species is relevant regarding HMF oxidation activity.

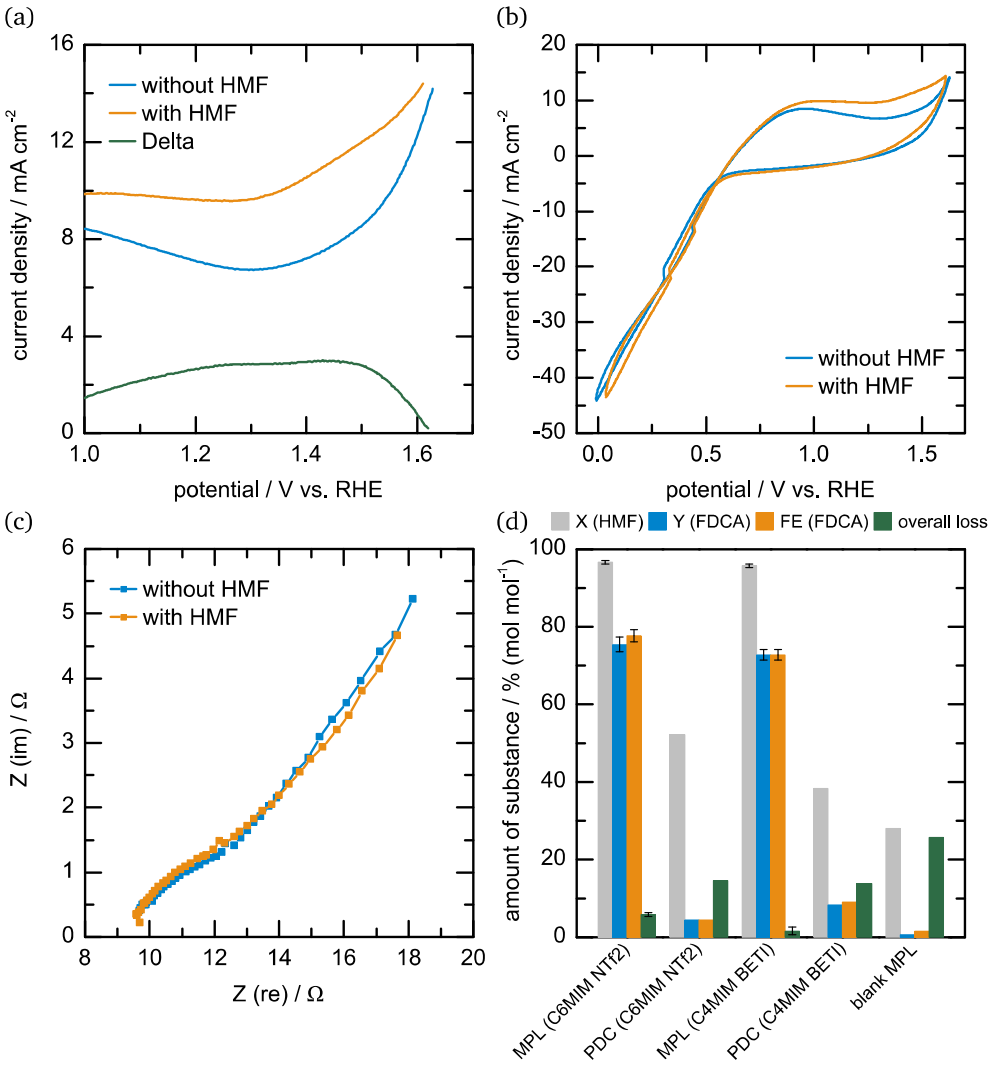

Figure 59: CVs at the HMF oxidation potential range (1.0 – 1.75 V vs. RHE) (a) and at a broad potential range (-0.3 – 1.75 V vs. RHE) (b) of MT in C4MIM BETI on PDC on MPL 39 BB without (blue), with 5 mM HMF (orange) and their difference (green) in 0.1 M KOH vs. Hg/HgO with Pt as CE. (c) EIS measurements of MT in C4MIM BETI on PDC on MPL 39 BB without (blue) and with 5 mM HMF (orange) in 0.1 M KOH vs. Hg/HgO with Pt as CE. (d) Conversion (*X* HMF, light grey), yield and faradaic efficiency towards FDCA (*Y* (FDCA) (blue) and *FE* (FDCA) (orange), respectively) as well as overall loss (green) for complete HMF electrolysis (5 mM) of MT in C4MIM BETI and C6MIM NTf_2 on PDC on MPL 39 BB in 0.1 M KOH at 1.8 V each vs. Pt at 30 °C and 600 rpm in a divided cell with the same inks without PDC ("MPL", 1.95 and 1.8 V, respectively) and blank MPL as comparison.

6.8.2. Amino TEMPO derivatives immobilized onto polymer derived carbon

In addition, C14-AT in C6MIM BETI has been immobilized onto PDC. Figure 60 (a) – (c) exhibits the CVs and EIS measurements, in which a similar behavior to MT on PDC can be observed. Firstly, the EIS measurement has to be taken into consideration, because the onset of the graph with HMF (orange) starts at 5 Ω more than without (blue). Therefore, the solution resistance seems to be higher with HMF present, leading to a shift of the CVs due to the potential drop correction (equation (1)). Nevertheless, the CV with HMF (orange) shows slightly higher current densities than the one without (blue), which can also be seen in the Delta curve (green), while the behavior at low potentials is the same as of pure PDC or MT on PDC. The electrolysis results are exhibited in Figure 60 (d), in which also the results of C14-AT in C6MIM BETI on MPL and of blank MPL are depicted for comparison. Additionally, the yield of FFCA (*Y* (FFCA)) is indicated here, since it is the main product of this electrolysis, as well as an electrolysis with three times the amount of charge as usual (39.09 C; "3x Q"). In comparison to the electrolysis without PDC, the same conversion of 94 % can only be reached with 3x Q (96 %), while only 35 % are converted under normal reaction conditions. Nearly the same can be observed for the yield of FDCA, which is 30 % on MPL and 7 or 25 % after 13.03 or 39.09 C, respectively. Comparing the *FE* leads to another result as the yield was only achieved with three times the amount charge and therefore electrons, which leads to a third of the yield and 8 % of *FE* for the result of 3x Q. It is comparable to the *FE* of the usual induced charge with 6 % but both are smaller than the *FE* on MPL with 30 %. As mentioned before, FFCA has been detected as the main product for C14-AT in C6MIM BETI as its yield is as high as 48, 26 and 71 % for the electrolysis on MPL, 1x Q and 3x Q, respectively. On the other hand, the PDC-based system does not contribute to any side reaction, as no loss is detected independent of the amount of charge induced to the system, whereas 16 % could be detected after the electrolysis on MPL. Thus, it seems that this catalyst is able to oxidize HMF fast enough to HMFCA as no loss is detected and afterwards to FFCA as well but the last step to FDCA is hindered.
Concluding these results, IL/TEMPO combinations immobilized onto PDC could enhance the reactivity towards HMF oxidation compared to commercial carbon black as substrate. Unfortunately, the HMF oxidation capability was lower than on pure MPL, so the possibility of these TEMPO/IL combinations could not be exploited effectively enough. As FFCA is the main product and using three times the applied charge does not shift the selectivity pattern towards the intended product FDCA, these SILP catalysts cannot be used for the desired reaction.

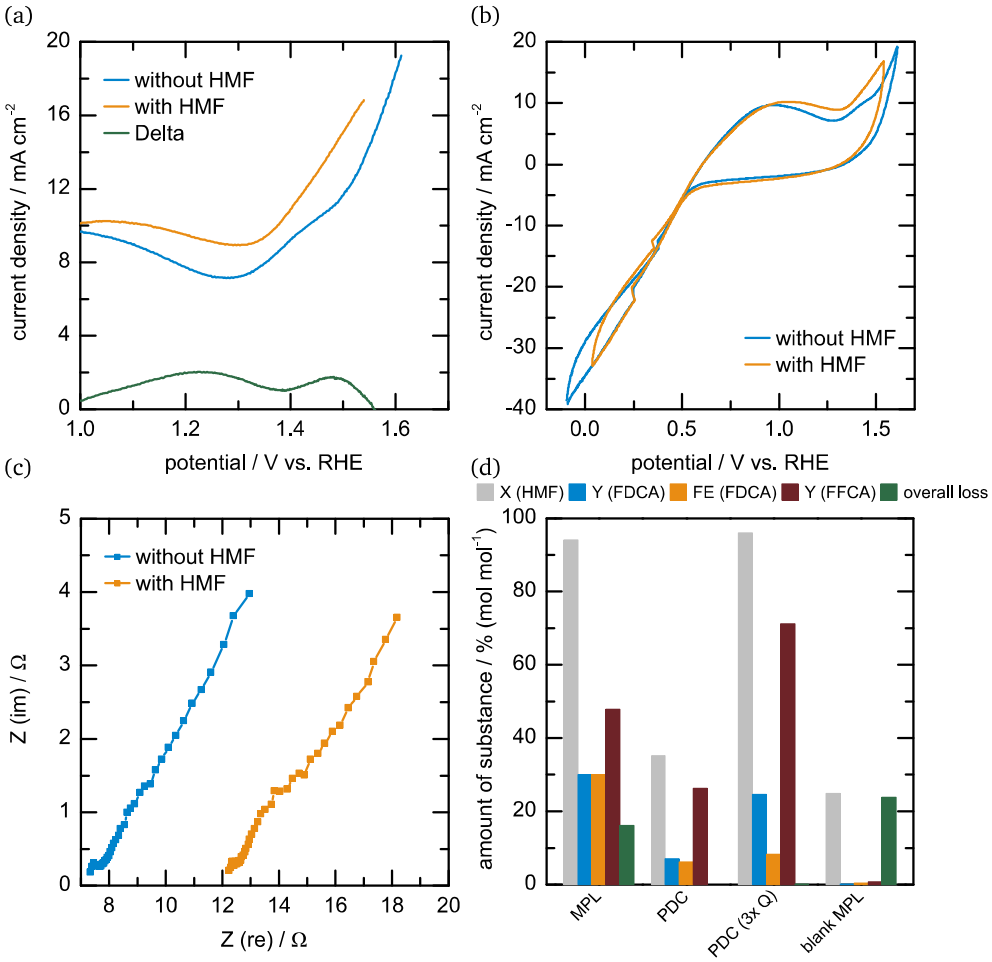

Figure 60: CVs at the HMF oxidation potential range (1.0 – 1.75 V vs. RHE) (a) and at a broad potential range (-0.3 – 1.75 V vs. RHE) (b) of C14-AT in C6MIM BETI on PDC on MPL 39 BB without (blue), with 5 mM HMF (orange) and their difference (green) in 0.1 M KOH vs. Hg/HgO with Pt as CE. (c) EIS measurements of C14-AT in C6MIM BETI on PDC on MPL 39 BB without (blue) and with 5 mM HMF (orange) in 0.1 M KOH vs. Hg/HgO with Pt as CE. (d) Conversion (*X* HMF, light grey), yield and faradaic efficiency towards FDCA (*Y* (FDCA) (blue) and *FE* (FDCA) (orange), respectively), yield towards FFCA (*Y* FFCA, dark red) as well as overall loss (green) for complete HMF electrolysis (5 mM) of C14-AT in C6MIM BETI on PDC on MPL 39 BB in 0.1 M KOH at 2.4 V vs. Pt at 30 °C and 600 rpm in a divided cell with the same ink without PDC ("MPL") (2.35 V), triple the amount of charge (39.09 C, "PDC (3x Q)") and blank MPL as comparison.

7 Conclusion

The present thesis focuses on the electrochemical oxidation of 5-hydroxymethylfurfural (HMF) using the supported ionic liquid phase (SILP) approach to upgrade water electrolysis. As introduced in the objectives and experimental approach, it divides itself into different sections, from which the most important ones are concluded subsequently.

Measurement protocol for electrochemical HMF oxidation

At first, a measurement protocol was developed, which allows the comparison between different catalytic systems regarding their HMF oxidation potential, starting with the stability of the involved molecules. Therefore, HMF, DFF, HMFCA, FFCA and FDCA have been dissolved separately in 0.01, 0.1, 1 and 3 M KOH solutions without applying any potential and their concentration were monitored over time using HPLC. HMFCA and FDCA did not show any signs of degradation, while HMF, DFF and FFCA degraded faster in more alkaline environment, which has to be kept in mind for the upcoming results. For the upcoming results, Cu-foam was used as an example catalyst. The aforementioned different alkaline solutions have been used for electrolysis to find the best electrolyte suited for the investigated catalyst system. Another aspect was the cell setup, in which the separation of anodic and cathodic chamber led to a 29 to 37 % higher yield and *FE* towards FDCA as well as 76 to 84 % less overall loss. Every following measurement was conducted using a divided cell. Next, BDD was found to be an inert but conductive electrode material, so measured activity can only stem from the applied catalyst. After Pt as CE material and the stirring rate at 600 rpm were set, the catalytic activity and selectivity could be tackled.
Therefore, the potential window with the highest HMF oxidation activity can be found in a three electrode setup by conducting CVs with and without HMF present and subtracting them from one another to get a “background subtraction” leaving a signal stemming from HMF oxidation. CA was performed at these potentials to get the overall cell voltage used for electrolysis in a two electrode setup. After electrolysis, HPLC is used to determine yield, faradaic efficiency and side product formation, which gives a hint about the selectivity pattern of measured catalyst. Furthermore, production rate is used as a new figure of merit to compare the activity of different catalysts by calculating the amount of produced product (FDCA) per time and per amount of catalyst.
This cell setup and measurement protocol was used for every catalytic system described in this work.

TEMPO as homogeneous catalyst for HMF oxidation

After implementing a protocol to determine HMF oxidation activity and selectivity of different catalytic systems, TEMPO could be evaluated as catalyst for aforementioned reaction.
At first, TEMPO was used as a classic homogeneous catalyst in reaction solution, which was changed to a phosphate buffer at pH 10 to assure the stability of TEMPO. Measurements in the three electrode setup indicated an HMF oxidation activity for TEMPO and even more for 4-methoxy-TEMPO (MT). The latter one was investigated in solution and on the MPL electrode leading to yields and *FEs* towards FCDA of 59 and 39 % as well as 63 and 40 %, respectively, while overall loss still reached 25 and 54 %, respectively. The production rate was around five times higher in solution. As these results indicated a fundamental activity towards HMF

oxidation, the next step was to immobilize TEMPO, 4-hydroxy-TEMPO-benzoate (TB), another TEMPO derivative, and MT in different ILs, in which the latter one had a radical impact on the performance. TEMPO itself and TB just converted HMF to FDCA in short chain ILs like C3MIM NTf_2, with poor yields towards FDCA of 21 and 4 %, respectively, and overall losses of 33 and 13 %, respectively. MT on the other hand reached his highest activity in these trials in C6 and C10MIM NTf_2 with yields and *FEs* towards FDCA of up to 57 %, while overall loss never exceeded 9 %. Another visible trend was the slower production rate with higher chain length as the viscosity of the IL grew.

TEMPO derivatives used as SILP catalyst on microporous carbon as support

Due to the aforementioned results, different TEMPO derivatives have been synthesized. These were tested as SILP catalysts and compared to commercial MT.

Synthesis of TEMPO derivatives and long chain ILs

Long chain ILs have been synthesized as well as further TEMPO derivatives. The recipe for long chain ILs followed an ionic exchange between a CnMIM halide and Li BETI, which resulted in CnMIM BETI with n = 6, 10, 12, 14. Every new IL could be confirmed successfully produced and dry via ^{1}H- and ^{19}F-NMR. The synthesized TEMPO derivatives had 4-hydroxy- (HT) or 4-amino-TEMPO as base material with acyl chlorides as their reaction partner. EDC and DMAP or just EDC were used to create the corresponding ester or amide named Cn-HT or Cn-AT, respectively, with n = 12, 14, 16, 18. These products were also confirmed successfully produced via ^{1}H-NMR by observing a chemical shift of the proton right next to the functional group after reaction, even if the radicals had to be scavenged by ascorbic acid first. Furthermore, ESR was used to verify the presence of radicals in the synthesized products and CVs to check for the usual transitions between the hydroxylamine, the aminoxyl radical and the oxoammonium cation, which could both be confirmed.
After the successful synthesis of these TEMPO derivatives, also pyrene-TEMPO (PT) was produced with the same procedure as all Cn-AT molecules and confirmed via ^{1}H-NMR and ESR. In a subsequent step, an approach to link TEMPO and IL was made by connecting HT and AT covalently to an imidazolium based cation using chloroacetic acid to build the corresponding ester or amide, respectively. Afterwards, 1-methylimidazole was added to create HTMIM Cl and ATMIM Cl before an ionic exchange with Li BETI once again led to the desired products HTMIM BETI and ATMIM BETI. These products werde confirmed by ^{1}H-, ^{19}F-NMR and ESR.

Activity of SILP catalysts using microporous carbon as support

Before using the SILP system, the microporous carbon support (MPL 39 BB) was once again investigated regarding its reactivity and a negligible to none could be found. Afterwards, pure ILs and pure HT and AT derivatives have been immobilized on MPL 39 BB, which resulted in poor performances from the HT derivatives reaching just 8 % as the highest yield towards FDCA and 29 % as the lowest overall loss, while C14- to C18-HT didn't even show any HMF oxidation activity. AT derivatives were more promising with only C18-AT showing no activity, yields towards FCDCA between 21 and 69 % and overall losses between 3 and 29 %. All ILs converted HMF from 29 to 66 % but none of them really produced FDCA with 3 % yield towards it as maximum as overall losses rose parallel to the conversion with 23 to 55 %.

Afterwards, MT was first tested with the new synthesized ILs and the results were promising as it could achieve a yield and *FE* towards FDCA of 99 % with no overall loss and a production rate of 1.03 $mmol_{FDCA}\ s^{-1}\ mmol_{cat}^{-1}$ in C12MIM BETI. Overall, yield and *FE* towards FDCA were never lower than 64 and 60 %, respectively, with the highest loss at 5 % and a production rate of 0.57 to 1.75 $mmol_{FDCA}\ s^{-1}\ mmol_{cat}^{-1}$. Next, HT and its derivatives have been investigated but HMF oxidation activity was as low as the plain results suggested with yield and *FE* towards FDCA below 9 %, overall loss between 13 and 40 % and no production rate higher than 0.13 $mmol_{FDCA}\ s^{-1}\ mmol_{cat}^{-1}$. AT and its derivatives show a different pattern with yields and *FEs* reaching up to 80 and 78 %, respectively, overall losses just one time detected with 29 % and production rates up to 1.78 $mmol_{FDCA}\ s^{-1}\ mmol_{cat}^{-1}$. PT could not reach these high numbers with a yield and *FE* towards FDCA of 60 and 64 %, respectively, no overall loss and a production rate of 0.26 $mmol_{FDCA}\ s^{-1}\ mmol_{cat}^{-1}$. From both covalently connected TEMPO/IL pairs, HTMIM BETI did not show any promising results as the HT derivative with a yield towards FDCA of 8 %, an overall loss of up to 43 % and a production rate of 0.06 $mmol_{FDCA}\ s^{-1}\ mmol_{cat}^{-1}$. ATMIM BETI in C12MIM BETI on the other hand could reach 93 % of yield and *FE* towards FDCA, overall loss as low as 2 % and a production rate of 1.11 $mmol_{FDCA}\ s^{-1}\ mmol_{cat}^{-1}$. Here, a difference between the ratios of ATMIM BETI to C12MIM BETI could be observed as well, as yield and *FE* dropped down with less pure IL mixed to the TEMPO/IL pair.

Stability of SILP catalysts using microporous carbon as support

After some TEMPO derivatives exhibited extraordinary activity towards HMF oxidation, their stability had to be investigated as well. One option was to check for leaching into the electrolyte, while the second one was to reuse an electrode again.
Starting with MT, which achieved the highest overall yield towards FDCA of 99 % with no loss and a production rate of over 1 $mmol_{FDCA}\ s^{-1}\ mmol_{cat}^{-1}$: It could not repeat this success by reusing the same electrode as no activity could be determined. A hint is the leaching test, in which MT clearly could be found in the electrolyte after a 12 or 24 h run. Since HT and its derivatives did not show any real activity towards HMF oxidation, their stability test was skipped. The most promising result could be achieved by C14-AT in C14MIM BETI because the results after reusing it once were in the same range as in the first run, even if conversion of HMF dropped from 94 to 80 %. Unfortunately, yield towards FDCA was only 34 to 30 % in the first and second run, respectively, with a production rate of 0.21 to 0.19 $mmol_{FDCA}\ s^{-1}\ mmol_{cat}^{-1}$. On top of that, a third run exhibited the same behavior as seen before with MT as activity dropped down to a yield towards FDCA of 5 % and a production rate of 0.03 $mmol_{FDCA}\ s^{-1}\ mmol_{cat}^{-1}$. PT also lost activity by reusing it as yield towards FDCA dropped down from 60 to 16 %, as did the production rate from 0.26 to 0.07 $mmol_{FDCA}\ s^{-1}\ mmol_{cat}^{-1}$. The other promising candidate ATMIM BETI on its own had a similar behavior as C14-AT regarding stability after one and two reuses but mixed with IL, its performance even decreased after one or reuse.

<u>TEMPO derivatives used as SILP catalyst on commercial and polymer derived carbon as support</u>

As the activity on microporous carbon as support was promising but the systems were not stable enough, Vulcan and polymer derived carbon (PDC) as different carbon support material might enhance the interaction to increase stability.
At first, Vulcan as a commercial carbon was tested with MT and C4MIM BETI as a short IL, but no activity at all could be seen in three or two electrode setup, it even resulted in the same outcome as with the blank MPL before that was investigated before. Therefore, polymer derived

carbon (PDC) was used as carbon support also for MT in C4MIM BETI. It exhibited a slightly higher activity and reached yields towards FDCA up to 8 % at an HMF conversion of 38 %. Active C14-AT in C6MIM BETI was also immobilized onto PDC and reached similar figures with a 35 % conversion of HMF and a 7 % yield and *FE* towards FDCA. Nevertheless, FFCA as main product could be observed with a yield of 26 %. Using three times the amount of charge tripled conversion, yield towards FFCA and FDCA, while *FE* stayed constant, which proves that FFCA is the main product of this SILP approach.
Due to the low activity of these systems, stability has not been analyzed.

Overall, the implementation of a measurement protocol to compare different catalytic systems for electrochemical HMF oxidation allowed screening a wide variety of catalyst systems in a short time. Focusing on SILP systems with TEMPO as oxidation catalyst, some systems with promising activity towards electrochemical HMF oxidation like MT or ATMIM BETI in C12MIM BETI could be detected. They reached yields and *FEs* of over 90 % with no overall loss and production rates above 1 $mmol_{FDCA}\ s^{-1}\ mmol_{cat}^{-1}$. Nevertheless, all efforts to enhance their stability with higher interaction between catalyst and support, covalently connected TEMPO and IL, as well as different carbon supports did not work as expected, which complicates a long term usage.

8 References

[1] J. J. Bozell, G. R. Petersen, *Green Chem.* **2010**, *12*, 539-554.
[2] P. T. Anastas, J. C. Warner, *Green Chemistry: Theory and Practice*, Oxford University Press, **1998**.
[3] M. Geissdoerfer, P. Savaget, N. M. P. Bocken, E. J. Hultink, *J. Clean. Prod.* **2017**, *143*, 757-768.
[4] R. A. Sheldon, *Catal. Today* **2011**, *167*, 3-13.
[5] P. Imhof, J. C. van der Waal, *Catalytic process development for renewable materials*, John Wiley & Sons - Books, **2013**.
[6] R. A. Sheldon, *Green Chem.* **2014**, *16*, 950-963.
[7] B. You, N. Jiang, X. Liu, Y. Sun, *Angew. Chem., Int. Ed. Engl.* **2016**, *55*, 9913-9917.
[8] J. A. Turner, *Science* **2004**, *305*, 972 - 974.
[9] F. Dawood, M. Anda, G. M. Shafiullah, *International Journal of Hydrogen Energy* **2020**, *45*, 3847-3869.
[10] D. Parra, L. Valverde, F. J. Pino, M. K. Patel, *Renewable and Sustainable Energy Reviews* **2019**, *101*, 279-294.
[11] IEA, The Future of Hydrogen - Seizing Today's Opportunities, **2019**.
[12] Y. Kwon, K. J. P. Schouten, J. C. van der Waal, E. de Jong, M. T. M. Koper, *ACS Catal.* **2016**, *6*, 6704-6717.
[13] S. K. Brar, S. J. Sarma, K. Pakshirajan, *Platform chemical biorefinery: future green chemistry*, **2016**.
[14] S. E. Davis, B. N. Zope, R. J. Davis, *Green Chemistry* **2012**, *14*, 143-147.
[15] C. Moreau, M. N. Belgacem, A. Gandini, *Topics In Catalysis* **2004**, *27*, 11-30.
[16] D. I. Collias, A. M. Harris, V. Nagpal, I. W. Cottrell, M. W. Schultheis, *Industrial Biotechnology* **2014**, *10*, 91-105.
[17] P. Harmsen, M. M. Hackmann, *Green building blocks for biobased plastics: biobased processes and market development*, Wageningen UR-Food & Biobased Research, **2013**.
[18] F. W. Lichtenthaler, VCH Publ.: Weinheim/New York, **1991**.
[19] F. W. Lichtenthaler, in *Ullmann's Encyclopedia of Industrial Chemistry*, **2000**.
[20] T. Werpy, G. Petersen, National Renewable Energy Lab., Golden, CO (US), **2004**.
[21] R. J. van Putten, J. C. van der Waal, E. de Jong, C. B. Rasrendra, H. J. Heeres, J. G. de Vries, *Chemical Reviews* **2013**, *113*, 1499-1597.
[22] J. M. Timko, D. J. Cram, *Journal of the American Chemical Society* **1974**, *96*, 7159-7160.
[23] V. Schiavo, G. Descotes, J. Mentech, *Bulletin de la Société chimique de France* **1991**, 704-711.
[24] R. Boopathy, H. Bokang, L. Daniels, *Journal of industrial microbiology* **1993**, *11*, 147-150.
[25] W. J. Pentz, Patent US4426460A, **1984**.
[26] M. Gomes, A. Gandini, A. J. D. Silvestre, B. Reis, *Journal of Polymer Science Part A: Polymer Chemistry* **2011**, *49*, 3759-3768.
[27] M. Sayed, S.-H. Pyo, N. Rehnberg, R. Hatti-Kaul, *ACS Sustainable Chemistry & Engineering* **2019**, *7*, 4406-4413.
[28] K. Mitsukura, Y. Sato, T. Yoshida, T. Nagasawa, *Biotechnology letters* **2004**, *26*, 1643-1648.
[29] H. Hirai, *Journal of Macromolecular Science: Part A - Chemistry* **1984**, *21*, 1165-1179.
[30] M. Munekata, G. Tamura, *Agricultural Biological Chemistry* **1981**, *45*, 2149-2150.
[31] M. A. Lilga, R. T. Hallen, J. Hu, J. F. White, M. J. Gray, Patent US7700788, **2010**.
[32] T. Haas, T. Tacke, J. C. Pfeffer, F. Klasovsky, M. Rimbach, M. Volland, M. Ortelt, World Patent 2012004069, **2012**.
[33] G. A. Halliday, R. J. Young, V. V. Grushin, *Organic letters* **2003**, *5*, 2003-2005.

[34] O. C. Navarro, A. C. Canós, S. I. Chornet, *Topics in Catalysis* **2009**, *52*, 304-314.
[35] K. T. Hopkins, W. D. Wilson, B. C. Bender, D. R. McCurdy, J. E. Hall, R. R. Tidwell, A. Kumar, M. Bajic, D. W. Boykin, *Journal of medicinal chemistry* **1998**, *41*, 3872-3878.
[36] M. Del Poeta, W. A. Schell, C. C. Dykstra, S. Jones, R. R. Tidwell, A. Czarny, M. Bajic, M. Bajic, A. Kumar, D. Boykin, *Antimicrobial Agents and Chemotherapy* **1998**, *42*, 2495-2502.
[37] A. Benahmed-Gasmi, P. Frere, M. Jubault, A. Gorgues, J. Cousseau, B. J. S. m. Garrigues, **1993**, *56*, 1751-1755.
[38] D. T. Richter, T. D. Lash, *Tetrahedron letters* **1999**, *40*, 6735-6738.
[39] D. W. Sheibley, M. A. Manzo, O. D. J. J. o. t. E. S. Gonzalez-Sanabria, **1983**, *130*, 255.
[40] P. D. Bloom, P. Venkitasubramanian, Patent US0018300A1, **2009**.
[41] A. S. Amarasekara, D. Green, L. D. Williams, *European Polymer Journal* **2009**, *45*, 595-598.
[42] V. Mittal, *Renewable Polymers: Synthesis, Processing, and Technology*, Scrivener Publishing LLC., **2012**.
[43] S. Koltzenburg, M. Maskos, O. Nuyken, in *Polymer Chemistry*, **2017**, pp. 1-16.
[44] J. Tinge, M. Groothaert, H. op het Veld, J. Ritz, H. Fuchs, H. Kieczka, W. C. Moran, in *Ullmann's Encyclopedia of Industrial Chemistry*, Wiley VCH Weinheim, **2018**.
[45] T. Buntara, S. Noel, P. H. Phua, I. Melián-Cabrera, J. G. de Vries, H. J. Heeres, *Angewandte Chemie* **2011**, *123*, 7221-7225.
[46] P. Werle, M. Morawietz, S. Lundmark, K. Sörensen, E. Karvinen, J. Lehtonen, in *Ullmann's Encyclopedia of Industrial Chemistry*, Wiley VCH Weinheim, **2012**.
[47] F. C. A. Figueiredo, E. Jordão, W. A. Carvalho, *Applied Catalysis A: General* **2008**, *351*, 259-266.
[48] M. Toba, S.-i. Tanaka, S.-i. Niwa, F. Mizukami, Z. Koppány, L. Guczi, K.-Y. Cheah, T.-S. Tang, *Applied Catalysis A: General* **1999**, *189*, 243-250.
[49] F. F. Bamoharram, M. M. Heravi, M. Roshani, A. Gharib, M. Jahangir, *Journal of Molecular Catalysis A: Chemical* **2006**, *252*, 90-95.
[50] S. Murahashi, T. Naota, K. Ito, Y. Maeda, H. Taki, *The Journal of Organic Chemistry* **2002**, *52*, 4319-4327.
[51] F. J. Van Natta, J. W. Hill, W. Carruthers, *Journal of the American Chemical Society* **1934**, *56*, 455-457.
[52] V. R. Sinha, K. Bansal, R. Kaushik, R. Kumria, A. Trehan, *International Journal of Pharmaceutics* **2004**, *278*, 1-23.
[53] C. X. F. Lam, S. H. Teoh, D. W. Hutmacher, *Polymer International* **2007**, *56*, 718-728.
[54] J. L. Hedrick, T. Magbitang, E. F. Connor, T. Glauser, W. Volksen, C. J. Hawker, V. Y. Lee, R. D. Miller, *Chemistry - A European Journal* **2002**, *8*, 3308-3319.
[55] Y. Ikada, H. Tsuji, *Macromolecular rapid communications* **2000**, *21*, 117-132.
[56] P. Joshi, G. Madras, *Polymer Degradation and Stability* **2008**, *93*, 1901-1908.
[57] K. Weissermel, H.-J. Arpe, *Industrial Organic Chemistry*, 3 ed., Wiley VCH Weinheim, **1997**.
[58] V. S. Bisaria, A. Kondo, *Bioprocessing of renewable resources to commodity bioproducts*, John Wiley & Sons - Books, **2014**.
[59] J. P. Oppenheim, G. L. Dickerson, *Adipic Acid*, **2014**.
[60] M. T. Musser, in *Ullmann's Encyclopedia of Industrial Chemistry*, Wiley VCH Weinheim, **2005**.
[61] R. Beerthuis, G. Rothenberg, N. R. Shiju, *Green Chemistry* **2015**, *17*, 1341-1361.
[62] M. Mounguengui-Diallo, F. Vermersch, N. Perret, C. Pinel, M. Besson, *Applied Catalysis A: General* **2018**, *551*, 88-97.
[63] E. L. Dias, V. J. Murphy, J. A. Shoemaker, Patent US9035094 B2, **2015**.
[64] T. R. Boussie, E. L. Dias, Z. M. Fresco, V. J. Murphy, Patent US8501989B2, **2013**.
[65] H. A. M. van Aert, M. H. P. van Genderen, G. J. M. L. van Steenpaal, L. Nelissen, E. W. Meijer, J. Liska, *Macromolecules* **1997**, *30*, 6056-6066.

[66] P. E. Adams, R. M. Lange, R. Yodice, M. R. Baker, J. G. Dietz, Patent US6177941, **2000**.
[67] M. Raidel, F. Aschenbrenner, World Patent 9843684, **1998**.
[68] M. Nakazato, Y. Konishi, Patent JPN06280041, **1995**.
[69] T. Oono, S. Saito, S. Shinohara, K. Takakuwa, Patent JPN08243787, **1996**.
[70] J. J. Bozell, L. Moens, D. C. Elliott, Y. Wang, G. G. Neuenschwander, S. W. Fitzpatrick, R. J. Bilski, J. L. Larnefeld, *Resources, Conservation and Recycling* **2000**, *28*, 227-239.
[71] Y. Guo, K. Li, X. Yu, J. H. Clark, *Applied Catalysis B: Environmental* **2008**, *81*, 182-191.
[72] B. Girisuta, L. P. B. M. Janssen, H. J. Heeres, *Green Chemistry* **2006**, *8*.
[73] J. Hietala, A. Vuori, P. Johnsson, I. Pollari, W. Reutemann, H. Kieczka, in *Ullmann's Encyclopedia of Industrial Chemistry*, Wiley VCH Weinheim, **2016**.
[74] S. da Cunha, G. P. Rangaiah, K. Hidajat, *Industrial & Engineering Chemistry Research* **2018**, *57*, 9554-9570.
[75] N. Norouzi, G. Kalantari, *Asian Journal of Green Chemistry* **2021**, *5*, 71-90.
[76] M. Grasemann, G. Laurenczy, *Energy & Environmental Science* **2012**, *5*.
[77] L. E. Manzer, *Applied Catalysis A: General* **2004**, *272*, 249-256.
[78] Z.-p. Yan, L. Lin, S. Liu, *Energy Fuels* **2009**, *23*, 3853-3858.
[79] J. Wang, S. Jaenicke, G.-K. Chuah, *Royal Society of Chemistry Advances* **2014**, *4*, 13481-13489.
[80] A. M. Hengne, C. V. Rode, *Green Chemistry* **2012**, *14*.
[81] D. Fegyverneki, L. Orha, G. Láng, I. T. Horváth, *Tetrahedron* **2010**, *66*, 1078-1081.
[82] I. T. Horváth, H. Mehdi, V. Fábos, L. Boda, L. T. Mika, *Green Chem.* **2008**, *10*, 238-242.
[83] L. Qi, I. T. Horváth, *ACS Catalysis* **2012**, *2*, 2247-2249.
[84] J. M. R. Gallo, D. M. Alonso, M. A. Mellmer, J. A. Dumesic, *Green Chemistry* **2013**, *15*, 85-90.
[85] J. P. Lange, R. Price, P. M. Ayoub, J. Louis, L. Petrus, L. Clarke, H. Gosselink, *Angew Chem Int Ed Engl* **2010**, *49*, 4479-4483.
[86] M. Chidambaram, A. T. Bell, *Green Chemistry* **2010**, *12*.
[87] API Research Project 45, **1956**.
[88] C. Wang, H. Xu, R. Daniel, A. Ghafourian, J. M. Herreros, S. Shuai, X. Ma, *Fuel* **2013**, *103*, 200-211.
[89] D. A. Rothamer, J. H. Jennings, *Fuel* **2012**, *98*, 203-212.
[90] R. Daniel, H. Xu, C. Wang, D. Richardson, S. Shuai, *Applied Energy* **2012**, *98*, 59-68.
[91] Y. Zu, P. Yang, J. Wang, X. Liu, J. Ren, G. Lu, Y. Wang, *Applied Catalysis B: Environmental* **2014**, *146*, 244-248.
[92] T. Thananatthanachon, T. B. Rauchfuss, *Angewandte Chemie International Edition English* **2010**, *49*, 6616-6618.
[93] S. Jia, Z. Xu, Z. C. Zhang, *Chemical Engineering Journal* **2014**, *254*, 333-339.
[94] N. Jiang, W. Qi, Z. Wu, R. Su, Z. He, *Catalysis Today* **2018**, *302*, 94-99.
[95] B. F. M. Kuster, *starch/stärke* **1990**, *42*, 314-321.
[96] M. J. Antal, W. S. L. Mok, G. N. Richards, *Carbohydrate Research* **1990**, *199*, 91-109.
[97] A. S. Amarasekara, L. D. Williams, C. C. Ebede, *Carbohydr Res* **2008**, *343*, 3021-3024.
[98] S. Xiao, B. Liu, Y. Wang, Z. Fang, Z. Zhang, *Bioresource Technology* **2014**, *151*, 361-366.
[99] L.-T. Fan, M. M. Gharpuray, Y.-H. Lee, *Cellulose hydrolysis, Vol. 3*, Springer Science & Business Media, **2012**.
[100] H. Wang, C. Zhu, D. Li, Q. Liu, J. Tan, C. Wang, C. Cai, L. Ma, *Renewable and Sustainable Energy Reviews* **2019**, *103*, 227-247.
[101] Y. Feng, M. Li, Z. Gao, X. Zhang, X. Zeng, Y. Sun, X. Tang, T. Lei, L. Lin, *ChemSusChem* **2019**, *12*, 495-502.
[102] M. B. Roberfroid, J. A. Van Loo, G. R. Gibson, *The Journal of nutrition* **1998**, *128*, 11-19.
[103] Y. Zhang, B. Li, W. Guan, Y. Wei, C. Yan, M. Meng, J. Pan, Y. Yan, *Cellulose* **2020**, *27*, 3037-3054.

[104] A. Mittal, H. M. Pilath, D. K. Johnson, *Energy & Fuels* **2020**, *34*, 3284-3293.
[105] P. H. Hoang, N. M. Dat, T. D. Cuong, D. T. Tung, *Royal Society of Chemistry Advances* **2020**, *10*, 13489-13495.
[106] A. Chinnappan, C. Baskar, H. Kim, *Royal Society of Chemistry Advances* **2016**, *6*, 63991-64002.
[107] A. S. Khan, Z. Man, A. Nasrullah, Z. Ullah, N. Muhammad, A. Rahim, A. Bustam, A. Idris, M. Uroos, in *Green Sustainable Process for Chemical and Environmental Engineering and Science*, **2020**, pp. 1-30.
[108] C. Lansalot-Matras, C. Moreau, *Catalysis Communications* **2003**, *4*, 517-520.
[109] G. Yong, Y. Zhang, J. Y. Ying, *Angewandte Chemie International Edition English* **2008**, *47*, 9345-9348.
[110] X. Qi, M. Watanabe, T. M. Aida, R. L. Smith, Jr., *ChemSusChem* **2010**, *3*, 1071-1077.
[111] M. Mathlouthi, P. Reiser, *Sucrose: properties and applications*, Springer Science & Business Media, **1995**.
[112] J. Shi, W. Liu, N. Wang, Y. Yang, H. Wang, *Catalysis Letters* **2013**, *144*, 252-260.
[113] G. Avigad, in *Plant Carbohydrates I*, Springer, **1982**, pp. 217-347.
[114] L. Zhou, R. Liang, Z. Ma, T. Wu, Y. Wu, *Bioresource Technology* **2013**, *129*, 450-455.
[115] J. A. Moore, J. E. Kelly, *Macromolecules* **1978**, *11*, 568-573.
[116] U. Fehrenbacher, O. Grosshardt, K. Kowollik, B. Tübke, N. Dingenouts, M. Wilhelm, *Chemie Ingenieur Technik* **2009**, *81*, 1829-1835.
[117] A. Gandini, A. J. D. Silvestre, C. P. Neto, A. F. Sousa, M. Gomes, *Journal of Polymer Science Part A: Polymer Chemistry* **2009**, *47*, 295-298.
[118] A. Gandini, in *Green Polymerisation Methods: Renewable Starting Materials, Catalysis and Waste Reduction, Vol. 29* (Eds.: R. T. Mathers, M. A. R. Meier), Wiley-VCH, Weinheim, **2011**, pp. 29-56.
[119] L. Dissanayake, L. N. Jayakody, *Front Bioeng Biotechnol* **2021**, *9*, 656465.
[120] S. K. Burgess, O. Karvan, J. R. Johnson, R. M. Kriegel, W. J. Koros, *Polymer* **2014**, *55*, 4748-4756.
[121] S. K. Burgess, R. M. Kriegel, W. J. Koros, *Macromolecules* **2015**, *48*, 2184-2193.
[122] S. K. Burgess, D. S. Mikkilineni, D. B. Yu, D. J. Kim, C. R. Mubarak, R. M. Kriegel, W. J. Koros, *Polymer* **2014**, *55*, 6870-6882.
[123] S. K. Burgess, D. S. Mikkilineni, D. B. Yu, D. J. Kim, C. R. Mubarak, R. M. Kriegel, W. J. Koros, *Polymer* **2014**, *55*, 6861-6869.
[124] S. K. Burgess, J. E. Leisen, B. E. Kraftschik, C. R. Mubarak, R. M. Kriegel, W. J. Koros, *Macromolecules* **2014**, *47*, 1383-1391.
[125] J. Lin, S. Shenogin, S. Nazarenko, *Polymer* **2002**, *43*, 4733-4743.
[126] T. L. Nguyen, F. Bédoui, P.-E. Mazeran, M. Guigon, *Polymer Engineering & Science* **2015**, *55*, 397-405.
[127] G. Stoclet, G. Gobius du Sart, B. Yeniad, S. de Vos, J. M. Lefebvre, *Polymer* **2015**, *72*, 165-176.
[128] E. de Jong, M. Dam, L. Sipos, G.-J. Gruter, in *Biobased monomers, polymers, and materials*, ACS Publications, **2012**, pp. 1-13.
[129] G. Z. Papageorgiou, V. Tsanaktsis, D. N. Bikiaris, *Phys Chem Chem Phys* **2014**, *16*, 7946-7958.
[130] Y. S. Hu, A. Hiltner, E. Baer, *Journal of Applied Polymer Science* **2005**, *98*, 1629-1642.
[131] Market update 2020: Bioplastics continue to become mainstream as the global bioplastics market is set to grow by 36 percent over the next 5 years. Available online: https://www.european-bioplastics.org/market-update-2020-bioplastics-continue-to-become-mainstream-as-the-global-bioplastics-market-is-set-to-grow-by-36-percent-over-the-next-5-years/ (accessed on 21st April 2021).
[132] Global Polyethylene Furanoate Market 2018-2025 - Ongoing Quest to Decrease the Global Carbon Footprint is a Major Driver. Available online: https://www.prnewswire.com/news-releases/global-polyethylene-furanoate-market-

2018-2025---ongoing-quest-to-decrease-the-global-carbon-footprint-is-a-major-driver-300689405.html (accessed on 21st April 2021).
[133] L. Chen, R. E. O. Pelton, T. M. Smith, *Journal of Cleaner Production* **2016**, *137*, 667-676.
[134] H. B. Aditiya, T. M. I. Mahlia, W. T. Chong, H. Nur, A. H. Sebayang, *Renewable and Sustainable Energy Reviews* **2016**, *66*, 631-653.
[135] Y. Li, B. Yue, S. Yan, W. Yang, Z. Xie, Q. Chen, H. He, *Catal. Lett.* **2004**, *95*, 163-166.
[136] S. Rebsdat, D. Mayer, in *Ullmann's Encyclopedia of Industrial Chemistry*, **2001**.
[137] H. Zimmermann, R. Walzl, in *Ullmann's Encyclopedia of Industrial Chemistry*, **2009**.
[138] Production capacity of ethylene glycol worldwide from 2014 to 2024. Available online: https://www.statista.com/statistics/1067418/global-ethylene-glycol-production-capacity/ (accessed 22nd April 2021).
[139] Mono-Ethylene Glycol (MEG): Production, Market, Price and its Properties. Available online: https://www.plasticsinsight.com/resin-intelligence/resin-prices/mono-ethylene-glycol-meg/ (accessed on 22nd April 2021).
[140] in *Market Research Future*, **2021**.
[141] R. J. Sheehan, in *Ullmann's Encyclopedia of Industrial Chemistry*, **2011**.
[142] K. Ziegler-Skylakakis, J. Fabri, U. Graeser, T. A. Simo, in *Ullmann's Encyclopedia of Industrial Chemistry*, **2019**, pp. 1-20.
[143] S. U. Gröne, Universität Ulm **2021**.
[144] Crude Oil Overview - Crude oil is an important global energy source. Available online: https://corporatefinanceinstitute.com/resources/knowledge/economics/crude-oil-overview/ (accessed on 22nd April 2021).
[145] Rainforest Energy to produce bio-gasoline from biomass using Infinity technology. Available online: https://biofuels-news.com/news/rainforest-energy-to-produce-bio-gasoline-from-biomass-using-infinity-technology/ (accessed on 22nd April 2021).
[146] V. Tsanaktsis, E. Vouvoudi, G. Z. Papageorgiou, D. G. Papageorgiou, K. Chrissafis, D. N. Bikiaris, *Journal of Analytical and Applied Pyrolysis* **2015**, *112*, 369-378.
[147] M. Vannini, P. Marchese, A. Celli, C. Lorenzetti, *Green Chemistry* **2015**, *17*, 4162-4166.
[148] L. W. McKeen, in *Permeability Properties of Plastics and Elastomers*, **2012**, pp. 89-106.
[149] Z. Jia, J. Wang, L. Sun, F. Liu, J. Zhu, X. Liu, *Journal of Applied Polymer Science* **2019**, *136*.
[150] N. F. Braga, A. M. LaChance, B. Liu, L. Sun, F. R. Passador, *Advanced Industrial and Engineering Polymer Research* **2019**, *2*, 121-125.
[151] S. Paszkiewicz, I. Pawelec, A. Szymczyk, Z. Špitalský, J. Mosnáček, A. Kochmańska, Z. Rosłaniec, *Polymer Engineering & Science* **2015**, *55*, 2222-2230.
[152] H. Hu, R. Zhang, J. Wang, W. B. Ying, L. Shi, C. Yao, Z. Kong, K. Wang, J. Zhu, *Green Chemistry* **2019**, *21*, 3013-3022.
[153] Z. Terzopoulou, L. Papadopoulos, A. Zamboulis, D. G. Papageorgiou, G. Z. Papageorgiou, D. N. Bikiaris, *Polymers (Basel)* **2020**, *12*.
[154] K. Luo, Y. Wang, J. Yu, J. Zhu, Z. Hu, *RSC Advances* **2016**, *6*, 87013-87020.
[155] A. Mitiakoudis, A. Gandini, *Macromolecules* **1991**, *24*, 830-835.
[156] E. G. Chatzi, J. L. Koenig, *Polymer-Plastics Technology and Engineering* **1987**, *26*, 229-270.
[157] T. J. Singh, S. Samanta, *Materials Today: Proceedings* **2015**, *2*, 1381-1387.
[158] R. Fittig, *Berichte der deutschen chemischen Gesellschaft* **1876**, *9*, 1189-1199.
[159] O. Sohst, B. Tollens, *Justus Liebigs Annalen der Chemie* **1888**, *245*, 1-27.
[160] G. Gonis, E. Amstutz, *The Journal of Organic Chemistry* **1962**, *27*, 2946-2947.
[161] R. Andrisano, A. Angelori, *Ann. Chim.* **1963**, *53*, 1658-1664.
[162] M. Sajid, X. Zhao, D. Liu, *Green Chemistry* **2018**, *20*, 5427-5453.
[163] W. Partenheimer, V. V. Grushin, *Advanced Synthesis & Catalysis* **2001**, *343*, 102-111.
[164] B. Saha, S. Dutta, M. M. Abu-Omar, *Catal. Sci. Technol.* **2012**, *2*, 79-81.
[165] T. S. Hansen, I. Sádaba, E. J. García-Suárez, A. Riisager, *Appl. Catal. A: General* **2013**, *456*, 44-50.

[166] Z. Zhang, K. Deng, *ACS Catalysis* **2015**, *5*, 6529-6544.
[167] S. Hameed, L. Lin, A. Wang, W. Luo, *Catalysts* **2020**, *10*.
[168] K. R. Vuyyuru, P. Strasser, *Catal. Today* **2012**, *195*, 144-154.
[169] S. Wöllner, T. Nowak, G. R. Zhang, N. Rockstroh, H. Ghanem, S. Rosiwal, A. Bruckner, B. J. M. Etzold, *ChemistryOpen* **2021**, *10*, 600-606.
[170] O. Casanova, S. Iborra, A. Corma, *ChemSusChem* **2009**, *2*, 1138-1144.
[171] J. Cai, H. Ma, J. Zhang, Q. Song, Z. Du, Y. Huang, J. Xu, *Chemistry* **2013**, *19*, 14215-14223.
[172] N. K. Gupta, S. Nishimura, A. Takagaki, K. Ebitani, *Green Chemistry* **2011**, *13*.
[173] T. Gao, T. Gao, W. Fang, Q. Cao, *Molecular Catalysis* **2017**, *439*, 171-179.
[174] P. Vinke, H. E. van Dam, H. van Bekkum, in *New Developments in Selective Oxidation*, **1990**, pp. 147-158.
[175] P. Verdeguer, N. Merat, A. Gaset, *Journal of Molecular Catalysis* **1993**, *85*, 327-344.
[176] H. Ait Rass, N. Essayem, M. Besson, *Green Chem.* **2013**, *15*, 2240-2251.
[177] S. Siankevich, G. Savoglidis, Z. Fei, G. Laurenczy, D. T. L. Alexander, N. Yan, P. J. Dyson, *Journal of Catalysis* **2014**, *315*, 67-74.
[178] S. E. Davis, L. R. Houk, E. C. Tamargo, A. K. Datye, R. J. Davis, *Catal. Today* **2011**, *160*, 55-60.
[179] B. Siyo, M. Schneider, M.-M. Pohl, P. Langer, N. Steinfeldt, *Catalysis Letters* **2014**, *144*, 498-506.
[180] B. Siyo, M. Schneider, J. Radnik, M.-M. Pohl, P. Langer, N. Steinfeldt, *Applied Catalysis A: General* **2014**, *478*, 107-116.
[181] Y. Wang, K. Yu, D. Lei, W. Si, Y. Feng, L.-L. Lou, S. Liu, *ACS Sustainable Chemistry & Engineering* **2016**, *4*, 4752-4761.
[182] G. Yi, S. P. Teong, Y. Zhang, *Green Chem.* **2016**, *18*, 979-983.
[183] D. K. Mishra, H. J. Lee, J. Kim, H.-S. Lee, J. K. Cho, Y.-W. Suh, Y. Yi, Y. J. Kim, *Green Chem.* **2017**, *19*, 1619-1623.
[184] T. Gao, Y. Yin, W. Fang, Q. Cao, *Molecular Catalysis* **2018**, *450*, 55-64.
[185] B. Saha, D. Gupta, M. M. Abu-Omar, A. Modak, A. Bhaumik, *Journal of Catalysis* **2013**, *299*, 316-320.
[186] E. Hayashi, Y. Yamaguchi, K. Kamata, N. Tsunoda, Y. Kumagai, F. Oba, M. Hara, *J Am Chem Soc* **2019**, *141*, 890-900.
[187] T. Gao, Y. Yin, G. Zhu, Q. Cao, W. Fang, *Catalysis Today* **2020**, *355*, 252-262.
[188] A. Jain, S. C. Jonnalagadda, K. V. Ramanujachary, A. Mugweru, *Catalysis Communications* **2015**, *58*, 179-182.
[189] E. Hayashi, T. Komanoya, K. Kamata, M. Hara, *ChemSusChem* **2017**, *10*, 654-658.
[190] L. Bao, F. Z. Sun, G. Y. Zhang, T. L. Hu, *ChemSusChem* **2020**, *13*, 548-555.
[191] D. Troiano, V. Orsat, M.-J. Dumont, *ACS Catalysis* **2020**, *10*, 9145-9169.
[192] W. P. Dijkman, D. E. Groothuis, M. W. Fraaije, *Angew Chem Int Ed Engl* **2014**, *53*, 6515-6518.
[193] W. P. Dijkman, C. Binda, M. W. Fraaije, A. Mattevi, *ACS Catalysis* **2015**, *5*, 1833-1839.
[194] H. G. Cha, K. S. Choi, *Nature Chemistry* **2015**, *7*, 328-333.
[195] M. G. Walter, E. L. Warren, J. R. McKone, S. W. Boettcher, Q. Mi, E. A. Santori, N. S. Lewis, *Chemical Reviews* **2010**, *110*, 6446-6473.
[196] H. Dau, C. Limberg, T. Reier, M. Risch, S. Roggan, P. Strasser, *ChemCatChem* **2010**, *2*, 724-761.
[197] D. Bellotti, M. Rivarolo, L. Magistri, *Energy Procedia* **2019**, *158*, 4721-4728.
[198] X. Liu, J. Chi, B. Dong, Y. Sun, *ChemElectroChem* **2019**, *6*, 2157-2166.
[199] B. M. Hunter, H. B. Gray, A. M. Muller, *Chemical Reviews* **2016**, *116*, 14120-14136.
[200] H. Yin, S. Zhao, K. Zhao, A. Muqsit, H. Tang, L. Chang, H. Zhao, Y. Gao, Z. Tang, *Nat. Commun.* **2015**, *6*, 1-8.
[201] G. Grabowski, J. Lewkowski, R. Skowroński, *Electrochimica Acta* **1991**, *36*, 1995.

[202] J. Weidner, S. Barwe, K. Sliozberg, S. Piontek, J. Masa, U. P. Apfel, W. Schuhmann, *Beilstein Journal of Organic Chemistry* **2018**, *14*, 1436-1445.
[203] D. J. Chadderdon, L. Xin, J. Qi, Y. Qiu, P. Krishna, K. L. More, W. Li, *Green Chem.* **2014**, *16*, 3778-3786.
[204] B. J. Taitt, D.-H. Nam, K.-S. Choi, *ACS Catal.* **2019**, *9*, 660-670.
[205] B. You, X. Liu, N. Jiang, Y. Sun, *J. Am. Chem. Soc.* **2016**, *138*, 13639-13646.
[206] W.-J. Liu, L. Dang, Z. Xu, H.-Q. Yu, S. Jin, G. W. Huber, *ACS Catal.* **2018**, *8*, 5533-5541.
[207] S. Barwe, J. Weidner, S. Cychy, D. M. Morales, S. Dieckhofer, D. Hiltrop, J. Masa, M. Muhler, W. Schuhmann, *Angew Chem Int Ed Engl* **2018**, *57*, 11460-11464.
[208] N. Zhang, Y. Zou, L. Tao, W. Chen, L. Zhou, Z. Liu, B. Zhou, G. Huang, H. Lin, S. Wang, *Angew. Chem., Int. Ed. Engl.* **2019**, *58*, 15895-15903.
[209] N. Jiang, B. You, R. Boonstra, I. M. Terrero Rodriguez, Y. Sun, *ACS Energy Lett.* **2016**, *1*, 386-390.
[210] Z. Zhou, C. Chen, M. Gao, B. Xia, J. Zhang, *Green Chemistry* **2019**, *21*, 6699-6706.
[211] D.-H. Nam, B. J. Taitt, K.-S. Choi, *ACS Catal.* **2018**, *8*, 1197-1206.
[212] L. Gao, S. Gan, J. Ma, Z. Sun, Z. Liu, L. Zhong, K. Zhou, F. Han, W. Wang, D. Han, L. Niu, *ChemElectroChem* **2020**, *7*, 4251-4258.
[213] S. R. Kubota, K. S. Choi, *ChemSusChem* **2018**, *11*, 2138-2145.
[214] R. Francke, R. D. Little, *Chem Soc Rev* **2014**, *43*, 2492-2521.
[215] J. E. Nutting, M. Rafiee, S. S. Stahl, *Chemical Reviews* **2018**, *118*, 4834-4885.
[216] D. Bowman, T. Gillan, K. Ingold, *Journal of the American Chemical Society* **1971**, *93*, 6555-6561.
[217] J. F. Keana, *Chemical Reviews* **1978**, *78*, 37-64.
[218] J. B. Mitchell, A. Samuni, M. C. Krishna, W. G. DeGraff, M. S. Ahn, U. Samuni, A. Russo, *Biochemistry* **1990**, *29*, 2802-2807.
[219] U. A. Nilsson, L. I. Olsson, G. Carlin, A. C. Bylund-Fellenius, *Journal of Biological Chemistry* **1989**, *264*, 11131-11135.
[220] M. Lafon-Cazal, S. Pietri, M. Culcasi, J. Bockaert, *Nature* **1993**, *364*, 535-537.
[221] B. J. Bergner, A. Schurmann, K. Peppler, A. Garsuch, J. Janek, *J Am Chem Soc* **2014**, *136*, 15054-15064.
[222] Z. Zhang, P. Chen, T. N. Murakami, S. M. Zakeeruddin, M. Grätzel, *Advanced Functional Materials* **2008**, *18*, 341-346.
[223] T. Janoschka, N. Martin, M. D. Hager, U. S. Schubert, *Angew Chem Int Ed Engl* **2016**, *55*, 14427-14430.
[224] K. Nakahara, K. Oyaizu, H. Nishide, *Chemistry Letters* **2011**, *40*, 222-227.
[225] J. M. Bobbitt, C. Brückner, N. Merbouh, in *Organic Reactions, Vol. 74*, Wiley VCH, **2009**, pp. 103-424.
[226] M. Tsunaga, C. Iwakura, H. Tamura, *Electrochimica Acta* **1973**, *18*, 241-245.
[227] J. R. Fish, S. G. Swarts, M. D. Sevilla, T. Malinski, *The Journal of Physical Chemistry* **1988**, *92*, 3745-3751.
[228] Y. Kato, Y. Shimizu, L. Yijing, K. Unoura, H. Utsumi, T. Ogata, *Electrochimica acta* **1995**, *40*, 2799-2802.
[229] D. P. Hickey, D. A. Schiedler, I. Matanovic, P. V. Doan, P. Atanassov, S. D. Minteer, M. S. Sigman, *J Am Chem Soc* **2015**, *137*, 16179-16186.
[230] J. B. Gerken, Y. Q. Pang, M. B. Lauber, S. S. Stahl, *The Journal of Organic Chemistry* **2018**, *83*, 7323-7330.
[231] V. Golubev, É. Rozantsev, M. Neiman, *Bulletin of the Academy of Sciences of the USSR, Division of chemical science* **1965**, *14*, 1898-1904.
[232] W. F. Bailey, J. M. Bobbitt, K. B. Wiberg, *The Journal of organic chemistry* **2007**, *72*, 4504-4509.
[233] M. F. Semmelhack, C. R. Schmid, D. A. Cortés, *Tetrahedron letters* **1986**, *27*, 1119-1122.
[234] M. Rafiee, B. Karimi, S. Alizadeh, *ChemElectroChem* **2014**, *1*, 455-462.

[235] K. Kloth, M. Brünjes, E. Kunst, T. Jöge, F. Gallier, A. Adibekian, A. Kirschning, *Advanced Synthesis & Catalysis* **2005**, *347*, 1423-1434.
[236] Y. Kato, R. Matsuo, A. Isogai, *Carbohydrate Polymers* **2003**, *51*, 69-75.
[237] M. Rafiee, K. C. Miles, S. S. Stahl, *J Am Chem Soc* **2015**, *137*, 14751-14757.
[238] V. P. Kashparova, V. A. Klushin, D. V. Leontyeva, N. V. Smirnova, V. M. Chernyshev, V. P. Ananikov, *Chemistry - An Asian Journal* **2016**, *11*, 2578-2585.
[239] T. Inokuchi, P. Liu, S. Torii, *Chemistry letters* **1994**, *23*, 1411-1414.
[240] T. Inokuchi, S. Matsumoto, S. Torii, *The Journal of Organic Chemistry* **1991**, *56*, 2416-2421.
[241] Y. N. Ogibin, A. K. Khusid, G. Nikishin, *Bulletin of the Russian Academy of Sciences, Division of chemical science* **1992**, *41*, 735-739.
[242] Y. Demizu, H. Shiigi, T. Oda, Y. Matsumura, O. Onomura, *Tetrahedron Letters* **2008**, *49*, 48-52.
[243] K. Schnatbaum, H. J. Schäfer, *Synthesis* **1999**, *1999*, 864-872.
[244] D. Liaigre, T. Breton, E. M. Belgsir, *Electrochemistry Communications* **2005**, *7*, 312-316.
[245] P. Parpot, K. Servat, A. P. Bettencourt, H. Huser, K. B. Kokoh, *Cellulose* **2010**, *17*, 815-824.
[246] A. Kerkenaar, A. Besemer, World Patent 9104988, **1991**.
[247] A. C. Cardiel, B. J. Taitt, K.-S. Choi, *ACS Sustainable Chemistry & Engineering* **2019**, *7*, 11138-11149.
[248] X. H. Chadderdon, D. J. Chadderdon, T. Pfennig, B. H. Shanks, W. Li, *Green Chemistry* **2019**, *21*, 6210-6219.
[249] M. Li, K. Klunder, E. Blumenthal, M. B. Prater, J. Lee, J. E. Matthiesen, S. D. Minteer, *ACS Sustainable Chemistry & Engineering* **2020**.
[250] A. Riisager, P. Wasserscheid, R. van Hal, R. Fehrmann, *Journal of Catalysis* **2003**, *219*, 452-455.
[251] C. P. Mehnert, R. A. Cook, N. C. Dispenziere, M. Afeworki, *Journal of the American Chemical Society* **2002**, *124*, 12932-12933.
[252] P. Wasserscheid, W. Keim, *Angewandte Chemie International Edition* **2000**, *39*, 3772-3789.
[253] M. George, G. R. Zhang, N. Schmitt, K. Brunnengraber, D. J. S. Sandbeck, K. J. J. Mayrhofer, S. Cherevko, B. J. M. Etzold, *ACS Catalysis* **2019**, *9*, 8682-8692.
[254] M. Freemantle, *Chemical & engineering news* **1998**, *76*, 32-37.
[255] K. R. Seddon, *Journal of Chemical Technology & Biotechnology* **1997**, *68*, 351-356.
[256] H. Stegemann, A. Rohde, A. Reiche, A. Schnittke, H. Füllbier, *Electrochimica Acta* **1992**, *37*, 379-383.
[257] P. Bonhote, A.-P. Dias, N. Papageorgiou, K. Kalyanasundaram, M. Grätzel, *Inorg Chem* **1996**, *35*, 1168-1178.
[258] M. Kosmulski, J. Gustafsson, J. B. Rosenholm, *Thermochimica Acta* **2004**, *412*, 47-53.
[259] R. E. Del Sesto, T. M. McCleskey, C. Macomber, K. C. Ott, A. T. Koppisch, G. A. Baker, A. K. Burrell, *Thermochimica Acta* **2009**, *491*, 118-120.
[260] A. A. Fannin Jr, D. A. Floreani, L. A. King, J. S. Landers, B. J. Piersma, D. J. Stech, R. L. Vaughn, J. S. Wilkes, J. L. Williams, *The Journal of Physical Chemistry* **1984**, *88*, 2614-2621.
[261] R. Gomes de Azevedo, J. M. Esperança, V. Najdanovic-Visak, Z. P. Visak, H. J. Guedes, M. Nunes da Ponte, L. P. Rebelo, *Journal of Chemical & Engineering Data* **2005**, *50*, 997-1008.
[262] R. L. Gardas, M. G. Freire, P. J. Carvalho, I. M. Marrucho, I. M. Fonseca, A. G. Ferreira, J. A. Coutinho, *Journal of Chemical & Engineering Data* **2007**, *52*, 80-88.
[263] R. L. Perry, K. M. Jones, W. D. Scott, Q. Liao, C. L. Hussey, *Journal of chemical and engineering data* **1995**, *40*, 615-619.

[264] J. Fuller, R. T. Carlin, R. A. Osteryoung, *Journal of The Electrochemical Society* **1997**, *144*, 3881.
[265] J. S. Wilkes, J. A. Lewisky, R. A. Wilson, C. L. Hussey, *Inorganic Chemistry* **1982**, *21*, 1263-1264.
[266] Y. Ye, Y. A. Elabd, *Macromolecules* **2011**, *44*, 8494-8503.
[267] K. M. Meek, Y. A. Elabd, *Macromolecules* **2015**, *48*, 7071-7084.
[268] S. P. F. Costa, A. M. O. Azevedo, P. Pinto, M. Saraiva, *ChemSusChem* **2017**, *10*, 2321-2347.
[269] A. Westerholt, M. Weschta, A. Bösmann, S. Tremmel, Y. Korth, M. Wolf, E. Schlücker, N. Wehrum, A. Lennert, M. Uerdingen, W. Holweger, S. Wartzack, P. Wasserscheid, *ACS Sustainable Chemistry & Engineering* **2015**, *3*, 797-808.
[270] F. López Sánchez, I. Otero, E. R. López, J. Fernández, *Tribology Transactions* **2014**, *57*, 637-646.
[271] M. Fan, D. Yang, X. Wang, W. Liu, H. Fu, *Industrial & Engineering Chemistry Research* **2014**, *53*, 17952-17960.
[272] B. Liu, N. Jin, *Current Organic Chemistry* **2016**, *20*, 2109-2116.
[273] W. Zhai, H.-j. Zhu, L. Wang, X.-m. Liu, H. Yang, *Electrochimica Acta* **2014**, *133*, 623-630.
[274] B. Mallick, B. Balke, C. Felser, A. V. Mudring, *Angew Chem Int Ed Engl* **2008**, *47*, 7635-7638.
[275] Q. Zhang, X. Ma, S. Liu, B. Yang, L. Lu, Y. He, Y. Deng, *Journal of Materials Chemistry* **2011**, *21*.
[276] E. Duan, B. Guo, D. Zhang, L. Shi, H. Sun, Y. Wang, *J Air Waste Manag Assoc* **2011**, *61*, 1393-1397.
[277] S. Kumar, J. H. Cho, I. Moon, *International Journal of Greenhouse Gas Control* **2014**, *20*, 87-116.
[278] W. Wu, B. Han, H. Gao, Z. Liu, T. Jiang, J. Huang, *Angew Chem Int Ed Engl* **2004**, *43*, 2415-2417.
[279] M. J. Earle, S. P. Katdare, K. R. Seddon, *Organic letters* **2004**, *6*, 707-710.
[280] X. Zhao, Y. Gu, J. Li, H. Ding, Y. Shan, *Catalysis Communications* **2008**, *9*, 2179-2182.
[281] J. Hu, J. Ma, H. Liu, Q. Qian, C. Xie, B. Han, *Green Chemistry* **2018**, *20*, 2990-2994.
[282] F. H. Hurley, T. P. Wier Jr, *Journal of The Electrochemical Society* **1951**, *98*, 203.
[283] R. J. Gale, R. A. Osteryoung, *Inorganic Chemistry* **1979**, *18*.
[284] S. K. Singh, A. W. Savoy, *Journal of Molecular Liquids* **2020**, *297*.
[285] J. S. Wilkes, J. Zaworotko, *Journal of the Chemical Society, Chemical Communications* **1992**, 965-967.
[286] G. R. Zhang, M. Munoz, B. J. Etzold, *ACS Applied Materials & Interfaces* **2015**, *7*, 3562-3570.
[287] M. Armand, F. Endres, D. R. MacFarlane, H. Ohno, B. Scrosati, *Materials for sustainable energy: a collection of peer-reviewed research and review articles from Nature Publishing Group* **2011**, 129-137.
[288] X. Tu, J. Zhang, M. Zhang, Y. Cai, H. Lang, G. Tian, Y. Wang, *RSC Advances* **2017**, *7*, 14790-14796.
[289] Y. Yang, S. Liu, C. Chi, J. Hao, J. Zhao, Y. Xu, Y. Li, *Journal of Materials Science: Materials in Electronics* **2020**, *31*, 9937-9945.
[290] P. Geysens, J. Fransaer, K. Binnemans, *RSC Advances* **2020**, *10*, 42021-42029.
[291] R. Al-Salman, S. Z. El Abedin, F. Endres, *Phys Chem Chem Phys* **2008**, *10*, 4650-4657.
[292] G. A. Giffin, *Journal of Materials Chemistry A* **2016**, *4*, 13378-13389.
[293] I. Osada, H. de Vries, B. Scrosati, S. Passerini, *Angew Chem Int Ed Engl* **2016**, *55*, 500-513.
[294] M. Barghamadi, A. S. Best, A. I. Bhatt, A. F. Hollenkamp, P. J. Mahon, M. Musameh, T. Rüther, *Electrochimica Acta* **2015**, *180*, 636-644.

[295] H. Sun, G. Zhu, X. Xu, M. Liao, Y. Y. Li, M. Angell, M. Gu, Y. Zhu, W. H. Hung, J. Li, Y. Kuang, Y. Meng, M. C. Lin, H. Peng, H. Dai, *Nat Commun* **2019**, *10*, 3302.
[296] A. Riisager, R. Fehrmann, M. Haumann, P. Wasserscheid, *European Journal of Inorganic Chemistry* **2006**, *2006*, 695-706.
[297] M. Rufete-Beneite, M. C. Román-Martínez, A. Linares-Solano, *Carbon* **2014**, *77*, 947-957.
[298] U. Kernchen, B. Etzold, W. Korth, A. Jess, *Chemical Engineering & Technology* **2007**, *30*, 985-994.
[299] G. R. Zhang, T. Wolker, D. J. S. Sandbeck, M. Munoz, K. J. J. Mayrhofer, S. Cherevko, B. J. M. Etzold, *ACS Catalysis* **2018**, *8*, 8244-8254.
[300] M. George, G. R. Zhang, N. Schmitt, K. Brunnengraber, D. J. S. Sandbeck, K. J. J. Mayrhofer, S. Cherevko, B. J. M. Etzold, *ACS Catal* **2019**, *9*, 8682-8692.
[301] S. Werner, N. Szesni, M. Kaiser, M. Haumann, P. Wasserscheid, *Chemical Engineering & Technology* **2012**, *35*, 1962-1967.
[302] J. Brünig, Z. Csendes, S. Weber, N. Gorgas, R. W. Bittner, A. Limbeck, K. Bica, H. Hoffmann, K. Kirchner, *ACS Catalysis* **2018**, *8*, 1048-1051.
[303] L. Goclik, L. Offner-Marko, A. Bordet, W. Leitner, *Chem Commun (Camb)* **2020**, *56*, 9509-9512.
[304] D. S. Newsome, *Catalysis Reviews Science and Engineering* **1980**, *21*, 275-318.
[305] S. Werner, N. Szesni, A. Bittermann, M. J. Schneider, P. Härter, M. Haumann, P. Wasserscheid, *Applied Catalysis A: General* **2010**, *377*, 70-75.
[306] U. Domańska, A. Rękawek, *Journal of Solution Chemistry* **2009**, *38*, 739-751.
[307] M. A. V. Vergara, I. V. Lijanova, N. V. Likhanova, D. J. Vigueras, O. O. Xometl, *The Canadian Journal of Chemical Engineering* **2014**, *92*, 1875-1881.
[308] A. P. de los Ríos, F. Hernandez-Fernandez, L. Lozano, S. Sanchez, J. Moreno, C. Godinez, *Journal of chemical and engineering data* **2010**, *55*, 605-608.
[309] D. Villemin, M. Didi, *Oriental Journal of Chemistry* **2013**, *29*, 1267-1284.
[310] S. Van Roosendael, J. Roosen, D. Banerjee, K. Binnemans, *Separation and Purification Technology* **2019**, *221*, 83-92.
[311] S. Van Roosendael, M. Regadío, J. Roosen, K. Binnemans, *Separation and Purification Technology* **2019**, *212*, 843-853.
[312] R. Höll, M. Kling, E. Schroll, *Ore Geology Reviews* **2007**, *30*, 145-180.
[313] Y. Li, Y. Tao, F. Zhu, M. Liao, F. Xiong, X. Deng, *Chinese Journal of Geochemistry* **2015**, *34*, 469-483.
[314] K. Binnemans, Y. Pontikes, P. T. Jones, T. Van Gerven, B. Blanpain, in *Proceedings of the 3rd international slag valorisation symposium: the transition to sustainable materials management*, Slag Valorisation Symposium, **2013**, pp. 191-205.
[315] D. Avdibegović, M. Regadío, K. Binnemans, *RSC Adv.* **2017**, *7*, 49664-49674.
[316] V. C. Ramos, W. Han, X. Zhang, S. Zhang, K. L. Yeung, *Current Opinion in Green and Sustainable Chemistry* **2020**, *25*.
[317] S. Yan, F. Han, Q. Hou, S. Zhang, S. Ai, *Industrial & Engineering Chemistry Research* **2019**, *58*, 13804-13818.
[318] A. A. Bryzhin, M. G. Gantman, A. K. Buryak, I. G. Tarkhanova, *Applied Catalysis B: Environmental* **2019**, *257*.
[319] K. Bica, H. Rodriguez, G. Gurau, O. A. Cojocaru, A. Riisager, R. Fehrmann, R. D. Rogers, *Chem Commun (Camb)* **2012**, *48*, 5422-5424.
[320] F. Herold, O. Leubner, P. Pfeifer, D. Zakgeym, A. Drochner, W. Qi, B. J. M. Etzold, *Carbon* **2021**, *171*, 658-670.
[321] H.-C. Shin, M. Liu, *Chem. Mater.* **2004**, *16*, 5460 - 5464.
[322] A. Dutta, M. Rahaman, N. C. Luedi, M. Mohos, P. Broekmann, *ACS Catalysis* **2016**, *6*, 3804-3814.
[323] S. Sen, D. Liu, G. T. R. Palmore, *ACS Catalysis* **2014**, *4*, 3091-3095.

[324] B. Schorr, H. Ghanem, S. Rosiwal, W. Geissdorfer, A. Burkovski, *World J Microbiol Biotechnol* **2019**, *35*, 48.
[325] M. Polyakov, A.-E. Surkus, A. Maljusch, S. Hoch, A. Martin, *ChemElectroChem* **2017**, *4*, 2109-2116.
[326] B. You, N. Jiang, M. Sheng, S. Gul, J. Yano, Y. Sun, *Chem. Mater.* **2015**, *27*, 7636-7642.
[327] M. J. Johnson, C. Majmudar, J. J. Skolimowski, M. Majda, *The Journal of Physical Chemistry B* **2001**, *105*, 9002-9010.
[328] A. Ikeda, K. Terada, M. Shiotsuki, F. Sanda, *Journal of Polymer Science Part A: Polymer Chemistry* **2011**, *49*, 3783-3796.
[329] I. Bertini, C. Luchinat, G. Parigi, *Solution NMR of paramagnetic molecules: applications to metallobiomolecules and models*, Elsevier, **2001**.
[330] J. J. Warren, J. M. Mayer, *Journal of the American Chemical Society* **2010**, *132*, 7784-7793.
[331] L. Xue, E. Gurung, G. Tamas, Y. P. Koh, M. Shadeck, S. L. Simon, M. Maroncelli, E. L. Quitevis, *Journal of Chemical & Engineering Data* **2016**, *61*, 1078-1091.
[332] A. Das, S. S. Stahl, *Angewandte Chemie International Edition* **2017**, *56*, 8892-8897.
[333] C.-X. Miao, L.-N. He, J.-Q. Wang, J.-L. Wang, *Advanced Synthesis & Catalysis* **2009**, *351*, 2209-2216.
[334] C. Gütz, B. Klöckner, S. R. Waldvogel, *Organic Process Research & Development* **2015**, *20*, 26-32.
[335] M. B. Stevens, L. J. Enman, A. S. Batchellor, M. R. Cosby, A. E. Vise, C. D. M. Trang, S. W. Boettcher, *Chem. Mater.* **2017**, *29*, 120-140.
[336] H. Walter, *Struktur adsorbierter Polyampholytschichten*, **1999**.
[337] J. Lyklema, J. F. Duval, *Adv Colloid Interface Sci* **2005**, *114-115*, 27-45.
[338] J. O. Howell, W. G. Kuhr, R. E. Ensman, R. M. Wightman, *J. Electroanal. Chem.* **1986**, *209*, 77-90.
[339] R. Nanda, G. Rai, A. Kumar, *Journal of Solution Chemistry* **2015**, *44*, 742-753.
[340] M. Hesse, H. Meier, B. Zeeh, *Spektroskopische Methoden in der organischen Chemie*, Georg Thieme Verlag, **2005**.
[341] S. T. Handy, M. Okello, *The Journal of Organic Chemistry* **2005**, *70*, 1915-1918.
[342] S. Zhao, X. Tian, Y. Ren, J. Wang, J. Liu, Y. Ren, *J Mol Model* **2016**, *22*, 195.
[343] A. M. Oickle, J. Tom, H. A. Andreas, *Carbon* **2016**, *110*, 232-242.
[344] A. E. Visser, J. D. Holbrey, R. D. Rogers, *Chemical Communications* **2001**, 2484-2485.
[345] N. Nakajima, Y. Ikada, *Bioconjugate chemistry* **1995**, *6*, 123-130.
[346] J. C. Sheehan, J. J. Hlavka, *The Journal of Organic Chemistry* **1956**, *21*, 439-441.
[347] B. Neises, W. Steglich, *Angewandte Chemie International Edition in English* **1978**, *17*, 522-524.

9 Appendix

9.1. Cross linking mechanism using EDC

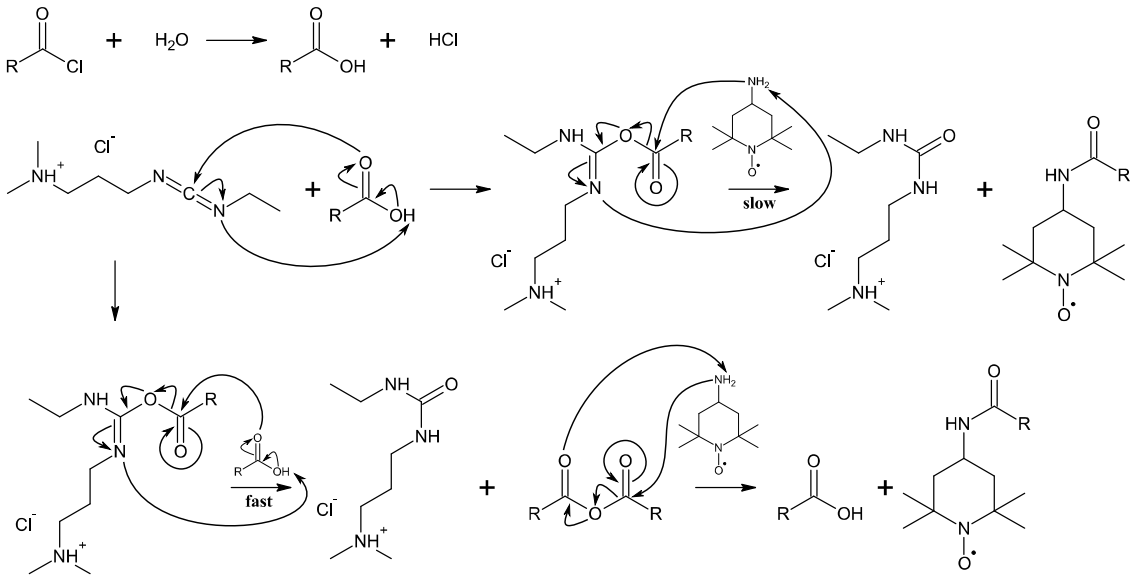

Figure 61: EDC cross linking mechanism.[345],[346]

9.2. Steglich esterification using DMAP

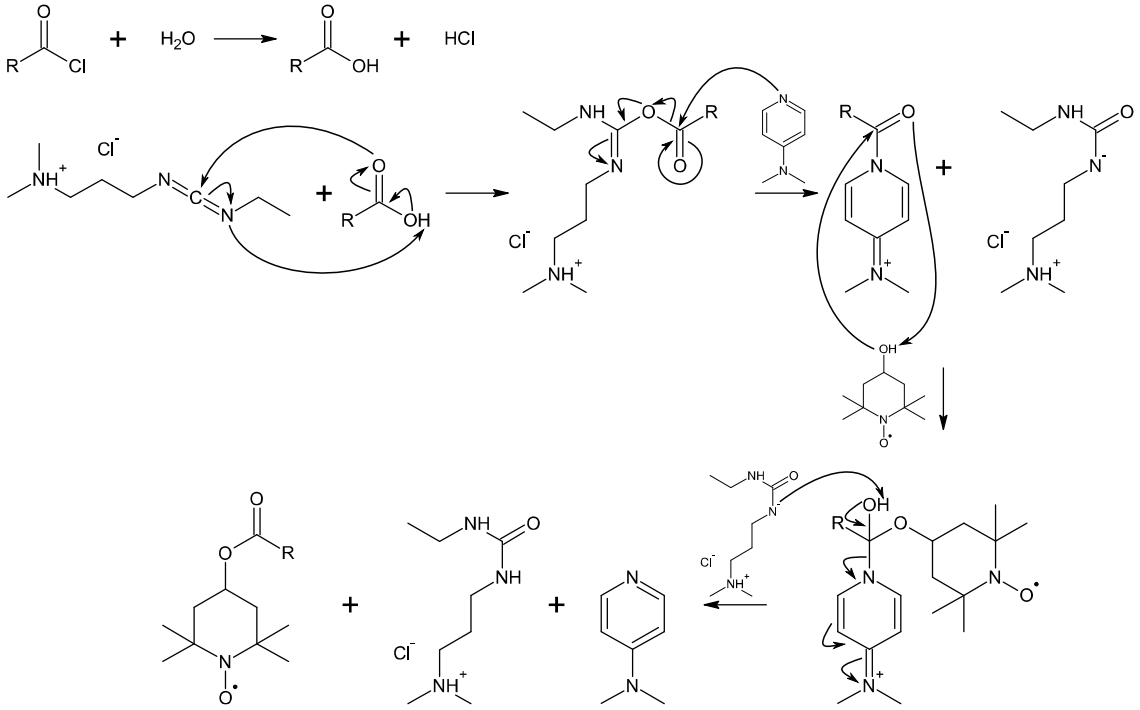

Figure 62: Steglich esterification using DMAP.[347]

9.3. ^{1}H-NMR of used chemicals

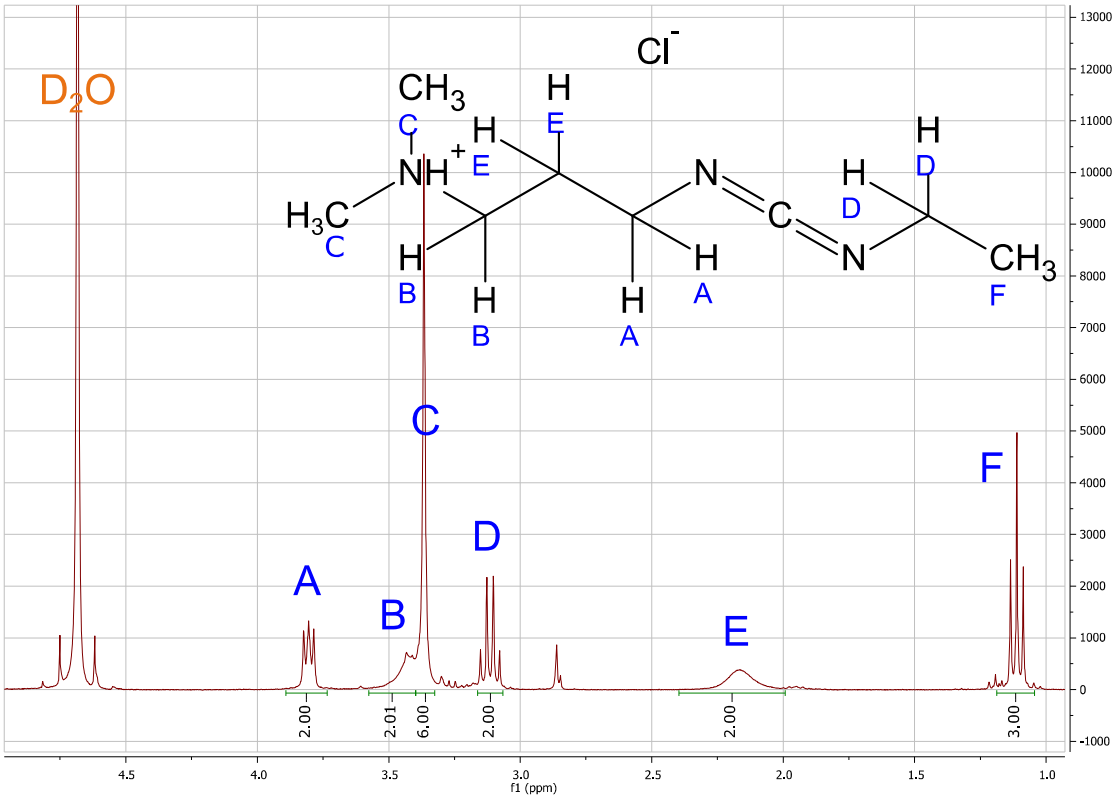

Figure 63: ^{1}H-NMR of EDC in D_2O.

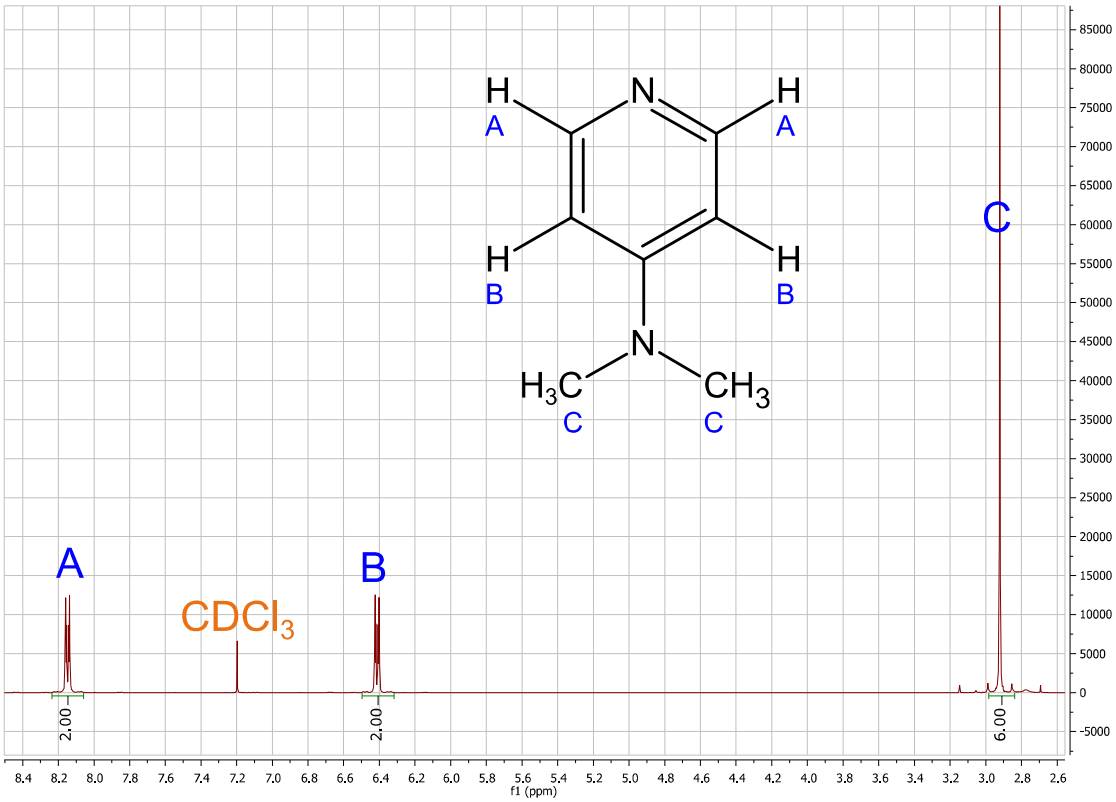

Figure 64: ^{1}H-NMR of DMAP in $CDCl_3$.

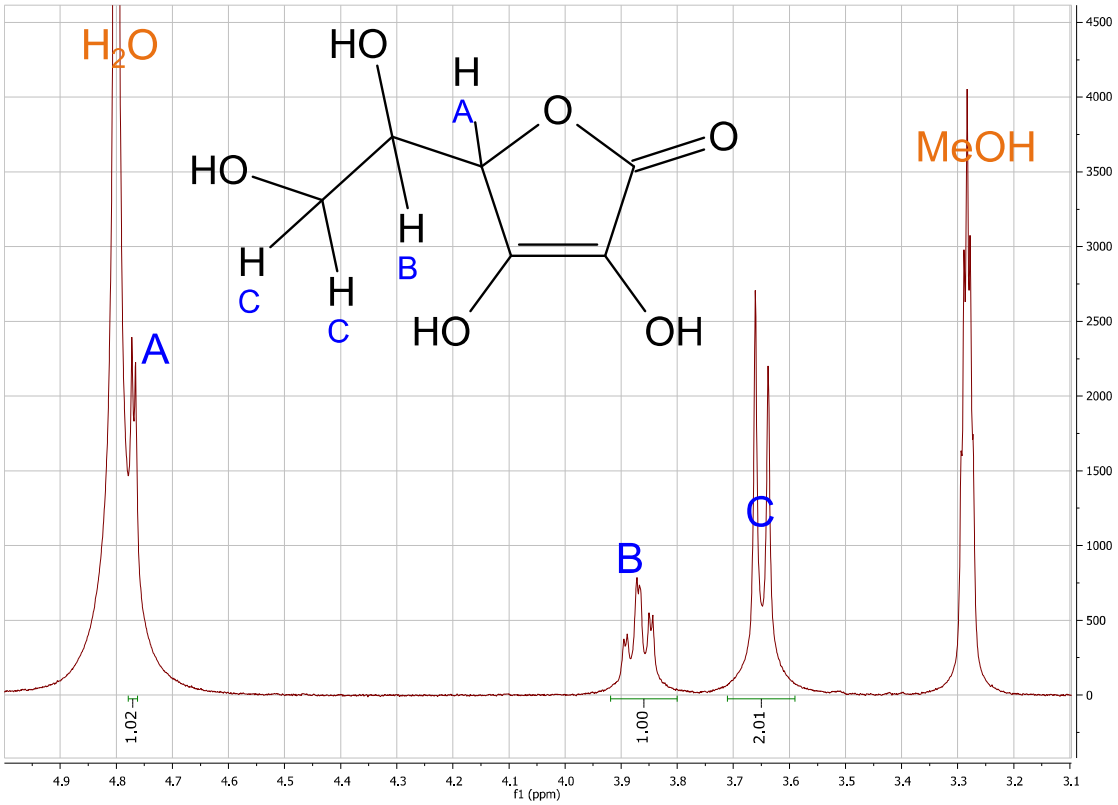

Figure 65: ^{1}H-NMR of ascorbic acid in MeOH-d$_4$.

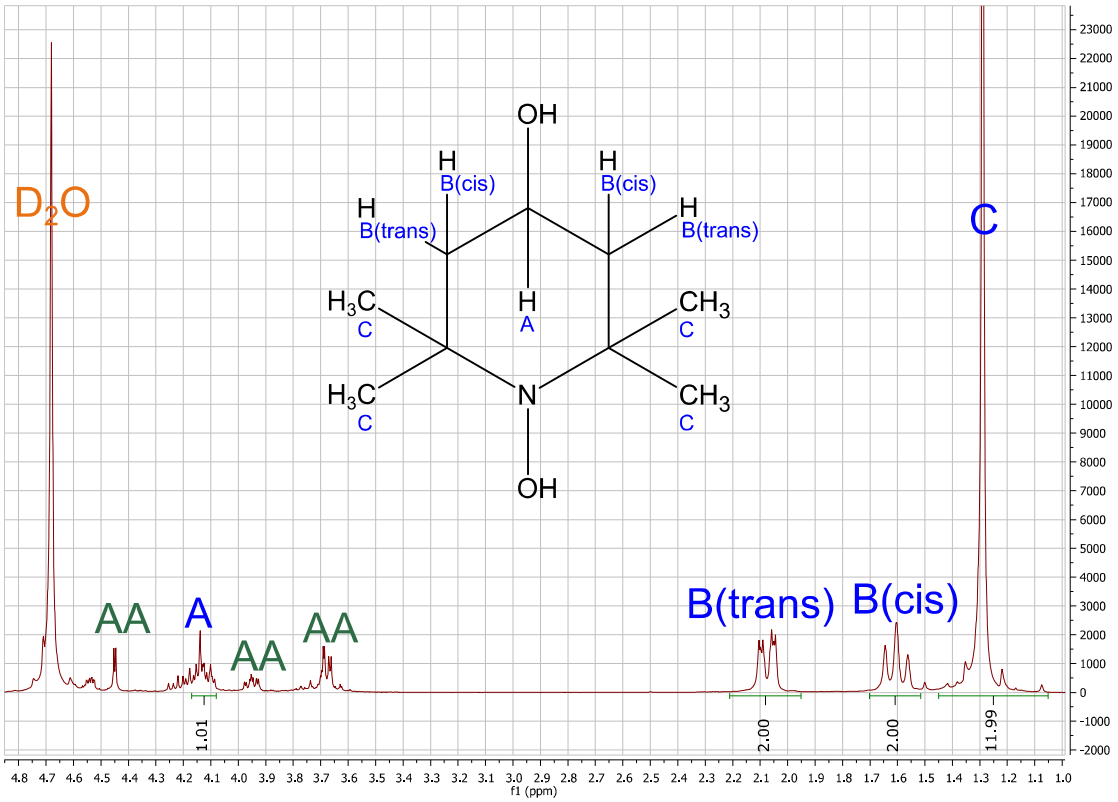

Figure 66: ^{1}H-NMR of HT in D$_2$O.

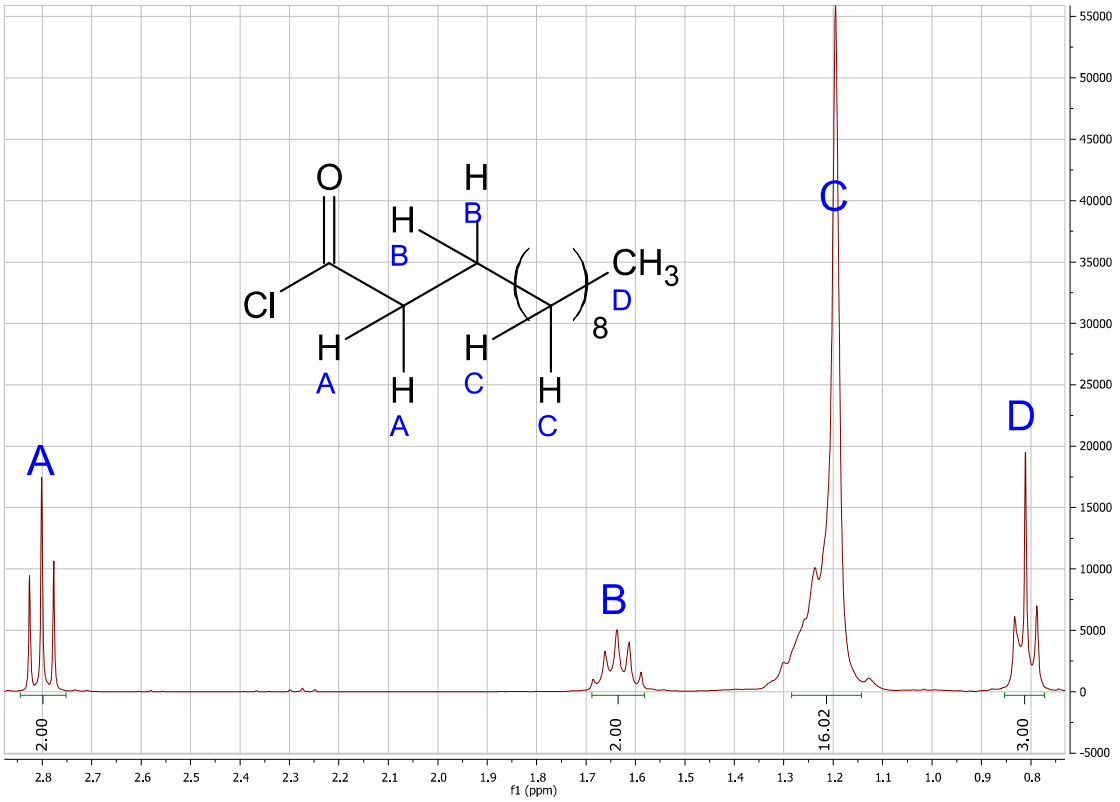

Figure 67: ^{1}H-NMR of C12OCl in D_2O.

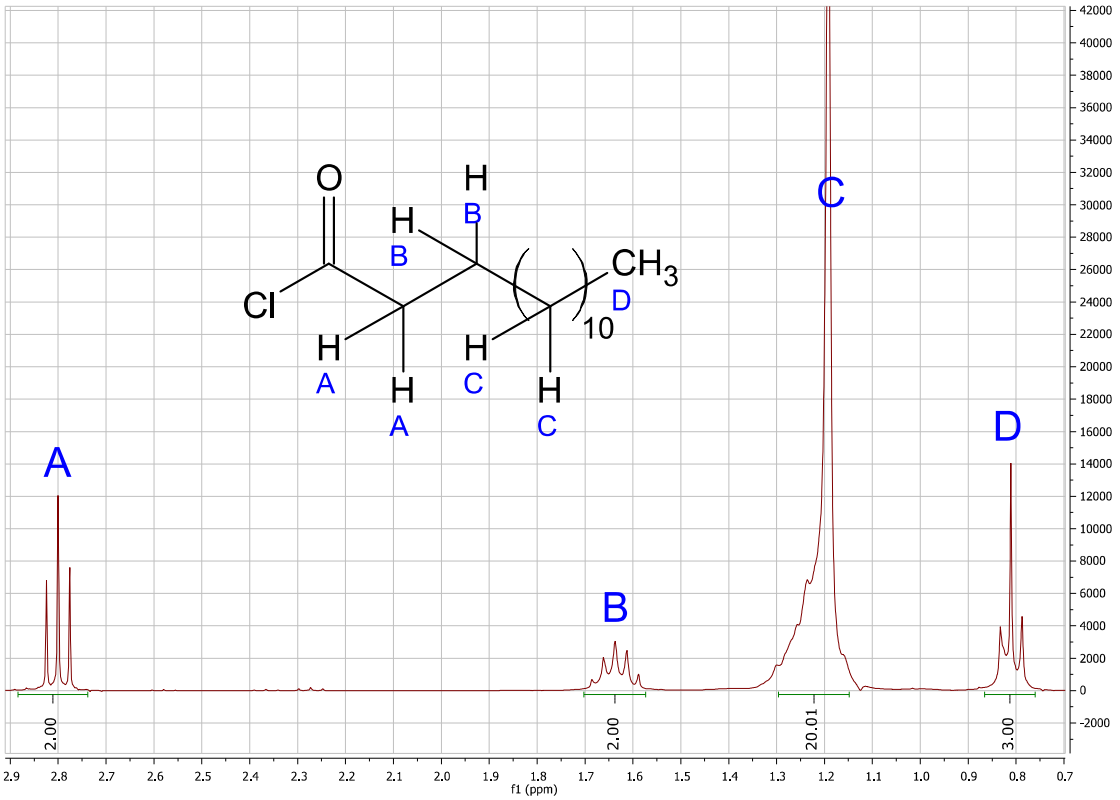

Figure 68: ^{1}H-NMR of C14OCl in D_2O.

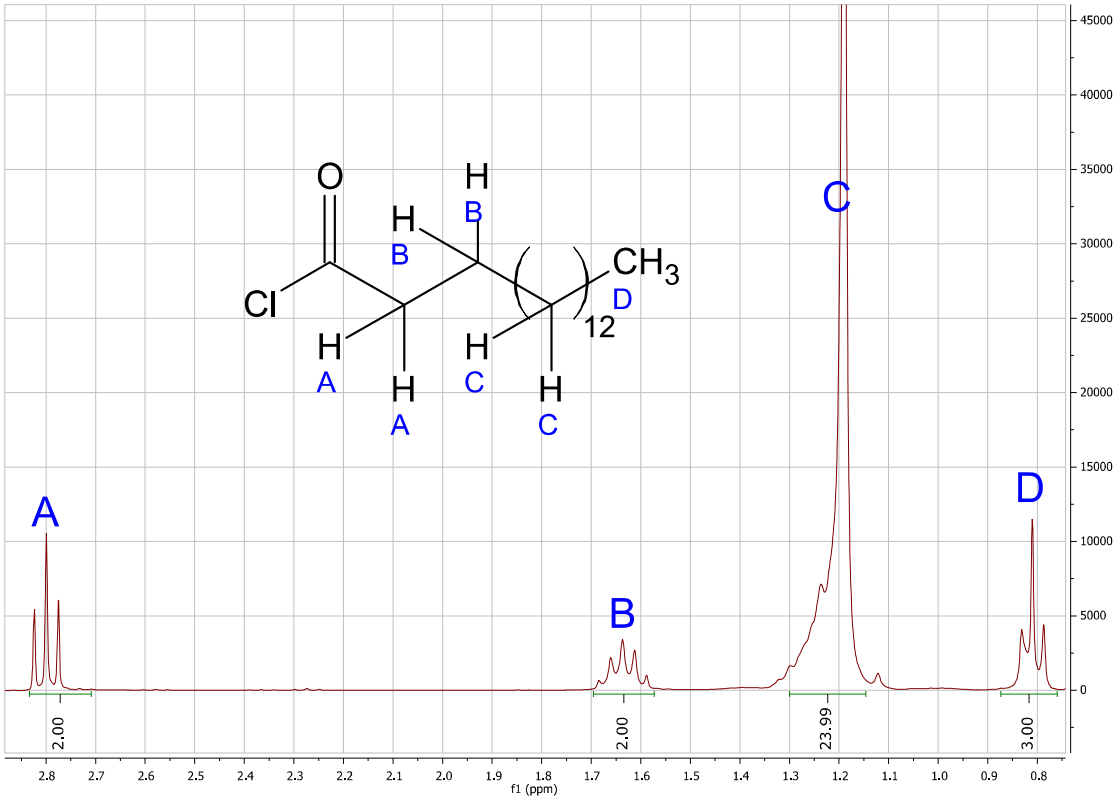

Figure 69: ^{1}H-NMR of C16OCl in D_2O.

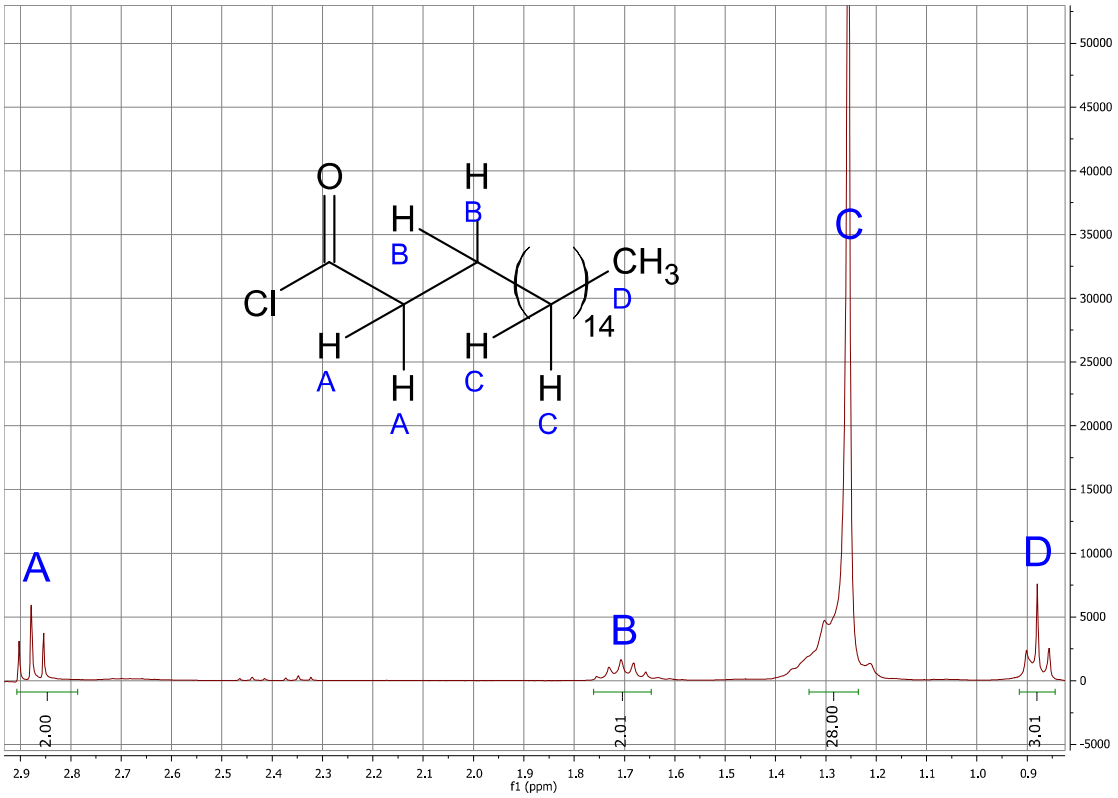

Figure 70: ^{1}H-NMR of C18OCl in D_2O.

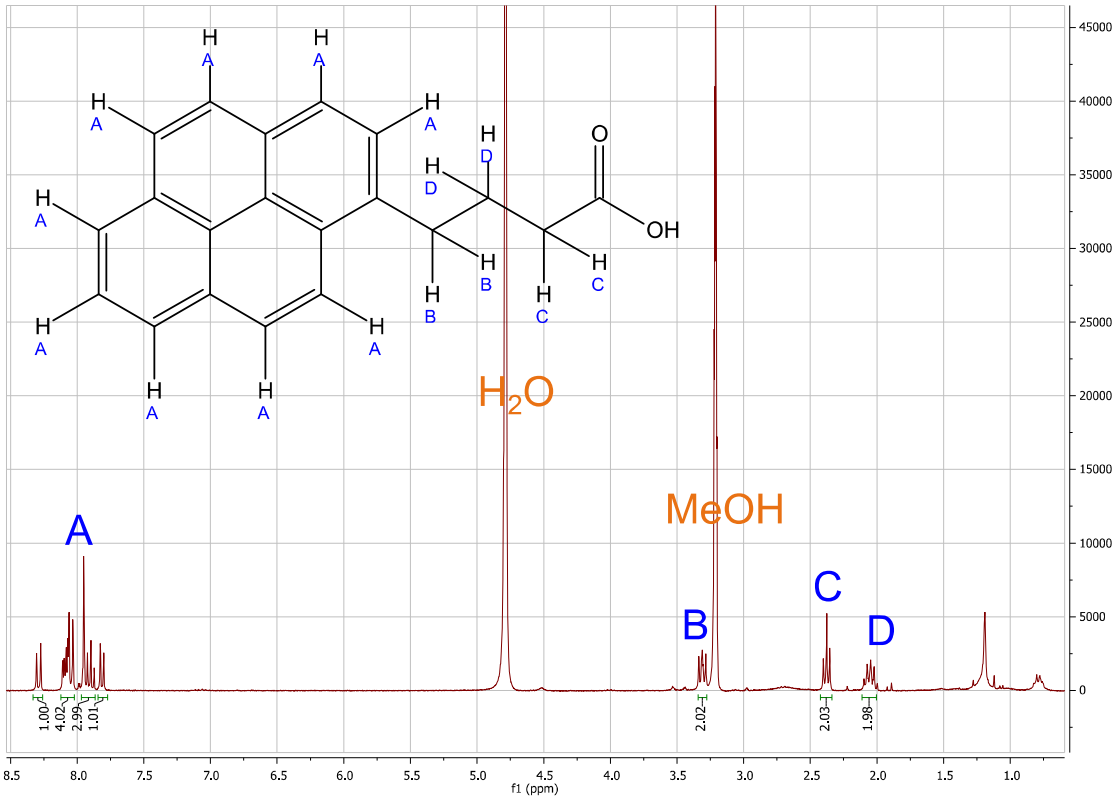

Figure 71: ^{1}H-NMR of pyrenebutyric acid in MeOH-d$_4$.

9.4. ^{1}H-NMR of synthesized TEMPO derivatives

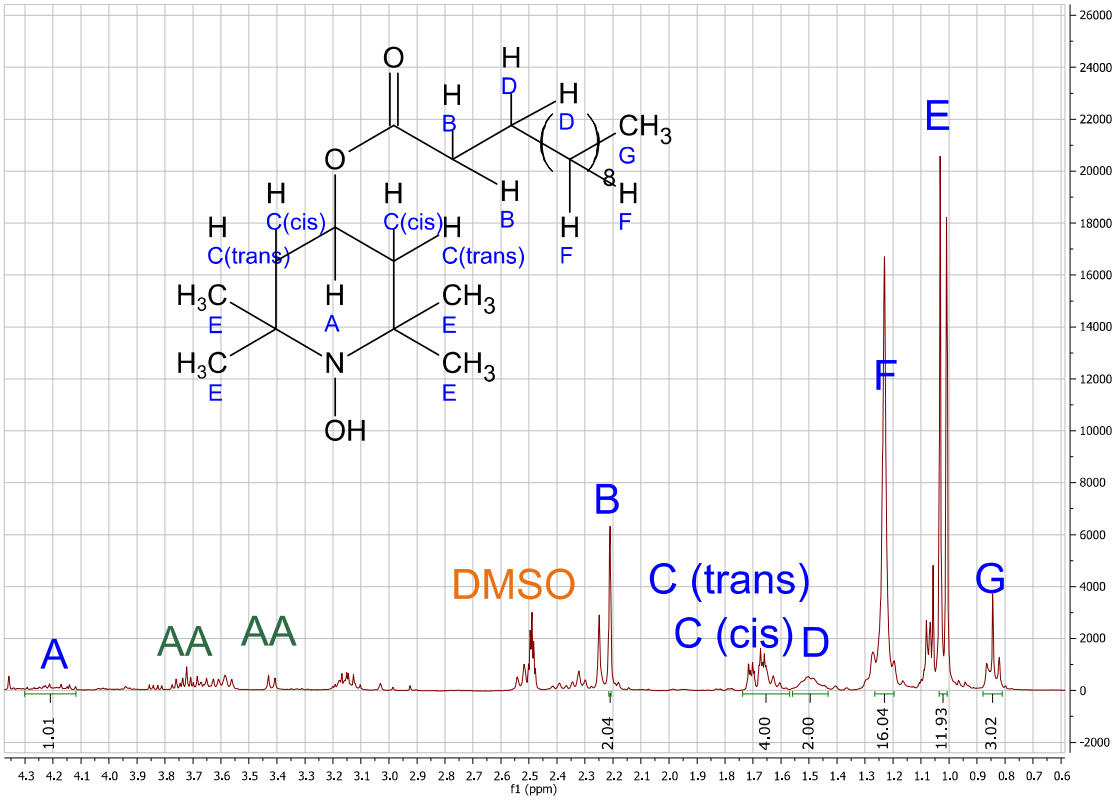

Figure 72: ^{1}H-NMR of C12-HT in DMSO-d$_6$.

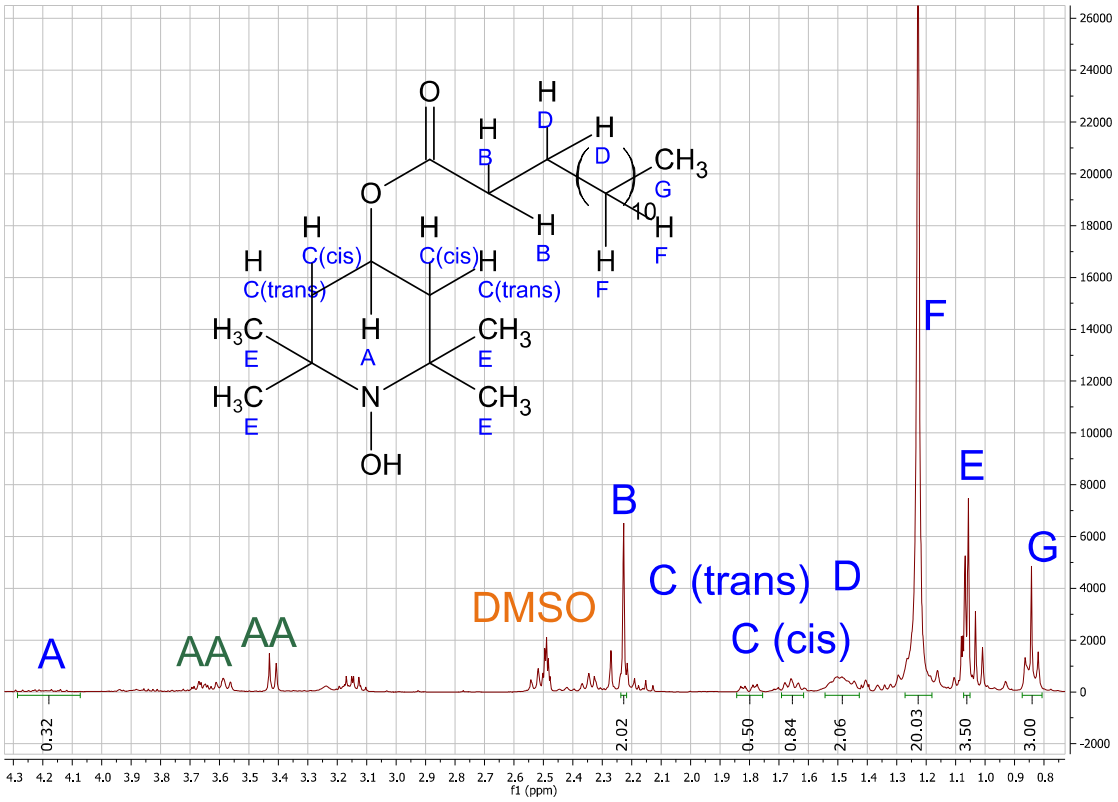

Figure 73: ^{1}H-NMR of C14-HT in DMSO-d_6.

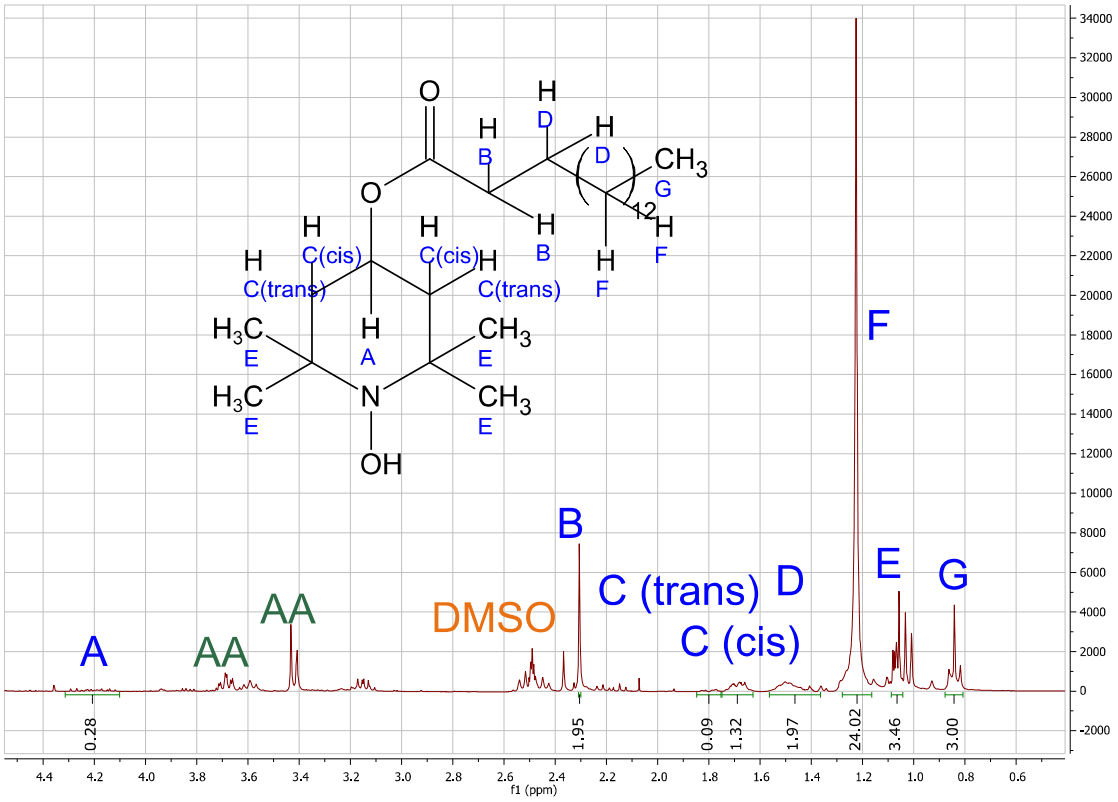

Figure 74: ^{1}H-NMR of C16-HT in DMSO-d_6.

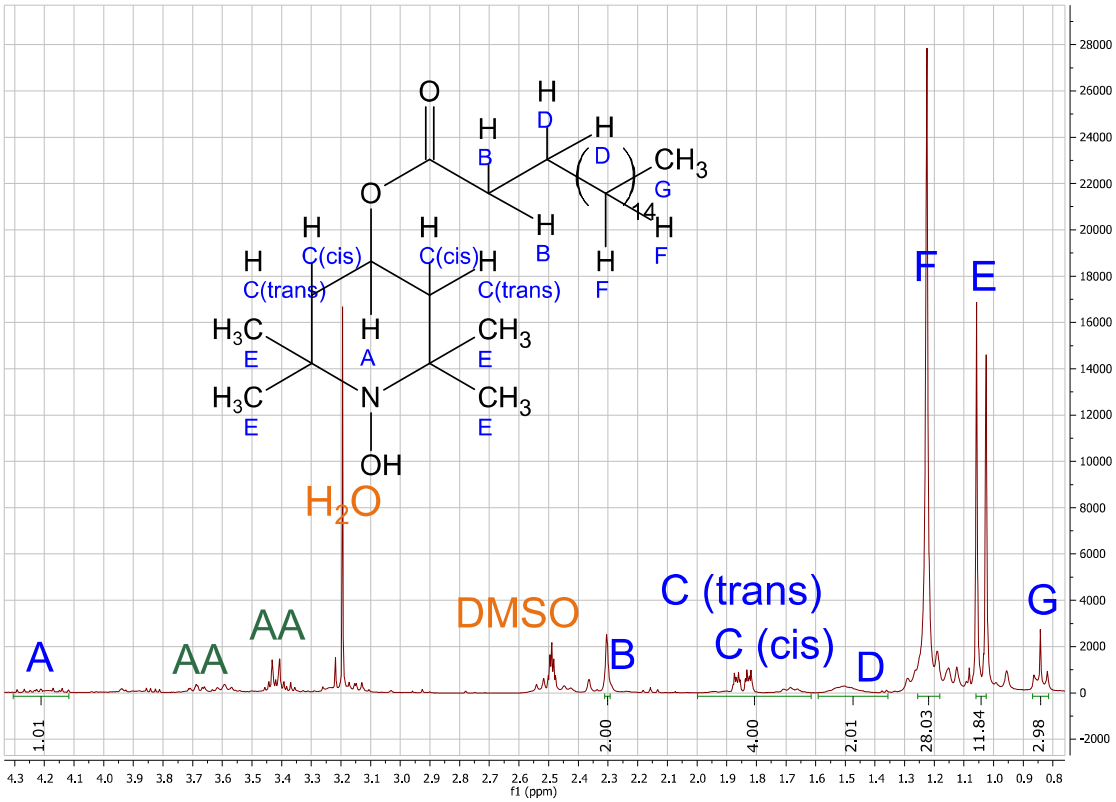

Figure 75: ^{1}H-NMR of C18-HT in DMSO-d_6.

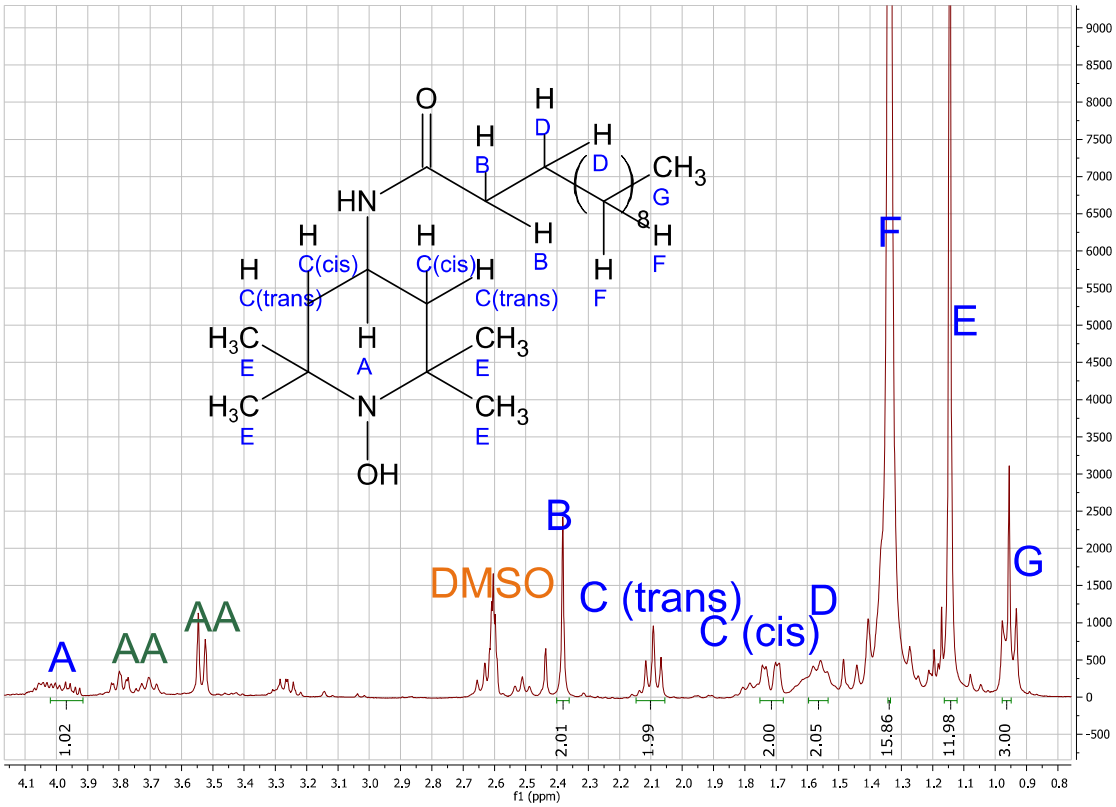

Figure 76: ^{1}H-NMR of C12-AT in DMSO-d_6.

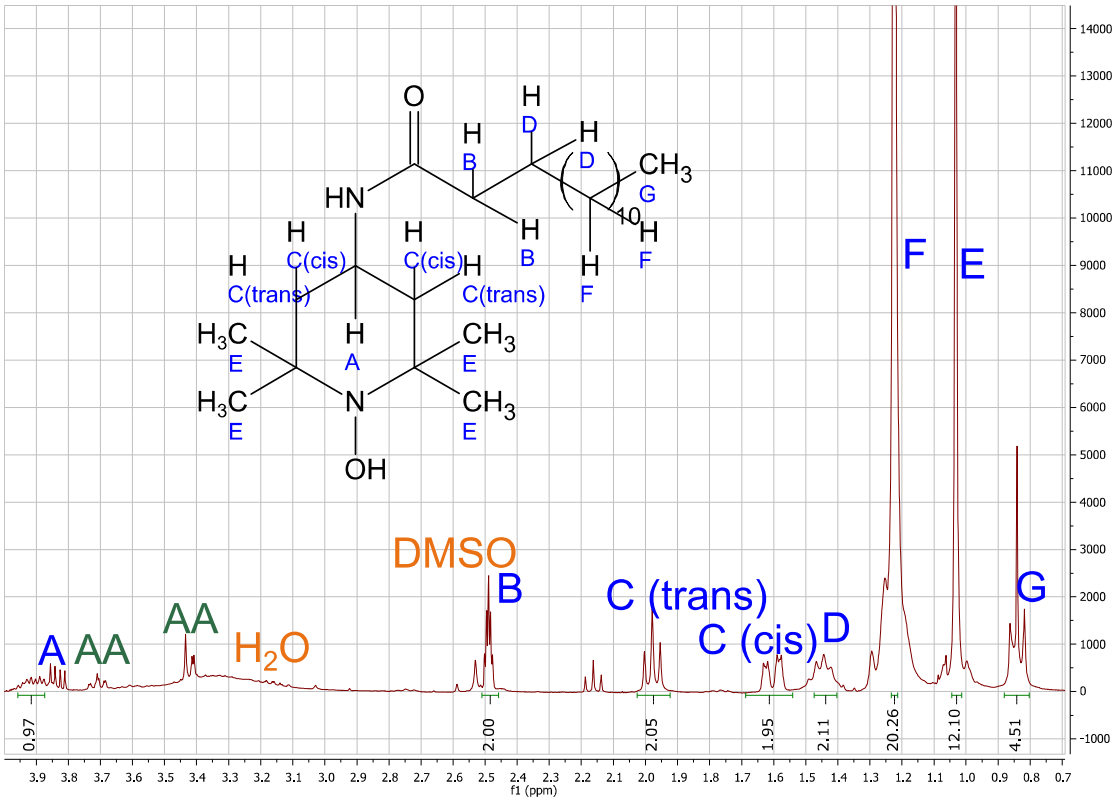

Figure 77: ^{1}H-NMR of C14-AT in DMSO-d_6.

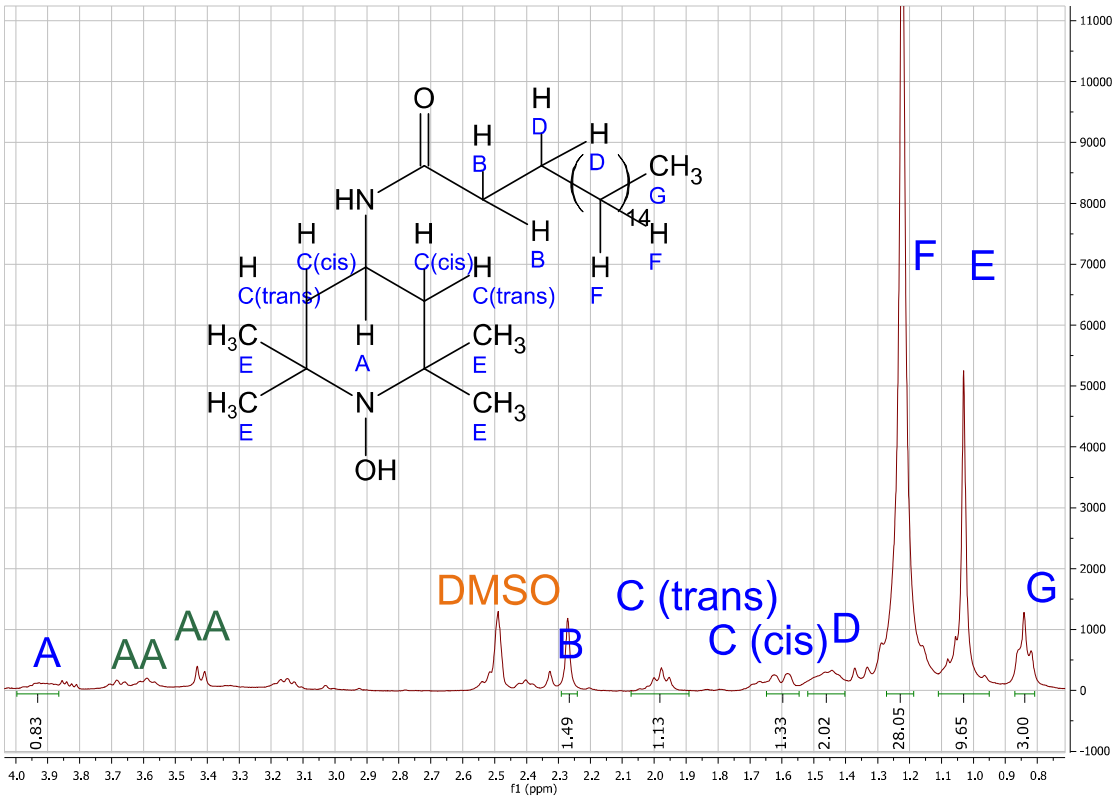

Figure 78: ^{1}H-NMR of C18-AT in DMSO-d_6.

9.5. ^{19}F-NMR of synthesized TEMPO derivatives

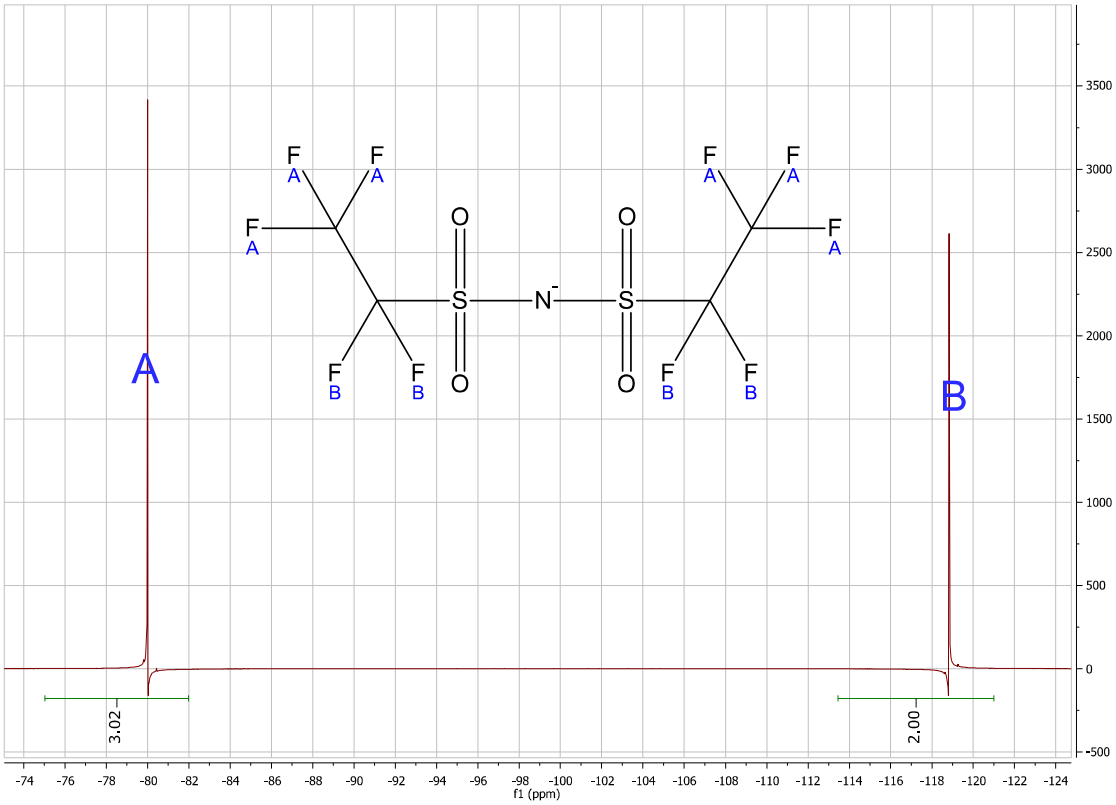

Figure 79: ^{19}F-NMR of the second step product of HTMIM BETI synthesis in DMSO-d$_6$.

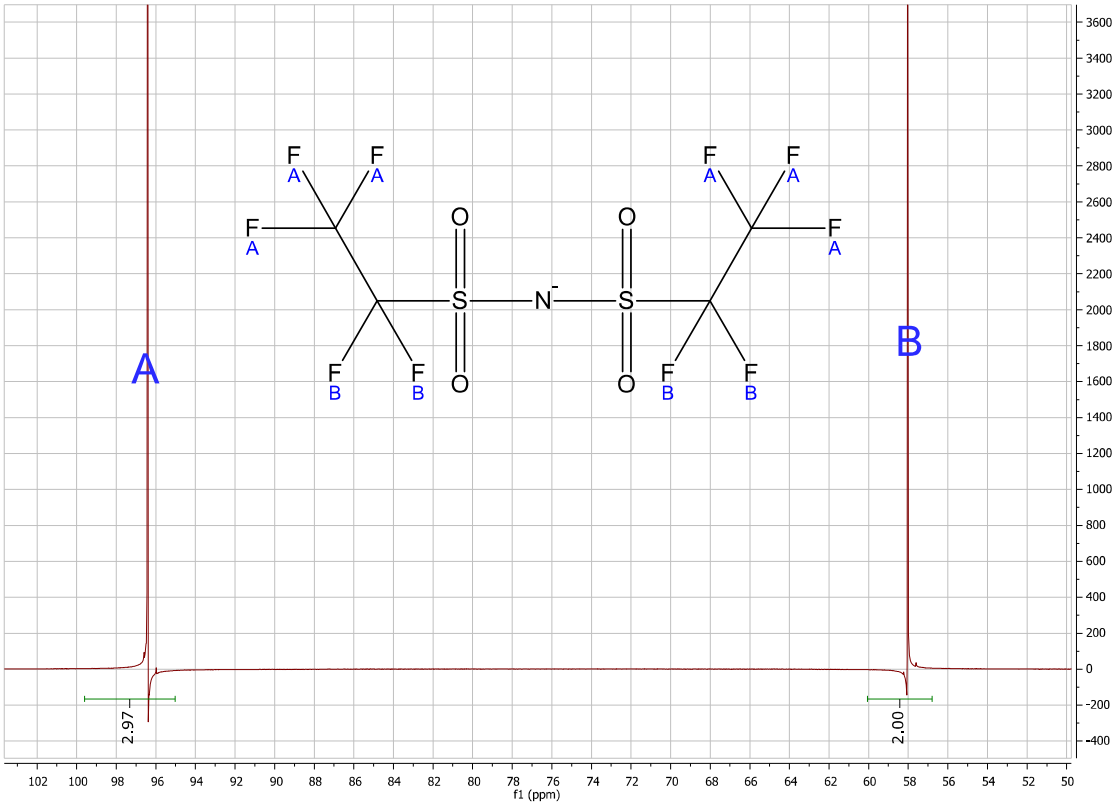

Figure 80: ^{19}F-NMR of the second step product of ATMIM BETI synthesis in DMSO-d$_6$.

9.6. ESR measurements of synthesized TEMPO derivatives

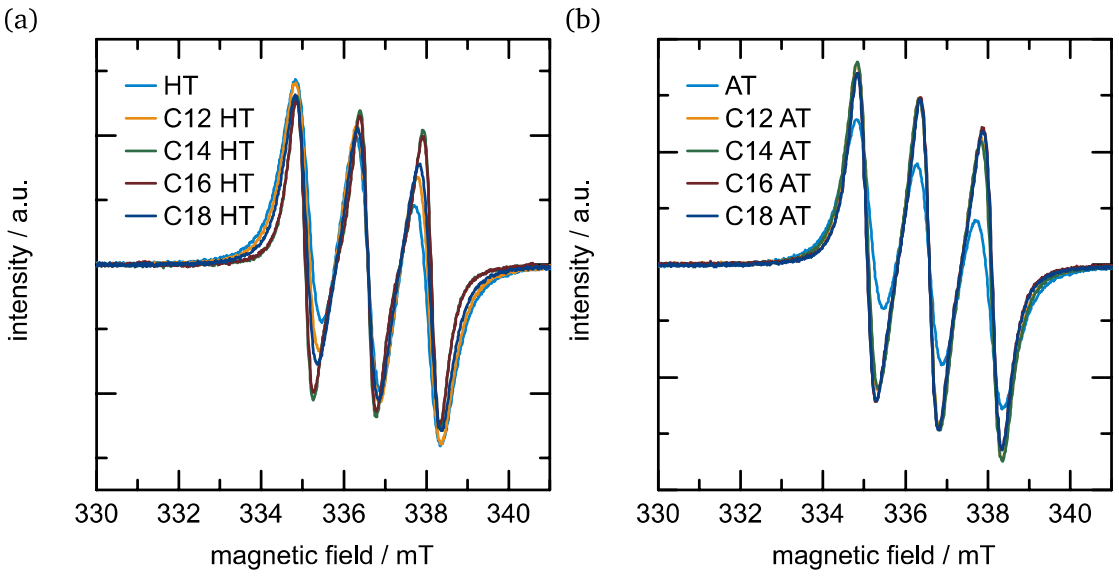

Figure 81: ESR measurements of HT and AT derivatives.

9.7. ^{1}H NMR of synthesized ILs

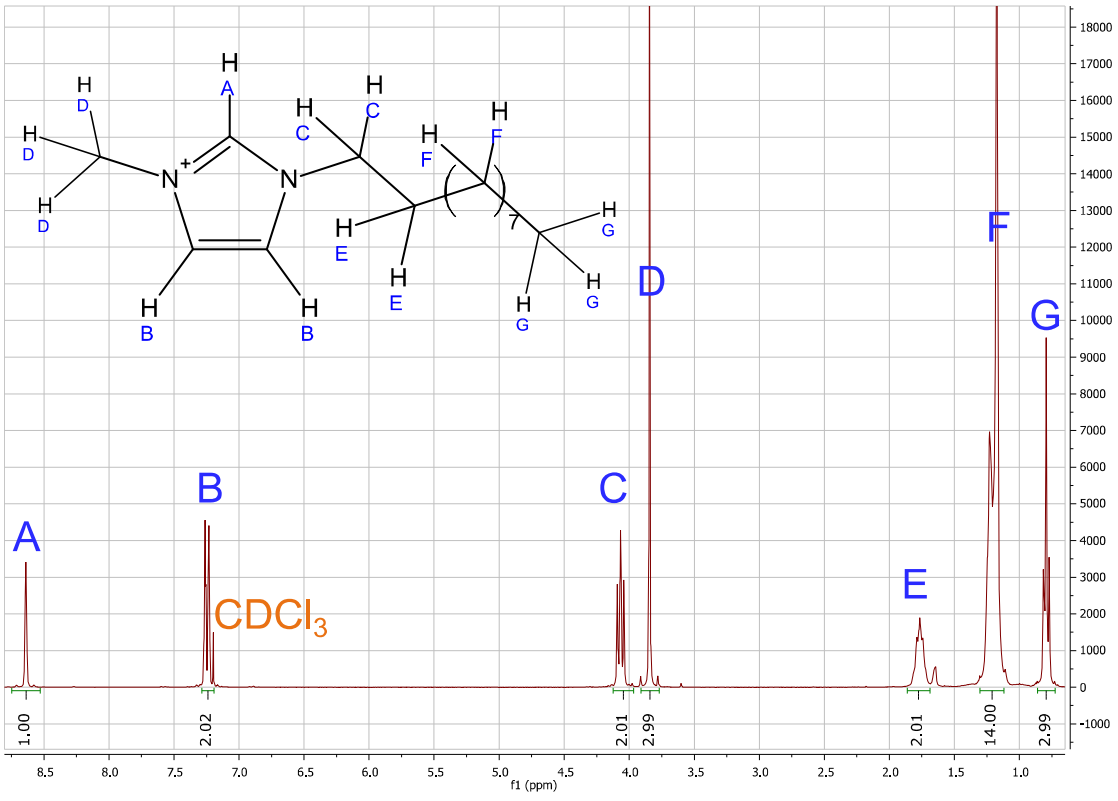

Figure 82: ^{1}H-NMR of C10MIM BETI in $CDCl_3$.

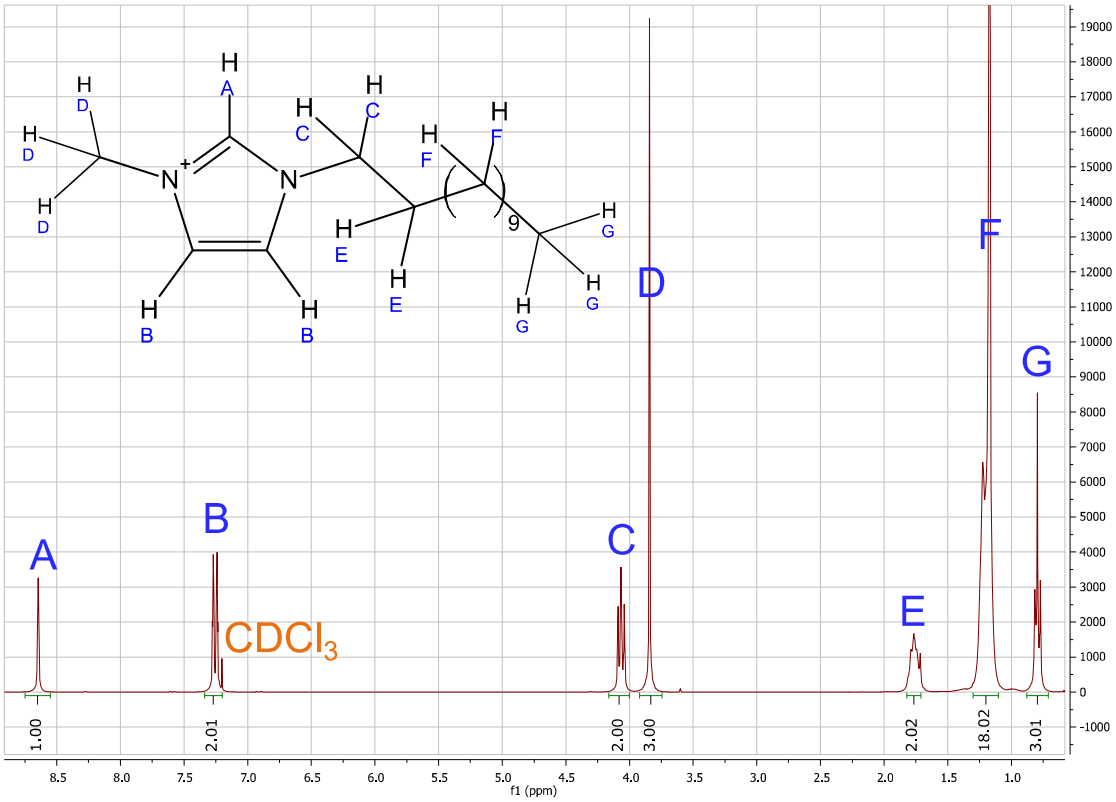

Figure 83: ^{1}H-NMR of C12MIM BETI in $CDCl_3$.

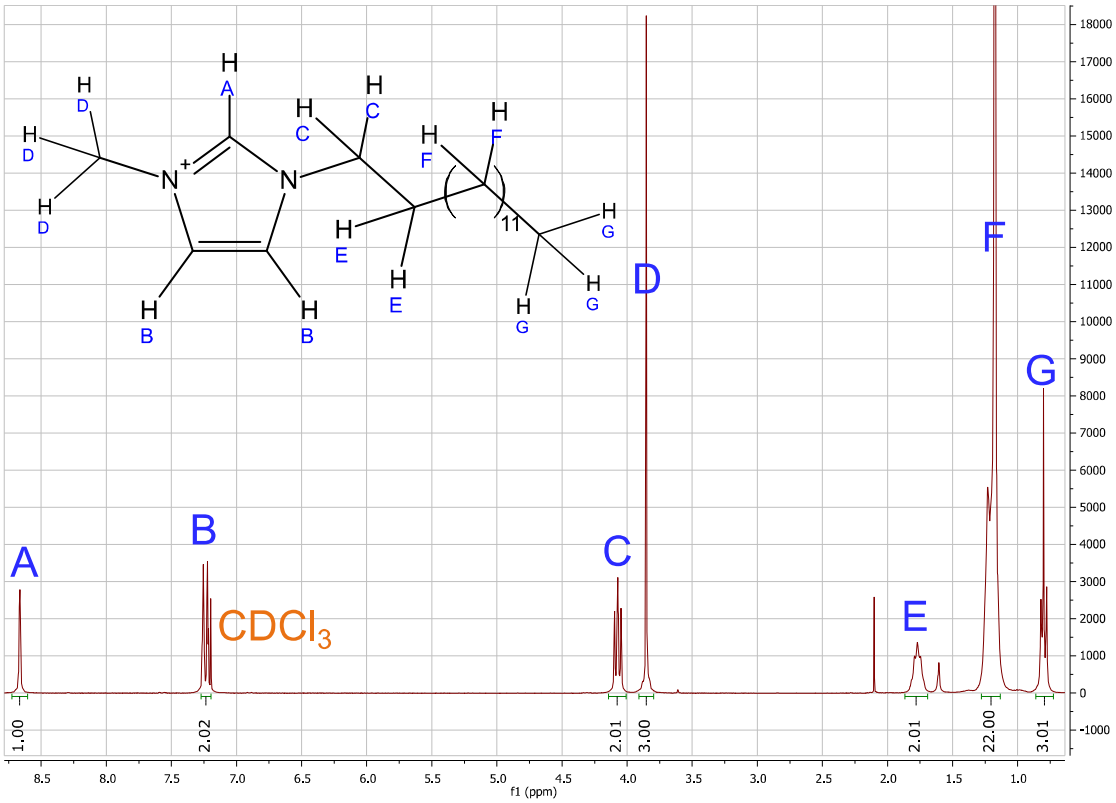

Figure 84: ^{1}H-NMR of C14MIM BETI in $CDCl_3$

9.8. SEM pictures of MPL 39 BB

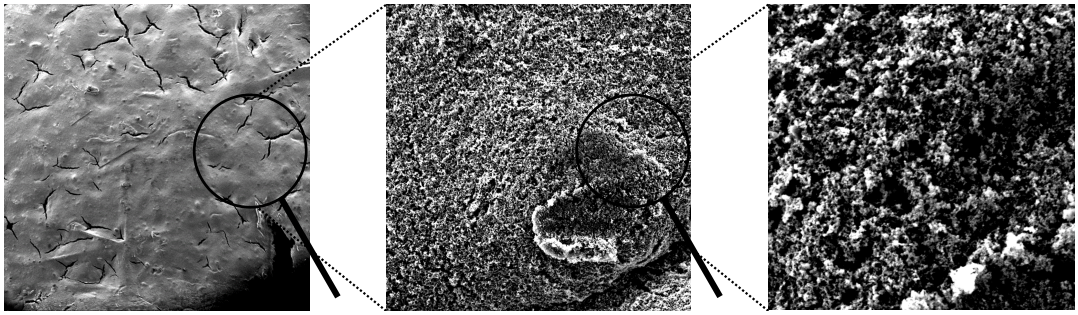

Figure 85: SEM pictures of MPL 39 BB with magnitude 49, 3000 and 12000 (left to right).

9.9. Additional electrochemical measurements

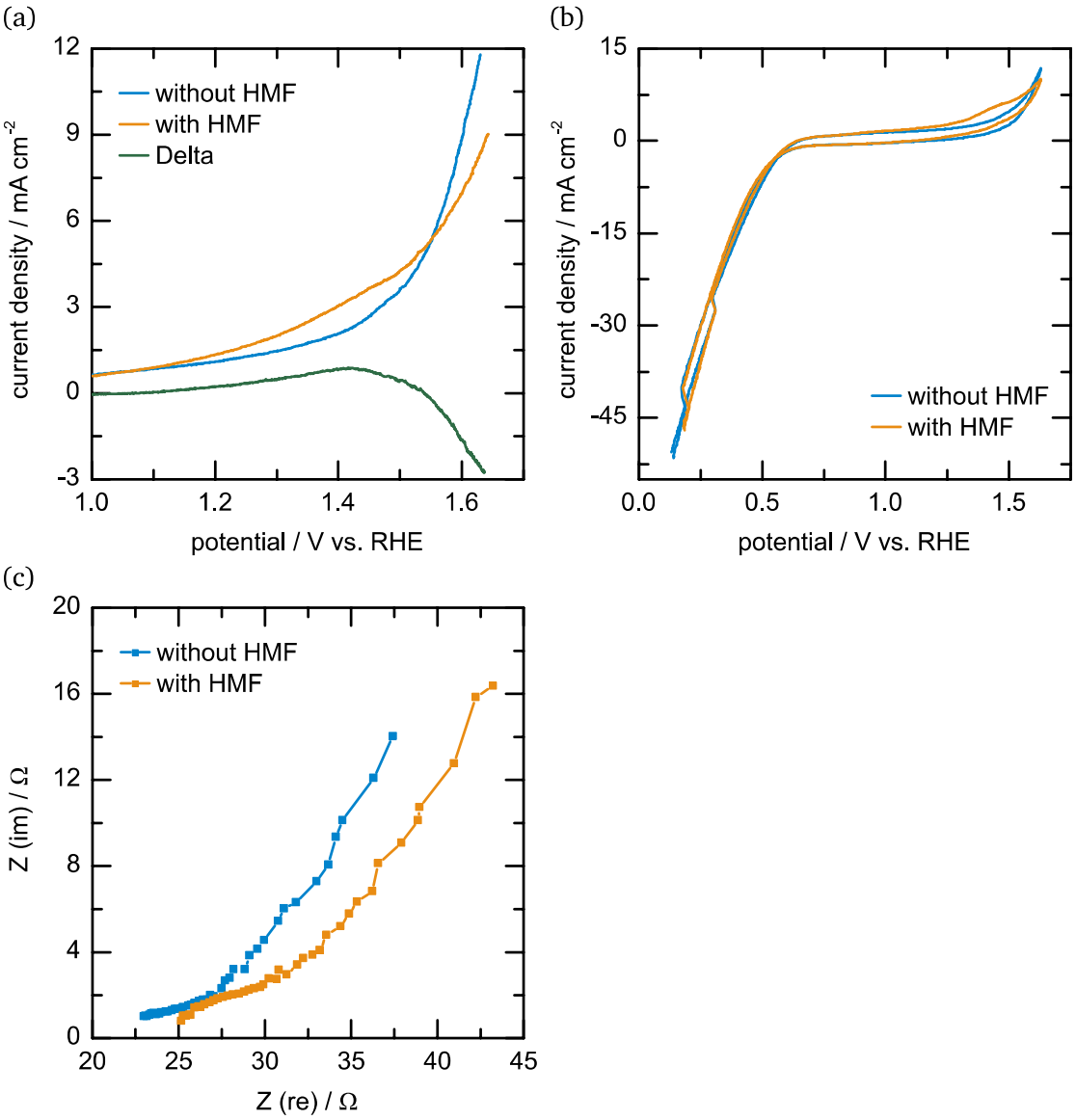

Figure 86: CVs at the HMF oxidation potential range (1.0 – 1.75 V vs. RHE) (a) and at a broad potential range (0 – 1.75 V vs. RHE) (b) of MT in C6MIM NTf_2 on PDC on MPL 39 BB without (blue), with 5 mM HMF (orange) and their difference (green) in 0.1 M KOH vs. Hg/HgO with Pt as CE. (c) EIS measurements of MT in C4MIM BETI on PDC on MPL 39 BB without (blue) and with 5 mM HMF (orange) in 0.1 M KOH vs. Hg/HgO with Pt as CE.

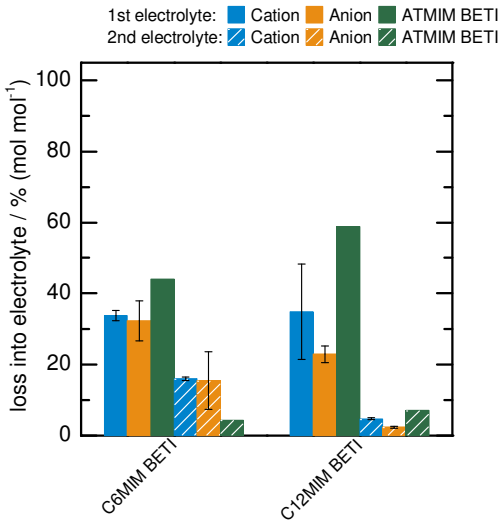

Figure 87: Loss into electrolyte of C6MIM or C12MIM (blue), BETI (orange) and ATMIM BETI (green) after the leaching test in the first (filled bars) and the second electrolyte (striped bars).